



HAL
open science

Comportement mécanique des carbonates peu poreux : étude expérimentale et modélisation micromécanique

Aurélien Pierre Nicolas

► **To cite this version:**

Aurélien Pierre Nicolas. Comportement mécanique des carbonates peu poreux : étude expérimentale et modélisation micromécanique. Sciences de la Terre. Ecole normale supérieure - ENS PARIS, 2015. Français. NNT : 2015ENSU0040 . tel-01598650

HAL Id: tel-01598650

<https://theses.hal.science/tel-01598650>

Submitted on 29 Sep 2017

HAL is a multi-disciplinary open access archive for the deposit and dissemination of scientific research documents, whether they are published or not. The documents may come from teaching and research institutions in France or abroad, or from public or private research centers.

L'archive ouverte pluridisciplinaire **HAL**, est destinée au dépôt et à la diffusion de documents scientifiques de niveau recherche, publiés ou non, émanant des établissements d'enseignement et de recherche français ou étrangers, des laboratoires publics ou privés.



Laboratoire de Géologie, École Normale Supérieure
École Doctorale des Sciences de la Terre

Thèse présentée en vue de l'obtention du titre de
DOCTEUR DE L'ÉCOLE NORMALE SUPÉRIEURE

Spécialité: Géophysique

par

AURÉLIEN NICOLAS

**Comportement mécanique des carbonates peu poreux:
Étude expérimentale et modélisation micro-mécanique**

Soutenance prévue le 27 Novembre 2015, devant le jury composé de:

Pr. T.F. WONG	Rapporteur	ESSC, Chinese University of Hong-Kong
Y.M. LEROY	Rapporteur	TOTAL, Pau, France
Pr. C. DAVID	Examineur	Université de Cergy-Pontoise, France
Pr. P. BAUD	Examineur	Université de Strasbourg, France
Pr. Y. GUÉGUEN	Directeur de Thèse	École Normale Supérieure, Paris, France
J. FORTIN	co-Directeur de Thèse	École Normale Supérieure, Paris, France
P. MARCHINA	Invité	TOTAL, Pau, France
A. DIMANOV	Invité	LMS, École Polytechnique, France

CONTENTS

Abstracts (Français & English)	1
Avant-propos	5
Remerciements	7
Introduction	11
1 Brittle and semibrittle behaviours of a carbonate rock: Influence of water and temperature	35
1.1 Introduction	36
1.2 Material and methods	38
1.2.1 Rock material and sample preparation	38
1.2.2 Experimental apparatus	40
1.2.3 Elastic wave velocities	41
1.2.4 Experimental procedure	41
1.3 Results	46
1.3.1 Mechanical behaviour during isostatic loading	46
1.3.2 Mechanical behaviour during deviatoric loading	46
1.3.3 Post mortem microstructural analysis	49
1.3.4 Evolution of elastic wave velocities during triaxial loading	52
1.4 Discussion	59
1.4.1 From inverted crack density to macroscopic deformation at isostatic stress	59
1.4.2 Crack densities under triaxial stresses	61
1.4.3 Onset and development of dilatancy in the brittle regime	64
1.4.4 Failure envelope in the brittle regime	66
1.4.5 From inelastic compaction to dilatancy in the semibrittle regime	67

Contents

1.4.6 Crack geometry	70
1.5 Concluding summary	74
Supplements	76
2 Micromechanical constitutive model for constant strain rate deformation of lime-	
stones	79
2.1 Introduction	80
2.2 Development of the constitutive model	82
2.2.1 Elastic moduli of the cracked and deformed solid	82
2.2.2 Macroscopic strains related to crack growth	83
2.2.3 Macroscopic strains related to dislocations	86
2.2.4 Crack nucleation from pile-ups	91
2.2.5 Stress strain relation during constant strain rate deformation	93
2.3 Choice of material properties and sensitivity to these parameters	94
2.3.1 Parameters relevant to elastic properties and cracks	94
2.3.2 Parameters relevant to plasticity and dislocations	95
2.4 Results and discussion	98
2.4.1 Prediction of the stress/strain response	98
2.4.2 Comparison with available data	101
2.4.3 Limits of the model and possible applications	107
2.5 Conclusion	109
3 Brittle and semibrittle creep in a carbonate rock	113
3.1 Introduction	114
3.2 Experimental methods	116
3.2.1 Rock material and sample preparation	116
3.2.2 Experimental apparatus	116
3.2.3 Elastic wave velocities	118
3.2.4 Experimental procedure	119
3.3 Results	120
3.3.1 Mechanical behaviour during constant strain rate deformation	121
3.3.2 Mechanical behaviour during stress-stepping creep experiments	122

3.3.3	Crack densities	130
3.3.4	Strain rates during stress-stepping creep experiments	133
3.4	Discussion	137
3.4.1	Mechanisms of deformation	137
3.4.2	Comparison with constant strain rate experiments	144
3.4.3	Maximum inelastic compaction	146
3.4.4	Stabilizing role of inelastic compaction	147
3.4.5	From case study to global concepts	147
3.5	Concluding summary	149
4 Micromechanical constitutive model for deformation of limestones under constant stress		153
4.1	Introduction	154
4.2	From constant strain rate deformation to creep	155
4.2.1	Subcritical crack growth	155
4.2.2	Ductile creep law and new crack nucleation	156
4.2.3	Properties of the material	156
4.2.4	Influence of previous deformation on the initial properties of calcite materials	157
4.2.5	Sensitivity analysis of the model	158
4.3	Results and discussion	161
4.3.1	Prediction of the strain evolution under constant stress	161
4.3.2	Comparison with available data	164
4.3.3	Limits of the model and comparison with constant strain rate deformation	170
4.4	Conclusion	171
5 Influence of strain rate on deformation and failure of a micritic limestone		173
5.1	Introduction	174
5.2	Experimental material and methods	175
5.3	Mechanical behaviour during deformation and rupture	175
5.4	Discussion	178
5.4.1	Effect of strain rate on deformation in the brittle regime	178

Contents

5.4.2 Ductile deformation under different strain rates	180
5.5 Conclusions and implications of these preliminary results	181
Conclusions & Perspectives	183
Bibliography	206

RÉSUMÉ

Avec l'augmentation de la pression de confinement, le comportement mécanique des calcaires passe d'un comportement fragile à un comportement ductile. Le régime fragile est caractérisé par une compaction élastique suivie d'une dilatance macroscopique due à des propagations de fissures. Lorsque les fissures coalescent, la rupture macroscopique est reliée à une chute de contrainte. Le régime ductile est caractérisé par une compaction élastique suivie d'une déformation macroscopique diffuse. La déformation est accommodée par une plasticité intracristalline (dislocations, macles) et/ou une fracturation des grains. L'objectif de cette thèse est d'examiner expérimentalement les paramètres influant sur le comportement mécanique des calcaires de porosité intermédiaire et de modéliser ce comportement. Les expériences ont été réalisées sur le calcaire de Tavel (porosité de 14.7%).

Des expériences de déformation triaxiale à vitesse constante et de fluage sous contrainte déviatorique constante ont été réalisées. La densité de fissures est calculée avec les vitesses ultrasoniques de propagation des ondes élastiques dans l'échantillon. Dans le cas des expériences de déformation triaxiale à vitesse constante, un comportement fragile est observé pour les confinements inférieurs ou égaux à 55 MPa, puis le comportement devient ductile lorsque la pression de confinement est augmentée. En régime ductile, une compaction inélastique est causée par l'effondrement des pores par plasticité intra-grains associée à une microfissuration. Une dilatance apparaît ensuite à cause de la nucléation de nouvelles fissures. La saturation en eau diminue la contrainte déviatorique nécessaire à la propagation des fissures et favorise la dilatance macroscopique. L'augmentation de la température diminue la pression de confinement à laquelle apparaît le comportement ductile. Un modèle de comportement macroscopique est dérivé à partir d'un modèle microscopique qui comprend (1) la propagation de fissures, (2) une loi de plasticité pour le milieu poreux et (3) une loi de nucléation de nouvelles fissures due aux empilements de dislocations. Le modèle prédit l'évolution de la déformation volumique, de la contrainte et de l'endommagement (densité de fissures) au cours de la déformation. Les prédictions sont en bon accord avec les résultats expérimentaux. Nous présentons ensuite des expériences de fluage par paliers pour caractériser l'effet du temps sur le comportement mécanique, en conditions sèches et saturées en eau. Les pressions de confinement considérées englobent la transition fragile-ductile. En régime fragile, une dilatance est observée lors des paliers de contrainte déviatorique constante. Cette dilatance est expliquée par la propagation sous-critique des fissures. Lorsque le comportement est semi-fragile (ductile), les premiers paliers de fluages présentent une compaction inélastique due à la micro-plasticité intra-cristalline. La déformation volumétrique devient ensuite dilatante. Cependant, la vitesse de déformation axiale reste contrôlée par les processus de plasticité. Au dernier palier, la vitesse de déformation axiale augmente significativement à cause de l'interaction des fissures menant à la rupture macroscopique. Les mécanismes de déformation observés lors des paliers sont similaires à ceux observés pendant les expériences

de déformation triaxiale à vitesse constante. En régime fragile, l'eau favorise la propagation des fissures. Pour prédire le comportement sous fluage, le modèle développé à partir des expériences de déformation à vitesse constante est enrichi avec une loi de croissance sous-critique des fissures et permet de simuler une dilatance à faible confinement. Ce modèle permet aussi de prédire une compaction inélastique suivie d'une dilatance lorsque la pression de confinement est supérieure à 55 MPa.

L'effet de la vitesse de déformation sur le comportement lors d'expériences de déformation triaxiale à vitesse constante est exploré. A faibles confinements, les résultats expérimentaux en régime fragile montrent une augmentation de la déformation axiale mais une diminution de la dilatance et une augmentation de la contrainte différentielle à la rupture. Ces observations peuvent être expliquées par la plasticité (par exemple par maclage) qui peut avoir lieu avec la diminution de la vitesse de déformation. En régime ductile, les résultats expérimentaux montrent que la plasticité est favorisée par la diminution de la vitesse de déformation. La déformation axiale à la rupture augmente très significativement lorsque la vitesse de déformation diminue. De plus, la chute de contrainte à la rupture diminue très fortement avec la diminution de la vitesse de déformation.

Les résultats montrent la complexité des mécanismes de déformation dans les calcaires. Les paramètres influents engendrent des différences de comportement macroscopique qui doivent être prises en compte dans les applications fondamentales et industrielles. L'extension de ces résultats à d'autres roches carbonatées (marbres, craies) reste à explorer.

Mots clefs: roches carbonatées, comportement mécanique, endommagement, plasticité, fluage, expériences de déformation à vitesse contrôlée

ABSTRACT

The mechanical behaviour of limestones is brittle at low confining pressure and becomes ductile with the increase of the confining pressure. The brittle behaviour is characterised by a macroscopic dilatancy due to crack propagation, leading to a stress drop when cracks coalesce at failure. The ductile behaviour is characterised by a diffuse deformation due to intra-crystalline plasticity (dislocation movements and twinning) and microcracking. The aim of this work is to examine the influence of temperature, pore fluid, strain rate, and time on the mechanical behaviour. Triaxial deformation experiments were performed on white Tavel limestone (porosity 14.7%). The macroscopic behaviour is then modelled.

Constant strain rate triaxial deformation experiments and stress-stepping creep experiments were performed. Elastic wave velocities were inverted in term of axial crack densities. The mechanical behaviour is brittle for constant strain rate deformation experiments performed at $P_c \leq 55$ MPa. In this case, inelastic deformation is due to cracks propagation. For $P_c \geq 70$ MPa, elastic compaction is followed by an inelastic compaction. Porosity collapse is due to intra-crystalline plasticity and micro-cracking. After some inelastic compaction, volumetric strain turns to dilatancy because crack nucleate at dislocation pile-ups and their contribution to the strain becomes predominant compared to plastic pore collapse. In the brittle regime, water-saturation decreases the differential stress at the onset of crack propagation and enhances macroscopic dilatancy. Temperature decreases the confining pressure at the brittle-semibrittle (ductile) transition. A model describing the macroscopic behaviour is derived from (1) a crack propagation law, (2) a plasticity law for a porous medium, and (3) a law for nucleation of news cracks due to local dislocation pile-ups. The model predicts the volumetric strain, the stress tensor, and the evolution of damage, as a function of applied deformation. Theoretical results are in good agreement with experimental observations.

Stress stepping creep experiments were performed in a range of confining pressures crossing the brittle-ductile transition, in dry and water-saturated conditions. In the brittle regime, the time-dependent axial deformation is coupled with dilatancy and a decrease of elastic wave velocities; which is characteristic of crack propagation and/or nucleation. In the semibrittle regime, the first steps are inelastic compactant because of plastic pore collapse. Following stress steps are dilatant because of crack nucleation and/or propagation. The axial strain rate is always controlled by plastic phenomena, until the last step; during which the axial strain rate increases significantly because of crack interactions leading to the macroscopic failure. Water-saturation enhances dilatancy. As the micromechanisms of deformation under constant stress are similar to those observed during constant strain rate experiments, the model developed for constant strain rate experiments is enriched with a subcritical crack growth law to predict the mechanical behaviour under constant stresses. Model predictions are in qualitative agreement with experimental results.

The influence of strain rate on the mechanical behaviour during constant strain rate triaxial

loading is investigated experimentally. At low confining pressures, the decrease of the axial strain rate leads to an increase of axial strain and peak stress at failure, and a decrease of volumetric strain. This can be explained by the micro-plasticity (for e.g. by twinning) that is enhanced by the decrease of strain rate. In the ductile regime, plasticity is enhanced by the decrease of strain rate. Axial strain at failure increases significantly as the strain rate is decreased. Moreover, the stress drop at failure decreases dramatically with the decrease of strain rate.

Results show the complexity of the deformation micromechanisms in limestones. The confining pressure, pore fluids, temperature and strain rate (i.e. time) have an influence on the micromechanisms of deformation and thus on the macroscopic behaviour. Finally, these results could be extended to other carbonate rocks (marbles, chalks), which remains to be explored.

Key words: carbonate rocks, mechanical behaviour, damage, plasticity, creep, constant strain rate experiments

AVANT-PROPOS

Nous pensons parfois être sur un point stable alors que tout est en mouvement dans notre univers. La croûte terrestre repose sur un manteau en convection. De façon plus imagée, nous vivons sur un tapis roulant. Notre planète se déplace autour de son étoile, elle-même en mouvement dans notre galaxie, dans un univers en expansion. Que de vitesse et de temps que nous ne percevons pas! Le relatif et les variations au cours du temps, sont notre présent rassurant.

Le temps est la valeur fondamentale de tout mouvement. Cependant, notre échelle de temps est très courte devant celle des phénomènes géologiques. A nos valeurs de temps, il ne se passe rien ou peu de chose. Nous ne percevons donc pas les phénomènes extrêmement puissants qui régissent notre univers. Sans base scientifique, comment expliquer la brutalité des événements sismiques ou volcaniques autrement que par la colère brutale d'un dieu? Le changement de rythme est difficile à comprendre lorsqu'on est dans la croyance de la stabilité. Mais cette stabilité est certainement l'exception dans notre univers. En changeant d'angle de lecture pour accepter le temps long, tout devient plus facile à comprendre. Ainsi, la compréhension de la géologie dans les derniers siècles n'a été possible qu'en acceptant que le temps ait une autre valeur que celle admise jusque-là. Le succès de la théorie de la dérive des continents s'appuie sur un changement de valeur caractéristique de la variable temps. Cependant, ce temps long dérange encore tellement qu'après avoir fait table rase de toutes explications pendant quelques années, il n'est pas anormal de voir revenir en force aujourd'hui des théories créationnistes basées sur un temps court à portée humaine.

Le temps est un élément fondamental des sciences géophysiques et sera au coeur de la recherche développée dans ce manuscrit. Le premier enjeu de ce manuscrit, qui fait l'objet des chapitres 1 et 2, est de décrire et comprendre les mécanismes de déformation de roches carbonatées, en discutant l'importance relative de certains paramètres. Ensuite, nous nous attarderons plus particulièrement sur le rôle fondamental du temps dans la déformation de ces roches dans les Chapitres 3 et 4. Enfin, nous proposerons une synthèse, unifiant les résultats des chapitres précédents, dans le Chapitre 5. Chaque Chapitre a été pensé comme appartenant à une étude d'ensemble, mais peut être lu indépendamment, ce qui peut engendrer quelques répétitions lors d'une lecture complète du manuscrit.

REMERCIEMENTS

Ce manuscrit est le résultat de trois années de recherche. Il peinera cependant à présenter les interactions humaines qui portent l'existence et le travail de tout chercheur. Cet avant-propos est dédié aux personnes qui ont accompagné le développement de la recherche présentée. Mes premiers remerciements vont à Yves Guéguen et Jérôme Fortin, qui ont dirigé cette thèse. Yves, vous avez balisé un chemin et m'avez guidé dans l'immensité de la mécanique terrestre. Vous avez su débloquer de nombreux problèmes scientifiques et administratifs, tempérer mon emballement parfois et trouver les mots réconfortants lors des échecs. Jérôme, tu m'as mis le pied à l'étrier des outils expérimentaux, tu as guidé mes (difficiles) rédactions d'articles, tu as même colmaté des fuites d'huile certains dimanches... Merci Jérôme pour tout (cela inclut tes trottoirs!).

Je remercie les collaborateurs industriels de ma thèse, Total, et en particulier Philippe Marchina qui a accepté de rejoindre un projet partant vers l'inconnu et a suivi son déroulement. Je tiens à remercier Teng-Fong Wong, Yves Leroy, Christian David, Patrick Baud, Alexandre Dimanov et Philippe Marchina d'avoir accepté de participer à mon jury de thèse et à l'évaluation de mon travail. J'ai une pensée particulière pour Yves Leroy qui m'a proposé cette thèse il y a trois ans. Merci à Patrick Baud et Serge Lugan pour les blocs de calcaire de Tavel qui ont été à la base de ce travail.

I warmly thank Teng-Fong for hosting me in Hong-Kong. I learned a lot there. I also thank Xiaoqiong with whom I had a great pleasure to work. Hui Hui, Hong Feng, Kang, Man Nin, Liu are rewarded for the evenings. Sally and Siu Lam for the paper work and Eric for the technical help, and the three of them for great lunch times.

Yann Gunzburger m'a soutenu dans mon projet de découvrir la recherche, projet concrétisé avec Alexandre Schubnel en stage de master... c'était si bien que je suis resté! Je pense aux interactions avec le LMS (Ecole Polytechnique) à travers la collaboration avec Alexandre Dimanov, Pierre Valli, Simon Hallais et Alexandre Tanguy. Je remercie Pauline Souloumiac pour son invitation à faire un séminaire. Sans oublier les personnes déjà citées et parmi beaucoup d'autres, les discussions avec Philippe Robion, Patrick Baud et Harsha S. Bhat m'ont permis de forger ma pensée scientifique.

Je remercie Yves Pinquier et Damien Deldicque pour leur aide expérimentale, tous les permanents, Micheline, Isabelle, Angélique, Françoise, Delphine, Pier-Paolo et Nasser qui ont souvent pu me sortir des tracas (du) quotidien(s). Merci à ceux qui ont quitté nos murs: Marianne¹, Fred², Céline, Stavros, Olivier, Adeline, Alexis, Eugénie, Julie, Silvia, Ohiane, Amaya, Aurélien, Olga, Gabriel, Dimitri, Florian. Je remercie mes cherch'eurêka-marades stagiaires, thésards et post-docs du labo et de l'IPGP. J'ai eu le grand bonheur de partager avec vous de petits tracas, de bons moments au bureau, dans les rues adjacentes, et plus (d?)ailleurs. Je

¹qui reste très présente!

²"je suis Fred"

Remerciements

pense à Audrey³, Emilie⁴, Tim, Sarah, Damian, Jan, Cédric, Xiaoping, Gianina, Suzanne, Lucas, Jacques, les Christians, Thomas, Amaury, H, Boris, Lambert, parmi d'autres. Si notre route fut parfois semée de détours dans son sac; les obstacles se franchissent beaucoup plus facilement ensemble.

L'amitié, ca naît (de) rien; et c'est presque tout. Merci Rémi, Laëti, Théo, Benoît, Benjamin² (BugeBuge et Sautterrrr), Claire, Mickaël, Louis, Clément, Marion, Céline, Rémy, JayBee, Krikri, Hélène⁵, Marianne, François, PAP, Melmel, Jean-François, J-Phi, Claudio, Cyril et Jakez; l'amitié est précieuse. Merci à mes colocs, l'appart est et a été la maison du bonheur. Merci à ma grande famille si sympa, à mes cousins qui m'ont fait oublier les difficultés et m'ont offert des moments familiaux d'un bonheur intense! Merci à ma soeur (Mutshi-Kiwi) et à mon frère (Dood'Hibou) qui me sont précieux et dont je suis très fier, malgré leurs doutes parfois. A la (calem)bourre, en intro rétrospective (ou rétro-introspective), je termine par la leçon de vie que l'on m'a inculquée au cours de ces trois ans: « Il ne sert à rien d'avoir raison lorsqu'on s'aveugle dans son vain combat contre ses passions comme lorsqu'on s'isole dans son monde idéal loin des hommes. Etre là simplement vrai avec les autres ». Merci Papa et Maman pour cette sage leçon et pour tout le reste. Je vous dois tant.

³ La musique dans la peau

⁴ Qui illumine le bureau, au sens littéral

⁵ Mc traquenard

"Savoir, penser, rêver. Tout est là."

Victor Hugo (1802-1885).

À ceux qui en veulent...

INTRODUCTION

Les déformations naturelles

Les mouvements tectoniques naturels sont responsables des reliefs qui peuvent être observés à la surface de la Terre. La tectonique des plaques engendre des déformations et induit des contraintes locales et/ou globales dans les couches géologiques qui constituent la lithosphère terrestre. L'accumulation de contraintes peut (i) induire une fracturation à toutes les échelles, du minéral à la frontière de plaques, qui peut engendrer des tremblements de terre dramatiques ou (ii) conduire à des déformations ductiles sans localisation de la déformation (i.e. sans fracture). Ces deux modes de déformation (fragile ou ductile) sont illustrés par la Figure 1: en (a), une faille traverse un paysage dans la baie d'Ethylos (Grèce) et en (b), le pli exhumé dans les Ardennes (France) ne présente pas de trace de fracturation à l'échelle macroscopique. La transition entre le comportement cassant (fragile) et non cassant (ductile) présente un intérêt particulier puisqu'elle pourrait améliorer la compréhension de la mécanique des failles et des tremblements de terre superficiels (Sibson, 1982). L'étude du comportement mécanique des carbonates, du fragile au ductile, est l'objet de cette thèse.

Lorsqu'un volume de roche se trouve en profondeur, il subit selon l'axe vertical une pression lithostatique créée par le poids de la colonne de roches sus-jacentes:

$$P = \rho g h, \tag{1}$$

avec ρ la masse volumique moyenne, g la constante de gravité et h la hauteur de roche au dessus du volume considéré. Si la masse volumique des roches est constante, la pression verticale augmente donc de façon linéaire avec la profondeur. Dans le plan horizontal, la roche subit l'action et la pression des roches voisines dues aux mouvements tectoniques (e.g. Gunzburger, 2010). Si les contraintes horizontales sont égales aux contraintes verticales, le champ de contrainte est isostatique. Cependant, dans la majorité des cas, la contrainte verti-

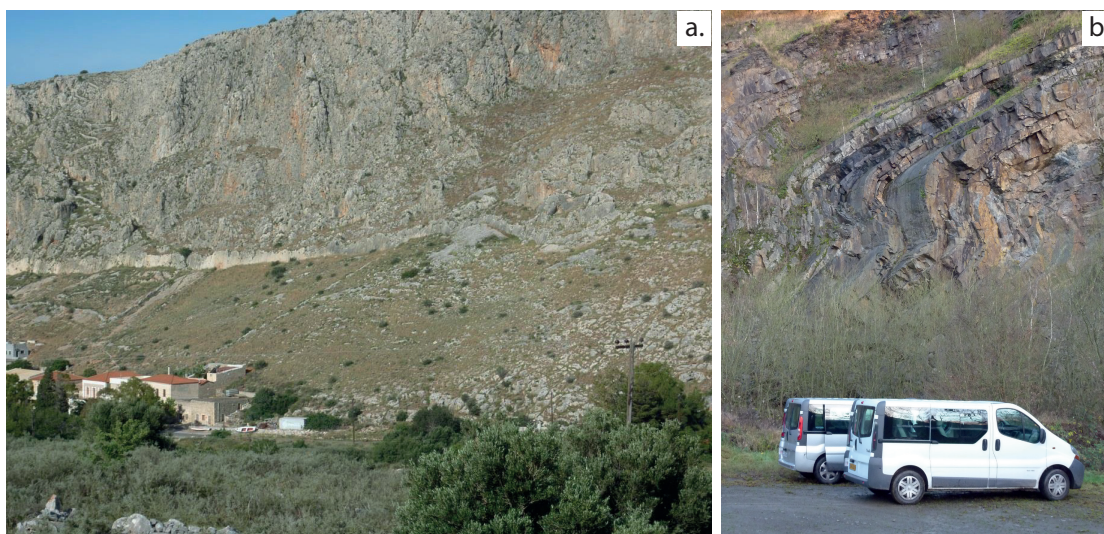


Figure 1 – (a) Faille traversant un paysage dans la baie d’Ethylos (Grèce). (b) Grès de l’Emsien (formation de Vireux) très légèrement métamorphisés dans une carrière de Vireux Mohlain (flanc nord du massif de Rocroi, Ardennes, France).

cale est supérieure aux contraintes horizontales et dans ce cas le champ de contrainte n’est plus isotrope. De plus, lorsque la lithologie varie avec la profondeur, la (ou les) contrainte(s) horizontale(s) dépend(ent) des propriétés des roches (e.g. [Gunzburger, 2010](#)). L’étude de la rhéologie des roches est donc essentielle pour comprendre les déformation naturelles et l’accumulation des contraintes dans la lithosphère, paramètre clé de la compréhension du cycle sismique ([Kohlstedt et al., 1995](#)).

Les modes de déformation non-élastiques (fragile ou ductile) dépendent de plusieurs paramètres tels que le champ de contraintes, la température, et vraisemblablement aussi de la vitesse de déformation et de la présence ou non de fluides. Comme l’évolution des propriétés de transport de fluides de la roche dépendent du mode de déformation, leur étude est également primordiale dans le cadre des exploitations humaines. En effet, les activités humaines peuvent conduire à la déformation et à la rupture des roches poreuses, par exemple durant l’exploitation des hydrocarbures, car leur pompage engendre une diminution de la pression de pore et donc une augmentation de la contrainte effective. Des problèmes peuvent aussi parfois apparaître lors de l’exploitation de mines ou de sites de stockage profonds, car les cavités induisent des concentrations de contraintes. Parmi les conséquences possibles, on trouve la subsidence de la surface ([Boutéca et al., 1996](#), [Nagel, 2001](#)), l’effondrement de forages, la sismicité induite ([Segall, 1989a](#), [Fredrich et al., 2000](#)) ou encore les changements de

perméabilité (Miller, 2002, Bemer & Lombard, 2010). Ces conséquences affectent directement l'exploitation géothermale ou des hydrocarbures, le stockage géologique de déchets radioactifs ou encore la séquestration géologique du dioxyde de carbone. Des études en laboratoire préalablement à l'exploitation peuvent amener à une meilleure compréhension des risques liés à la déformation des roches due à l'exploitation humaine et des réponses potentielles pour les éviter.

Caractérisation expérimentale du comportement

Le développement de la mécanique des roches a permis de caractériser, comprendre et quantifier en laboratoire le comportement des roches qui était observé *in situ* à la surface du globe par les géologues. La grande majorité des expériences est réalisée sur des carottes (cylindriques) de roches naturelles. Des roches synthétiques et d'autres géométries d'échantillons sont aussi, dans une moindre mesure, utilisées.

Deux types d'expériences sont majoritairement réalisés: (1) le chargement hydrostatique (contrainte constante tout autour de l'échantillon) qui modélise par exemple un enfouissement et (2) le chargement triaxial. L'essai triaxial classique sur une carotte cylindrique consiste à avoir une pression radiale (pression de confinement P_c) inférieure à la pression axiale. La pression hydrostatique est équivalente à la pression due à l'enfouissement dans le cas naturel et le déviateur peut simuler un chargement tectonique. Sur certaines machines, il est aussi possible de contrôler le type et la pression du fluide dans les pores de l'échantillon.

En mécanique des roches (contrairement à la mécanique des matériaux), par convention, les contraintes en compression et les raccourcissements sont comptés positivement. Dans la suite de ce manuscrit, les contraintes principales maximales et minimales seront respectivement notées σ_1 et σ_3 . Dans un essai triaxial classique (pression radiale constante sur un échantillon cylindrique), la contrainte effective moyenne est donc:

$$P = \frac{P_{ax} + 2P_c}{3} - \alpha P_p, \quad (2)$$

avec $P_{ax} = \sigma_1$ la pression axiale, $P_c = \sigma_3 = \sigma_2$ la pression de confinement, α le coefficient de Biot et P_p la pression de pore. Dans la suite de ce travail, le coefficient de Biot est considéré

Introduction

égal à 1. On définit aussi la contrainte différentielle Q :

$$Q = \sigma_1 - \sigma_3. \quad (3)$$

La déformation volumique est calculée au premier ordre par:

$$\varepsilon_{vol} = \varepsilon_{ax} + 2\varepsilon_{rad}, \quad (4)$$

avec ε_{ax} la déformation axiale et ε_{rad} la déformation radiale.

Presses triaxiales utilisées

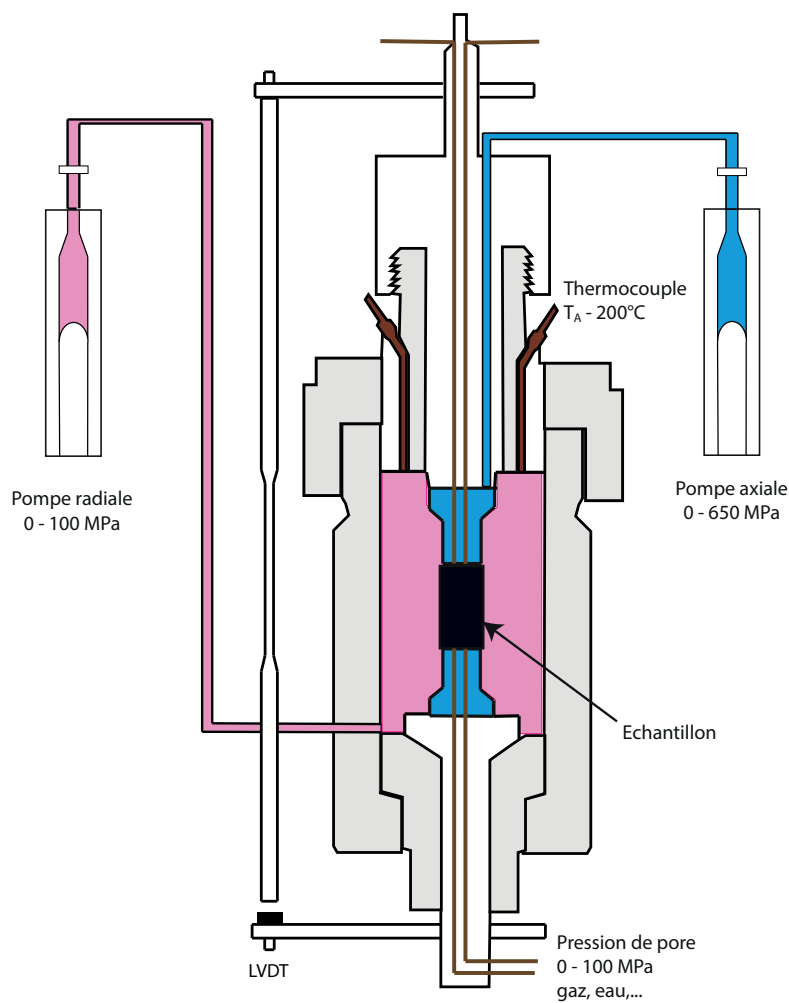


Figure 2 – Schéma de principe de la presse triaxiale du Laboratoire de Géologie de l'ENS. Le schéma a été modifié d'après Mallet (2014).

La grande majorité des expériences présentées dans ce mémoire ont été réalisées avec une presse triaxiale installée au Laboratoire de Géologie de l'École Normale Supérieure (ENS).

Quatre expériences présentées dans le dernier chapitre ont été réalisées sur la cellule triaxiale de la Chinese University of Hong-Kong (CUHK). Les deux presses sont construites selon le même modèle (Sanchez ST Tri-X 200). Nous décrivons ici brièvement la presse de l'ENS mais les remarques valent également pour la machine installée à la CUHK. Une description détaillée de la presse triaxiale peut être trouvée dans [Brantut et al. \(2011\)](#), [Ougier-Simonin et al. \(2011\)](#). La presse triaxiale de l'ENS permet de contrôler et faire varier indépendamment la contrainte axiale σ_1 , la pression de confinement $\sigma_2 = \sigma_3$, la pression de pore P_p (avec différents fluides) et la température entre la température ambiante et 200°C. Il est possible de réaliser des expériences en régime hydrostatique (si $\sigma_1 = \sigma_3$) ou déviatorique (avec $\sigma_1 > \sigma_3$). Les échantillons cylindriques utilisés dans cette étude ont un diamètre de 40 mm et une longueur d'environ 80 mm. Pour cette taille d'échantillons, la pression de confinement peut varier entre 0 à 100 MPa, et la pression axiale maximale est de 650 MPa. La pression de pores peut atteindre 100 MPa.

Le système d'acquisition permet de mesurer la déformation de l'échantillon avec 4 jauges doubles (composées d'une jauge axiale et d'une radiale) collées directement sur l'échantillon et 3 LVDTs placés autour de la cellule. La déformation mesurée avec les LVDTs est corrigée de la déformation de la machine. Les jauges mesurent une déformation locale alors que les LVDTs intègrent la déformation axiale sur toute la hauteur de l'échantillon.

Des capteurs acoustiques collés sur l'échantillon permettent de mesurer la variation des vitesses de propagation des ondes P et S (mode actif) ou d'enregistrer les émissions acoustiques (mode passif). En mode actif, une onde élastique est émise par un capteur et enregistrée par les autres. En mode passif, tous les capteurs enregistrent les ondes émises par la propagation de fissures dans l'échantillon. Dans le cas des carbonates testés, très peu d'émissions acoustiques ont été enregistrées et les émissions acoustiques ne seront donc pas considérées.

Chemins de chargement de contrainte

Lors d'un chargement hydrostatique, l'augmentation de la pression moyenne ($\sigma_{moy} = \sigma_1 = \sigma_3 = P_c$) appliquée à une roche poreuse engendre une compaction de l'échantillon et une diminution de la porosité (de fissures et de pores). La compaction peut être élastique ou inélastique. Le comportement mécanique d'une roche soumise à un chargement de contrainte hydrostatique est discuté ultérieurement.

Pour obtenir un état de contrainte triaxial à partir d'un état de contrainte hydrostatique sur un échantillon cylindrique, il est soit possible d'augmenter la contrainte axiale σ_1 , soit de diminuer la pression de confinement $P_c = \sigma_2 = \sigma_3$. Le protocole classique consiste à augmenter la contrainte axiale. Deux types d'essais sont les plus couramment utilisés:

(1) Les essais à vitesse de déformation contrôlée consistent à déformer axialement l'échantillon en contrôlant le taux de raccourcissement, tout en maintenant la pression de confinement constante (e.g. [Wong et al., 1997](#), [Baud et al., 2000a](#)). La déformation axiale varie donc linéairement avec le temps et la contrainte axiale et la déformation volumique sont mesurées. La déformation axiale engendre une déformation volumique qui peut être compactante ou dilatante et peut passer d'un régime à l'autre au cours de la déformation (e.g. [Wong et al., 1997](#), [Baud et al., 2000a](#)). Ces différents comportements sont discutés dans la prochaine section.

(2) Les essais de fluage consistent à maintenir la contrainte axiale à une valeur donnée ($\sigma_1 > \sigma_3$). Pour atteindre cette contrainte différentielle voulue, soit l'échantillon est déformé à vitesse de déformation contrôlée, soit la contrainte est augmentée à une vitesse donnée. Au cours du palier de fluage ($\sigma_1 = Cste$), les déformations axiales et volumiques sont mesurées. La déformation à contrainte différentielle constante peut engendrer une compaction (e.g. [Niemeijer et al., 2002](#), [Zhang et al., 2010](#)), ou une dilatance qui peut mener à la ruine de l'échantillon par fatigue (e.g. [Brantut et al., 2013](#)).

Les deux types de protocoles ont été réalisés au cours de ce travail. Les comportements mécaniques des roches lors de chacun de ces deux types d'essais sont donc présentés plus en détails dans la suite du manuscrit.

Comportement mécanique macroscopique d'une roche déformée

Chargement hydrostatique

Lorsque la déformation est élastique, une diminution de la pression permet à l'échantillon de retrouver ses dimensions initiales. Lorsque la déformation est inélastique, elle engendre un endommagement irréversible et une déformation durable due à un changement de microstructure (e.g. Fortin et al., 2005, 2007). Les micromécanismes de déformation et leurs conséquences sont discutés ultérieurement.

Après une déformation élastique, la déformation devient inélastique (Figure 5 a) au-delà d'une contrainte seuil notée P^* (Wong et al., 1997). Plusieurs types de mécanismes physiques peuvent expliquer la compaction inélastique et l'effondrement de la porosité: (i) les processus de fracturation Hertziens qui engendrent la fracturation des grains (e.g. Zhang et al., 1990, Fortin et al., 2005, 2007), (ii) les rotations et réarrangements de grains (e.g. Guéguen & Palciauskas, 1994), (iii) la plasticité intra-cristalline (e.g. Curran & Carroll, 1979, Baud et al., 2000a), ou (iv) des processus chimiques (Niemeijer et al., 2002, Zhang et al., 2010, Croize et al., 2013). En fonction de la roche considérée (composition chimique, structure, porosité, taille des grains etc), un ou plusieurs de ces mécanismes est prépondérant(s). De manière générale, l'augmentation de la porosité et/ou de la taille des grains diminue(nt) la valeur de la pression critique P^* .

Relation contrainte-déformation en régime triaxial et localisation de l'endommagement

Comme dans le cas naturel, les expériences en laboratoire montrent que différents comportements peuvent être observés dans les roches déformées, soit menant à une rupture (équivalente à un séisme sur une faille), soit déformant sans localiser l'endommagement sur une faille (équivalent à la formation d'un pli par exemple) ce qui caractérise le comportement ductile (les caractérisations précises sont discutées ci-après). Parmi les nombreux paramètres susceptibles d'influer sur le mode de déformation d'une roche, on peut retenir les principaux: la température, la pression et la vitesse de déformation (e.g. Rutter, 1974a). Ces paramètres peuvent par exemple favoriser des processus de plasticité (penser au verre que l'on chauffe pour le façonner), engendrer des réorientations cristallines (par exemple le maillage dans la

Introduction

calcite) voire des transitions de phase de certains minéraux (Brantut et al., 2010, Schubnel et al., 2013). Les fluides peuvent aussi jouer un rôle, à cause de leur réactivité chimique (e.g. Gunzburger, 2010, Rostom et al., 2013), de la modification de l'énergie de surface du matériau (de Leeuw & Parker, 1997, Røyne et al., 2011), ou à cause de la pression de pore qu'ils engendrent (e.g. Duda & Renner, 2013).

A température ambiante, lorsqu'un échantillon de roche est déformé triaxialement, il subit d'abord une compaction élastique puis, en fonction de la pression de confinement, une compaction inélastique ou une dilatance, voire une dilatance après un régime compactant. La dilatance post-régime élastique (comportement fragile) est observée à faible pression de confinement et la compaction inélastique (comportement ductile) à plus haut confinement (e.g. Wong et al., 1997, Baud et al., 2000a). La transition entre ces deux régimes dépend de paramètres tels que la porosité et la taille des grains (e.g. Vajdova et al., 2004).

Macroscopiquement, on caractérise essentiellement la déformation fragile par la localisation de la déformation sur une faille macroscopique et l'existence d'un pic de contrainte suivi d'une chute au cours du glissement sur le plan de fracture. D'un point de vue microscopique, la déformation fragile (post-régime élastique) est expliquée par la croissance et coalescence de micro-fissures (qui mène à la faille macroscopique) à partir de défauts tels que des pores ou des fissures pré-existantes (Sammis & Ashby, 1986, Ashby & Hallam, 1986, Ashby & Sammis, 1990). La croissance des fissures engendre une augmentation de volume du milieu poreux fissuré, c'est-à-dire une dilatance. Par ailleurs, la propagation des micro-fissures peut produire des émissions acoustiques (comme des micro-séismes) qu'il est possible d'enregistrer (Lockner & Byerlee, 1977). En utilisant plusieurs capteurs, il est possible de localiser la source de l'émission acoustique et donc d'obtenir la localisation spatio-temporelle de l'endommagement (Lockner et al., 1992).

Le comportement ductile est macroscopiquement caractérisé par une déformation diffuse, ce qui interdit la formation d'une fracture macroscopique et une chute de contrainte (e.g. Heard, 1960). Il existe cependant des cas intermédiaires qui seront discutés ultérieurement dans le cas des carbonates. L'augmentation de pression et/ou de température inhibe l'interaction des fissures (Ashby & Sammis, 1990), tout en favorisant les processus de plasticité intracristalline (e.g. les mouvements de dislocations (Meyers et al., 1999)) et la fracturation des grains (voir le chargement hydrostatique). Il convient cependant de séparer le comportement ductile

à basse température et haute pression, qui est souvent au moins en partie associé à de la micro-fissuration (e.g. [Wong & Baud, 2012](#)), et le comportement ductile à haute température qui peut être expliqué uniquement par la plasticité (e.g. [Renner et al., 2002](#), [Dimanov et al., 2007](#)). Lorsque des processus de plasticité sont uniquement impliqués dans le comportement ductile, la température et la vitesse de déformation sont des paramètres clés: une augmentation de la température et une diminution de la vitesse de déformation favorisent la plasticité. Dans la suite de ce travail, nous utiliserons les définitions de [Evans et al. \(1990\)](#) pour caractériser le comportement fragile ou ductile. Un résumé des principales caractéristiques de ces comportements est donné en Figure 3.

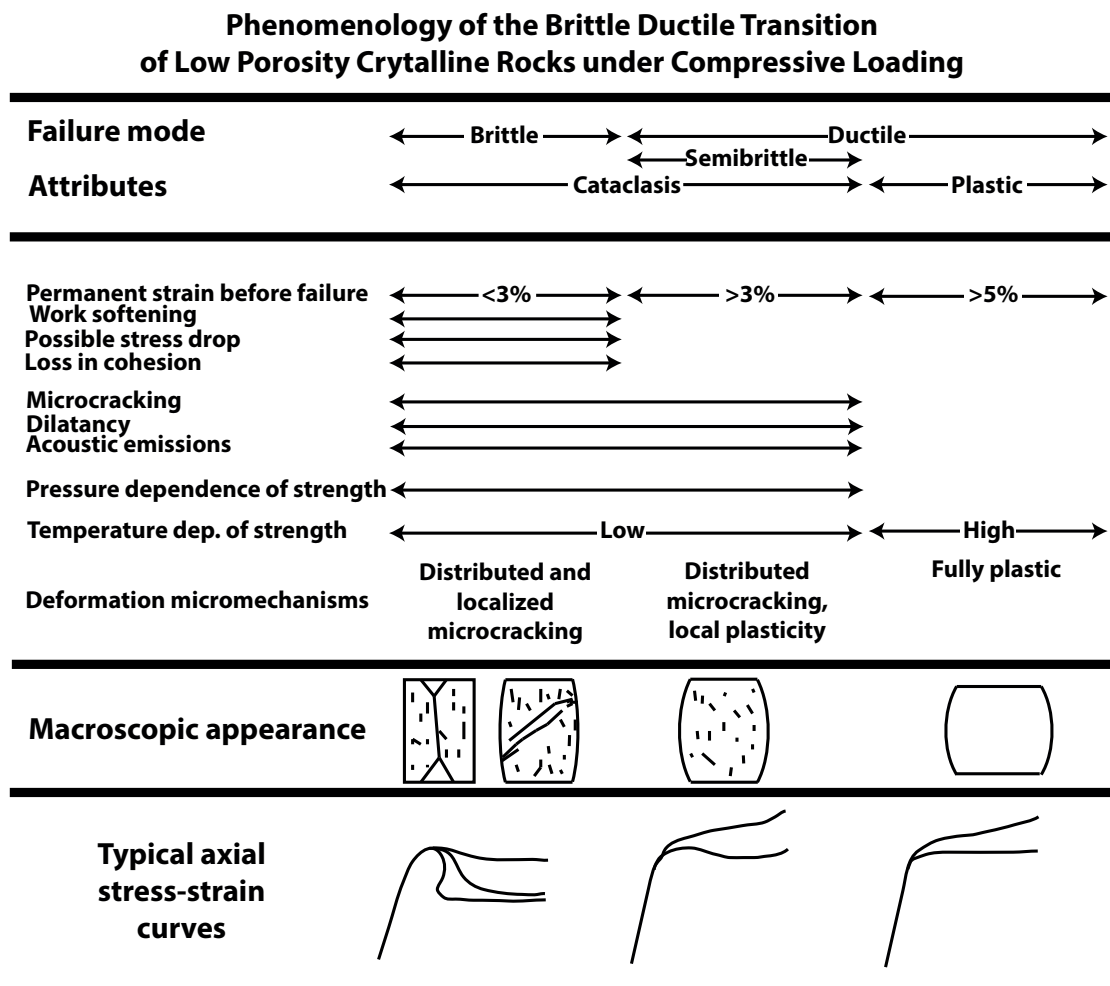


Figure 3 – Schematic diagram illustrating the phenomenology of the brittle-ductile transition. Modified after [Evans et al. \(1990\)](#).

Enveloppe de rupture: représentation des changements de relations contrainte-déformation

La pression moyenne et la contrainte différentielle ont le plus souvent un effet contraire: la contrainte moyenne induit une compaction alors que la contrainte différentielle favorise très souvent la dilatance. On peut néanmoins citer le contre-exemple de la compaction favorisée par le cisaillement ou *shear-enhanced compaction* (Curran & Carroll, 1979). Une enveloppe de rupture est la représentation des limites des régimes de déformation (régime élastique, inélastique compactant ou dilatant) et des contraintes à la rupture dans un espace $P - Q$. Ainsi, la construction d'enveloppes de rupture permet de comparer l'effet relatif de chaque composante des contraintes appliquées. Pour un chargement hydrostatique, on représente l'initiation de la compaction inélastique à la pression P^* . Pour un régime triaxial, il convient de différencier les régimes de déformation fragile et ductile. Dans le régime fragile, on retient les états de contrainte à la fin du régime élastique (initiation de la dilatance, C') et au maximum de la contrainte différentielle (*peak stress*). Dans le régime ductile, on retient l'initiation de la compaction inélastique (fin du domaine élastique, C^*), puis éventuellement de la dilatance post-compaction inélastique (C^*).

Dans le régime fragile, les modèles d'endommagement par développement de *wing cracks* montrent que la contrainte axiale à l'initiation de la dilatance est une fonction affine du confinement (Cotterell & Rice, 1980, Horii & Nemat-Nasser, 1986, Ashby & Sammis, 1990):

$$\sigma_1 = \frac{\sqrt{1+\mu^2} + \mu}{\sqrt{1+\mu^2} - \mu} \sigma_3 + \left(\frac{\sqrt{3}}{\sqrt{1+\mu^2} - \mu} \right) \frac{K_{IC}}{\sqrt{\pi a}}, \quad (5)$$

où μ est le coefficient de friction sur les microfissures, a est le rayon des fissures pré-existantes, et K_{IC} est le facteur d'intensité de contrainte critique du matériau. Les modèles de *wing cracks* montrent que la contrainte maximale à la rupture (*peak stress*) peut aussi être considérée comme une fonction affine de la pression de confinement (Horii & Nemat-Nasser, 1986, Ashby & Sammis, 1990, Kemeny & Cook, 1991, Baud et al., 2000a):

$$\sigma_1 = A(\mu, D_0) \sigma_3 + B(\mu, D_0) \frac{K_{IC}}{\sqrt{\pi a}}, \quad (6)$$

où A et B dépendent du coefficient de friction μ et de l'endommagement initial $D_0 = \pi(a \cos \psi)^2 N_A$, avec N_A le nombre de fissures d'orientation uniforme (à un angle ψ par rapport à σ_1) pré-existantes par unité de surface et qui vont glisser et développer des "ailes". Il convient de noter que ces modèles ont été développés en 2D puis appliqués avec succès à la 3D (Ashby &

[Sammis, 1990](#)). D'autres interprétations de la forme des enveloppes fragiles sont possibles, comme une surface elliptique ([Wong et al., 1997](#)). Voir [Guéguen & Fortin \(2013\)](#) pour une discussion plus approfondie.

Dans le régime ductile, la fin du domaine élastique est caractérisée par une accélération de la compaction (à C^*). Comme dans le régime fragile, différentes formes d'enveloppes ont été proposées. Lorsque la compaction inélastique est due à la fracturation des grains, [Wong et al. \(1997\)](#) montre une enveloppe elliptique, mais [Guéguen & Fortin \(2013\)](#) prédisent une droite décroissante avec l'augmentation du confinement, en accord avec certaines données expérimentales. Pour comparer des échantillons de porosités initiales différentes, on normalise les différentes valeurs des contraintes caractéristiques par la pression d'effondrement des pores P^* ([Wong et al., 1997](#)). Lorsque la compaction inélastique est due à l'initiation de la plasticité intracristalline autour de pores, des modèles différents peuvent être utilisés. [Curran & Carroll \(1979\)](#) a par exemple modélisé la compaction plastique de pores sphériques isolés dans une matrice plastique, en utilisant un critère de Von Mises.

Micromécanismes de déformation des grès

Le comportement mécanique des grès est assez bien documenté. En effet, les grès sont les roches sédimentaires qui ont été étudiées en premier en raison de leur microstructure. Les grès sont formés de grains de quartz. Ils forment donc un milieu granulaire. De plus le quartz est peu réactif et ne se déforme pas plastiquement à température ambiante.

Le cas hydrostatique

La compaction inélastique des grès est caractérisée par une diminution de la porosité et une augmentation de la densité de fissures. La compaction inélastique est caractérisée par une accélération de la déformation avec l'augmentation de contrainte par rapport au régime élastique (e.g. [Wong et al., 1997](#), [Fortin et al., 2005, 2007](#)). Le micromécanisme de déformation est la fracturation des grains (Figure 4). Les changements de microstructure engendrent des changements des propriétés pétrophysiques de la roche. Par exemple, une diminution de la perméabilité et des vitesses de propagation des ondes élastiques sont observées dans le cas de la compaction de certains grès ([David et al., 1994](#), [Fortin et al., 2005](#), [Benson et al., 2006](#), [Fortin](#)

Introduction

et al., 2007).

Pour modéliser la compaction due à une fracturation des grains, Zhang et al. (1990) utilise un

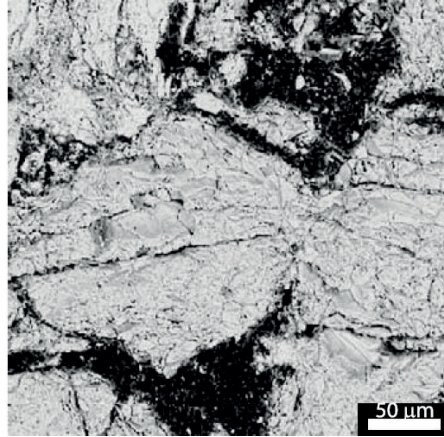


Figure 4 – SEM micrograph (backscattered) of Bleurswiller sandstone deformed. Grains are fractured at grain-grain contacts. Taken from (Fortin et al., 2007).

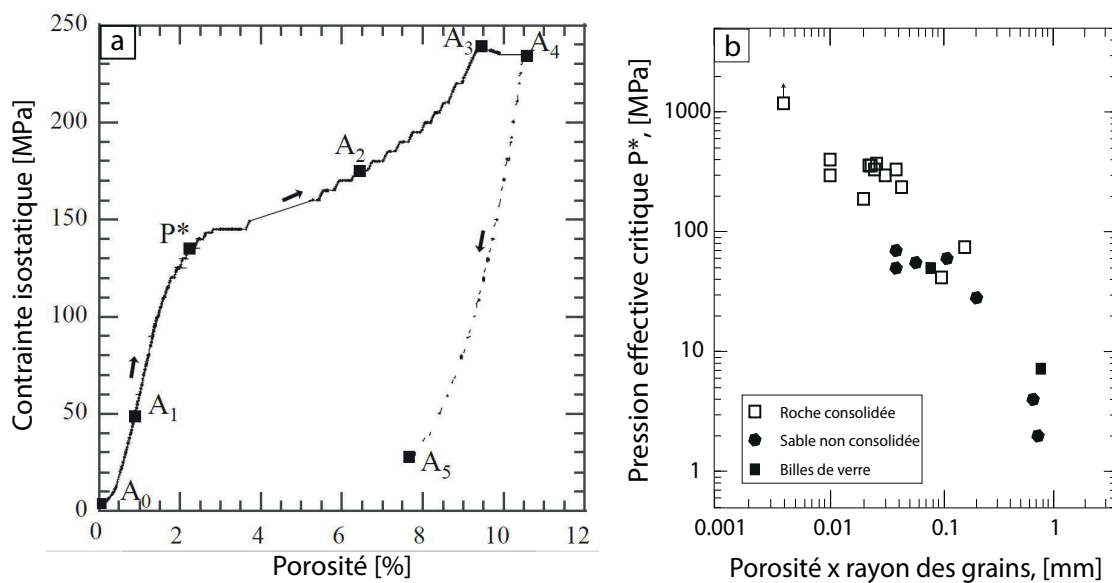


Figure 5 – (a) Compression hydrostatique du grès de Bleurswiller. La contrainte hydrostatique est tracée en fonction de la réduction de porosité. Figure modifiée d'après Fortin et al. (2005). (b) Pression effective critique pour l'initiation du broyage des grains sous contrainte hydrostatique (P^*), en fonction de la porosité initiale et du rayon des grains. Les données suivent approximativement une tendance linéaire avec une pente de $-3/2$, en accord avec le modèle de Zhang et al. (1990). Figure modifiée d'après Wong et al. (1997).

modèle d'empilement de grains initialement développé par Brandt (1955). La force de contact entre deux sphères est calculée en fonction de la pression appliquée autour du milieu. La

pression critique obtenue dépend des propriétés élastiques du matériau, du facteur d'intensité de contrainte critique K_{IC} , de la porosité ϕ , de la taille des grains s selon:

$$P^* = 2.2 \left(\frac{1 - \nu^2}{E} \right)^2 \left(\frac{K_{IC}}{(1 - 2\nu)\sqrt{\phi s}} \right)^3, \quad (7)$$

où ν est le coefficient de Poisson des grains, et E leur module de Young. La comparaison de ce modèle théorique avec des données expérimentales pour des roches silicatées (Figure 5 b) présente un accord satisfaisant.

Le cas déviatorique

Les grès déformés à température ambiante ont un comportement fragile dilatant à faible confinement qui devient un comportement ductile cataclastique compactant lorsque la pression de confinement augmente. Wong et al. (1997) ont montré empiriquement que dans les grès, la transition entre un comportement fragile dilatant et un comportement ductile cataclastique compactant se fait à une pression effective triaxiale (P_{bdt}) qui est reliée à la pression isostatique nécessaire pour casser les grains (P^*):

$$P_{bdt} \propto (\phi R)^n, \quad (8)$$

où ϕ est la porosité, R est la taille des grains et $n \approx -3/2$. Il convient de noter que cette relation ne s'applique pas forcément aux roches carbonatées dans lesquelles les phénomènes physiques responsables de la transition fragile-ductile peuvent différer des grès (compaction due au cisaillement contre grains cassés). Ceci est discuté dans la prochaine section.

Le cas spécifique du comportement mécanique des carbonates

Les roches carbonatées représentent 7% de la surface terrestre. Elles sont utilisées comme matière première dans l'industrie et sont proposées comme roche de réservoir pour la séquestration géologique du dioxyde de carbone. De plus, elles renferment environ 60% des réserves mondiales de pétrole. Il est donc primordial de bien comprendre leur comportement mécanique sous contrainte et leurs modes de rupture et de fracturation.

Similitudes avec le comportement des grès

De précédentes études se sont intéressées au comportement mécanique des calcaires et des marbres. Parmi les roches naturelles utilisées, on trouve les calcaires de Solnhofen (Heard, 1960, Rutter, 1974a, Baud et al., 2000a), d'Indiana (Vajdova et al., 2004), de Majella (Baud et al., 2009), de Saint-Maximin (Baud et al., 2009), ou de Tavel (Vajdova et al., 2004, 2010). Parmi les marbres, la majorité des études se concentrent sur le marbre de Carrare (Rutter, 1974a, Renner et al., 2002, Schubnel et al., 2006b).

La porosité initiale est un paramètre clef qui contrôle en partie le mode de déformation et de rupture des calcaires (Vajdova et al., 2004). Les différences de porosité initiale engendrent de grandes disparités dans le comportement mécanique et les micro-mécanismes responsables de la déformation. Cette étude s'intéresse au comportement des carbonates peu poreux, que nous avons considérés comme ayant une porosité inférieure à 15%.

Le mode de rupture des calcaires dépend de leur porosité initiale mais également de son évolution avec la contrainte effective appliquée. A faible confinement, la déformation est reliée à une dilatance qui engendre une localisation du cisaillement et donc une rupture cassante (Brace, 1978), comme la majorité des autres roches. D'un point de vue microscopique, le comportement fragile est le plus souvent associé au développement de microfissures et de glissement frictionnel entre les grains (Baud et al., 2000a, Vajdova et al., 2004, 2010, Wong & Baud, 2012), comme décrit précédemment.

A plus haut confinement, une plasticité cristalline à volume solide constant peut se développer (Paterson, 1978, Baud et al., 2000a, Paterson & Wong, 2005), vraisemblablement accompagné de micro-fissuration (Vajdova et al., 2004). Ce type de comportement à température ambiante est différent du comportement inélastique compactant qui est observé dans les grès par exemple. Dans le cas des grès, la compaction inélastique macroscopique et l'effondrement de la porosité des grès sont dus au broyage des grains (Wong et al., 1997), donc à des mécanismes microscopiques fragiles puisqu'il s'agit de fractures dans les grains. Au contraire, dans les calcaires, le comportement macroscopique ductile avec durcissement ("strain-hardening") peut être engendré par des mécanismes microscopiques plastiques à température ambiante (mailage, mouvements de dislocations) favorisés par le cisaillement, et qui entraînent une compaction inélastique. On parle alors de compaction favorisée par le cisaillement ("shear-

enhanced compaction"), comme discuté par exemple par [Baud et al. \(2000a\)](#). Après une étape de durcissement assez longue, la roche peut repasser en régime de dilatance car les défauts cristallins ne peuvent pas s'éliminer ce qui engendre leur empilement qui induit des contraintes locales suffisantes pour nucléer de nouvelles fissures ([Baud et al., 2000a](#)). La transition entre le comportement fragile et ductile dans les calcaires est discutée plus en détails ultérieurement.

Compression isostatique élastique des carbonates

La Figure 6 (a) présente la déformation volumique en fonction de la pression de confinement au cours d'un chargement isostatique du calcaire de Solnhofen, pour une expérience présentée par [Baud et al. \(2000a\)](#). La réponse isostatique est non-linéaire jusqu'à une pression de ~ 200 MPa, au-delà de laquelle la courbe devient linéaire avec une pente correspondant à une compressibilité de $\beta = 0.016 \text{ GPa}^{-1}$. En utilisant le modèle de [Walsh \(1965a\)](#), [Baud et al. \(2000a\)](#) ont montré qu'une telle réponse mécanique est caractéristique d'une roche dont les pores sont de deux types: des micro-fissures et des pores équants. La fermeture progressive des micro-fissures avec l'augmentation de la pression engendre la non-linéarité observée durant l'augmentation initiale de la contrainte isostatique. Le volume de micro-fissures fermées est d'environ 0.2%. Le module d'incompressibilité d'un matériau constitué d'une matrice solide et de pores équants peut être calculée selon:

$$\frac{K_m}{K} = 1 + \frac{3(1-\nu_m)}{2(1-2\nu_m)} \frac{\phi}{(1-\phi)}, \quad (9)$$

où K est le module d'incompressibilité du matériau constitué de la matrice solide et des pores équants, K_m est le module d'incompressibilité de la matrice, ν_m est le coefficient de Poisson de la matrice solide, et ϕ est la porosité due aux pores équants. Pour un agrégat de calcite à une pression de 300 MPa, le module d'incompressibilité K_0 et le coefficient de Poisson ν_0 sont respectivement $K_0 = 73 \text{ GPa}$ et $\nu_0 = 0.33$ ([Simmons & Wang, 1971](#)). En utilisant ces valeurs, [Baud et al. \(2000a\)](#) ont montré que le module d'incompressibilité du calcaire de Solnhofen correspond à une roche de porosité de 3%, en accord avec les mesures de porosité. Une compilation des compressibilités de différentes roches carbonatées issue de [Vajdova et al. \(2004\)](#), est donnée en Figure 6 (b). La compressibilité prédite par le modèle de [Mackenzie \(1950\)](#) est aussi montrée. La compressibilité prédite par le modèle de [Mackenzie \(1950\)](#) et

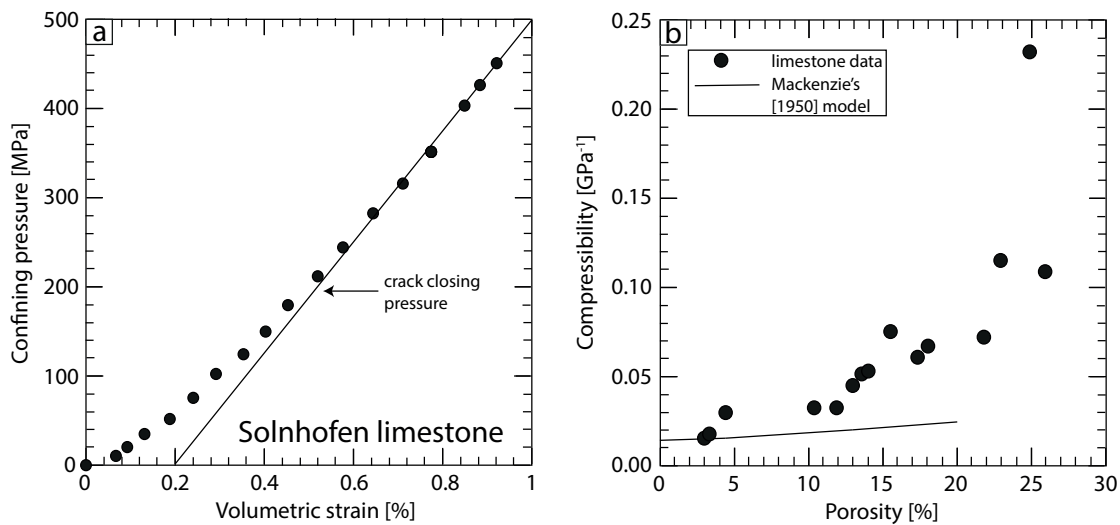


Figure 6 – (a) Confining pressure is plotted versus volumetric strain for the isostatic loading of Solnhofen limestone. Data are taken from [Baud et al. \(2000a\)](#). (b) Compilation of compressibility data on limestones. Model curve shows [Mackenzie's](#) model prediction of the compressibility based on equation 9 in the text.

les données expérimentales augmentent avec la porosité. A faible porosité, les données expérimentales sont proches des valeurs prédites par le modèle. Plus la porosité augmente et plus les données expérimentales s'éloignent des prédictions théoriques. Cette différence peut être expliquée par le fait que l'hypothèse des pores dilués est inappropriée pour les hautes porosités. Un modèle approprié devrait donc prendre en compte l'interaction des pores ([Vajdova et al., 2004](#)).

Au delà du régime élastique, la compaction due à la plasticité autour de pores ronds inclus dans une matrice peut être étudiée avec des modèles tels que celui développé par [Carroll & Holt \(1972\)](#). Il faut alors spécifier une loi de plasticité pour la matrice.

Compaction inélastique et transition fragile-ductile

Dans le cas des carbonates, la transition fragile-ductile n'est pas toujours très bien définie. Des régimes mixtes dont les caractéristiques sont en partie fragiles et en partie ductiles peuvent apparaître. [Heard \(1960\)](#) avait ainsi défini la pression de confinement à la transition fragile-ductile comme la pression à laquelle la roche peut se déformer axialement d'au moins 5% avant la rupture. Dans la suite de ce travail, nous utiliserons les définitions de [Evans et al. \(1990\)](#), selon lesquelles la limite entre le régime fragile et le régime ductile se fait pour une

déformation à la rupture de 3%. Le régime ductile est ensuite divisé entre *semibrittle* comme observé par [Fredrich et al. \(1989, 1990\)](#) et complètement plastique si la déformation de la roche est d'au moins 5% avant la rupture. Ces différentes caractéristiques sont rappelées dans la Figure 3. On peut noter que même avec les descriptions précises de [Evans et al. \(1990\)](#), les limites peuvent parfois rester floues, comme par exemple pour un échantillon qui se déforme à plus de 3% avec de la micro-fissuration. La transition fragile-ductile est particulièrement aisée à étudier dans les carbonates car elle est accessible à température ambiante et à de relativement basses pressions de confinement. Pour les calcaires compris dans la gamme de porosité considérée, la compaction inélastique est expliquée par des micro-mécanismes différents. [Baud et al. \(2000a\)](#) ont ainsi montré que la compaction inélastique d'un calcaire de porosité 3% peut être expliquée par une compaction favorisée par le cisaillement (*shear-enhanced compaction*) et expliquée par un modèle d'effondrement des pores par plasticité ([Curran & Carroll, 1979](#)). Des photographies (TEM et optique) de microstructures d'un marbre de Carrare déformé dans le régime semi-fragile sont montrées dans la Figure 8. En effet, il est établi depuis longtemps que même à température ambiante, contrairement au quartz par exemple, la calcite peut se déformer grâce à des processus tels que le maclage mécanique ou les glissements de dislocations selon les plans r- ou f- de la calcite ([Turner et al., 1954](#), [Griggs et al., 1960](#)).

[Vajdova et al. \(2004\)](#) ont plus tard examiné si ces conclusions pouvaient être extrapolées à des calcaires et des craies de porosités supérieures. Ces auteurs en ont conclu que la compaction favorisée par le cisaillement devait être principalement due à un maclage mécanique pour les roches les plus poreuses alors que les mouvements de dislocations sont favorisés pour les moins poreuses. Cependant, les défauts cristallins ne peuvent pas disparaître à température ambiante. Les dislocations, par exemple, s'empilent; ce qui crée une contrainte interne capable de nucléer des fissures. Ainsi, la micro-fissuration et la plasticité cristalline peuvent être simultanées, ce qui engendre des comportements transitionnels tels que le régime semi-fragile. Des micro-mécanismes comme le "cataclastic flow", caractérisé par une micro-fracturation homogène ([Fredrich et al., 1989](#)), des mouvements des grains et de la plasticité intra-grain (maclage ([Vajdova et al., 2004](#)) et mouvements de dislocations ([Fredrich et al., 1989](#))); sont alors responsables de la déformation (Figure 3). Ces différents mécanismes peuvent engendrer une dilatance, comme observé par [Fredrich et al. \(1989\)](#) sur un marbre de Carrare très peu

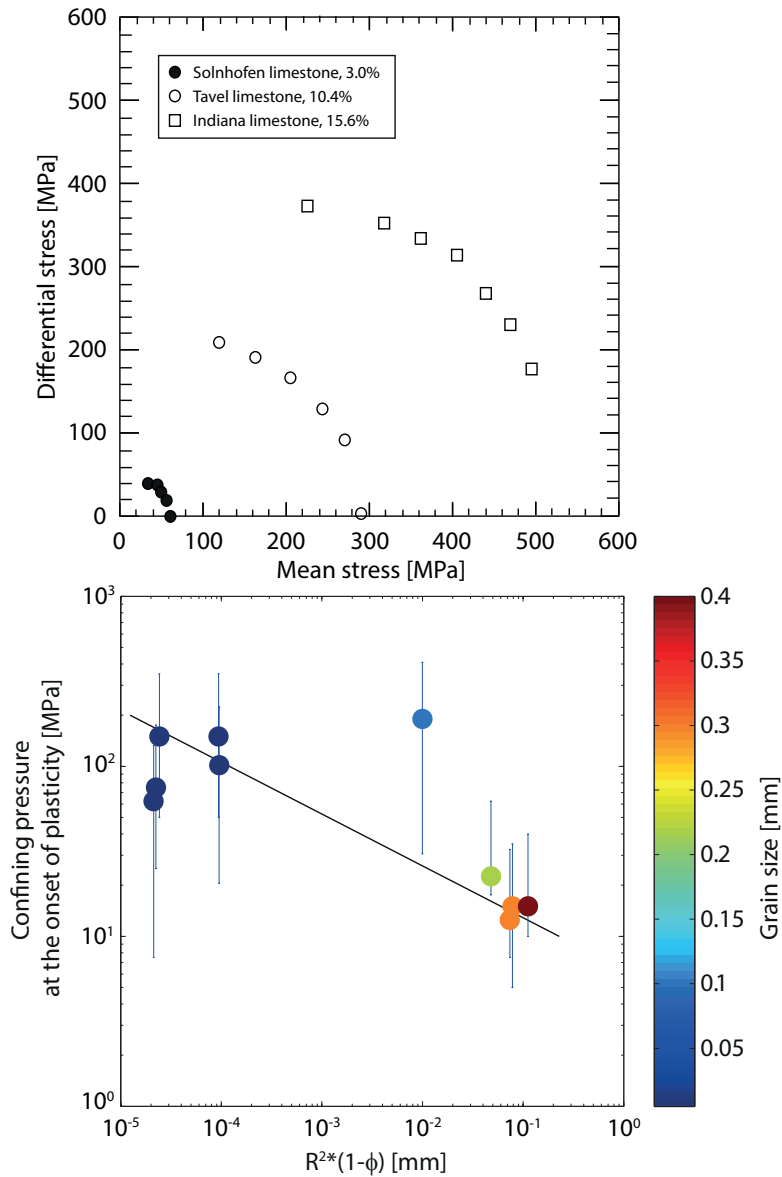


Figure 7 – (a) Compilation of compactive cataclastic flow yield envelopes for low porosity limestones. Modified from [Vajdova et al. \(2004\)](#). (b) La pression de confinement à la transition fragile-ductile est tracée en fonction de $R^2(1 - \phi)$, avec R le rayon moyen de grains et ϕ la porosité, pour différents calcaires et marbres. Les données issues de la littérature sont présentées dans la Table 1.

poreux, ou une compaction, comme montré par [Baud et al. \(2000a\)](#), [Vajdova et al. \(2004, 2010\)](#), [Wong & Baud \(2012\)](#) sur des calcaires et des craies de porosités variées.

Les données mécaniques disponibles dans la littérature montrent que la rupture fragile et la rupture cataclastique (ductile) dépendent différemment la pression. Dans le domaine fragile,

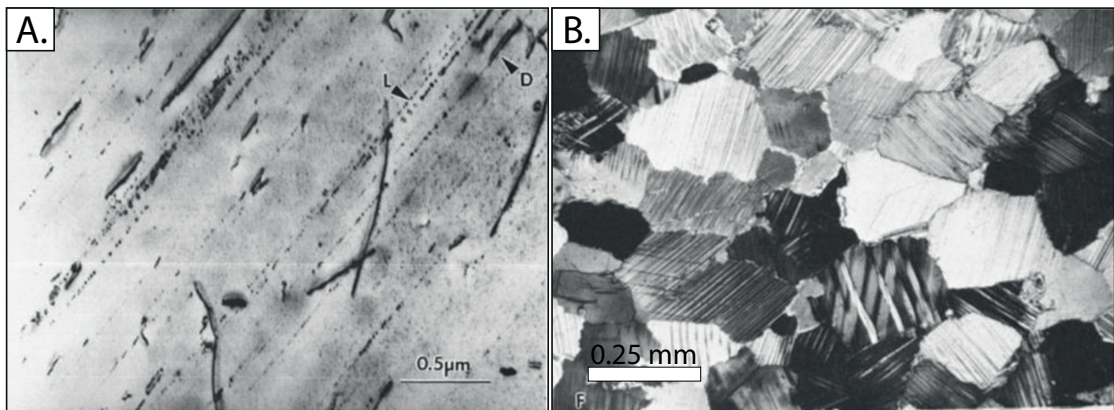


Figure 8 – A - TEM micrograph of a deformed sample of Carrara marble. Dislocation glide apparently occurs in some grains in samples deformed at confining pressures as low as 50 MPa. Taken from [Fredrich et al. \(1989\)](#). B - Optical micrograph of Carrara marble deformed in the semibrittle regime. The density of twins increases with strain and twinning is complex. Single grains often twin on more than one system. Taken from [Fredrich et al. \(1989\)](#).

il y a une corrélation positive entre la contrainte maximale atteinte par l'échantillon et la pression effective moyenne (équation 6), comme attendu pour une rupture de type *Mohr-Coulomb*. En revanche, en régime cataclastique, dont l'enveloppe est indiquée par la pression seuil pour l'initiation de la compaction inélastique C^* , il existe une corrélation négative entre la pression moyenne P et la contrainte déviatorique Q . De plus, l'enveloppe de compaction (*compactive yield cap*) s'accroît lorsque la porosité de la roche diminue (Figure 7). La transition fragile-ductile correspond à l'intersection entre la droite de rupture fragile et l'enveloppe dessinée par l'évolution de la contrainte à l'initiation de la compaction inélastique C^* .

A priori, la pression de confinement à la transition fragile-ductile devrait décroître avec la porosité. En utilisant le modèle de [Brandt \(1955\)](#) pour un milieu granulaire, la pression de confinement à l'initiation de la compaction inélastique devrait être reliée à $R^2(1 - \phi)$, avec R le rayon moyen de grains et ϕ la porosité ([Guéguen & Fortin, 2013](#)). Cette hypothèse est comparée avec des données issues de la littérature compilées dans la Table 1 (Figure 7 b) et semble cohérente malgré l'hypothèse forte d'un milieu granulaire. Cette hypothèse est vraisemblablement fautive pour les roches de faible porosité.

Introduction

Rock	porosity (%)	Av. grain size (mm)	P_{conf} transition (MPa)	reference
Oak Hall l.	0.3	0.1	159-220	Byerlee 1968
Carrara m.	1.1	$70 * 10^{-3}$ -0.22	30-300	Fredrich et al. 1989
Solnhofen l.	3	$5 * 10^{-3}$	50-100	Baud et al. 2000
Solnhofen l.	4.8	$10 * 10^{-3}$	81-122	Byerlee 1968
Lithographic l. (Soln. ?)	5.9	$10 * 10^{-3}$	100-200	Edmond and Paterson 1972
Tavel l.	10.4	$5 * 10^{-3}$	30-100 1 ^c	Vajdova et al. 2004
Indiana l.	13	$5 * 10^{-3}$ -0.3	10-20	Vajdova et al. 2004
Tavel l.	14.7	$5 * 10^{-3}$	55-70	this study
Indiana l.	17.8	$5 * 10^{-3}$ -0.3	5-20	Vajdova et al. 2012
Majella l.	30	$50 * 10^{-3}$ -0.4	5-25	Vajdova et al. 2012

Table 1 – Résumé des données issues de la littérature utilisées pour examiner l'évolution de la pression de confinement à la transition fragile-ductile avec la porosité et la taille des grains.

Le calcaire de Tavel

Les expériences réalisées dans le cadre de ce travail ont été effectuées sur le calcaire de Tavel (blanc). Ce calcaire a déjà été utilisé dans des travaux précédents de [Vincké et al. \(1998\)](#), [Vajdova et al. \(2004, 2010\)](#). L'observation au Microscope Electronique à Balayage (MEB) montre une composition d'environ 99% de calcite (voir chapitre 1), ce qui est en accord avec les résultats de [Vajdova et al. \(2004\)](#) qui avaient mesuré une composition formée de calcite à 98%. La présence variable d'oxydes engendre les différentes teintes du calcaire de Tavel. Tous les échantillons ont été carottés dans le même bloc, dans lequel plusieurs lames minces ont été faites afin de contrôler l'homogénéité de la microstructure. Les lames minces sont imprégnées d'époxy coloré en bleu afin de visualiser l'espace poreux.

La porosité moyenne est de 14.7%, avec une variation maximale de 0.5% autour de la moyenne. Les valeurs de porosité sont obtenues (1) en utilisant la densité des échantillons secs en supposant une composition de 100% calcite et (2) avec une procédure de triple pesée. La porosité mesurée est supérieure à celle des échantillons de [Vajdova et al. \(2004\)](#), qui était de 10.4%. A noter que les deux blocs proviennent de la même carrière (Tavel, France).

Le calcaire de Tavel est un calcaire micritique microporeux. La roche est principalement constituée de particules de micrite grossières (5 μm) coalescentes, formant de plus gros agrégats. Dans cette micrite, on peut distinguer des micropores plus larges ($\leq 10\mu\text{m}$) *sensu* [Lønøy](#)

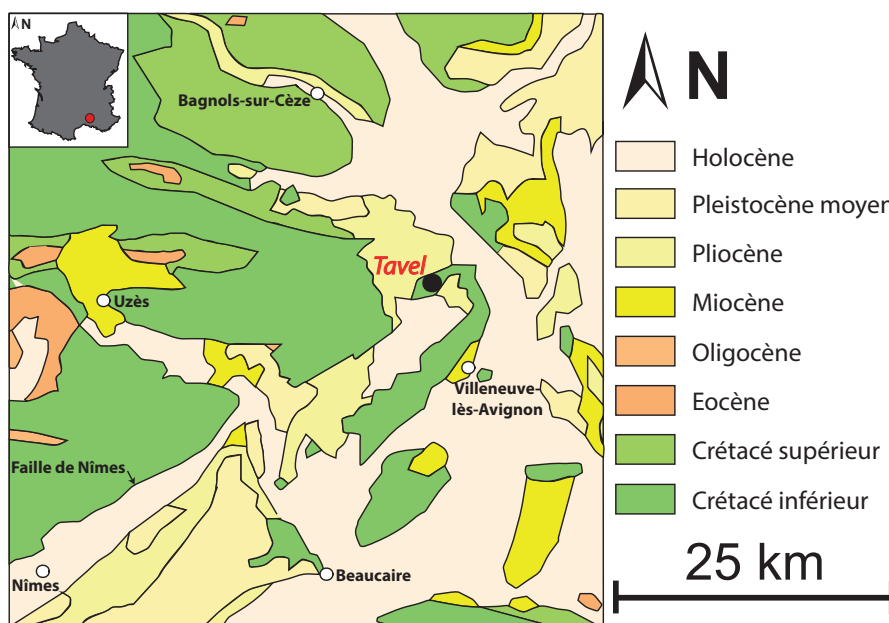


Figure 9 – Carte géologique de la région de Tavel (France). On remarque un synclinal orienté SW-NE, dont le flanc nord est bordé par la faille de Nîmes.

(2006), où la cimentation/recristallisation en sparite de grains pré-existants (bioclastes) est incomplète. Une observation détaillée d'un échantillon préparé avec polissage ionique révèle la présence de petites fissures pré-existantes localisées entre les agrégats de micrite et/ou entre les particules de micrite. Ces caractéristiques du matériau utilisé sont vraisemblablement héritées de l'histoire géologique de la formation (e.g. Lavenu et al., 2013), qui est discutée très succinctement ci-après.

Le calcaire de Tavel est extrait d'un massif formé au Crétacé inférieur, à la fin de l'ère secondaire (Figure 9). A cette époque (environ 110 millions d'années), une mer chaude a permis la formation d'une barrière de corail dont une partie des vestiges sont les collines calcaires de la zone de Tavel et Lirac. La pierre de Tavel utilisée dans cette étude est extraite de ces veines de calcaire dur. On y retrouve de façon fréquente des fossiles de coquillages comme les ammonites. Les collines calcaires font partie du massif des garrigues du Gard, qui s'étend entre Uzès et Tavel (Figure 9). Son altitude varie autour de 250 mètres d'altitude, dominant la plaine de 150 mètres (Figure 10 a).

La carrière d'extraction se situe dans une dépression calcaire dominée au nord par le plateau calcaire de la Montagne et au sud par le plateau calcaire de la forêt de Tavel-Rochefort. Le gisement est en flanc monoclinale très homogène orienté Nord 110-120° à pendage Est 30-35°.

Introduction

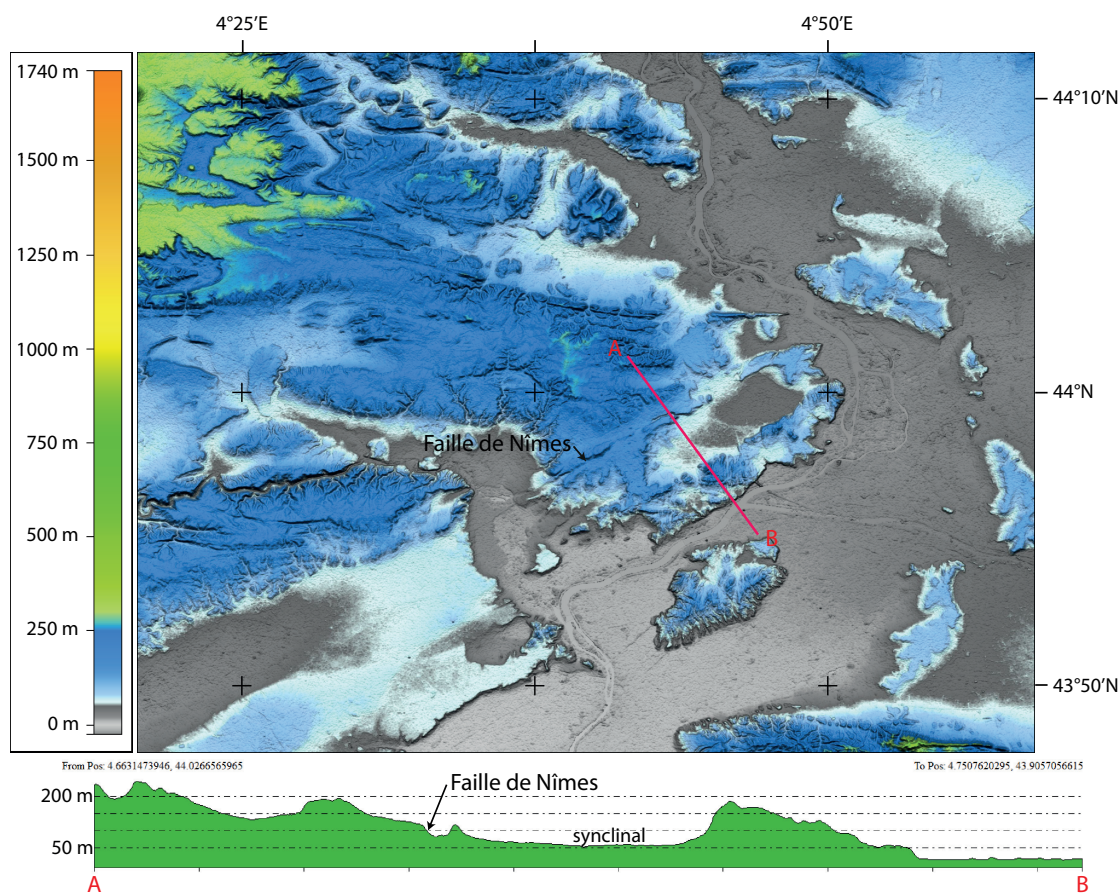


Figure 10 – (a) Carte des reliefs de la région de Tavel (France). On remarque un synclinal orienté SW-NE, dont le flanc nord est très abrupt car il est bordé par la faille de Nîmes. (b) Coupe (NW-SE) orientée perpendiculairement au synclinal. On distingue les flancs abrupts du synclinal et la faille de Nîmes.

La fracturation macroscopique est faible et également très homogène. La fracturation présente une direction principale (N340°-N20° subverticale 85° Ouest) et une associée (N90°-N190° subverticale 80° Sud).

En observant plus précisément la carte topographique (Figure 10 a), on peut distinguer la faille de Nîmes orientée SW-NE (Figure 10 a et b). La faille suit le synclinal dans le flanc duquel se situe la carrière de Tavel. La formation calcaire de laquelle sont extraits les blocs a donc subi une compression, ce qui a un impact sur la microstructure (formation de fissures, etc...) et les propriétés pétrophysiques de la roche (e.g. [Nelson, 2001](#)).

Plan du mémoire

L'objectif général de cette étude est la caractérisation du comportement mécanique des carbonates peu poreux et des paramètres influents (eau, température, vitesse de déformation). Une partie du travail réalisé a consisté en une étude expérimentale sur un calcaire micritique (calcaire de Tavel, porosité 14.7%) puis une modélisation micro-mécanique. Ce manuscrit est divisé en cinq grands axes suivis d'une conclusion générale présentant les perspectives de travail.

- Le premier chapitre présente l'étude expérimentale sur le comportement mécanique du calcaire de Tavel déformé à vitesse constante. On examine l'influence de la pression de confinement, de l'eau et de la température sur la déformation et les micro-mécanismes de déformation.
- Le deuxième chapitre propose un modèle micro-mécanique du comportement d'un calcaire peu poreux déformé à vitesse constante, à partir des micro-mécanismes de déformation identifiés lors de l'étude expérimentale.
- Le troisième chapitre s'intéresse au comportement mécanique du calcaire de Tavel à contrainte différentielle constante. L'influence de la pression de confinement et de l'eau sur la déformation a été examinée.
- Le quatrième chapitre présente la modélisation des expériences de fluage à contrainte différentielle constante.
- Enfin, le dernier chapitre porte sur l'étude de l'influence de la vitesse de déformation sur le comportement mécanique lors d'expériences à vitesse de déformation contrôlée.

**BRITTLE AND SEMIBRITTLE BEHAVIOURS OF
A CARBONATE ROCK: INFLUENCE OF WATER
AND TEMPERATURE**

Ce premier chapitre s'intéresse à la caractérisation du comportement mécanique du calcaire de Tavel. Les questions qui sont posées sont: *Quels sont les micro-mécanismes responsables de la déformation macroscopique? Comment la nature du fluide de pore et la température influencent-ils ces mécanismes de déformation?* Nous présenterons les résultats d'expériences de déformation à vitesse de déformation contrôlée sous conditions triaxiales, à différents confinements inclus dans l'intervalle 0-85 MPa, à 20°C en conditions sèches et saturées en eau, et à 70°C en conditions sèches. Au cours de la déformation, l'évolution des vitesses des ondes P et S a été mesurée. Comme montré par [Sayers & Kachanov \(1995\)](#), [Fortin et al. \(2005\)](#), [Schubnel et al. \(2006b\)](#), [Benson et al. \(2006\)](#), [Fortin et al. \(2007\)](#) parmi d'autres, leur évolution est très sensible à la présence de micro-fissures, ce qui en fait un outil de mesure de l'endommagement. Une étude microscopique permettra de confirmer les conclusions dressées à partir des mesures d'ondes élastiques. Cette étude a fait l'objet d'un article soumis à *Geophysical Journal International*.

Abstract

Inelastic deformation can either occur with dilatancy or compaction, implying differences in porosity changes, failure and petrophysical properties. In this study, the roles of water as a pore fluid, and of temperature, on the deformation and failure of a micritic limestone (white Tavel limestone, porosity 14.7%) were investigated under triaxial stresses. For each sample, a hydrostatic load was applied up to the desired confining pressure (from 0 MPa up to 85 MPa) at either room temperature or at 70°C. Two pore fluid conditions were investigated at room

Chapter 1. Brittle and semibrittle behaviours of a carbonate rock: Influence of water and temperature

temperature: dry and water saturated. The samples were deformed up to failure at a constant strain rate of $\sim 10^{-5}\text{s}^{-1}$. The experiments were coupled with elastic wave velocity surveys to monitor crack densities. The linear trend between the axial crack density and the relative volumetric strain beyond the onset of dilatancy suggests that cracks propagate at constant aspect ratio. The decrease of elastic wave velocities beyond the onset of inelastic compaction in the semibrittle regime indicate the ongoing interplay of shear-enhanced compaction and crack development. Water has a weakening effect on the onset of dilatancy in the brittle regime, but no measurable influence on the peak strength. Temperature lowers the confining pressure at which the brittle-semibrittle transition is observed but does not change the stress states at the onset of inelastic compaction and at the post-yield onset of dilatancy.

1.1 Introduction

Human activities can lead to deformation and failure of porous rocks, for example during hydrocarbon exploitation because the pore pressure decreases, which leads to an increase of the effective stress, or in mines or underground storages, due to stress concentration. Many consequences are known: surface subsidence (e.g. [Boutéca et al., 1996](#), [Fredrich et al., 2000](#), [Nagel, 2001](#)), well bore failure (e.g. [Peška & Zoback, 1995](#)), induced seismicity (e.g. [Talwani & Acree, 1984](#), [Simpson et al., 1988](#), [Segall, 1989a](#)) and permeability changes (e.g. [David et al., 1994](#), [Miller, 2002](#), [Bemer & Lombard, 2010](#)). These consequences may impact hydrocarbon or geothermal exploitation, as well as underground storage.

Limestones are one of the main groups of sedimentary rocks. They host more than 60% of the oil reserves, represent 7% of land surfaces, are used as an industrial material and have been proposed as reservoirs for the geological sequestration of carbon dioxide. At field scale, elastic wave velocities may be used to monitor changes in elastic properties, possible indicators of irreversible damage (4D seismic). However, these changes are not straightforward to interpret ([Hexsel Grochau et al., 2014](#)).

Limestone failure modes depend on their initial porosity and change with applied effective stress (e.g. [Wong & Baud, 2012](#), [Ji et al., 2015](#)). Deformation can either be coupled with dilatancy, leading to shear localization and therefore brittle failure ([Brace, 1978](#), [Paterson & Wong, 2005](#)), or result from microscopic plastic flow that does not involve any volumetric change

(Paterson, 1978). It has been known for a long time that calcite deforms by processes such as mechanical twinning or r-, f- dislocation glide at room temperature (Turner et al., 1954, Griggs et al., 1960, De Bresser & Spiers, 1997). The induced brittle-ductile transition is of special interest for porous rocks, because it could provide some insight into fault mechanics and shallow earthquakes (Sibson, 1982, Rutter, 1986). The brittle-ductile transition in carbonate rocks is relatively easy to achieve in experiments because it is accessible at room temperature for confining pressures attainable in the laboratory (e.g., Robertson, 1955, Paterson, 1958, Heard, 1960, Rutter, 1972, 1974a). Previous studies have already focused on limestones (e.g. Solnhofen limestone: Robertson (1955), Heard (1960), Rutter (1972, 1974a), Hugman III & Friedman (1979), Baud et al. (2000a), Tavel limestone: Vajdova et al. (2004, 2010), Indiana limestone: Vajdova et al. (2012), Majella limestone: Baud et al. (2009), Vajdova et al. (2012), Estailledes limestone: Dautriat et al. (2011a,b)) and marbles (e.g. Carrara marble: Rutter (1972, 1974a), Fredrich et al. (1989), Schubnel et al. (2006b), Yule marble: Hugman III & Friedman (1979)).

Dilatancy and plastic flows can combine their effects, leading to transitional behaviour named cataclastic flow, characterized by homogeneously-distributed microcracking, grain rotations and grain plasticity (twinning and dislocations), as discussed by Fredrich et al. (1989). Cataclastic flow can either lead to dilatancy as shown by Fredrich et al. (1989) on a very low porosity Carrara marble or to inelastic compaction as observed by Baud et al. (2000a), Vajdova et al. (2004, 2010), Wong & Baud (2012) on limestones and chalks of various porosities. However, compactive cataclastic flow is commonly observed to be a transient phenomenon. Indeed the failure mode evolves with increasing strain to dilatant cataclastic flow and ultimately shear localization (Baud et al., 2000a).

Initial porosity is a key parameter that controls the deformation and failure modes of limestones (Vajdova et al., 2004). Dautriat et al. (2011a) showed that structural heterogeneities can influence the localisation of damage and Zhu et al. (2010), Regnet et al. (2015b) showed that the microporosity distribution also plays a role. Pore fluid and temperature are also important parameters (Rutter, 1972, 1974a). Water generally reduces the brittle strength, as a result of adsorption: water as a pore fluid decreases the surface energy, promotes subcritical crack growth and stress corrosion (Clarke et al., 1986, Atkinson & Meredith, 1987, Costin, 1987, Baud et al., 2000b, Risnes et al., 2005, Røyne et al., 2011, Liteanu et al., 2013), which

Chapter 1. Brittle and semibrittle behaviours of a carbonate rock: Influence of water and temperature

can have effects on co-seismic sliding friction (Violay et al., 2013). Temperature modifies the short-term strength and time-dependent creep behavior of sandstones (Heap et al., 2009a), and is likely to have the same effects on limestones. As pore fluid and temperature may vary in natural conditions, the study of the deformation and failure modes should be performed under varying P-T conditions in dry and water-saturated samples.

This study focuses on the mechanical behaviour of a limestone with an initial porosity of 14.7%. The question we address is: How do water as a pore fluid and temperature influence the deformation mechanisms? We report results of conventional triaxial experiments performed at various confining pressures in the range of 0-100 MPa, at 20°C under dry and water-saturated conditions, and at 70°C under dry conditions. During these experiments, evolution of P- and S-wave velocities were measured. As shown by several authors (e.g., Fortin et al., 2005, Schubnel et al., 2006b, Benson et al., 2006, Fortin et al., 2007, Regnet et al., 2015a), their evolution is very sensitive to the presence of microcracks, which makes them a good tool to track the evolution of irreversible damage.

1.2 Material and methods

1.2.1 Rock material and sample preparation

Experiments shown in this paper were performed on white Tavel, a micritic and microporous limestone. This rock is mainly composed of coarse grained micrite particles (mean diameter $\sim 5 \mu\text{m}$) fused from one to another, leading to larger micritic aggregates (Figure 3.1 A and B). In this general micritic layout, some larger micropores (diameter between $2 \mu\text{m}$ and $10 \mu\text{m}$) can be observed in sparitic parts, where cementation or recrystallization of pre-existing bioclasts is incomplete (Figure 3.1 A and C). A more detailed observation on ionic polished thin-sections reveals the presence of a low initial crack porosity, located between micritic aggregates and/or micrite particles (Figure 3.1 D). This limestone was used in previous studies by Vincké et al. (1998), Vajdova et al. (2004, 2010). Scanning Electron Microscope (SEM) investigation showed that the composition of this Tavel limestone is almost 99% calcite, in good agreement with Vajdova et al. (2004) who measured a composition of more than 98% calcite. All samples were cored in the same block, and thin sections have been made in several samples, allowing us to

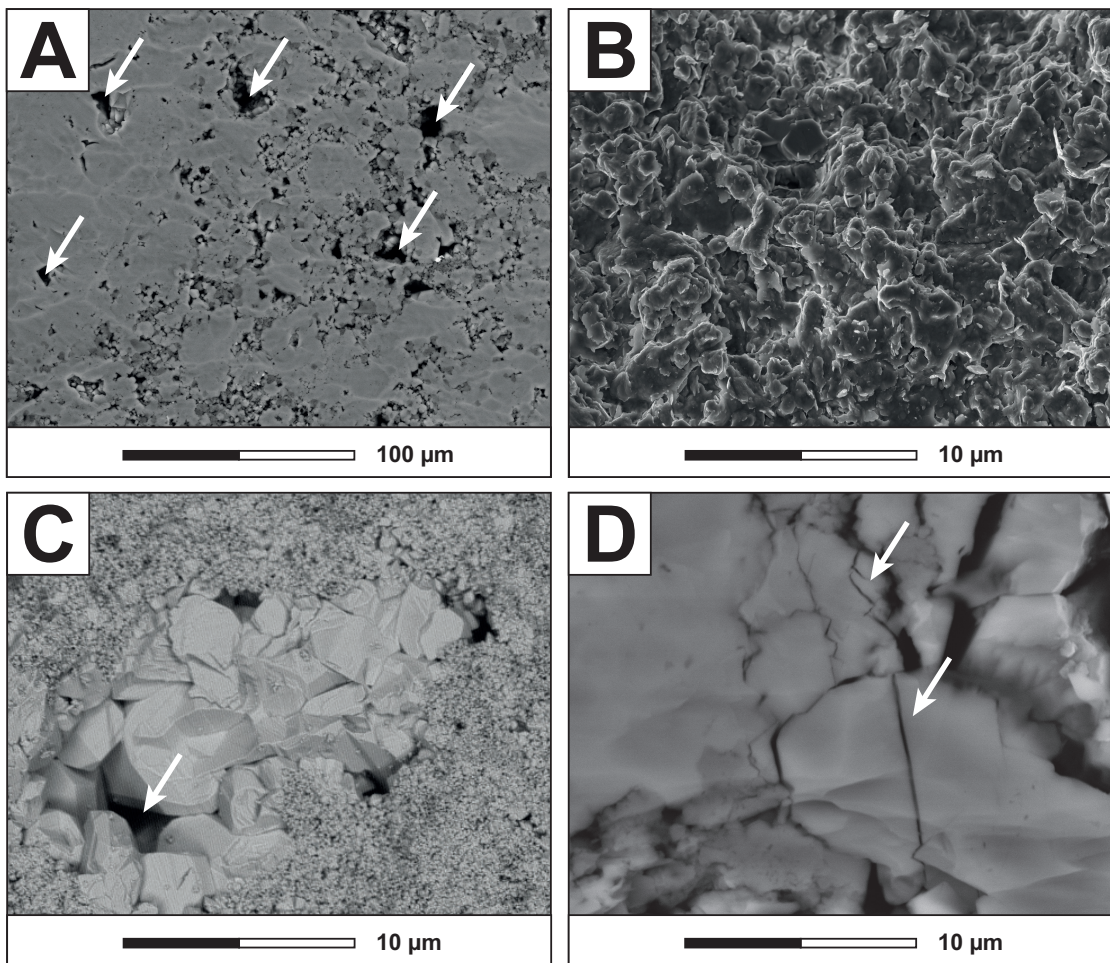


Figure 1.1 – Micrographs of Tavel Limestone in Scanning Electron Microscope. A - General observations of the layout. Larger micropores (white arrows) can be observed between or within micritic aggregates. B - Micritic aggregate composed of coarse anhedral micrite particles ($\geq 4 \mu\text{m}$) with fused to indistinct contacts. C - Incomplete sparitic cementation in a pre-existing bioclast, at the origin of larger micropores (white arrow). D - Micritic aggregate observed on an ionic polished thin section. Initial crack porosity can be observed (regular or wing cracks, white arrows).

have a robust control on the microstructure, avoiding heterogeneous samples. Thin sections were impregnated with blue-died epoxy to visualize the pore space.

Average porosity is 14.7%, with maximum porosity variations of about 0.5% around the average value. Porosity values were obtained from two measurements: (1) using the density of dried samples and assuming a 100% calcite matrix composition and (2) using a triple weight procedure. The porosity is slightly higher than that of [Vajdova et al.](#)'s samples, which was found to be 10.4%. Note that the two sets of samples are from the same quarry (Tavel, France).

Chapter 1. Brittle and semibrittle behaviours of a carbonate rock: Influence of water and temperature

No obvious bedding is identified but all samples are cored parallel to avoid any problem of preferential direction. This isotropy of the elastic properties of the rock is verified with elastic velocity measurements and discussed later in the article. The diameter of our cylindrical samples is 40 mm and their length is 86 mm. After coring, faces are ground to ensure a good parallelism. Strain gauges (*Tokyo Sokki TML* type FCB 2-11 for experiments at room temperature and *Tokyo Sokki TML* type QFCB 2-11 for experiments at higher temperature) are directly glued onto the sample surface. These gauges are each composed of one axial and one radial gauge. Neoprene tubing is used to separate the sample from oil confining medium. Before an experiment, samples are dried in an oven at $\sim 40^\circ\text{C}$ for several days.

1.2.2 Experimental apparatus

The pressure vessel used in this study is a conventional triaxial cell installed in the Laboratoire de Géologie at the École Normale Supérieure in Paris. In this paper, compressive stresses and compactive strains are counted positive. The principal stresses will be denoted σ_1 and σ_3 , σ_1 being the highest principal stress. The differential stress $\sigma_1 - \sigma_3$ will be denoted Q and the mean stress $(\sigma_1 + 2\sigma_3)/3$ will be denoted P . The confining pressure ($\sigma_2 = \sigma_3$) is measured by a pressure transducer with an accuracy of about 10^{-2} MPa. Effective pressure was calculated as $P_{eff} = P - P_{pore}$, P_{eff} being the effective pressure, and P_{pore} the pore pressure. The effective confining pressure was calculated as $\sigma_{3,eff} = \sigma_3 - P_{pore}$, where σ_3 is the confining pressure. Axial load is applied by an axial piston, and is measured with an accuracy of about 10^{-2} MPa. Radial strains are measured with four radial strain gauges. The axial displacement is measured with three displacement transducers (DCDT) mounted out of the pressure vessel between the moving piston and the fixed lower platen and corrected for the stiffness of the cell. We consider their mean displacement. We do not use the axial strain gauges because under large strains ($\varepsilon_{ax} \geq 2\%$) attainable with carbonate rocks, strain gauges break, whereas DCDTs have no strain limitation. Radial gauges are used because they undergo much smaller strains. Uncertainty in strain measured with gauges is estimated to be of the order of 10^{-5} ; and DCDT signals have a lower accuracy of about 10^{-4} .

The volumetric strain is calculated as $\varepsilon_v = \varepsilon_{ax} + 2\varepsilon_r$, where ε_{ax} and ε_r are the axial and radial strains, respectively. This formula neglects second-order contributions of strains to the volume

change that may be appreciable at relatively large strains. For water-saturated experiments, pore pressure can be controlled at the top and the bottom of the sample with two micro-volumetric pumps (Quizix) with an accuracy of about 10^{-2} MPa.

Some experiments were performed at room temperature (20°C, controlled by air conditioning) while others were performed at 70°C. For the latter ones, the triaxial cell is equipped with a heating system. The maximum heating rate is approximately 1°C/min. The temperature inside the vessel is recorded via two thermo-couples, one being plunged in the confining oil and the other touching the bottom end of the lower steel plug.

1.2.3 Elastic wave velocities

Eight piezoelectric transducers (PZTs) were directly glued onto the sample surface. We used four PZT sensors sensitive to P-waves and four sensitive to S-waves. Both types of PZT sensors have a resonant frequency around 1 MHz. The small number of PZT sensors does not allow us to relocate acoustic emissions (AE). However, no significant AE activity was recorded. Therefore PZT sensors were only used to measure the evolution of P-wave and S-wave velocities during the experiment. Every 1 or 2 minutes during the experiment, a 250 V high frequency signal is pulsed on each sensor while the others are recording. The electrical signal received is amplified at 40 dB. The position of each sensor is known and is corrected for the sample deformation during the experiment. P- or S-wave travel time allows us to calculate the P-wave velocities at an angle of 90° and ~ 53° with the axis of symmetry, as well as the horizontal SH- and vertical SV-wave velocities at an angle of 90° (Figure 1.2). Arrival times are known with an accuracy of 0.1 µs, which leads to an accuracy on ultrasonic velocity of ~ 5%.

1.2.4 Experimental procedure

The 18 complete and 11 incomplete triaxial experiments were performed at effective confining pressures ranging from 0 MPa (uniaxial experiment) to 85 MPa. A set of experiments was conducted at 20°C in dry and water saturated conditions and in dry conditions at 70°C. Experimental conditions of each experiment (confining pressure, pore fluid and temperature) can be found in Tables 5.1 and 1.2.

Chapter 1. Brittle and semibrittle behaviours of a carbonate rock: Influence of water and temperature

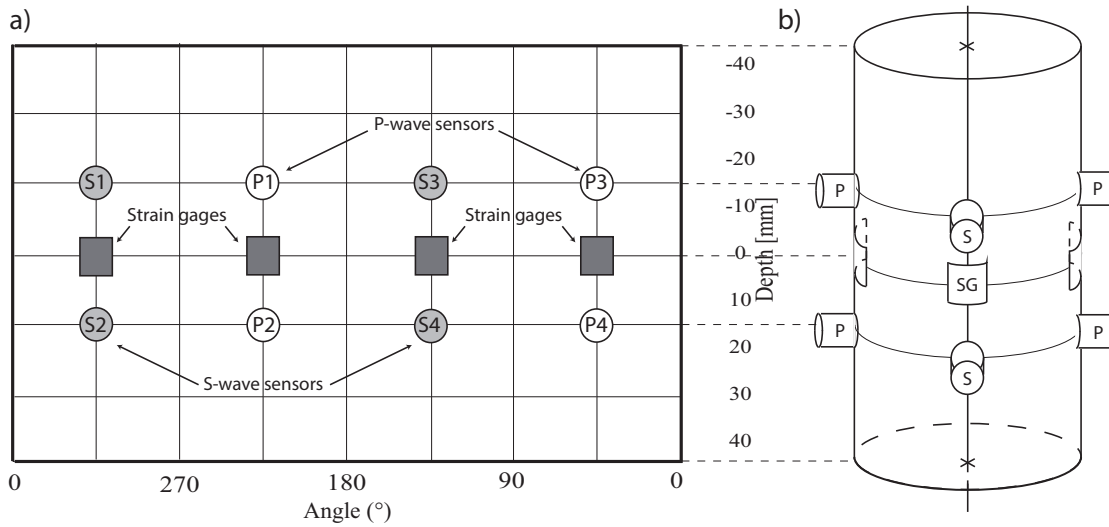


Figure 1.2 – (a) Sensor map used for the experiments. Elastic wave velocities (P and S) were measured on directions forming an angle of 53° and 90° with the sample axis. A schematic view of a prepared sample is given in (b).

N°	pore fluid	P_{eff} (MPa)	P_p (MPa)	Temperature ($^\circ\text{C}$)	C' (MPa)	C^* (MPa)	$C^{*'}$ (MPa)	Peak stress (MPa)	ϕ ($^\circ$)
1	dry	0	0	20	20 ± 5	-	-	32	-
2	dry	20	0	20	56 ± 5	-	-	77.4	16
3	dry	35	0	20	80 ± 7.5	-	-	114.3	25
4	dry	55	0	20	105 ± 10	-	-	136.7	30
5	dry	70	0	20	-	117 ± 7.5	161.3	-	29
6	dry	85	0	20	-	134 ± 7.5	181.5	-	-
7	dry	85	0	20	-	133 ± 7.5	174	-	-
8	water	20	5	20	45 ± 10	-	-	87.5	19
9	water	35	5	20	63 ± 5	-	-	103.1	28
10	water	55	5	20	94 ± 10	-	-	141.6	29
11	water	70	5	20	-	126 ± 7.5	161.8	-	-
12	water	85	5	20	-	134 ± 10	178.3	-	-
13	dry	5	0	70	28 ± 7.5	-	-	55	-
14	dry	20	0	70	55 ± 5	-	-	74.5	21
15	dry	35	0	70	82 ± 5	-	-	101.8	20
16	dry	55	0	70	-	106 ± 10	140.6	-	19
17	dry	70	0	70	-	118 ± 10	152.7	-	25
18	dry	85	0	70	-	131 ± 10	173	-	-

Uncertainty is less than 0.2 MPa for these stress states.

ϕ corresponds to the angle between the vertical axis and the macroscopic fault trace in the sample.

Table 1.1 – Summary of the mechanical data obtained on white Tavel limestone and presented in Figure 3.4. This Table gives effective mean stresses for the onset of dilatancy (C'), onset of inelastic compaction (C^*), post-yield onset of dilatancy ($C^{*'}$) and peak stresses.

N ^o	pore fluid	P _{eff} (MPa)	P _p (MPa)	C' (MPa)	C* (MPa)	C*' (MPa)	Peak stress (MPa)
1	dry	20	0	58 ± 5	-	-	-
2	dry	35	0	78 ± 5	-	-	-
3	dry	55	0	95 ± 7.5	-	-	-
4	dry	70	0	-	121 ± 5	158	-
5	dry	70	0	-	120 ± 5	-	-
6	dry	85	0	-	132 ± 5	-	-
7	dry	85	0	-	135 ± 5	-	-
8	water	20	5	48 ± 5	-	-	-
9	water	35	5	62 ± 5	-	-	-
10	water	55	5	88 ± 5	-	-	-
11	water	85	5	-	120 ± 5	-	-

Uncertainty is less than 0.2 MPa for these stress states.

Table 1.2 – Summary of the additional mechanical data obtained on white Tavel limestone. These samples were not deformed up to failure, thus they are not presented in Figure 3.4 but they are presented in the appendix (Figure S1.1). However, from these experiments it is possible to get effective mean stresses for the onset of dilatancy (C'), onset of inelastic compaction (C^*), and for one experiment post-yield onset of dilatancy (C^{*}).

Samples deformed in dry conditions at 20°C were first loaded isostatically up to the desired confining pressure. The differential stress is then applied by deforming the sample at a controlled strain rate of $\sim 10^{-5}\text{s}^{-1}$. Concerning experiments conducted in dry conditions at 70°C, the dry sample is first loaded isostatically up to a pressure of 20 MPa. Confining pressure is kept constant at 20 MPa during heating (~ 18 hours). The temperature is considered to be homogeneous when the difference between the two thermo-couples is lower than 1°C. At that point, the procedure becomes similar to that for dry samples at room temperature.

For water-saturated experiments, the dry sample is loaded isostatically up to a pressure of 20 MPa and saturated with water at equilibrium with calcite. Saturation is controlled with the microvolumetric pumps. Full saturation is assumed to be reached when the total injected volume of water is stable. At that point, a pressure difference of 1 MPa is applied between the bottom and the top of the sample during ~ 30 minutes in order to flush the air trapped within the sample. Then, the pore pressure is maintained constant at a pressure of 5 MPa during all

Chapter 1. Brittle and semibrittle behaviours of a carbonate rock: Influence of water and temperature

the experiment and the procedure becomes similar to that for dry samples.

The hydromechanical behaviour of a permeable rock is directly related to the condition of drainage during deformation (e.g. Guéguen & Boutéca, 1999, Duda & Renner, 2013). A key point before conducting water-saturated experiments is to check whether we are in drained conditions or not. Characteristic time t for diffusion over a distance l (to get fluid pressure equilibrium) can be approximated by (Carslaw & Jaeger, 1959, Ge & Stover, 2000, Duda & Renner, 2013):

$$t \sim \frac{l^2}{D}, \quad (1.1)$$

where D is the hydraulic diffusivity. The hydraulic diffusivity D can be approximated by (Kümpel, 1991):

$$D \sim \frac{kBK_d}{\eta\alpha}, \quad (1.2)$$

where k is the permeability, B is Skempton's coefficient, K_d is the drained bulk modulus, η is the fluid viscosity, and α is Biot's coefficient. For white Tavel limestone and water, $k = 10^{-16} \text{ m}^2$, $\eta = 1.002 \times 10^{-3} \text{ Pa.s}$, and $K_d = 27 \text{ GPa}$. Assuming that Skempton's coefficient and Biot's coefficient to be of the order of unity, one obtains $D \sim 2.7 \cdot 10^{-3} \text{ m}^2\text{s}^{-1}$. For $l = 4 \text{ cm}$ (half length of the sample), one gets $t \sim 1 \text{ s}$, which is a short time compared to that of our experiments (between 10 min and 1h). Thus, our experiments can be considered as conducted in drained conditions.

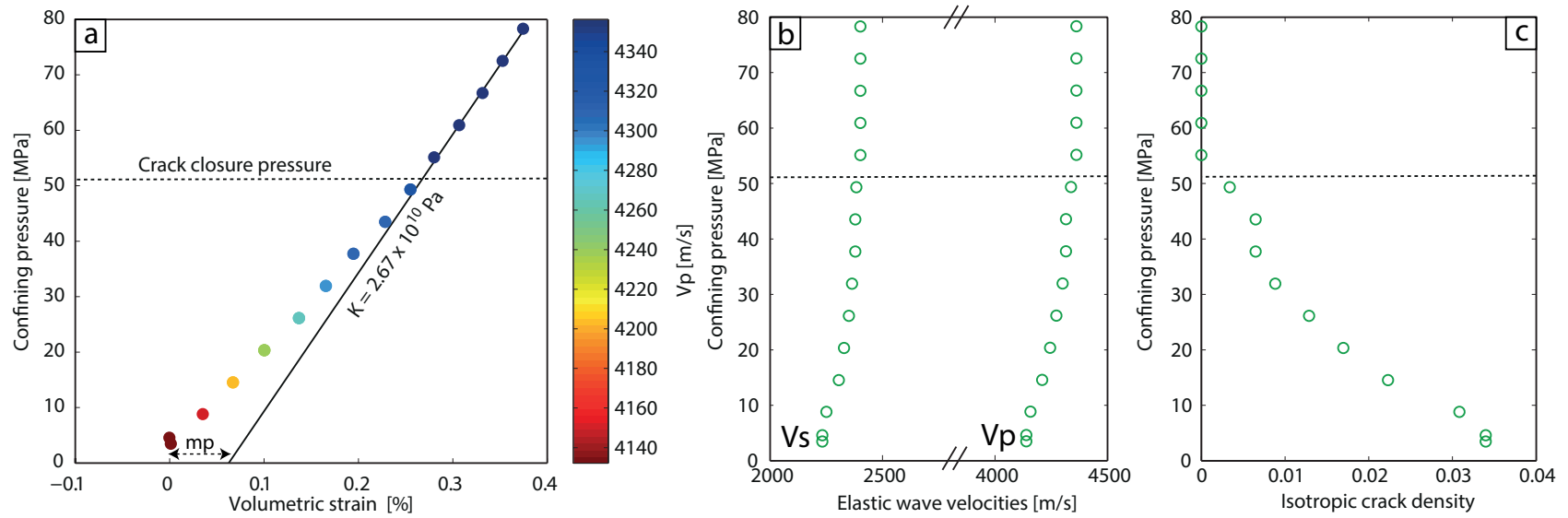


Figure 1.3 – (a) Evolution of the volumetric strain plotted versus confining pressure. The color of the points are related to the P-wave velocities measured during the loading. The black line corresponds to a linear elastic behaviour for a bulk modulus of 26.7 GPa. The dashed line corresponds to the crack closure pressure inferred from the volumetric strain. The microcrack porosity is shown by an arrow labelled *mp* on the Figure. (b) Evolution of the elastic wave velocities plotted against the confining pressure. The dashed line corresponds to the crack closure pressure inferred from (a). (c) Evolution of the isotropic crack density plotted against the confining pressure. The dashed line corresponds to the crack closure pressure inferred from (a).

1.3 Results

1.3.1 Mechanical behaviour during isostatic loading

Results for a hydrostatic loading experiment with up to 85 MPa of confining pressure performed on a dry sample at a temperature of 20°C are presented in Figure 1.3. The hydrostatic response was non-linear up to a pressure of ~ 52 MPa, beyond which the stress-strain curve became linear with a slope corresponding to a bulk modulus of $K = 26.7$ GPa (Figure 1.3 a). The non-linearity observed below 52 MPa can be explained by the progressive closure of pre-existing microcracks (Baud et al., 2000a, Vajdova et al., 2004), such as the one present in Figure 3.1 (a). Comparing the volumetric strain measured and the perfectly elastic trend, microcrack porosity can be estimated to be ~ 0.07% (Walsh, 1965a). The closure of pre-existing cracks is also highlighted by the evolution of the ultrasonic P and S wave velocities (Figure 1.3 b). As pressure is increased from 0 to 52 MPa, P and S wave velocities increase from 4135 m/s and 2200 m/s to 4350 m/s and 2350 m/s, respectively. Above 52 MPa, P and S wave velocities remain constant at 4350 m/s and 2350 m/s, respectively. Using these last values, dynamic bulk modulus K_0 is found to be $K_0 = 26.9$ GPa.

1.3.2 Mechanical behaviour during deviatoric loading

The mechanical behaviour observed during experiments conducted on dry samples at 20°C depend upon the confining pressure (Figures 3.4 a and d). For P_c lower than 55 MPa, the mechanical behaviour and failure mode are typical of the brittle faulting regime. The axial strain versus differential stress curves first show a linear trend classical of an elastic behaviour (Figure 3.4 a). At higher differential stress, the axial strain increase is larger than the elastic one. Finally, the differential stress reaches a peak, beyond which strain softening is taking place (Figure 3.4 a). The same features are inferred in the volumetric strain versus mean stress curves (Figures 3.4 d): samples show an elastic compactant behaviour until a critical stress state denoted C' (Wong et al., 1997) beyond which the volumetric strain deviates from linear elasticity (onset of dilatancy). The critical stress state C' is determined manually at the point of divergence of the curve of volumetric strain versus mean stress and the linear elastic compaction of each experiment. To our knowledge, no previous article gave error bars for the

onset of dilatancy, which remains somehow subjective. The error bar given for each critical stress in this article correspond to an upper bound and account for the subjective part of the critical stress determination. Note that although error bars are wide, results remain well reproducible (Tables 5.1 and 1.2). The differential stress levels at the onset of dilatancy (C') and peak stress show a positive confining pressure dependence (Figure 3.4 and Tables 5.1 and 1.2).

For P_c equal or higher than 70 MPa, the mechanical behaviour is different from the one at lower pressures and is characterised by three different stages: a compactive elastic behaviour, beyond which an inelastic compactive regime takes place. The transition between these two domains is characterised by the stress C^* (Wong et al., 1997). The critical stress state C^* is determined manually at the point of divergence of the curve of volumetric strain versus mean stress and the linear elastic compaction of each experiment. This inelastic compaction is characterised by a decrease in volume larger than the elastic one and is referred to as shear-enhanced compaction (Wong et al., 1992, 1997). In these experiments, inelastic compaction is a transient phenomenon. Indeed, the volumetric strain evolves with increasing strain to dilatant cataclastic flow beyond a critical state denoted $C^{*'} (Wong et al., 1997)$. Between the onset of inelastic compaction (stress state C^*) and the post-yield onset of dilatancy (stress state $C^{*'}$), compaction and dilatancy are likely to take place simultaneously (e.g. Edmond & Paterson, 1972, Dresen & Evans, 1993) but compaction is dominant. At $C^{*'}$, dilatancy overcomes compaction. The critical stresses at the onset of post-yield dilatancy ($C^{*'}$) exhibit a positive dependence on confining pressure (Figure 1.5 a). Relying on our experiments, the lack of data make it impossible to conclude about a possible pressure dependence of the stress state at the onset of inelastic compaction (C^*), although it is known that C^* has a negative pressure dependence (Baud et al., 2000a). The mechanical behaviour observed for P_c equal or higher than 70 MPa can be considered as semibrittle as defined by Evans et al. (1990). The semibrittle regime is characterized by macroscopically distributed deformation involving crystal plasticity and microcracking (Evans et al., 1990). Comparing the volumetric strain versus mean stress of all samples, the brittle-semibrittle transition occurs at a confining pressure between 55 MPa and 70 MPa, under dry conditions at 20°C.

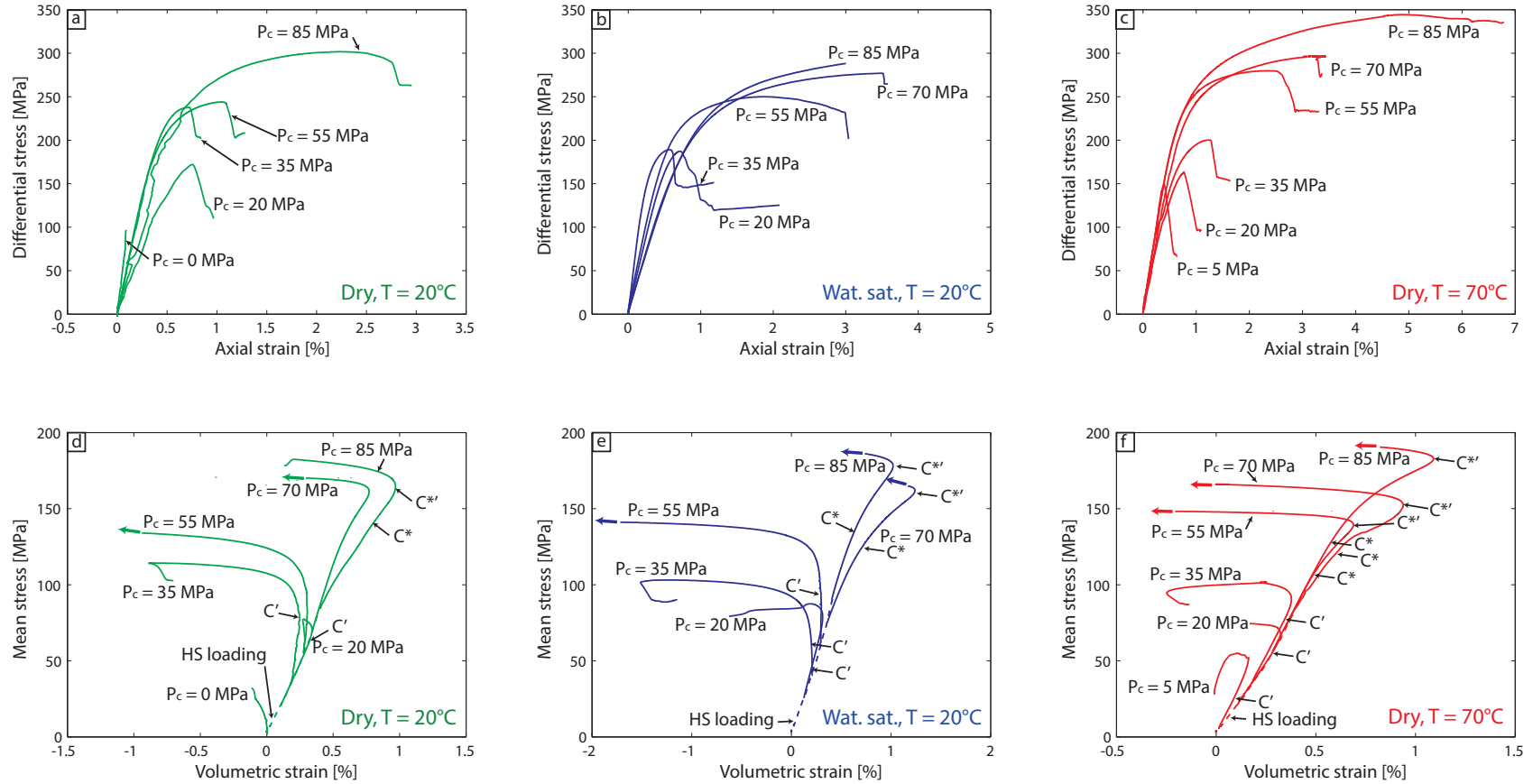


Figure 1.4 – Compilation of mechanical data for complete experiments. The differential stress is plotted versus axial strain for experiments on a) dry samples at 20°C , b) water saturated samples at 20°C , and c) dry samples at 70°C . The mean stress versus volumetric strain curves for these three sets of experiments are shown in (d), (e) and (f). Stress states at the onset of dilatancy C' , onset of inelastic compaction C^* and post-yield onset of dilatancy $C^{*'}$ are shown for references on some experiments. Note that the radial strain gages broke at strains larger than 1%, so that the last part of these plots are missing and symbolized by an arrow.

In water-saturated conditions, the mechanical behaviour is very similar to that observed in dry experiments. For P_c lower than 55 MPa, the mechanical response and failure mode are typical of the brittle faulting regime, showing dilatancy and strain softening (Figure 3.4 b and e). For P_c equal to, or higher than, 70 MPa, the mechanical behaviour clearly shows an inelastic compaction identified as shear-enhanced compaction, which induces strain hardening but ultimately switches from shear-enhanced compaction to dilatancy (Figures 3.4 b and e). Water has a weakening effect in the brittle regime: stresses at the onset of dilatancy (C') in water-saturated experiments are lower than that obtained in dry experiments (Figure 1.5 a). On the contrary, no clear effect is recorded 1) on the peak strength, 2) on the stress state at the onset of inelastic compaction (C^*) and 3) on the stress state at the post-yield onset of dilatancy (C^{**}). The brittle-semibrittle transition is occurring at a confining between 55 MPa and 70 MPa, at similar values than those obtained for dry conditions.

The behaviour observed during the experiments performed in dry conditions at 70°C is qualitatively similar to the previous ones. At 5 and 35 MPa of confining pressure, the mechanical response and failure mode are typical of the brittle faulting regime (Figures 3.4 c and f). For P_c higher than 55 MPa, the mechanical behaviour shows shear-enhanced compaction, which ultimately switches to dilatancy. Stresses at the onset of dilatancy (C'), onset of inelastic compaction (C^*), onset of post-yield dilatancy (C^{**}) and peak stress are identical for experiments performed at $T = 20^\circ\text{C}$ and $T = 70^\circ\text{C}$ in dry conditions (Figure 1.5 b). However, the brittle-semibrittle transition occurs for a confinement between 35 MPa and 55 MPa, a lower value than that obtained at room temperature (Figure 1.5 b). At $T = 20^\circ\text{C}$, the experiment performed at a confining pressure of 55 MPa clearly exhibits a brittle behaviour, whereas the one performed at the same confinement but at $T = 70^\circ\text{C}$ shows shear-enhanced compaction (Figure 1.6).

1.3.3 Post mortem microstructural analysis

Samples were unloaded and retrieved from the pressure vessel at the end of the experiments. The deformed samples were first impregnated with epoxy and then sawed along a plane parallel to the axial direction to prepare petrographic thin sections. To characterise deformation-related features in the most detailed way, Scanning Electron Microscope (SEM) was used.

Chapter 1. Brittle and semibrittle behaviours of a carbonate rock: Influence of water and temperature

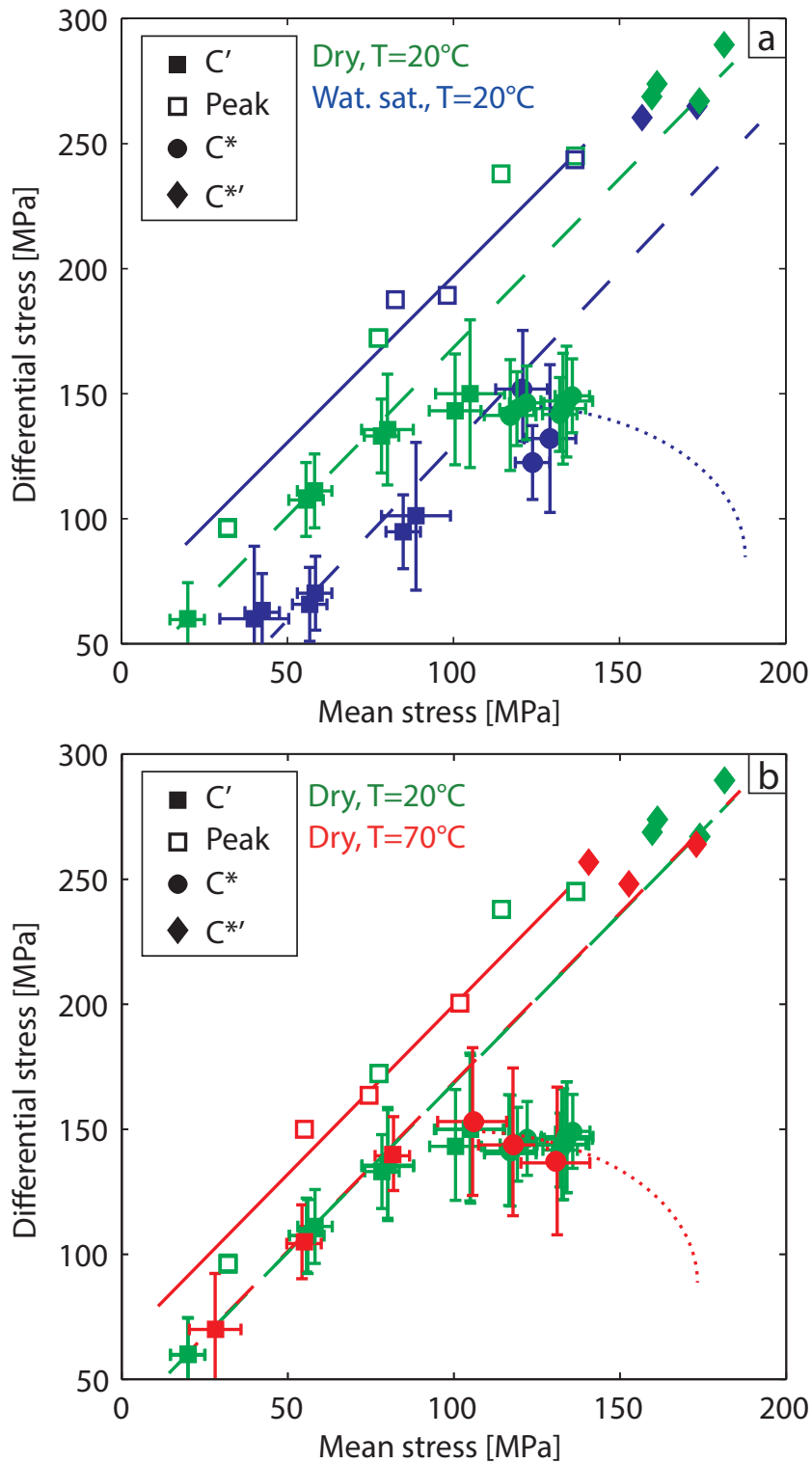


Figure 1.5 – Peak stress (empty squares), and thresholds C' (plain squares), C^* (plain dots), and C^{*} (plain diamonds) from Tables 5.1 and 1.2 are shown in the $P - Q$ space for a) dry samples at 20°C (green) and water-saturated samples at 20°C (blue), and b) dry samples at 20°C (green) and dry samples at 70°C (red).

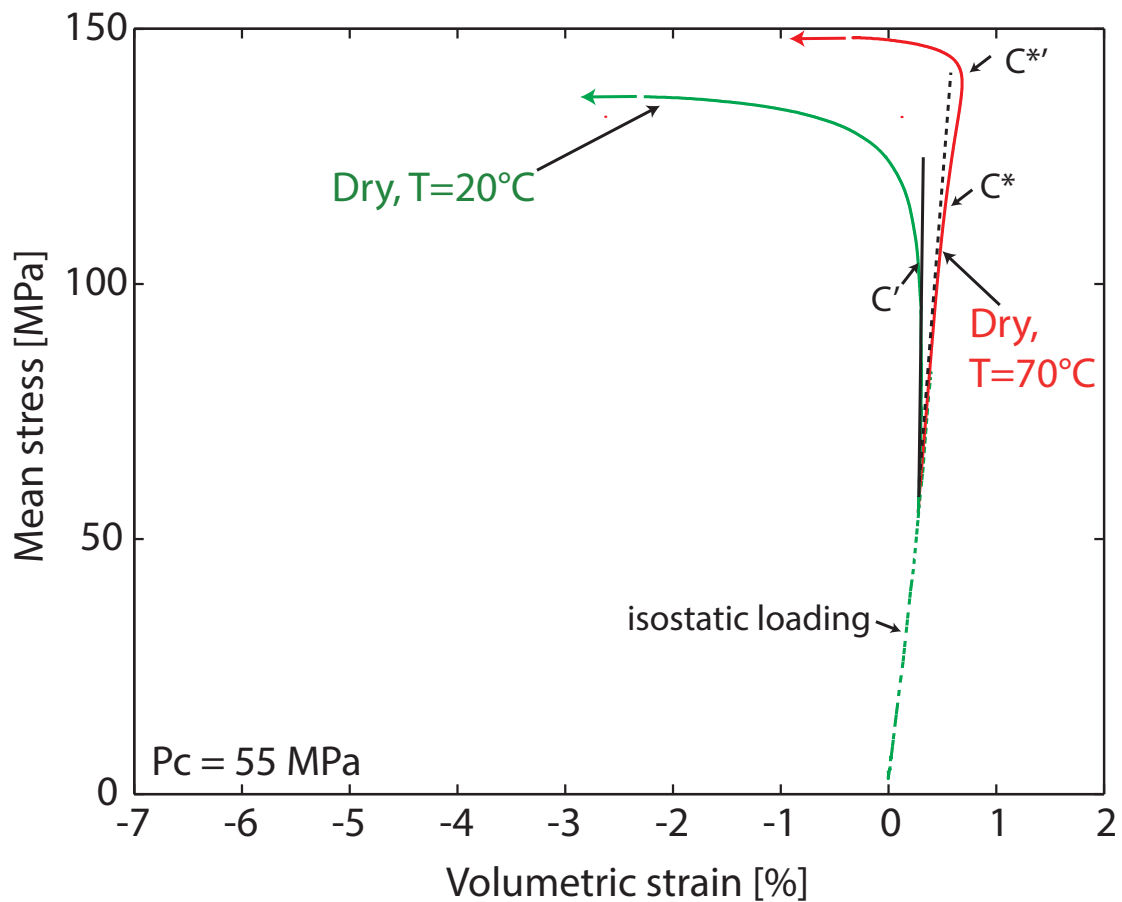


Figure 1.6 – Volumetric strain versus mean stress for experiments performed in dry conditions at a confining pressure of 55 MPa at 20 °C and 70 °C. At 20 °C, the mechanical response is typical of the brittle faulting regime, whereas the mechanical response is typical of the semibrittle regime at 70 °C.

Figure 1.7 presents a selection of pictures for samples deformed at $P_c = 20$ MPa and $P_c = 85$ MPa, which illustrate the two observed mechanical behaviours (brittle and semibrittle, respectively).

Samples of the brittle fracture regime are characterized by the localization of deformation on a low-angle shear fracture ($\sim 30^\circ$) (Figure 1.7 A). Microcracking seems to be the dominant mechanism of dilatant failure in brittle faulting in Tavel Limestone, although a very low twinning activity was also observed. Observations show a complex fracture and crack network mainly developed in micritic parts, but also in sparite crystals (Figure 1.7 B and C). Those deformation-related fractures/cracks are coloured and highlighted by the blue-died epoxy, and account for a non-negligible porosity creation, especially when considering the displacement

Chapter 1. Brittle and semibrittle behaviours of a carbonate rock: Influence of water and temperature

on the main shear fracture (Figure 1.7 D). Overall, those features are characteristic of the brittle fault regime, and in good agreement with the observed mechanical behaviour.

Samples of the semi-brittle fracture regime (ductile type of behaviour) show no localization of the deformation but a slight barrel shape after the experiment (Figure 1.7 E). Microscopic observations reveal an intense twinning activity within the sparite crystals (Figure 1.7 F) which appears to be an important deformation mechanism in those samples. This twinning activity is often coupled with grain-crushing (Figure 1.7 G) and non-coalescent microcracks within sparite crystals (Figure 1.7 H). Those stress-induced cracks are preferentially aligned and propagated sub-parallel to σ_1 . Those features are in good agreement with deformation mechanism found in the semibrittle regime.

1.3.4 Evolution of elastic wave velocities during triaxial loading

During the initial stage of elastic loading, no variation of velocities are recorded for experiments performed at $P_c \geq 55$ MPa, neither for P-waves nor for S-waves (Figures 1.8 and 1.9). Beyond the stage of elastic loading, variations of elastic wave velocities depend upon the confining pressure.

In the brittle regime, i.e. for P_c below 55 MPa for experiments performed at $T = 20^\circ\text{C}$ and for P_c below 35 MPa for experiments performed at $T = 70^\circ\text{C}$, V_p and V_s start decreasing at the onset of dilatancy (C') (Figures 1.8 c-f and Figures 1.9 c-f). Comparing the elastic wave velocity decrease to the volumetric change (e.g. Figure 1.10 for P-wave velocity), the decrease in velocities is sharper around the onset of dilatancy (C'). Just beyond C' , velocities continue to decrease as the sample is deformed until failure. The overall decrease for both V_p and V_s reaches 25% to 30% for all the experiments. The same features are observed in water-saturated conditions and at $T = 70^\circ\text{C}$ (Figures 1.8 d-f and Figures 1.9 d-f).

In the semibrittle regime, i.e. for P_c above 55 MPa for experiments performed at $T = 20^\circ\text{C}$ and for P_c above 35 MPa for experiments performed at $T = 70^\circ\text{C}$, the evolution of elastic wave velocities is different than that observed in the brittle regime. In the elastic compaction stage, no change of V_p and V_s is measured (Figures 1.8 c-f and Figures 1.9 c-f). Beyond the onset of inelastic compaction (C^*) elastic wave velocities start to decrease, and the decrease rate accelerates as the post-yield onset of dilatancy ($C^{*'}\text{'}$) is approached. At $C^{*'}\text{'}$ V_p and V_s a

decrease of 10% to 20% is observed. Around C^* , the decrease of V_p and V_s as a function of the volumetric change is maximum (Figure 1.10, experiment performed at $P_c = 85$ MPa). Beyond the post-yield onset of dilatancy C^* , in the dilatancy stage, V_p and V_s continue to decrease down to values 30% to 40% lower than their initial value (Figures 1.8 c-f and Figures 1.9 c-f). For experiments performed at $T = 70^\circ\text{C}$, the decrease of elastic wave velocities around C^* seems to be slightly less important than for experiments performed at $T = 20^\circ\text{C}$ (Figures 1.8 c-f and Figures 1.9 c-f). Finally, the evolution of elastic wave velocities can be added to the mechanical data (Figure 1.11) and is directly correlated to dilatancy.

Chapter 1. Brittle and semibrittle behaviours of a carbonate rock: Influence of water and temperature

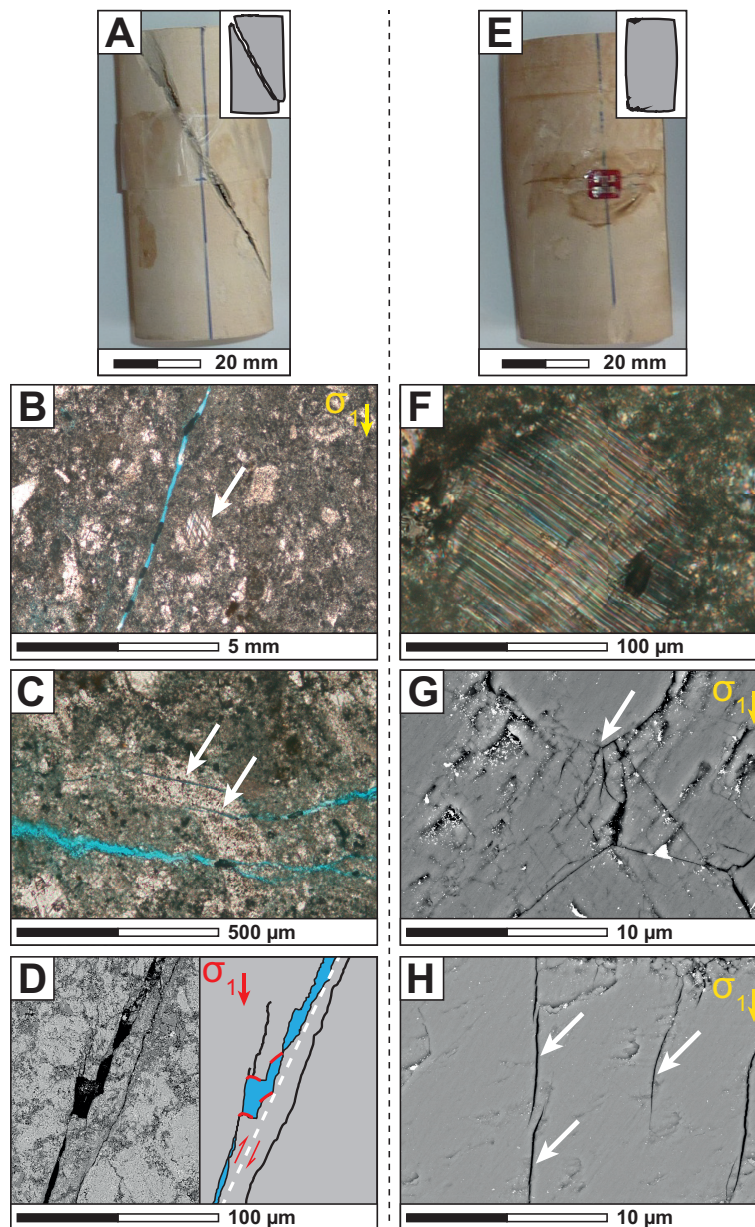


Figure 1.7 – Pictures and micrographs of two samples characterised by brittle (A, B, C and D) and semibrittle (E, F, G and H) behaviours after unloading (optical microscopy and SEM). A - Deformation localization on a shear fracture for the sample deformed at $P_c = 20$ MPa. B - Shear fracture under optical microscopy (blue-coloured) that propagated in the micritic part of the rock. Note the low twinning activity in the sparite crystal (white arrow), associated with intragranular cracks. C - Stress-induced fracture and crack network in micrite and sparite, respectively (white arrows). D - Displacement on the main fracture, leading to porosity creation. E - A stress-induced barrel-shape is observed after deformation for the sample deformed at $P_c = 85$ MPa. F - Intense twinning activity in a sparite. G - Grain-crushing phenomenon between two large sparites. Cracks propagate sub-parallel to σ_1 . H - Wing cracks in a large sparite, sub-parallel to σ_1 . Those cracks do not coalesce from one to another.

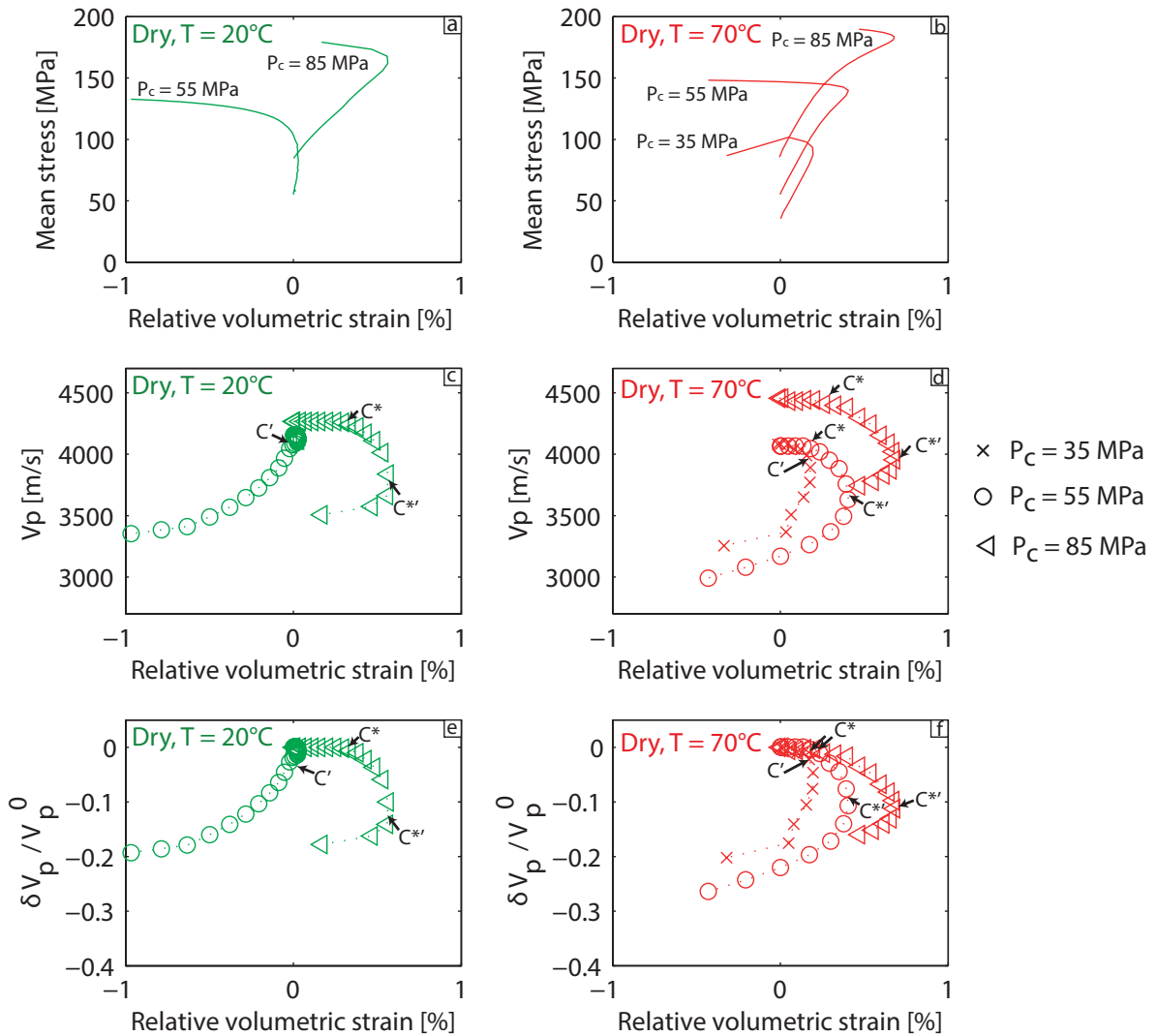


Figure 1.8 – Compilation of mechanical and P-waves data for selected experiments. Note that strains are "relative strains", i.e. the zero strain is that at the end of the hydrostatic loading. Relative volumetric strain versus mean stress is shown for reference in (a) and (b) for dry experiments at 20°C and dry experiments at 70°C, respectively. (c) and (d) show the evolution of P-wave velocities perpendicular to σ_1 versus the relative volumetric strain for the two sets of experiments. (e) and (f) show the evolution of $\delta V_p / V_p^0$ versus relative volumetric strain, where V_p^0 is the P-wave velocity at the beginning of the triaxial loading.

Chapter 1. Brittle and semibrittle behaviours of a carbonate rock: Influence of water and temperature

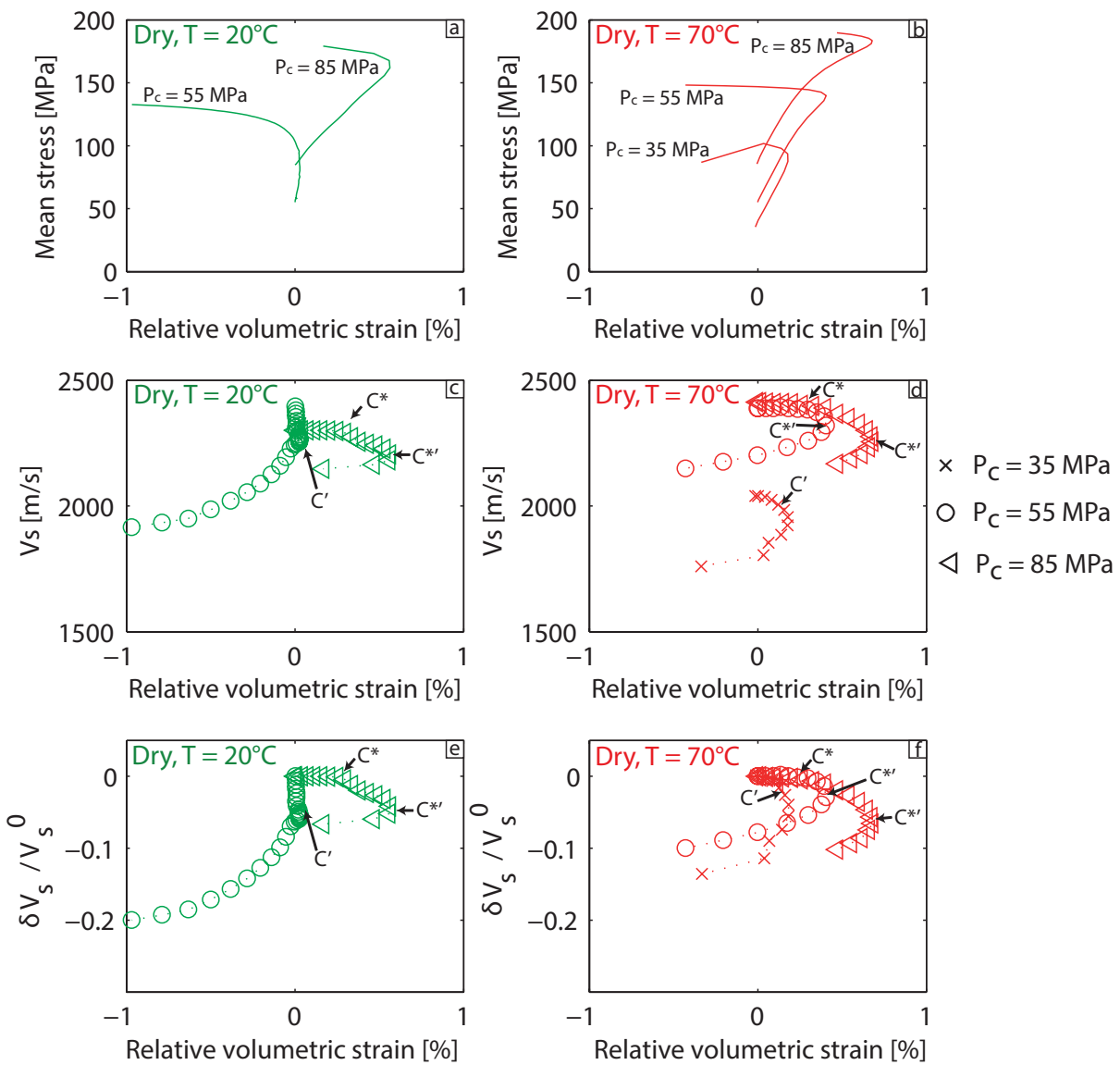


Figure 1.9 – Compilation of mechanical and S-waves data for selected experiments (same as those presented in Figure 1.8). Relative volumetric strain versus mean stress is shown for reference in (a) and (b) for dry experiments at 20°C and dry experiments at 70°C, respectively. Note that strains are "relative strains", i.e. the zero strain is that at the end of the hydrostatic loading. (c) and (d) show the evolution of S-wave velocities perpendicular to σ_1 versus the relative volumetric strain for the two sets of experiments. (e) and (f) show the evolution of $\delta V_s / V_s^0$ versus relative volumetric strain, where V_s^0 is the S-wave velocity at the beginning of the triaxial loading.

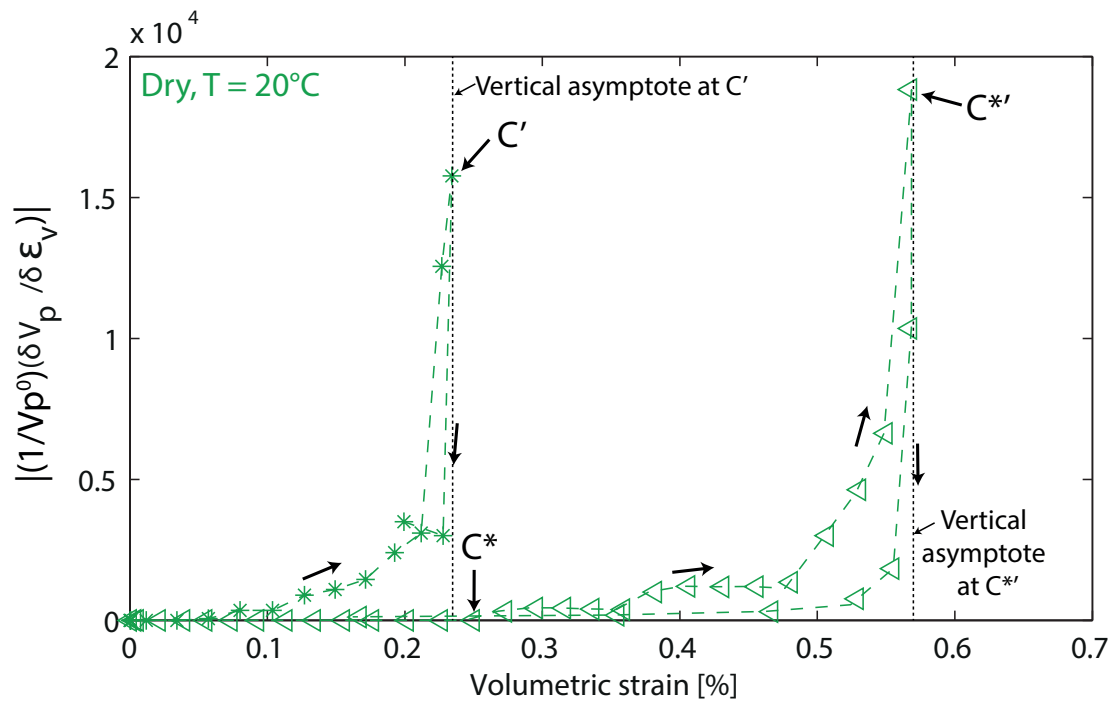


Figure 1.10 – The absolute value of the P-wave velocity derivative with respect to the volumetric strain is plotted versus the volumetric strain for experiments conducted at $P_c = 20$ and 85 MPa in dry conditions. The maximum value is found for C' and $C^{*'}$ for the brittle and semibrittle behaviours, respectively.

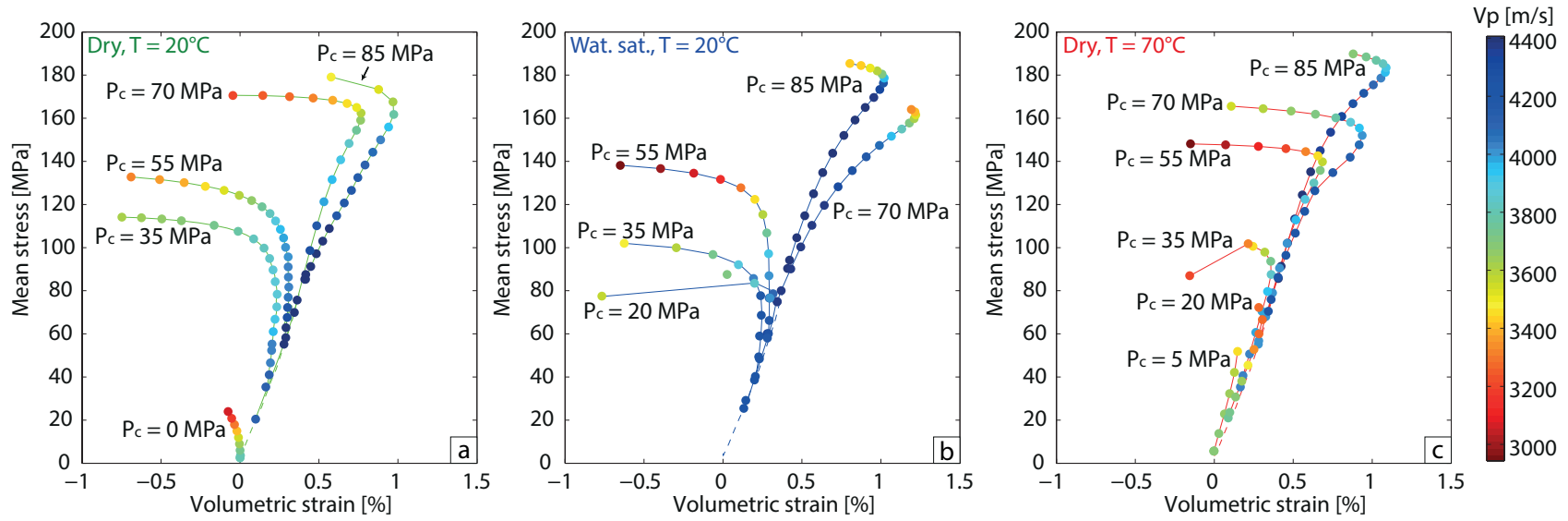


Figure 1.11 – Representative data for P-wave velocity evolution during deformation. Volumetric strain is plotted versus the mean stress P . The confining pressure is indicated on each curve. The color of the dots represents P-wave velocity perpendicular to σ_1 . The color caption is given on the right.

1.4 Discussion

1.4.1 From inverted crack density to macroscopic deformation at isostatic stress

The mechanical response of Tavel limestone subjected to isostatic loading (Figure 1.3) is typical of a rock with microcracks and equant pores (Walsh, 1965a), in agreement with microstructural observations of the intact rock (Figure 3.1). To interpret theoretically and quantitatively the evolution of the ultrasonic velocities, we consider a porous rock as made of a mixture of solid grains, spherical pores, and penny-shaped cracks. Using Kachanov (1993), the effective elastic properties of the porous rock may be expressed in a unique manner as a function of the overall porosity ϕ and the crack density ρ_c . The crack density is defined as:

$$\rho_c = \frac{1}{V} \sum_{i=1}^n c_i^3, \quad (1.3)$$

where c_i is the radius of the i th crack and N is the total number of cracks embedded in the representative elementary volume (REV) V .

From mechanical data (Figure 1.3 a), the non-linearity at the beginning of the loading shows crack closure (Walsh, 1965a), up to a hydrostatic stress of 52 MPa. Porosity due to microcracks is estimated to be around $\phi_c = 0.07\%$. Crack closure pressure and crack porosity are similar to that obtained by Vajdova et al. (2004) on their samples of Tavel limestone (40 MPa and 0.1%, respectively).

Under isostatic stress conditions, our results show that elastic wave velocities are independent from their pathway, indicating that the medium composed of matrix with embedded pores and cracks is isotropic. In dry conditions, the effective bulk modulus K (which can be directly inverted from a combination of the P- and S-wave velocities), can be expressed as (Kachanov, 1993, Fortin et al., 2007):

$$\frac{K_0}{K} = 1 + \frac{\rho_c}{1-\phi} \frac{h}{1-2\nu_0} \left(1 - \frac{\nu_0}{2}\right), \quad (1.4)$$

where K_0 is the bulk moduli of the crack-free matrix, ν_0 is Poisson's ratio of the crack-free matrix, ρ_c is the crack density and h is a factor describing the penny-shaped geometry,

$$h = \frac{16(1-\nu_0^2)}{9(1-\nu_0/2)}. \quad (1.5)$$

The elastic properties K_0 and ν_0 of the calcite aggregate composed of the solid matrix and embedded pores were estimated from velocities measured at $P_c = 85$ MPa, a pressure far above

Chapter 1. Brittle and semibrittle behaviours of a carbonate rock: Influence of water and temperature

the crack closing pressure (see section 1.3.1 and Figure 1.3). As pressure is increased isostatically from 0 to 52 MPa, the isotropic crack density decreased from 0.035 to 0 (Figure 1.3 c). Inverted crack density evolution is consistent with the crack closure inferred from mechanical data. Above 52 MPa, crack density remains constant at a value of 0 as a consequence of using elastic wave velocities at $P_c = 85$ MPa to calculate K_0 and ν_0 .

Following Walsh (1965a), the crack closure pressure P_{cl} for isotropic stress state can be related to the crack aspect ratio defined as $\xi = w/2c$, where w is the crack aperture:

$$P_{cl} = \frac{\pi \xi E_0}{4(1 - \nu_0^2)}. \quad (1.6)$$

Using the elastic properties of the crack-free material and $P_{cl} = 52$ MPa, equation 1.6 gives $\xi = 1.9 \times 10^{-3}$, a value close to those reported in the literature (Baud et al., 2000a). If cracks are assumed to be characterized by a penny-shape geometry, then crack porosity is given by (Guéguen & Kachanov, 2011):

$$\phi^{crack} = 2\pi \rho_c \langle \xi \rangle, \quad (1.7)$$

where $\langle \xi \rangle$ is the average crack aspect ratio defined as $\langle \xi \rangle = \langle w/2c \rangle$. Taking $\langle \xi \rangle = 1.9 \times 10^{-3}$ and $\rho = 3.5 \times 10^{-2}$ (isotropic crack density inverted at $P_c = 0$ MPa), one finds an initial crack porosity $\phi_c^i \simeq 0.042\%$. This value is of the order of the crack volume inferred from the mechanical data shown in Figure 1.3 a ($\phi_c = 0.07\%$).

Above the crack closure pressure, the rock is assumed to be composed of the solid matrix and embedded pores. Walsh (1965a) modelled the effective bulk modulus K of dilute spherical pores embedded in an elastic matrix as:

$$\frac{K_m}{K} = 1 + \frac{3(1 - \nu_m)}{2(1 - 2\nu_m)} \frac{\phi}{(1 - \phi)}. \quad (1.8)$$

where ϕ is the porosity of the equant pores, and K_m and ν_m are the intrinsic incompressibility and Poisson ratio of the solid grain, respectively. For a calcite aggregate at 300 MPa pressure, the Reuss averages are $K_m = 73$ GPa for the intrinsic bulk modulus and $\nu_m = 0.33$ for the intrinsic Poisson's ratio (Simmons & Wang, 1971). Using these values, the bulk modulus found for our 14.7% porosity limestone is $K = 47.6$ GPa, which is larger than $K = 26.7$ GPa measured experimentally. This discrepancy between theory and experimental data for limestones of porosity higher than 10% was already observed by Vajdova et al. (2004), who explained it by the fact that the model considered dilute pores whereas interaction among the pores is likely to

occur for high porosities. Another explanation could be that Walsh's [1965a] model considers spherical pores embedded in a solid matrix. Considering a four-sided hypotrochoidal and a triangular pore, Zimmerman (1990) showed that the compressibility is twice and 1.6 times higher than that of a spherical pore of same volume, respectively. As shown by Figure 3.1 (a), pores in Tavel limestone are not spherical, which could explain the discrepancy between experimental and theoretical values.

Measured static ($K_{stat} = 26.7$ GPa for $P_c \geq 52$ MPa) and dynamic ($K_{dyn} = 26.9$ GPa for $P_c \geq 52$ MPa) moduli are very close for white Tavel limestone, contrary to what is commonly observed (Eissa & Kazi, 1988, Fiona & Cook, 1995, Ciccotti & Mulargia, 2004). This could be explained by the microstructure of Tavel limestone, which is composed of cemented micritic grains (Figure 3.1). Grain boundaries are fused (Figure 3.1 B), thus reducing the difference between static and dynamic moduli because grain sliding and rearrangements are prevented (Regnet et al., 2015a).

1.4.2 Crack densities under triaxial stresses

Under triaxial stresses, our results show that elastic wave velocities depend on the pathway, indicating that cracks are not randomly oriented. The maximum decrease is observed for the pathway perpendicular to σ_1 (90°), which suggests that the propagating and/or nucleating cracks are mainly axial (Mavko et al., 1995, Ayling et al., 1995, Fortin et al., 2011). Thus, we invert elastic wave velocities in terms of axial crack density (Sayers & Kachanov, 1995) assuming: (1) a transverse isotropic crack geometry; (2) an isotropic matrix, in agreement with the isotropic elastic waves velocities measured under hydrostatic conditions; (3) non-interacting cracks, an assumption which is valid for crack densities up to at least 0.15 and probably 0.2-0.25 (Grechka & Kachanov, 2006); (4) a random crack center distribution; and (5) penny-shape cracks of radius c and aperture w . The effective mechanical properties of the calcite aggregate composed of the solid matrix and embedded pores (Young modulus $E_0 = 32.8$ GPa and Poisson's ratio $\nu_0 = 0.29$) were estimated from velocities measured at $P_c = 85$ MPa, a pressure far above the crack closing pressure (see Figure 1.3). The detailed procedure is given in appendix 3.5.

When the differential stress is increased, the evolution of the crack density depends upon the

Chapter 1. Brittle and semibrittle behaviours of a carbonate rock: Influence of water and temperature

deformation mode. The axial crack density remains constant during the elastic compaction of all experiments (Figure 1.12). Beyond that stage, changes in crack density depend upon the confining pressure. In the brittle regime, the axial crack density increases immediately beyond the onset of dilatancy (C') and reaches values between 0.1 and 0.27 at macroscopic failure (Figure 1.12). Inverted crack densities are slightly higher in water-saturated conditions than in dry ones, suggesting that water enhances crack propagation. At $T = 70^{\circ}\text{C}$, crack densities are almost identical to those measured in dry conditions at $T = 20^{\circ}\text{C}$.

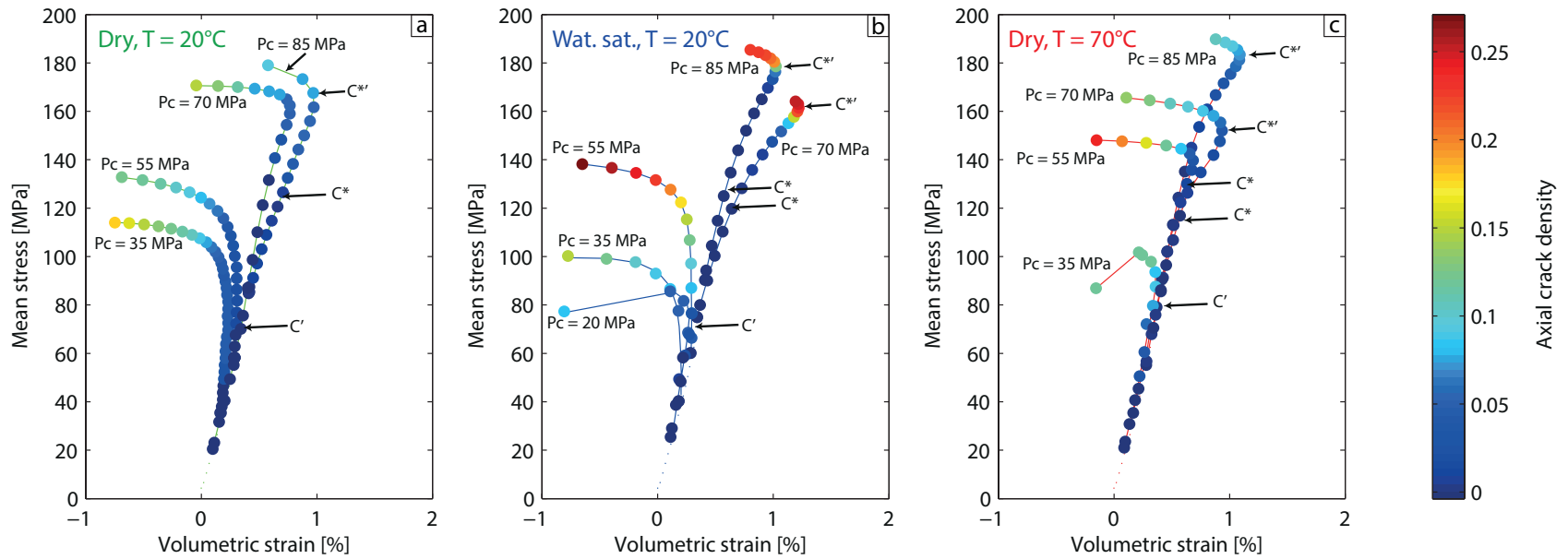


Figure 1.12 – Volumetric strain plotted versus mean stress for experiments performed under dry conditions at 20°C (a), water saturated conditions at 20°C (b) and dry conditions at 70°C (c). Axial crack density evolution is superimposed for each experiment. The color caption is given on the right.

Chapter 1. Brittle and semibrittle behaviours of a carbonate rock: Influence of water and temperature

In the semibrittle regime, axial crack density increases beyond the onset of inelastic compaction (C^*). However, between C^* and the post-yield onset of dilatancy ($C^{*'}), the induced crack density remains low. For example, in dry conditions, for $P_c = 70$ MPa and $T = 70^\circ\text{C}$, the crack density increases from 0 at C^* to 0.01 at $C^{*'}$. During the inelastic compaction stage and as the post-yield onset of dilatancy ($C^{*'}$) is approached, crack density increase rate with respect to the volumetric strain accelerates. Beyond $C^{*'}$, crack density increases rapidly up to 0.15-0.25 (Figure 1.12). In water-saturated conditions, crack densities are slightly higher than in the dry case, especially for the experiments performed at $P_c = 70$ MPa. At $T = 70^\circ\text{C}$, crack densities are slightly lower than at $T = 20^\circ\text{C}$, suggesting that temperature enhances plastic phenomena.$

1.4.3 Onset and development of dilatancy in the brittle regime

Brittle faulting can be modeled by a sliding wing crack model (Cotterell & Rice, 1980). With this interpretation, the end of the elastic behaviour in the brittle regime (onset of dilatancy denoted C') is considered as the point of initiation of wing cracks. Assuming an isotropic rock (in agreement with path-independent elastic wave velocities under hydrostatic pressure), initial cracks are considered as randomly oriented. Under triaxial stresses, wing cracks should preferentially initiate at an angle of $\psi = (1/2) \tan^{-1}(1/\mu)$ to the largest remote compressive stress σ_1 , where μ is the friction coefficient of the initial crack. The onset of dilatancy is expected at an axial stress (Cotterell & Rice, 1980, Horii & Nemat-Nasser, 1986, Ashby & Sammis, 1990):

$$\sigma_1 = \frac{\sqrt{1+\mu^2} + \mu}{\sqrt{1+\mu^2} - \mu} \sigma_3 + \left(\frac{\sqrt{3}}{\sqrt{1+\mu^2} - \mu} \right) \frac{K_{IC}}{\sqrt{\pi a}}, \quad (1.9)$$

where a is the radius of initial cracks and K_{IC} is the intrinsic fracture toughness of the material. From linear regressions of the data (Figure 1.13), one gets $\mu = 0.6 \pm 0.1$ and $K_{IC}/(\pi a)^{1/2} = 17.1 \pm 1$ MPa for the experiments performed in dry conditions at $T = 20^\circ\text{C}$ and $T = 70^\circ\text{C}$ (Table 1.3).

For water saturated experiments, linear regressions lead to $\mu = 0.35 \pm 0.1$. This reduction of friction coefficient in water-saturated conditions was already observed for sandstones

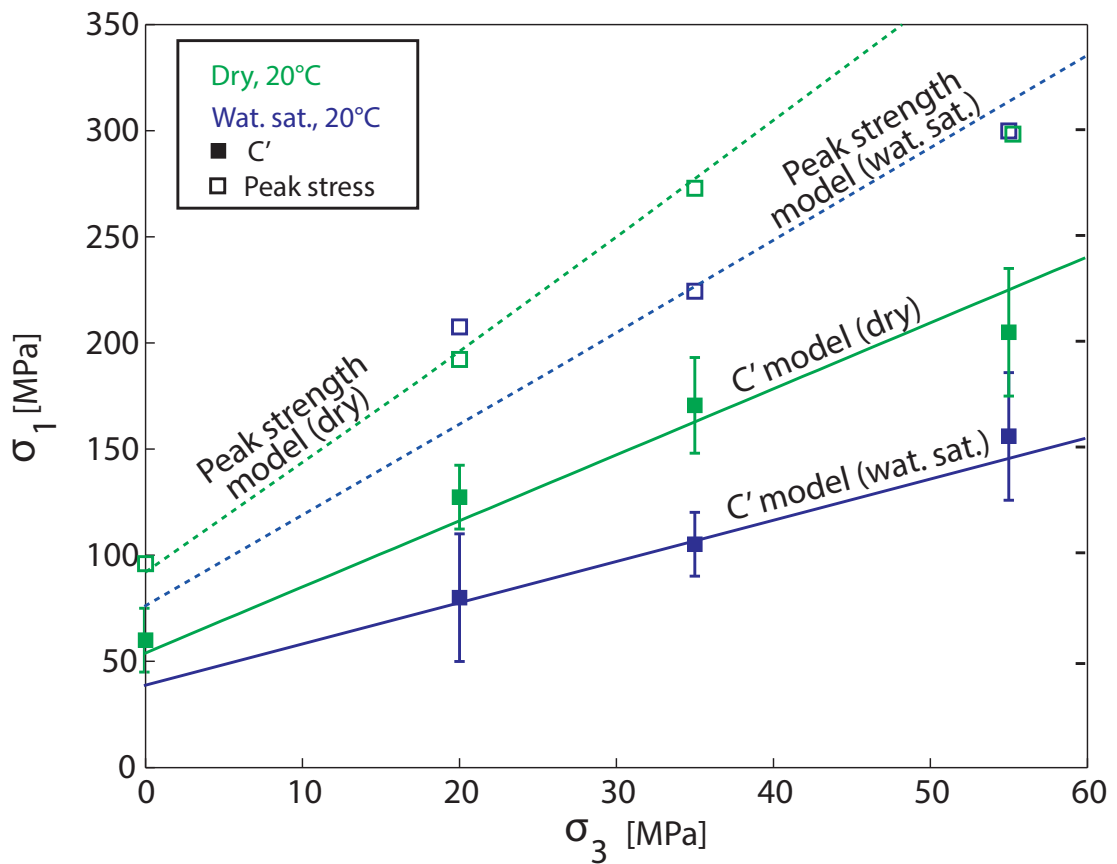


Figure 1.13 – Experimental stress states C' and peak stresses (in green for experiments performed in dry conditions and in blue for experiments performed in water-saturated conditions) are compared to theoretical predictions. Predicted stresses at C' and peak stresses are modeled by equations 5.1 and 5.2, respectively. Modeled C' and peak stresses are represented by the plain and dashed lines, respectively.

Condition	μ	$K_{IC}/(\pi a)$ (MPa)	D_0
dry	$\mu = 0.6 \pm 0.1$	17.1 ± 1	0.055
wat. sat.	$\mu = 0.35 \pm 0.1$	16 ± 1	0.055

Table 1.3 – Wing crack and energy parameters inferred from mechanical data.

(Baud et al., 2000b) but the friction coefficient drop was only 10 %. For water saturated experiments, one gets from the data $K_{IC}/(\pi a)^{1/2} = 16 \pm 1$ MPa, a value that is slightly lower than that in dry conditions ($K_{IC}/(\pi a)^{1/2} = 17.1 \pm 1$ MPa). The decrease of surface energy can be calculated considering that the crack initial mean size, a , is the same for dry and water

Chapter 1. Brittle and semibrittle behaviours of a carbonate rock: Influence of water and temperature

saturated experiments:

$$\frac{K_{IC}^{dry}}{K_{IC}^{wat.}} = \left(\frac{\gamma^{dry}}{\gamma^{wat.}} \right)^{1/2} = 1.07 \pm 0.06, \quad (1.10)$$

where γ^{dry} and $\gamma^{wat.}$ are the dry and water-saturated surface energies, respectively. The ratio between dry and water saturated surface energies is then: $\gamma^{dry}/\gamma^{wat.} = 1.14 \pm 0.12$. The ratio between dry and water saturated surface energies obtained in this study is comparable to that obtained by [Baud et al. \(2000b\)](#) on sandstones and of the same order as what [de Leeuw & Parker \(1997\)](#) obtained by numeric simulations. Water adsorption on the internal pore surface leads to a reduction of surface free energy ([de Leeuw & Parker, 1997](#), [Røyne et al., 2011, 2015](#)) that chemically weakens the rock ([Rutter, 1972](#), [Henry et al., 1977](#), [Baud et al., 2000b](#)). This observation of chemical weakening of the rock is in agreement with the higher crack density obtained during triaxial deformation in water-saturated conditions than in dry conditions (Figure 1.12 a and b).

An increase of 50°C in temperature does not modify the differential stress at the onset of dilatancy (C') and the development of dilatancy. Qualitatively similar mechanical behaviour and similar strains are observed at $T = 20^\circ\text{C}$ and $T = 70^\circ\text{C}$ (Figures 3.4 d and f).

1.4.4 Failure envelope in the brittle regime

Previously presented two-dimensional (plane strain) models ([Ashby & Sammis, 1990](#)) are used to analyse failure. To a first approximation (detailed explanation is given in appendix 1.5), the failure envelope for the wing crack model ([Horii & Nemat-Nasser, 1986](#), [Ashby & Sammis, 1990](#), [Kemeny & Cook, 1991](#), [Baud et al., 2000a](#)) can be described by a linear relation:

$$\sigma_1 = A(\mu, D_0)\sigma_3 + B(\mu, D_0) \frac{K_{IC}}{\sqrt{\pi a}}, \quad (1.11)$$

where A and B are constants which depend on μ and $D_0 = \pi(a \cos \psi)^2 N_A$, where N_A is the number of sliding cracks of uniform orientation ψ per unit area initially present. The constant D_0 characterises the initial damage. Using equation 5.2 with $K_{IC}/(\pi a)^{1/2}$ and μ that were inverted from equation 5.1 for dry conditions, one finds $D_0 = 0.055$, a lower value to that reported in [Vajdova et al. \(2004\)](#) for white Tavel. As shown by Figure 1.13, experimental data are in reasonable agreement with the obtained theoretical prediction (green dashed line). A question remains: Is $D_0 = 0.055$ in agreement with the initial crack density inverted

from elastic wave velocities? From velocity data, inverted initial 3D isotropic crack density is $\rho = 0.035$. The failure envelope for the wing crack model (equation 5.2) is 2D. Converting 3D crack density into 2D leads to $\rho_{2D} = \rho_{3D}^{2/3}$. Then, from elastic wave velocity measurements and using $\psi = (1/2) \tan^{-1}(1/\mu)$, one gets $D_0 = \pi \rho^{2/3} \cos^2 \psi = 0.25$. The value inverted from the failure envelope (equation 5.2) being $D_0 = 0.055$, this suggests that the sliding cracks (those of uniform orientation around ψ) represent approximately 20 % of the initially present cracks. Model predictions for peak strength depend upon μ , K_{IC} , D_0 and a . The initial damage D_0 and initial crack length a are likely to remain constant whatever the pore fluid is but μ and K_{IC} are modified in the presence of water compared to dry conditions. Using $K_{IC}/(\pi a)^{1/2} = 16$ MPa, $\mu = 0.35$ (values inverted from C' model for water-saturated conditions) and $D_0 = 0.055$ (same value as for dry samples), model predictions for peak strengths are lower in water-saturated conditions than in dry ones (Figure 1.13). Water-weakening on peak stress is experimentally obtained for the experiments performed at $P_c = 35$ MPa but not for the others (Figure 1.5 b). As a conclusion, a water-weakening effect is evidenced for the onset of dilatancy (C') but not for the peak strength, which is similar to what was observed in cracked granites (Wang et al., 2013) but not to what has been observed in sandstones (Baud et al., 2000b).

1.4.5 From inelastic compaction to dilatancy in the semibrittle regime

For $P_c \geq 70$ MPa at $T = 20^\circ\text{C}$ and $P_c \geq 55$ MPa at $T = 70^\circ\text{C}$, inelastic compaction of Tavel limestone is observed beyond the stress state C^* . Beyond elastic compaction, Dautriat et al. (2011b) showed that cataclastic compaction is coupled with an elastic wave velocity decrease by approximately 30 % in a very porous limestone (Estailades limestone, porosity: 28%). This observation also holds for porous sandstones (Fortin et al., 2005, 2007). In our experiments, V_p and V_s decrease by 10% to 15 % between C^* and C^{**} (Figures 1.8 and Figures 1.9), and inverted crack densities remain low between these stress states (Figures 1.12 and 1.14). The elastic wave velocities decrease rate with respect to volumetric strain increases as the post-yield onset of dilatancy (C^{**}) is approached (Figure 1.10), indicating that cracks develop although macroscopic inelastic compaction is recorded. At this stage, compaction due to plastic pore collapse and dilatancy due to development of cracks take place simultaneously. However, compaction strain associated with pore collapse appears to be predominant. Microstructural analyses

Chapter 1. Brittle and semibrittle behaviours of a carbonate rock: Influence of water and temperature

show an intense twinning activity (Figure 1.7 F), and small cracks that did not coalesce in large sparites (Figure 1.7 G and H). These observations suggest that deformation beyond C^* in the semibrittle regime and inelastic pore collapse are controlled by plastic micromechanisms associated with some microcracking. This conclusion is in good agreement with results from [Vajdova et al. \(2004\)](#) who showed that limestones with low porosities ($\leq 15\%$) undergo inelastic compaction associated with dislocation slip processes, twinning and some microcracking. [Baud et al. \(2000a\)](#) drew similar conclusions and interpreted shear-enhanced compaction in Solnhofen limestone as resulting from plastic collapse of spherical pores embedded in a solid matrix, as initially modeled by [Curran & Carroll \(1979\)](#). The insensitivity of the onset of inelastic compaction (C^*) to the variations of the experimental conditions (pore fluid and temperature) explored by our experiments seems to be at odds with the notion of plastic pore collapse. Possibly the range in investigated temperatures is simply too small.

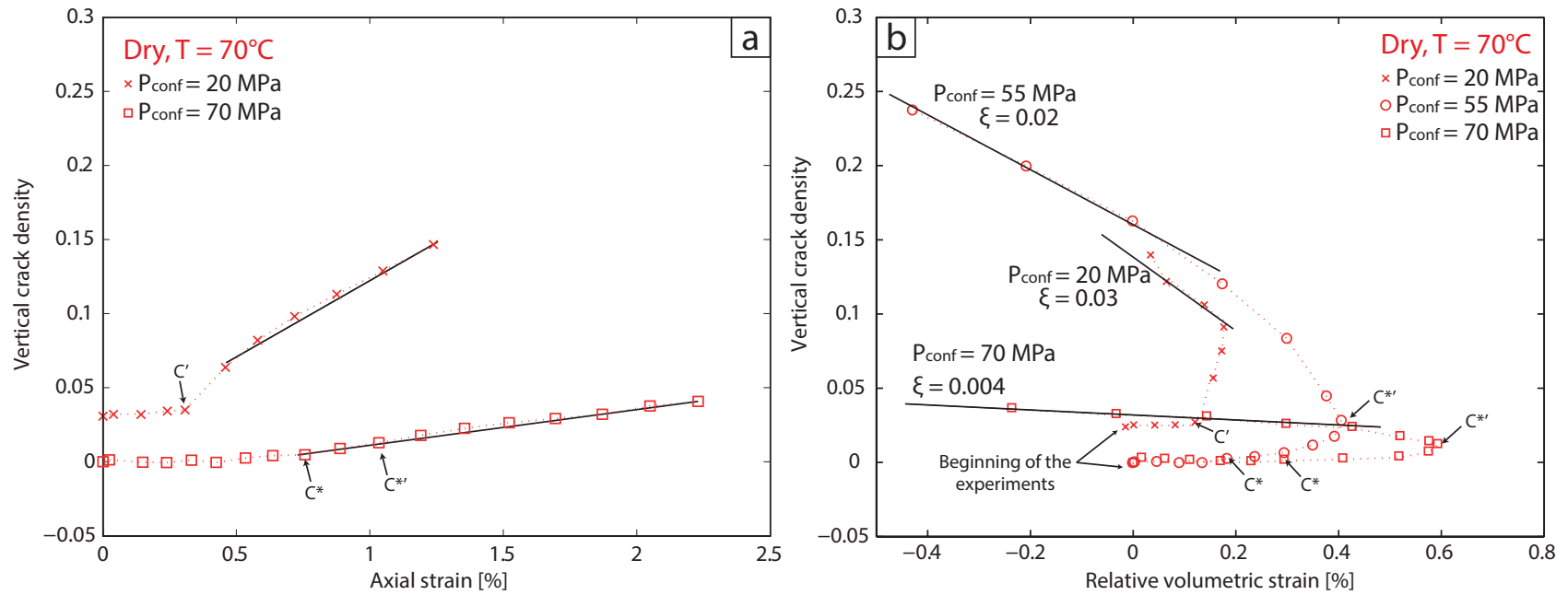


Figure 1.14 – (a) Evolution of axial crack density as a function of axial strain. The rate of increase is linear with respect to axial strain and increases with the increase of the confining pressure. (b) Cracks density is plotted as a function of volumetric strain. The slope of the linear fit corresponds to the mean crack aspect ratio $\langle \xi \rangle$ (equation 1.14).

Chapter 1. Brittle and semibrittle behaviours of a carbonate rock: Influence of water and temperature

At the post-yield onset of dilatancy (C^*), the competition between shear-enhanced compaction and dilatancy leads to a switch from overall compaction to overall dilatancy. Around C^* , the decrease of V_p and V_s compared to the volumetric change is maximum (Figure 1.10, experiment performed at $P_c = 85$ MPa). Volumetric strain close to peak stress can be due to crack propagation but also to shearing and rotation of fragments (Peng & Johnson, 1972, Guéguen & Boutéca, 2004, Vajdova et al., 2012). Thus, the decrease of elastic wave velocities is due to crack nucleation and/or propagation but may also be affected by the porosity induced by rotation of fragments.

Water saturation and a temperature increase of $\Delta T = 50^\circ\text{C}$ have no measurable effect on the post-yield onset of dilatancy (C^*). Water saturation might promote the development of cracks beyond the onset of inelastic compaction (C^*) but not sufficiently to observe a change in the macroscopic behaviour and on the post-yield onset of dilatancy (C^*). As no temperature effect is observed on C^* (Figure 1.5), it may be again that a temperature increase of $\Delta T = 50^\circ\text{C}$ is not sufficient to get a measurable effect on C^* .

The inelastic compaction observed in this study is qualitatively similar to that of Solnhofen limestone (Baud et al., 2000a) and of Tavel and Indiana limestones (Vajdova et al., 2004, 2010). A comparison of the yield envelope obtained by Vajdova et al. (2004) for a 10.5 % porosity Tavel limestone with those reported in this paper for a porosity of 14.7 % (Figure 1.15) underlines that porosity plays a major role in lowering the confining pressure at which the brittle-ductile transition occurs, in agreement with the work of Wong et al. (1997).

1.4.6 Crack geometry

Inverted crack densities offer a quantitative description of the damage due to cracks (Nasseri et al., 2007, Mallet et al., 2013, 2014). More precisely, Mallet et al. (2013, 2014) showed that crack densities inverted from ultrasonic velocities in a cracked glass were in very good agreement with optically measured ones. Thus, it is interesting to consider crack densities inverted from elastic wave velocities in addition to mechanical data. Here the concept of crack density and mean aspect ratio is understood as a statistical generalization of the concept of porosity for non-spherical inclusions. For example, a porous space between two grains is considered as a crack (Guéguen & Kachanov, 2011, Ghabezloo, 2015). Note that volumetric strain due to

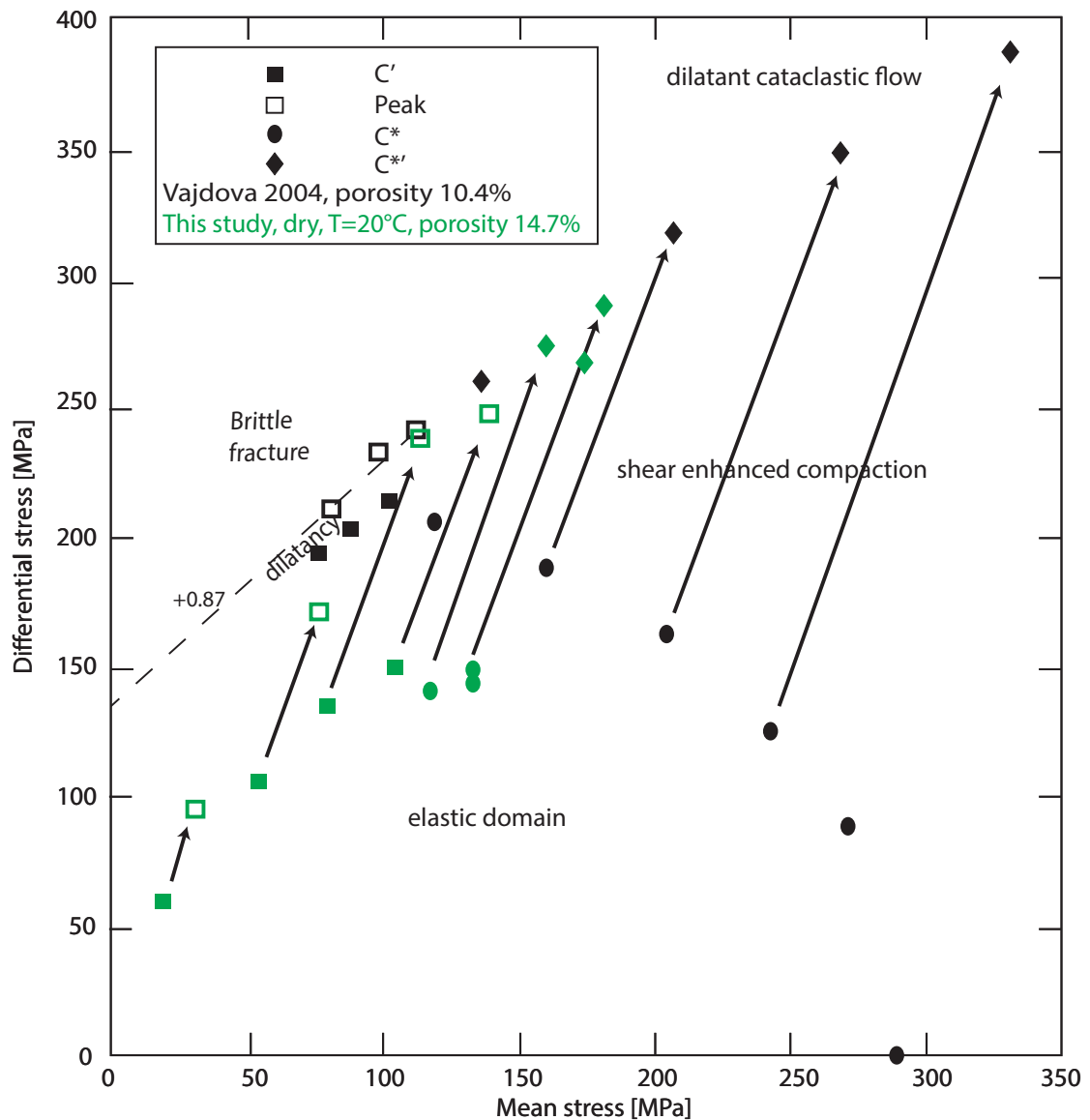


Figure 1.15 – The failure envelope (dry conditions at 20°C) from this study is compared with the one obtained by Vajdova et al. (2004).

shearing and rotation of fragments and porosity that they induce is taken into account in the crack porosity through the mean aspect ratio parameter derived hereafter.

Beyond the onset of dilatancy (C') and the post-yield onset of dilatancy (C^{*}), elastic wave velocities revealed important variations (Figures 1.8 and 1.9), which may be interpreted as variations in crack densities. Beyond these stress states, crack density increases almost linearly with axial strain (Figure 1.14 a). The linearity observed in this study is consistent with previous observations made by Brantut et al. (2011) on gypsum deformed across the brittle-ductile

Chapter 1. Brittle and semibrittle behaviours of a carbonate rock: Influence of water and temperature

transition.

Focusing on volumetric strain, in a first approximation, inelastic volumetric strain, ε^{in} , can be decomposed as:

$$\varepsilon^{in} \approx \Delta\phi = \Delta\phi^{cracks} + \Delta\phi^{pore}, \quad (1.12)$$

where $\Delta\phi$ is the porosity variation, $\Delta\phi^{cracks}$ is the porosity variation due to cracks and $\Delta\phi^{pore}$ is the porosity variation due to pore collapse. Note that during crack propagation and pore collapse, $\Delta\phi^{cracks}$ and $\Delta\phi^{pore}$ are of opposite sign. In the brittle regime, dilatancy is occurring beyond C' and thus $|\Delta\phi^{cracks}| > |\Delta\phi^{pore}|$. In the semibrittle regime, $|\Delta\phi^{cracks}| < |\Delta\phi^{pore}|$ between the onset of inelastic compaction (C^*) and the post-yield onset of dilatancy (C^*) and beyond C^* , $|\Delta\phi^{cracks}| > |\Delta\phi^{pore}|$. Therefore, beyond the onset of dilatancy (C') in the brittle regime and beyond the post-yield onset of dilatancy (C^*) in the semibrittle regime, one gets:

$$\min(\Delta\phi^{cracks}) = \varepsilon^{in}. \quad (1.13)$$

Combining equations 1.13 and 3.5, one gets:

$$\frac{\partial \varepsilon^{in}}{\partial \rho_c} = 2\pi \min\langle \xi \rangle. \quad (1.14)$$

Figure 1.14 b gives the relative volumetric strain (i.e. relative to the end of the hydrostatic loading) versus the inverted crack density for three experiments performed at 20 MPa, 55 MPa and 70 MPa, and $T = 70^\circ\text{C}$.

In the brittle regime, i.e. for $P_c = 20$ MPa, the initial axial crack density is 0.02 and remains constant until the onset of dilatancy (C') is reached. Then, crack density increases at almost constant relative volumetric strain. The lack of volume change may be explained by a balance between dilation associated with cracking and elastic compaction. Finally, a linear trend appears between the axial crack density and the relative volumetric strain. Using equation 1.14, the minimum average crack aspect ratio can be estimated to be $\xi = 0.03$.

In the semibrittle regime, i.e. for $P_c = 55$ and 70 MPa, the initial crack density is 0, as the confining pressure is higher than the pre-existing crack closure pressure. Crack density remains at 0 below the onset of inelastic compaction (C^*). Between C^* and the post-yield onset of dilatancy (C^*), crack density increases to 0.025 and 0.01 for experiments performed at $P_c = 55$ MPa and $P_c = 70$ MPa, respectively. During this stage, inelastic compaction is taking place as evidenced by volumetric strain evolution but as elastic wave velocities are not strongly

sensitive to spherical pores (Fortin et al., 2007), they cannot provide a useful information on variations of equant porosity. At some point beyond the post-yield onset of dilatancy (C^*), a linear trend between the axial crack density and the relative volumetric strain is observed, and the minimum average crack aspect ratio is found to be equal to $\xi = 0.02$ and $\xi = 0.004$ for the experiments performed under a confining pressure of 55 MPa and 70 MPa, respectively. Beyond the onset of dilatancy (C') in the brittle regime or the post-yield onset of dilatancy (C^*) in the semibrittle regime, the linear trend between the axial crack density and the relative volumetric strain suggests that crack propagate at constant average crack aspect ratio.

The linear relations between crack densities and volumetric strains (Figure 1.14 b) give decreasing minimum average crack aspect ratios of 0.03, 0.02 and 0.004 for confining pressures increasing from $P_c = 20$, 55 and to 70 MPa, respectively. Note that these values are all higher than aspect ratios calculated for pre-existing cracks (section 1.4.1). This discrepancy can be explained by the fact that i) the vertical cracks induced by the deformation have a geometry different from that of pre-existing cracks and ii) the inverted axial crack density during triaxial loading may take into account shearing and rotation of fragments .

Using linear elastic fracture mechanics for non-interacting opening mode fractures under two-dimensional, plane strain conditions in an homogeneous isotropic medium, Pollard & Segall (1987) found:

$$\xi = \Delta\sigma_I \frac{2(1-\nu^2)}{E}, \quad (1.15)$$

where $\Delta\sigma_I$ is the opening mode driving stress, ν is Poisson's ratio and E is Young's modulus. Using the previously presented model for crack growth from initial flaws (Ashby & Sammis, 1990), the opening driving stress is the wedging force on the pre-existing crack, which depends on the σ_1 and σ_3 . Thus, linear fracture mechanics for non-interacting opening mode fractures predicts a constant aspect ratio for cracks propagating at constant stress state. During constant strain rate experiments, the confining pressure is constant but the differential stress is not. However, for each experiment, constant aspect ratios are observed when the axial stress does not increase much (Figure 3.4 f). For example, focusing on the experiment performed at a confining pressure of 70 MPa, crack propagation at constant aspect ratio is observed when crack propagation is occurring at constant confining pressure and when axial stress variations remain lower than 10 MPa. However, this simple approach could be improved by a more

detailed model ([Renshaw & Park, 1997](#), [Olson, 2003](#)).

1.5 Concluding summary

In this study, we show the complexity of the mechanisms accommodating the deformation of a porous limestone at different confining pressures and explore the role of pore fluid and temperature. At low confining pressure, inelastic deformation is due to the development of cracks, which leads to the macroscopic failure of the sample. At high confining pressure, the onset of inelastic compaction is associated with shear-enhanced compaction. Then, beyond a stress state denoted C^* , the macroscopic volumetric strain switches to dilatancy that eventually leads to localized failure. The measurements of elastic wave velocities during the experiments clearly indicate the ongoing interplay of shear-enhanced compaction and development of cracks between the onset of inelastic compaction C^* and post-yield onset of dilatancy C^{*} . The post-yield onset of dilatancy (C^{*}) marks a change in relative dominance rather than in occurring mechanisms.

The comparison of our data to that reported in [Vajdova et al. \(2004\)](#) on the same rock but with a smaller average porosity of 10.5% (Figure 1.15) indicates that porosity plays a major role in reducing the confining pressure at which the brittle ductile transition occurs, in agreement with the work of [Wong et al. \(1997\)](#).

We inverted elastic wave velocities to axial crack density. Above the onset of dilatancy C' (brittle regime) or post-yield onset of dilatancy C^{*} (semibrittle regime), the linear trend between the axial crack density and the relative volumetric strain suggest that cracks propagate at constant average crack aspect ratio. The calculated average crack aspect ratio decreases as the confining pressure increases.

Water has a weakening effect on the onset of dilatancy in the brittle regime but no effect could be identify on the peak strength, on stress state at the onset of inelastic compaction (C^*), nor on the stress state at the post-yield onset of dilatancy (C^{*}). An increase in temperature of $\Delta T = 50^\circ\text{C}$ has no effect on the onset of dilatancy in the brittle regime (C') nor on the peak strength at low confining pressures leading to brittle behaviour. While the increase of temperature lowers the confining pressure at which the brittle-ductile transition occurs, it does not lead to changes in the values of the stress states at the onset of inelastic compaction

(C^*) and post-yield onset of dilatancy (C^*).

Supplements

Crack density inversion

Axial crack densities were inverted from elastic wave velocity measurements. Here, we recall the inversion process for dry solids but water-saturated solids can be considered in a similar manner (Shafiro & Kachanov, 1997). First, the effective mechanical properties of the calcite aggregate composed of the solid matrix and embedded spherical pores were obtained by inverting the velocity data obtained at $P_c = 85$ MPa hydrostatic stress. The effective Young modulus E_0 and effective Poisson's ratio ν_0 are calculated as:

$$\nu_0 = \left(\frac{1}{2} \left(\frac{V_p}{V_s} \right)^2 - 1 \right) / \left(\left(\frac{V_p}{V_s} \right)^2 - 1 \right), \quad (1.16)$$

$$E_0 = 2\rho(1 + \nu_0)V_s^2, \quad (1.17)$$

where V_p , V_s and ρ are the P-wave velocity, S-wave velocity and the rock density, respectively.

Using $V_p = 4350$ m/s, $V_s = 2350$ m/s and $\rho = 2295$ kg/m³, we get $E_0 = 32.8$ GPa, and $\nu_0 = 0.29$.

For a transverse isotropic symmetry along axis 3, the crack density tensor α is:

$$\alpha = \begin{pmatrix} \alpha_{11} & 0 & 0 \\ 0 & \alpha_{11} & 0 \\ 0 & 0 & \alpha_{33} \end{pmatrix} \quad (1.18)$$

where α_{11} is the axial crack density and α_{33} is the radial crack density. In the case of the non interacting approximation, the relation between the stiffness tensor C and α is given by (Sayers & Kachanov, 1995):

$$\left\{ \begin{array}{l} C_{11} + C_{12} = (1/E_0 + \alpha_{33})/D \\ C_{11} - C_{12} = 1/((1 + \nu_0)/E_0 + \alpha_{11}) \\ C_{33} = ((1 + \nu_0)/E_0 + \alpha_{11})/D \\ C_{44} = 1/(2(1 + \nu_0)/E_0 + \alpha_{11} + \alpha_{33}) \\ C_{13} = (\nu_0/E_0)/D \\ C_{66} = 1/(2(1 + \nu_0)/E_0 + 2\alpha_{11}) \end{array} \right. \quad (1.19)$$

where

$$D = (1/E_0 + \alpha_{33})((1 - \nu_0)/E_0 + \alpha_{11}) - 2(\nu_0/E_0)^2. \quad (1.20)$$

1.5. Concluding summary

From the effective stiffness tensor, we calculate the wave phase velocity along the propagation angles ϕ corresponding to our sensors set-up (Mavko et al., 1998):

$$V_p(\phi) = \left[(C_{11} \sin^2(\phi) + C_{33} \cos^2(\phi) + C_{44} + \sqrt{M}) / (2\rho) \right]^{1/2}, \quad (1.21)$$

$$V_p(\phi) = \left[(C_{11} \sin^2(\phi) + C_{33} \cos^2(\phi) + C_{44} - \sqrt{M}) / (2\rho) \right]^{1/2}, \quad (1.22)$$

$$V_p(\phi) = \left[(C_{66} \sin^2(\phi) + C_{44} \cos^2(\phi)) / \rho \right]^{1/2}, \quad (1.23)$$

where

$$M = ((C_{11} - C_{44}) \sin^2(\phi) - (C_{33} - C_{44}) \cos^2(\phi))^2 + ((C_{13} + C_{44}) \sin(2\phi))^2. \quad (1.24)$$

We then use a least square procedure to compare predicted synthetic data and measured velocities. The inverted axial crack density corresponds to the value leading to the minimum distance between predicted and measured velocities.

Peak stress model

In the brittle regime, the evolution of the peak stress at failure with respect to the confining pressure is modeled by equation 5.2. This equation is obtained using Ashby & Sammis' [1990] two-dimensional (plane strain) model. Wings are assumed to grow from initial cracks, which induces a crack density $D = \pi(l + a \cos \psi)^2 N_A$, where l is the length of the wing and N_A is the number of sliding cracks of uniform orientation ψ per unit area initially present. Before wings nucleate their length is $l = 0$ and the initial damage is $D_0 = \pi(a \cos \psi)^2 N_A$. The remotely applied principal stresses evolve with damage in accordance with equation (17) of Ashby & Sammis (1990), written here with the convention of positive compression stresses:

$$\sigma_1 = \left(C_1 + \frac{C_4(\sqrt{D/D_0} - 1)}{1 + \sqrt{\pi D_0} \frac{\sqrt{D/D_0} - 1}{1 - \sqrt{D}}} \right) \sigma_3 + \left(\frac{\sqrt{\sqrt{D/D_0} - 1} + 0.1 / \cos \psi}{1 + \sqrt{\pi D_0} \frac{\sqrt{D/D_0} - 1}{1 - \sqrt{D}}} \right) \left(\frac{C_4}{\sqrt{\cos \psi}} \right) \frac{K_{IC}}{\sqrt{\pi a}}, \quad (1.25)$$

where

$$C_1 = \frac{\sqrt{1 + \mu^2} + \mu}{\sqrt{1 + \mu^2} - \mu}, \quad (1.26)$$

Chapter 1. Brittle and semibrittle behaviours of a carbonate rock: Influence of water and temperature

and

$$C_4 = \frac{\sqrt{30} \cos \psi}{\sqrt{1 + \mu^2} - \mu}. \tag{1.27}$$

Specifying the material parameters D_0 , $K_{IC}/(\pi a)^{1/2}$, and μ , the evolution of the principal stress σ_1 at a fixed confining pressure σ_3 can be calculated as a function of damage D using equation 1.25. At some point, the stress attains a peak beyond which instability sets in. The calculation can be repeated for different values of fixed confining pressure σ_3 , which allows to map out the peak stress at failure in the P-Q map (Figure 1.13).

Additional mechanical data

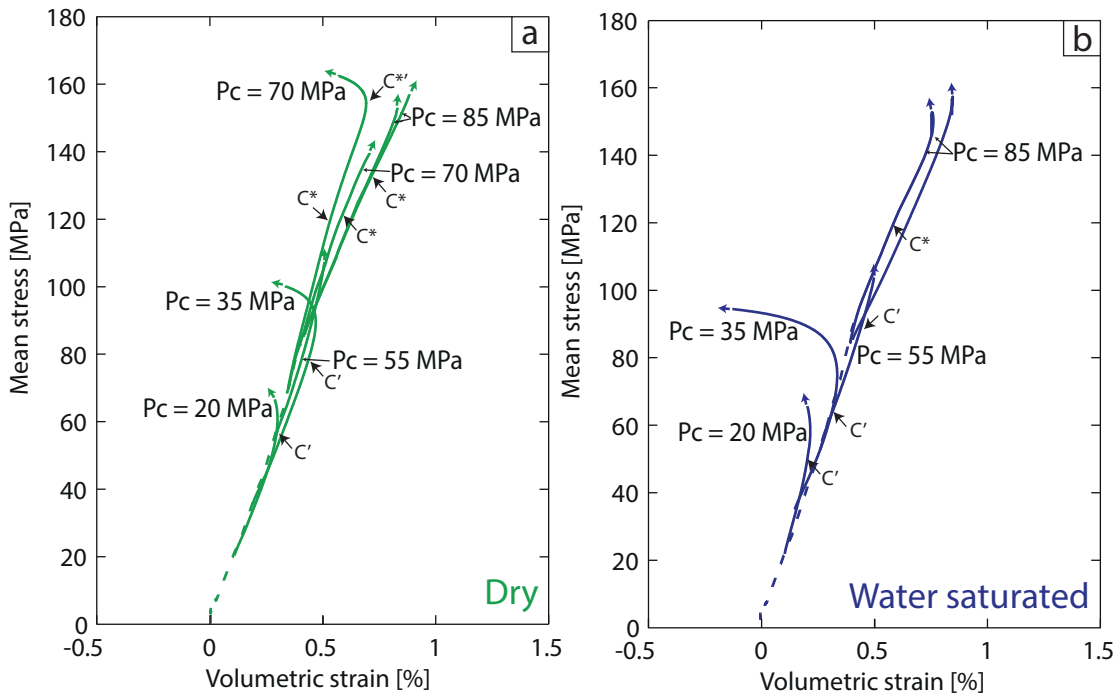


Figure S.1.1 – Compilation of mechanical data for uncomplete experiments (Table 1.2). The mean stress is plotted versus volumetric strain for (a) dry and (b) water-saturated experiments performed at 20°C. Stress states at the onset of dilatancy C' , onset of inelastic compaction C^* and post-yield onset of dilatancy $C^{*'}$ are shown for references on some experiments. Arrows mean that samples did not attain failure and could experience further deformation.

**MICROMECHANICAL CONSTITUTIVE MODEL
FOR CONSTANT STRAIN RATE DEFORMATION
OF LIMESTONES**

Ce chapitre a pour objectif de dériver un modèle constitutif permettant la prédiction de la déformation macroscopique lors d'une déformation à vitesse constante; en se basant sur les micro-mécanismes responsables de la déformation qui ont été identifiés dans le chapitre précédent. Le modèle s'articule donc selon (1) la dérivation des modules élastiques pour le milieu poreux fracturé, (2) le calcul de la déformation macroscopique due à la croissance des fractures (la dérivation des facteurs d'intensité de contrainte pour un réseau de fractures en interaction et la loi de croissance de ces fractures qui en découle sont explicitées en annexe), (3) la description de la plasticité cristalline à l'échelle microscopique, le calcul de la loi de plasticité macroscopique qui en résulte, et la prise en compte de l'espace poral dans la loi de plasticité, (4) un modèle de nucléation de nouvelles fractures due à la micro-plasticité et leur croissance, et enfin (5) le calcul de l'évolution de la contrainte macroscopique au cours de la déformation.

Abstract

Deformation and failure of rocks are important for a better understanding of many crustal geological phenomena such as faulting and compaction. In carbonate rocks among others, deformation can either occur with dilatancy or compaction, having implications for porosity changes, failure and petrophysical properties. Hence, a thorough understanding of all the micro-mechanisms responsible for deformation is of great interest. In this study, a constitutive model for the deformation of low-porosity carbonate rocks is derived from the micro-mechanisms identified in previous studies. The micro-mechanical model is based on

Chapter 2. Micromechanical constitutive model for constant strain rate deformation of limestones

(1) brittle crack propagation, (2) a plasticity law for porous media with hardening and (3) crack nucleation due to dislocation pile-ups. The model predicts stress-strain relations and the evolution of damage during deformation. The model adequately predicts a brittle behaviour at low confining pressures, which switches to a semibrittle behaviour characterized by inelastic compaction followed by dilatancy at higher confining pressures. Model predictions are compared to experimental results from previous studies and are found to be in close agreement with experimental results. This suggests that micro-physical phenomena responsible for the deformation are sufficiently well captured by the model. The porosity range of applicability and limits of the model are discussed.

2.1 Introduction

Carbonates represent more than 50% of reservoir rocks, have been proposed as reservoirs for the geological sequestration of carbon dioxide, are crossed by faults zones ([Armijo et al., 1992](#), [Willemse et al., 1997](#), [Mouslopoulou et al., 2014](#)) and constitute the basement under some volcanoes ([Heap et al., 2013](#)). Thus, understanding and predicting their mechanical behaviour is of great interest.

Experimental studies have already been conducted on limestones (e.g. [Heard, 1960](#), [Baud et al., 2000a](#), [Vincké et al., 1998](#), [Vajdova et al., 2004, 2010](#)), marbles (e.g. [Rutter, 1974a](#), [Fredrich et al., 1989](#), [Renner et al., 2002](#), [Schubnel et al., 2006b](#)), chalks (e.g. [Rhett & Farrell, 1991](#), [Risnes et al., 2005](#)). Focusing on limestones, these studies have shown that depending on the confining pressure, samples can have a brittle or a ductile behaviour, even at room temperature. The brittle-ductile transition depends on grain size and porosity ([Vajdova et al., 2004](#), [Wong & Baud, 2012](#)).

At low confining pressure, features are typical of the brittle regime: i) samples undergo an elastic compaction until a point denoted C' ([Wong et al., 1997](#)) beyond which dilatancy takes place; ii) the differential stress reaches a peak beyond which strain softening is occurring, which is typical of shear localization ([Brace, 1978](#)); iii) Observation of the samples after deformation in the post-peak regime indicates that the deformation was localized in a shear fault. Deformation at microscopic scale is accommodated by microcrack nucleation and/or propagation and eventually their coalescence.

At high confining pressure (higher than 70 MPa for Tavel limestone, as shown in chapter 1), samples exhibit (1) an elastic compaction and (2) an inelastic shear-enhanced compaction associated with strain hardening beyond a critical stress denoted C^* (Baud et al., 2000a). Yet, inelastic compaction is transient and volumetric strain reverses from inelastic compaction to dilatancy beyond a critical stress denoted $C^{*'} (Wong et al., 1997)$. These features (i) involving macroscopically distributed, dilatant deformation by both crystal plasticity and microcracking; (ii) leading to strains lying in the range 3-5% at failure and (iii) inducing a pressure-dependent strength; are typical of the semibrittle (ductile) regime as defined by Evans et al. (1990). The importance of this semibrittle regime has been well recognized (Kohlstedt et al., 1995). At the microscale, microplasticity (mechanical twinning and dislocation glide) is active even at room temperature (Turner et al., 1954, Griggs et al., 1960, De Bresser & Spiers, 1997). However, at room temperature, dislocations and twins can only slip in their plane, micro-defects accumulate and no recovery process takes place. Localized residual stresses due to pile-ups can be sufficient to nucleate new microcracks (Smith & Barnby, 1967, Evans et al., 1980, Wong, 1990). Temperature plays a role (Rutter, 1974a) but room temperature only is considered in this article.

Interplay of brittle and ductile micromechanisms leads to transitional behaviours such as cataclastic flow, characterized by homogeneously-distributed microcracking, grain rotations and plasticity (dislocation creep, twinning) (e.g. Fredrich et al., 1989). It can either lead to dilatancy as shown by Fredrich et al. (1989) on a very low porosity Carrara marble or to inelastic compaction as observed by Baud et al. (2000a), Vajdova et al. (2004, 2010) among others. Thus, volumetric strain is a key parameter to understand and predict failure in limestones.

This study focuses on the development of a constitutive model for the prediction of the mechanical behaviour of limestones undergoing constant strain rate deformation at room temperature and various confining pressures. This model is micro-mechanically motivated: assuming the micro-mechanisms discussed previously, the aim is to predict the stress-strain relation. The model prediction are then compared to data available in the literature.

2.2 Development of the constitutive model

Porous limestones are heterogeneous in terms of microstructure (e.g. grain type and size, porosity distribution, cementation), physical properties and mechanical behaviour (Regnet et al., 2015a), and key parameters are not easy to identify. Regnet et al. (2015b) showed that the mechanical behaviour of two limestones with similar physical properties depends on the microporosity distribution. For simplicity, in this model we assume that the microstructure is characterized by (1) a matrix composed of pure calcite, (2) a porosity made-up of equant pores and (3) cracks.

Predicting the mechanical behaviour of limestones implies to embody all the possible micro-mechanisms. Thus, the derivation of the micro-mechanically motivated constitutive model includes five key steps: (i) derive the effective elastic moduli for the cracked porous medium to get the elastic strains, (ii) calculate the macroscopic strains related to crack growth of an array of interacting cracks, (iii) calculate the macroscopic strains related to dislocations from crystal plasticity, (iv) account for crack nucleation and growth from dislocation pile-ups, and (v) finally calculate the macroscopic stress evolution during constant strain rate loading.

In this paper, compressive stresses and compactive strains are counted positive. The principal stresses will be denoted σ_1 and σ_3 , σ_1 being the highest principal stress. The mean stress σ_m and the von-Mises effective stress σ_e are $\sigma_m = \sigma_{kk}/3$ and $\sigma_e = \sqrt{(3/2)S_{ij}S_{ij}}$, respectively, S_{ij} being the deviatoric stress defined as $S_{ij} = \sigma_{ij} - \delta_{ij}\sigma_m$, where δ_{ij} is the Kronecker delta. Stress triaxiality x is defined as $x = \sigma_m/\sigma_e$ and differential stress ($\sigma_1 - \sigma_3$) is denoted Q .

2.2.1 Elastic moduli of the cracked and deformed solid

Cracks and porosity have an impact on elastic moduli of porous materials (Mackenzie, 1950, Walsh, 1965a,b). Elastic moduli increase when porosity is closed and decrease with crack density increase (Bristow, 1960, Budiansky & O'connell, 1976) because although microcracks represent an extremely small amount of porosity, they are very compliant. In the model, voids are made-up of spheroidal pores and penny-shaped cracks. Effective elastic moduli are expressed as a function of the overall porosity and the crack density ρ (Kachanov, 1993, Shafiro & Kachanov, 1997, Fortin et al., 2007). We use Budiansky & O'connell's definition of

crack density ρ_c :

$$\rho_c = \frac{1}{V} \sum_{i=1}^N c_i^3, \quad (2.1)$$

where c_i is the radius of the i th crack and N is the total number of cracks embedded in the representative elementary volume (REV) V . In the dry case, for an isotropic distribution of crack orientations, the shear modulus G and bulk modulus K of a medium containing spheroidal pores and cracks can be expressed as a function of the shear and bulk moduli of the crack- and porosity-free matrix, and its Poisson's coefficient (e.g. Fortin et al., 2007). When the model is used for rocks of known elastic moduli, neglecting porosity variation, these moduli vary as:

$$\begin{aligned} \frac{G_i}{G} &\approx 1 + \Delta\rho_c \frac{h}{1+\nu_i} \left(1 - \frac{\nu_i}{5}\right), \\ \frac{K_i}{K} &\approx 1 + \Delta\rho_c \frac{h}{1-2\nu_i} \left(1 - \frac{\nu_i}{2}\right). \end{aligned} \quad (2.2)$$

where G_i and K_i are the initial shear and bulk moduli, ν_i is the initial Poisson's coefficient and $\Delta\rho$ is the crack density variation during deformation. The factor h describes the penny-shaped geometry and is expressed as:

$$h = \frac{16(1-\nu_i^2)}{9(1-\nu_i/2)}. \quad (2.3)$$

Young modulus E and Poisson ratio ν of the cracked porous medium are calculated from G and K .

Note that the overall crack orientations distribution may be anisotropic. In that case, the above calculations have to be extended to the anisotropic appropriate symmetry (Schubnel & Guéguen, 2003). Moreover, in water-saturated cases, frequency dependence can be important and should be accounted for (Pimienta et al., 2015).

2.2.2 Macroscopic strains related to crack growth

Crack growth from a pre-existing isolated sharp inclined crack under compressive stresses can be described by wing crack models initially developed by Nemat-Nasser & Horii (1982), and later revisited by Ashby & Hallam (1986), Ashby & Sammis (1990), Bhat et al. (2011, 2012), Mallet et al. (2015), among others. In their article, Ashby & Sammis (1990) compared their theoretical predictions to experimental data on granite, aplite, dunite, eclogite, gabbro,

Chapter 2. Micromechanical constitutive model for constant strain rate deformation of limestones

sandstone, limestone, marble and salt and showed that the agreement was excellent.

We use Ashby & Sammis's approach to calculate the stress intensity factor K_I in a three-dimensional setting (Figure 2.1). Wing cracks are assumed to grow from pre-existing flaws and form an array of interacting cracks in an isotropic linear elastic surrounding medium subjected to compressive stresses (Figure 2.1 a). Isolated initial penny-shaped crack of radius a are inclined at an angle ψ with respect to the maximum principal stress (X_1 -axis), (Figure 2.1 b). Wings of length denoted l can grow from each end of the initial crack, parallel to the X_1 -axis. The faces of the initial crack, in contact, can slide with some friction characterized by a Coulomb friction coefficient μ . The crack can also open, as discussed later.

Subcritical crack growth is not considered here and cracks grow when the stress intensity at

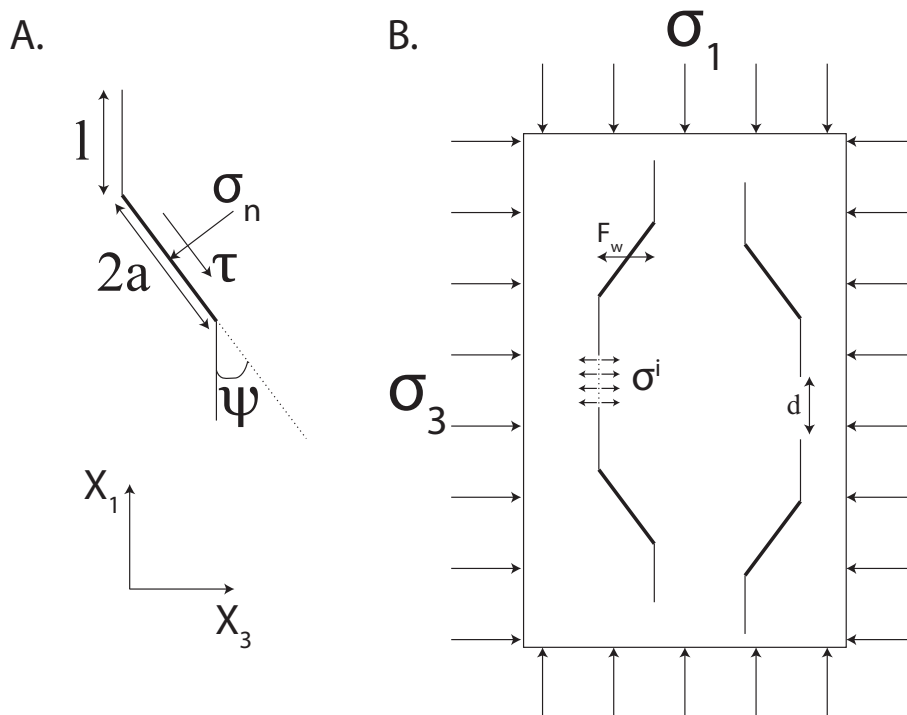


Figure 2.1 – A - An isolated wing-crack is subjected to remote stress. Wings develop from an initial flaw of radius a , parallel to σ_1 (direction X_1). B - Geometry of the crack network used for the stress-intensity factor, K_I , calculated at a crack tip.

their tips K_I exceeds the fracture toughness K_{IC} of the solid. Thus, the condition for crack growth is:

$$K_I \geq K_{IC}. \quad (2.4)$$

Then, cracks propagate until K_I falls to K_{IC} . Until the cracks start to interact strongly, K_I decreases as l increases: each increment of crack advance requires an increment of load and growth is stable.

The previous condition for crack propagation is valid when (i) frictional sliding is enabled by the stress conditions, and (ii) the flanks of the initial crack remain in contact. Three regimes need to be considered (Deshpande & Evans, 2008):

Regime I: Relative sliding on the flanks of the initial crack cannot take place because of friction, and K_I is set to 0, preventing cracks from growing.

Regime II: Relative sliding is possible and Ashby & Sammis's approach is used. Expression of the stress intensity K_I at the tip of interacting cracks forming an array can be found in Ashby & Sammis (1990).

Regime III: Contact between the flanks of the initial crack is lost. The situation reduces to the classical problem for a cracked elastic solid (Bristow, 1960, Budiansky & O'Connell, 1976, Tada et al., 2000). For an isotropic distribution of cracks, K_I is a quadratic function of the stresses σ_m and σ_e :

$$K_I = [\pi a(C^2 \sigma_m^2 + F^2 \sigma_e^2)]^{1/2}, \quad (2.5)$$

where C and F are given in Deshpande & Evans (2008) and depend on the initial damage D_0 and current damage $D = (4/3)N_v\pi(l + a \cos \psi)^3$, where N_v is the number of cracks per unit volume. Initial damage is calculated with $l = 0$. The damage parameter D is equivalent to the crack density as defined in equation 2.1, and $D = (4/3)\pi\rho_c$. The current damage parameter does not take into account cracks that are nucleated during the experiment. This assumption is discussed further.

Based on the strain energy density, K_I and elastic strains ε_{ij} continuities between regimes II and III, Deshpande & Evans (2008) found that the transition between regime II and regime III occurs at a stress triaxiality:

$$x_{II \rightarrow III} = \frac{AB}{C^2 - A^2}, \quad (2.6)$$

where A and B depend on the initial and current damage and are given in Deshpande & Evans (2008).

Strains at the macroscale ε_{ij} due to microcracks are calculated from the strain energy density

Chapter 2. Micromechanical constitutive model for constant strain rate deformation of limestones

W via the work conjugate relation (Deshpande & Evans, 2008):

$$\varepsilon_{ij} = \frac{\partial W}{\partial \sigma_{ij}}. \quad (2.7)$$

Regime I: As cracks are closed and their flanks cannot slide, they have no influence on the elastic response of the solid. The strain energy density is equal to that of the uncracked porous solid:

$$W = W_0 = \frac{1}{4G} \left[\frac{2}{3} \sigma_e^2 + \frac{3(1-2\nu)}{1+\nu} \sigma_m^2 \right], \quad (2.8)$$

where ν is the Poisson's ratio of the uncracked porous medium.

Regime II: Noting ΔW the strain energy per crack, the strain energy density becomes $W = W_0 + N_\nu \Delta W$. Total strain energy density is Deshpande & Evans (2008):

$$W = W_0 + \frac{\pi D_0}{4\alpha^3 G(1+\nu)} (A\sigma_m + B\sigma_e)^2. \quad (2.9)$$

Regime III: Penny-shaped initial cracks open. Total strain energy density is (Deshpande & Evans, 2008):

$$W = W_0 + \frac{\pi D_0}{4\alpha^3 G(1+\nu)} (C^2 \sigma_m^2 + F^2 \sigma_e^2). \quad (2.10)$$

2.2.3 Macroscopic strains related to dislocations

Mechanical twinning and r-, f- dislocation glides are accessible at room temperature and relatively low confining pressures in calcite (Turner et al., 1954, Griggs et al., 1960, De Bresser & Spiers, 1997). It leads to microscopic plastic flow without volumetric change at the scale of the grains (Paterson, 1978, Paterson & Wong, 2005). At room temperature, the micro-plasticity can account for the ductile behaviour (Fredrich et al., 1989, 1990, Evans et al., 1990, Miguel et al., 2001). For simplicity, we only consider dislocation glide here, even though twinning could be accounted for in a similar manner. The plastic strain-rate $\dot{\varepsilon}^P$ induced by dislocation slip (assuming all dislocations to be mobile) is (Orowan, 1954):

$$\dot{\varepsilon}^P = \dot{\varepsilon}^d = \rho_d b v, \quad (2.11)$$

where ρ_d is the dislocation density, b is their Burgers vector and v their average slip velocity. This approach is valid for stationary average microstructures with mobile dislocations. At room temperature in calcite, dislocations are blocked at obstacles such as grain boundaries and local defects, implying that (1) ρ_d is not constant and (2) dislocations are not all mobile.

2.2. Development of the constitutive model

Furthermore, (3) dislocation slip motions are confined on specific planes. To deal with these complexities, let us separate dislocations into mobile and immobile ones: $\rho_d = \rho_{md} + \rho_{id}$, where ρ_{md} and ρ_{id} are mobile and immobile dislocation densities, respectively. Mobile dislocations are responsible for the deformation whereas immobile ones are trapped and are assumed to contribute for a negligible strain. Thus, ρ_d is replaced by ρ_{md} in equation 5.3. Under the assumption that dislocation slip motions are isotropic because of the random grain orientation, the micro-plastic flow due to mobile dislocations is approximately:

$$\dot{\epsilon}^{md} = \rho_{md} b v, \quad (2.12)$$

Although interactions of dislocations can lead to complex patterns (e.g. Miguel et al., 2001), at low temperature, the mean dislocation velocity is assumed to follow a power law stress-dependence (Meyers et al., 1999):

$$v = V_0 \left(\frac{\sigma}{\sigma_0} \right)^m, \quad (2.13)$$

where V_0 is a temperature-dependent parameter, σ is applied stress, and σ_0 is the stress at which $v = V_0$. Combining equations 2.12 and 2.13, one gets:

$$\dot{\epsilon}^{md} = \rho_{md} b V_0 \left(\frac{\sigma}{\sigma_0} \right)^n = (\rho_d - \rho_{id}) b V_0 \left(\frac{\sigma}{\sigma_0} \right)^n. \quad (2.14)$$

The amplitude of any stress component induced by a dislocation at a distance r is $\sigma = Gb/(2\pi r)$, (Hirth & Lothe, 1982) and the total dislocation density is $\rho_d = 1/h^2$, where h is the mean spacing between dislocations. Thus, the average internal stress amplitude is:

$$\sigma = \frac{Gb}{2\pi} \rho_d^{1/2} = \frac{Gb}{2\pi} (\rho_{id} + \rho_{md})^{1/2}. \quad (2.15)$$

Using equation 2.12, ρ_{md} can be calculated from the micro-plastic strain rate. Let us separate immobile dislocations into initially present ones and newly nucleated ones: $\rho_{id} = \rho_{id}^{init} + \rho_{id}^{new}$. Mobile dislocations are assumed to be trapped when they cross another dislocation. The probability for a dislocation to be trapped can thus be assumed to be proportional to the mobile dislocation density and to their velocity. We define a characteristic time constant for dislocation movements as:

$$\tau_d = \frac{Lg}{v}, \quad (2.16)$$

Chapter 2. Micromechanical constitutive model for constant strain rate deformation of limestones

where L_g is the grain size. Using this characteristic time, the increase rate of immobile dislocations is approximated as:

$$\frac{d\rho_{id}}{dt} = \frac{\rho_{md}}{\tau_d} = \frac{\dot{\varepsilon}^{md}}{bL_g}. \quad (2.17)$$

Integrating equation 2.17 over time, one gets $\rho_{id}^{new} = \varepsilon^{md} / (bL_g)$, and finally:

$$\rho_{id} = \rho_{id}^{init} + \frac{\varepsilon^{md}}{bL_g}. \quad (2.18)$$

Combining equations 2.14, 2.15, and 2.18, one gets:

$$\dot{\varepsilon}^{md} = \left[\left(\frac{2\pi}{Gb} \right)^2 \sigma^2 - \left(\rho_{id}^{init} + \frac{\varepsilon^{md}}{bL_g} \right) \right] bV_0 \left(\frac{\sigma}{\sigma_0} \right)^n. \quad (2.19)$$

Defining the following constants:

$$A_p = \left(\frac{2\pi}{Gb} \right)^2; \quad B_p = \rho_{id}^{init}; \quad C_p = \frac{1}{bL_g}; \quad D_p = bV_0 \left(\frac{1}{\sigma_0} \right)^n, \quad (2.20)$$

we get the following polynomial expression for the plastic strain rate:

$$\dot{\varepsilon}^{md} = [A_p \sigma^2 - B_p - C_p \varepsilon^{md}] D_p \sigma^n, \quad (2.21)$$

in which hardening is introduced through $C_p \varepsilon^{md}$.

The above model accounts for dislocations-induced plastic flow and hardening. The assumptions made have led to introduce four constants (equations 2.20). However, only two out of the four are known (A_p and C_p). Previous authors have used an empirical stress-dependent power law (e.g. [Xiao & Evans, 2003](#)), different from 2.21:

$$\dot{\varepsilon}^p = \dot{\varepsilon}_0 (\sigma / \sigma_p)^n, \quad (2.22)$$

where $\dot{\varepsilon}_0$ and σ_p are reference values, and n is a material constant that will be discussed later. This empirical law is different from 2.21 but describes a similar hardening, as discussed below. A discussion of this macroscopic power-law description can be found in [Renner & Evans \(2002\)](#). The reference stress σ_p is assumed to account for the material hardening and following [Danas & Castaneda \(2012\)](#), the matrix phase is assumed to exhibit an isotropic strain hardening law described as:

$$\sigma_p = \sigma_p^i \left[1 + \frac{\varepsilon^p}{\varepsilon_0} \right]^M, \quad (2.23)$$

where σ_p^i and ε_0 denote the initial yield stress and yield strain of the matrix material, respectively. The strain hardening exponent is taken as: $M \leq 1$.

Hardening is produced by an increase of the internal stress, resulting from dislocation density

increase. Let us compare the hardening law (equation 2.23) with the evolution of internal stress. Local stresses due to pile-ups are not considered at this point. Using equations 2.12, 2.15, and 2.18 leads to the following internal stress evolution:

$$\sigma_i = \frac{Gb}{2\pi} \left[\rho_{id}^{init} + \frac{\dot{\varepsilon}^{md}}{bv} + \frac{\varepsilon^{md}}{bL_g} \right]^{1/2}. \quad (2.24)$$

Assuming a negligible ρ_{id} and $\dot{\varepsilon}^{md} = C^{st}$, we retrieve experimental results presented in [Taylor \(1934\)](#) for stress-strain relation in single crystals. Assuming a significant immobile dislocation density, equation 2.24 is similar to that derived in [Kassner \(2004\)](#) for a stationary regime (constant $\dot{\varepsilon}^{md}$). For polycrystals of calcite, [De Bresser \(1996\)](#) showed that experimental results are in agreement with this relation for mean stresses above 40 MPa, which is the case here.

From equation 2.24, defining $\sigma_i^i = [Gb(\rho_{id}^{init})^{1/2}]/(2\pi)$, $\dot{\varepsilon}_0^p = bv\rho_{id}^{init}$ and $\varepsilon_0^p = bL_g\rho_{id}^{init}$, one gets the macroscopic internal stress hardening law:

$$\sigma_i = \sigma_i^i \left[1 + \frac{\dot{\varepsilon}^p}{\dot{\varepsilon}_0^p} + \frac{\varepsilon^p}{\varepsilon_0^p} \right]^{1/2}. \quad (2.25)$$

Neglecting $\dot{\varepsilon}^p/\dot{\varepsilon}_0^p$, this expression becomes similar to the strain hardening power law (equation 2.23), with a strain hardening exponent $M = 1/2$. Note that this micro-derived internal stress law could be modified in order to take into account temperature effects.

Although both equations 2.21 and 2.22 exhibit the same trend, we use 2.22 in the following to keep equations similar to those of previous authors. The above plastic law is for a non-porous medium. Dislocation glide does not lead to volumetric strain. Porosity changes can account for it. [Rice & Tracey \(1969\)](#) first treated the ductile growth of voids as a problem of continuum plasticity by considering the asymmetric deformation of spherical voids embedded in an elastically rigid and incompressible plastic material. [Budiansky et al. \(1982\)](#) later accounted for non-linear viscosity. [Baud et al. \(2000a\)](#) modelled the inelastic compaction of a 3%-porosity limestone at room temperature using a plastic pore collapse model ([Curran & Carroll, 1979](#)). [Xiao & Evans \(2003\)](#) reproduced general trends of the deformation of a porous calcite-quartz aggregate at high temperature with a model of an isolated equivalent void in a incompressible non-linear viscous matrix. Following these works, we use a creep model ([Budiansky et al., 1982](#)) to analyse the inelastic compaction at a macroscale. The porous rock is modeled as a medium containing isolated equivalent voids. Each void is assumed to be spherical and its surface to be traction-free.

Chapter 2. Micromechanical constitutive model for constant strain rate deformation of limestones

As we focus on the mechanical behaviour of carbonate rocks under differential stress, plasticity is set to 0 for high triaxiality ($|x| > 1$), and thus inelastic compaction does not occur. For low triaxiality ($|x| < 1$), plasticity develops. Based on the numerical results of [Budiansky et al. \(1982\)](#), [Duva & Hutchinson \(1984\)](#) derived an approximate normalised dilation rate:

$$\frac{\dot{V}}{\dot{\epsilon}V} = k(n)[x - x^*(n)], \quad (2.26)$$

where V is void volume, \dot{V} the rate of change of volume and $\dot{\epsilon}$ the remote volumetric strain rate. Values of k and x^* are listed in Table 2.1. [Duva & Hutchinson \(1984\)](#) derived an approximate constitutive relation for the creep rate at low triaxiality:

$$\epsilon_{ij}^{mp} = \frac{3}{2}\dot{\epsilon}_0 \left(\frac{\sigma_e}{\sigma_p}\right)^{n-1} \frac{S_{ij}}{\sigma_p} + p\dot{\epsilon}_0 \left(\frac{\sigma_e}{\sigma_p}\right)^n \left\{ \frac{3}{2}[(n+1)f^* + \frac{1}{2}k(n-1)x^2] \frac{S_{ij}}{\sigma_e} + \frac{1}{3}kx\delta_{ij} \right\}, \quad (2.27)$$

where p is the overall porosity. Values of f^* depend on the strain rate exponent n and are listed in Table 2.1. As the differential stress is increased, porosity is updated using the strain rate of the voids provided by equation 2.26. The new plastic creep strain rate is then calculated with equation 2.27.

n	f^*	x^*	k
1	0.833	0	2.25
1.5	0.965	-0.019	2.42
2	1.05	-0.031	2.55
3	1.16	-0.045	2.71
5	1.26	-0.058	2.88
10	1.35	-0.070	3.06
∞	1.46	-0.083	3.30

Table 2.1 – Values considered in the plasticity law for a porous medium that are taken from [Duva & Hutchinson \(1984\)](#).

In this study, pores are idealized as spheres. The initial shape and evolution of pores probably has a substantial effect upon the behaviour of the porous solid. However, a model accounting for other pore shapes is beyond this work.

The general formulation of equation 2.27 is equivalent to considering the matrix material as an incompressible, non-linearly viscous material ([Renner & Evans, 2002](#)). When $n = 1$, the material is linearly viscous whereas when $n \rightarrow \infty$, it is rigid-perfectly plastic. The real situation is likely to be between these two end-members.

2.2.4 Crack nucleation from pile-ups

At room temperature, in calcite, dislocation and twin slips are blocked at grain boundaries and defects, resulting in pile-ups. These pile-ups creates local stress concentrations that can be sufficient to nucleate new cracks (e.g. Stroh, 1954, 1957, Smith & Barnby, 1967, Wong, 1990). Thus, at room temperature, microplastic deformation can induce cracking and the two micromechanisms reported in sections 2.2.2 and 2.2.3 are coupled.

Considering a dislocation pile-up of length L (Figure 2.2), Wong (1990) found the following condition for crack nucleation:

$$K_{IC} = \frac{4\sqrt{2}}{\sqrt{3\pi}} \tau^* \sqrt{L}, \quad (2.28)$$

where the driving shear stress is $\tau^* = \tau_a - \tau_f$, where τ_a and τ_f are the resolved shear stress and lattice friction stress, respectively. Following Eshelby et al. (1951), the number of dislocations N_{di} contained in a pile-up is:

$$N_{di} = \frac{\pi(1-\nu)L\tau^*}{bG}. \quad (2.29)$$

Considering pile-ups of length $L = L_g/2$ and using equations 2.28 and 2.29, the critical number of dislocations in the pile-up N_{di}^{crit} to nucleate a crack is:

$$N_{di}^{crit} = \frac{\pi\sqrt{3\pi L_g}}{8Gb} (1-\nu) K_{IC}. \quad (2.30)$$

New crack nucleation will occur when the number of dislocation per pile-up N_{di}^{pu} reaches N_{di}^{crit} . Immobile dislocation (i.e. dislocations trapped in pile-ups) density is linked to the plastic strain undergone by the medium (equation 2.18). Dislocation densities represent average values whereas crack nucleation is controlled by high local concentration of dislocations in pile-ups (equation 2.30). It is possible to find relations between these two parameters. A simplified model assumes that the overall immobile dislocation density is approximately given by the largest pile-ups. The number of immobile dislocations intersecting a surface S is:

$$N_{di} = \rho_{id} S. \quad (2.31)$$

If Λ_{pu} is the number of significant pile-ups over the area S , then the average number of dislocations per pile-up is:

$$N_{di}^{pu} = \frac{\rho_{id} S}{\Lambda_{pu}}. \quad (2.32)$$

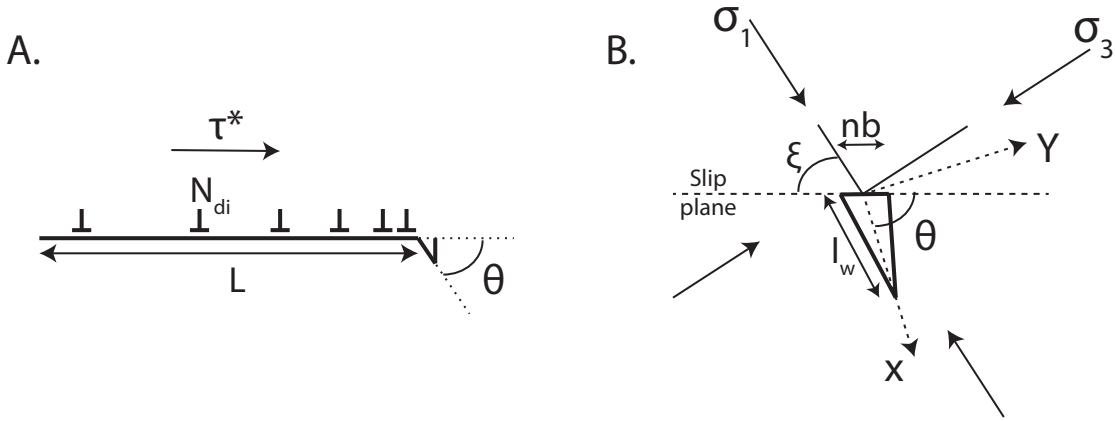


Figure 2.2 – A - A pile-up of N_{di} positive edge dislocations (Burgers vector magnitude b) nucleating a tensile microcrack on a plane at an angle θ . The length of the pile-up is L . The driving shear stress is τ^* . B - The wedge crack length is l , and the wedge opening at one end is nb due to the coalescence of n dislocations of Burgers vector b . The remotely applied two-dimensional stress field has principal components σ_1 and σ_3 with the maximum principal compressive stress at an angle ξ to the dislocation pile-up.

Defining L_{pu} as the average spacing between pile-ups, the number of pile-ups intersecting the surface S is:

$$\Lambda_{pu} = \frac{S}{L_{pu}^2}. \quad (2.33)$$

The density of pile-ups is then defined as $\rho_{pu} = 1/(L_{pu})^2$. This pile-up density is likely to be linked to the crystalline network of calcite, as discussed later. Combining equations 2.32 and 2.33, the number of dislocations per pile-up is:

$$N_{di}^{pu} = \frac{\rho_{id}}{\rho_{pu}}. \quad (2.34)$$

Using equation 2.30, the condition for nucleating new cracks becomes:

$$\rho_{id} = \rho_{pu} \frac{\pi \sqrt{3\pi L_g}}{8Gb} (1 - \nu) K_{IC}. \quad (2.35)$$

Following Wong (1990), the mode I stress intensity factor of the wedge crack nucleated by a dislocation pile-up can be calculated as:

$$K_I = \frac{G_0 N_{di}^{pu} b}{(1 - \nu)} \frac{\sin \theta}{\sqrt{2\pi l_w}} - \sigma_w \sqrt{\pi l_w / 2}, \quad (2.36)$$

where θ is the angle between the wedge crack and the pile-up plane (Figure 2.2 b), l_w is the length of the wedge crack and $\sigma_w = (\sigma_1 + \sigma_3)/2 - (1/2)(\sigma_1 - \sigma_3) \cos(2[\theta - \gamma_w])$ is the resolved normal stress acting on the wedge crack. In this last expression, γ_w is the angle between

the maximum principal stress and the pile-up plane (Figure 2.2 b). Then, the wedge crack propagation is described by equation 2.4.

The volumetric strain induced by wedge cracks is calculated with equation 2.7. The free energy change ΔW due to the wedge crack is (Wong, 1990):

$$\Delta W = \frac{\pi(1-\nu^2)}{4G}(\sigma_w^2 + \tau_w^2)l_w - 2\gamma_s, \quad (2.37)$$

where τ_w is the shear stresses acting on the wedge crack, and γ_s is the surface energy. Deriving this expression with respect to σ_{ij} , it leads to:

$$\varepsilon_{vol}^{wc} = \frac{\pi(1-\nu^2)l_w}{2G} [\sigma_1 \cos^2(\theta - \gamma_w) + 2\sigma_3 \sin^2(\theta - \gamma_w)]. \quad (2.38)$$

The current damage due to new cracks is $D_w = \rho_{pu}^{3/2} l_w^3$.

2.2.5 Stress strain relation during constant strain rate deformation

The overall stress-strain curve of the porous material submitted to a constant strain rate can finally be derived from the previous steps. Total strain is the sum of (i) the elastic, (ii) the crack-induced and (iii) the microplasticity-induced strains. During a short time dt , total strain $d\varepsilon$ is:

$$d\varepsilon = d\varepsilon^e + d\varepsilon^{cracks} + d\varepsilon^{mp}, \quad (2.39)$$

where $d\varepsilon^e$, $d\varepsilon^{cracks}$ and $d\varepsilon^{mp}$ are the elastic, crack and porous material microplastic strain increments, respectively. Total axial strain is $d\varepsilon_{ax} = \dot{\varepsilon}_{ax} dt$, where $\dot{\varepsilon}_{ax}$ is the imposed constant axial strain rate. The crack and creep axial strains are calculated with the work conjugate relation and equation 2.27, respectively. Then, the macroscopic axial stress increment $d\sigma_1$ is:

$$d\sigma_1 = E d\varepsilon_1^e, \quad (2.40)$$

where E is the evolving Young modulus of the cracked porous medium and $d\varepsilon_1^e$ the axial strain increment. This incremental procedure is repeated to obtain the entire constitutive stress-strain relation.

2.3 Choice of material properties and sensitivity to these parameters

2.3.1 Parameters relevant to elastic properties and cracks

Calcite Young's modulus $E_0 = 84$ GPa and Poisson's ratio $\nu_0 = 0.28$ are taken from [Homand et al. \(2000\)](#). Any other set of independent elastic constants of calcite are calculated from these values. Elastic constants of porous cracked medium are calculated with equations 2.2, using the porosity and crack density of the material. If the material elastic moduli are known, equation 2.2 is used. Critical stress intensity factor is $K_{IC} = 0.0217$ MPa for dry calcite ([Olusunle et al., 2009](#)). Surface energy for dry calcite can be found in [Røyne et al. \(2011\)](#).

The porosity, crack density and crack mean size depend on the rock modelled. Crack density can be inferred from elastic wave velocity measurements (e.g. [Sayers & Kachanov, 1995](#), [Fortin et al., 2005](#)) or SEM images (e.g. [Fredrich et al., 1989](#), [Mallet et al., 2013](#)). Crack mean size can be inferred from SEM images (e.g. [Mallet et al., 2013](#)) or taken as equal to the grain size. The friction coefficient on pre-existent penny-shaped cracks can be inferred from a linear failure envelope, assuming that friction is equal on a macroscopic fault and microcracks.

The influence of porosity, initial crack length, initial crack density and friction coefficient is explored hereafter (Figure 4.1). The value of each parameter is varied by 20% around an average value. Average values are taken equal to the set of parameters used in the comparison to white Tavel limestone and are given in Table 4.3. Porosity and initial penny-shaped crack radii have a small influence on the model prediction (Figure 4.1 a and b). Initial crack density has a strong influence on the peak stress (Figure 4.1 c). A variation of 20% around the average value induces variations of 15% in the predicted peak stress. Finally, the friction coefficient has the most important influence (Figure 4.1 d). Its variation has an influence on the onset of dilatancy C' (represented by arrows), on the peak stress and on the volumetric strain at the peak stress. As the friction coefficient increases, the onset of dilatancy C' , the peak stress and the volumetric strain at peak stress increase.

2.3. Choice of material properties and sensitivity to these parameters

	porosity %	ρ_c	a μm	μ	n	$\dot{\epsilon}_0$ s^{-1}	σ_p^{init} MPa	ρ_{pu} m^{-2}
Solnhofen limestone	3	0.035	1	0.53	3	3e-6	175	9e6
White Tavel limestone	15	0.035	5	0.6	3	1.6e-7	30	1.6e8

Table 2.2 – Microstructural parameters used to predict the macroscopic mechanical behaviour of Solnhofen limestone at a confining pressure of 200 MPa and macroscopic mechanical behaviour of white Tavel limestone.

2.3.2 Parameters relevant to plasticity and dislocations

The ductile behaviour of the matrix material is described by equations 2.22 and 2.25 and the ductile behaviour of the porous material is described by equation 2.27. A simplified form of equation 2.25 has been used. The second term of equation 2.25 has been neglected, which seems acceptable for low strain rates and is in good agreement with experimental results from (Kassner, 2004). All parameters of the plasticity and hardening laws are microstructure-dependent. Grain size can be obtained from SEM images, shear-modulus is an elastic constant provided by equation 2.2. Burgers vector in calcite is $a_0 = 6.4 \times 10^{-10}$ m (De Bresser, 1996).

For the non-porous matrix, the micro-parameters that need to be fixed *a priori* are the mobile and immobile dislocation densities (or equivalently $\dot{\epsilon}_0$ and σ_p^i) and the stress sensitivity n . In addition, for porous materials, porosity has to be known (equation 2.27). The sensitivity of the model to each parameter is explored thereafter. The value of each parameter is varied independently. Stress sensitivity n has a strong influence on the inelastic compaction (Figure 4.2 a). When n is increased, inelastic compaction for a given stress level is enhanced. The data from Renner et al. (2002) agree with a power law relation with a stress sensitivity $n = 4.5$. However, their study focuses on high temperature deformation. At low temperature, n is likely to be lower because the plastic creep rate increases with temperature (e.g. Wang et al., 1996). A constant value of $n = 3$ is used in this study even though creep tests indicate that the stress exponent is actually not constant (Renner et al., 2002). When the reference strain rate $\dot{\epsilon}_0$ is increased by 20%, volumetric strain rate increases (Figure 4.2 b). The initial yield stress σ_p^i has the exact opposite influence: when it is increased, volumetric strain tends to decrease (Figure 4.2 c). The strain hardening exponent M has been fixed at $M = 0.5$. However, given

Chapter 2. Micromechanical constitutive model for constant strain rate deformation of limestones

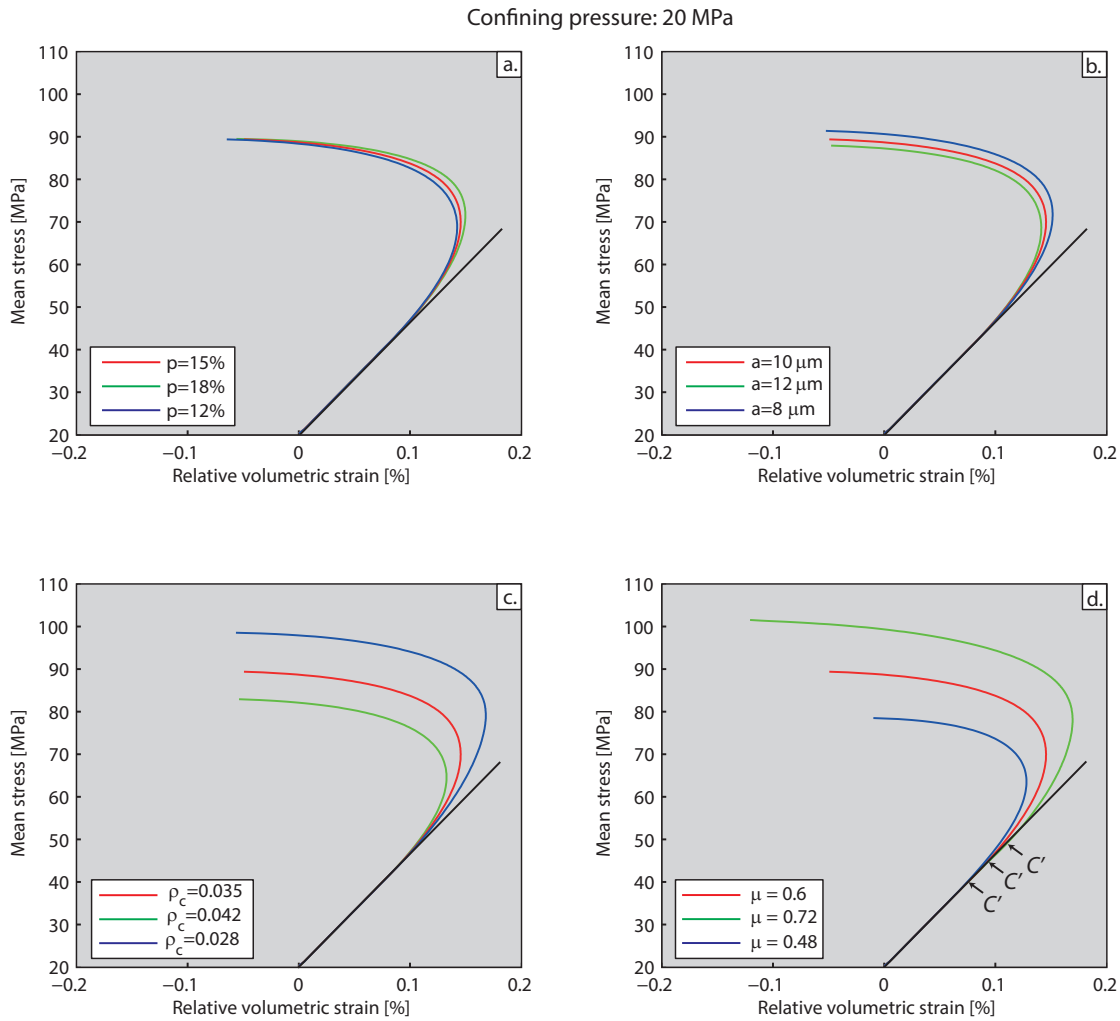


Figure 2.3 – Influence of the input parameters characterizing the brittle behaviour. The model is run for a confining pressure of 20 MPa. Each parameter is changed by 20% around an average value. (a) Influence of a 20% variation of porosity around the average value. (b) Influence of a 20% variation of initial penny-shaped crack radii around the average value. (c) Influence of a 20% variation of the initial crack density around the average value. (d) Influence of a 20% variation of the friction coefficient on the initial penny-shaped cracks around the average value. Arrows represent the onset of dilatancy C' for each value of friction coefficient.

its importance, the sensitivity to this parameter is also examined (Figure 4.2 d). When M is increased, volumetric strain tends to decrease (Figure 4.2 d). Finally, inelastic compaction rate increases with initial porosity (Figure 2.5 a). Porosity also has an influence on the post-yield onset of dilatancy (C^*), due to new crack nucleation (Figure 2.5 b). When porosity is increased, the onset of dilatancy takes place at a higher volumetric strain but a lower differential stress. Allowing pre-existent crack to propagate does not change these conclusions (Figure 2.5 c), but

2.3. Choice of material properties and sensitivity to these parameters

increases the dilatancy attained at rupture (Figures 2.5 b and c).

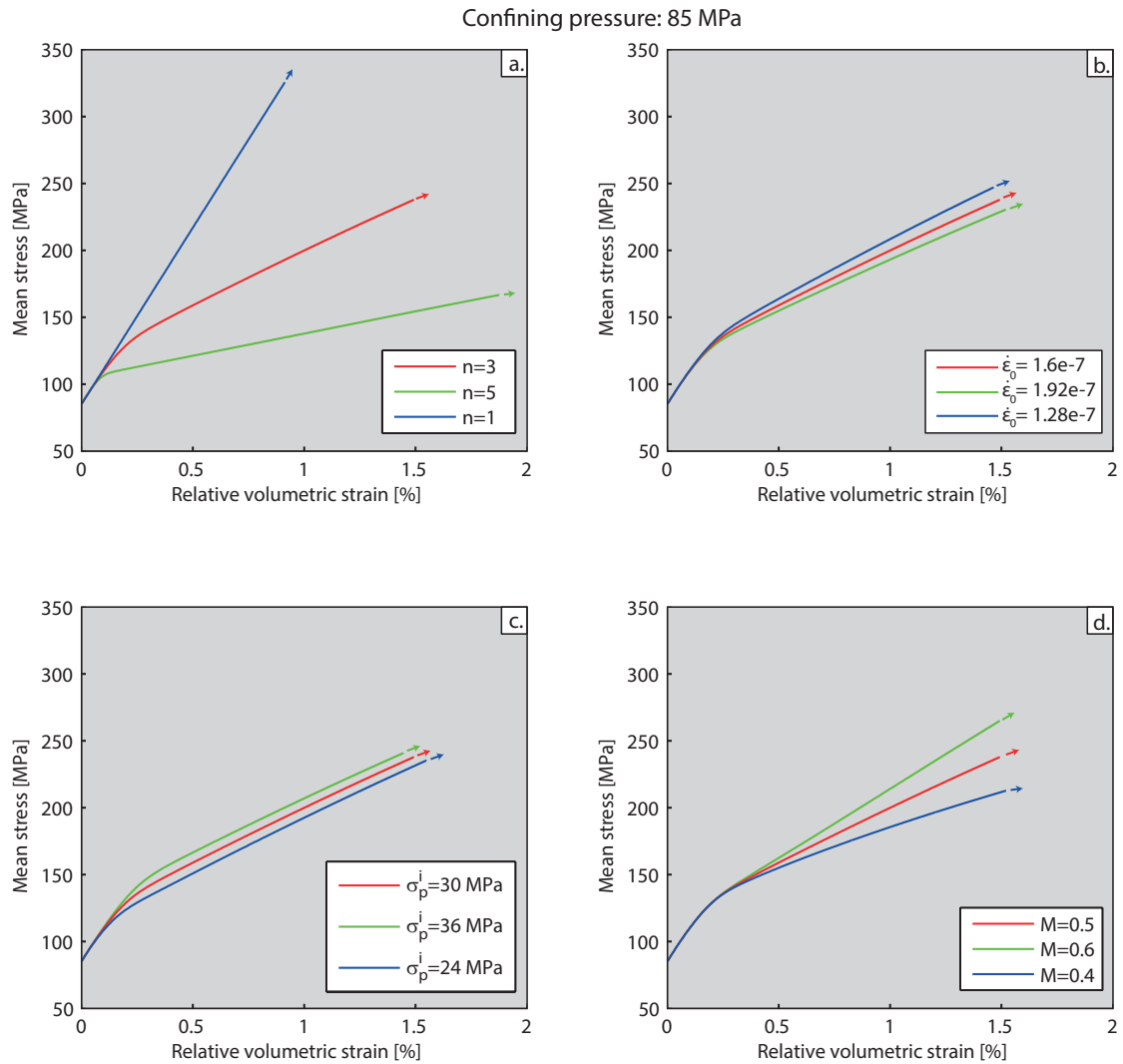


Figure 2.4 – Influence of the input parameters characterizing the ductile behaviour. The model is run for a confining pressure of 85 MPa. (a) Influence of a variation of the stress sensitivity n . (b) Influence of a 20% variation of the reference strain rate around the average value. (c) Influence of a 20% variation of the initial yield stress σ_p^i around the average value. (d) Influence of a 20% variation of the strain hardening exponent around the average value.

2.4 Results and discussion

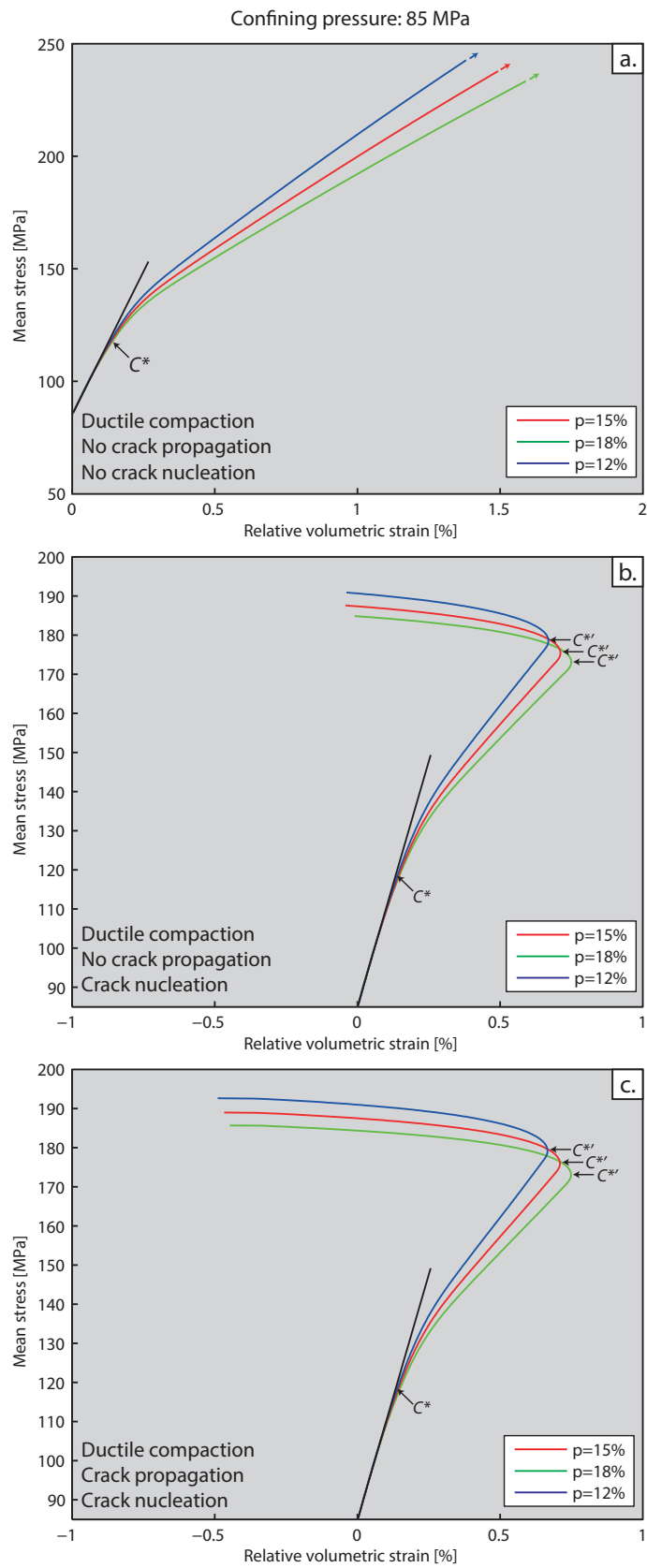
2.4.1 Prediction of the stress/strain response

We investigate the model predictions for $\dot{\epsilon}_{ax} = 10^{-5} \text{ s}^{-1}$ and for the parameters of Tavel limestone given in Table 4.3. At a confining pressure of 20 MPa, no significant plastic flow and no crack nucleation takes place (Figure 4.3). The volumetric strain versus mean stress curves first show an elastic compactant behaviour until a critical stress state denoted C' (Wong et al., 1997) beyond which the volumetric strain deviates from elasticity because of the onset of dilatancy (Figure 4.3). Elastic and wing crack deformations are responsible for the major part of the total deformation. Details on the brittle behaviours are given in Figure 2.7. At low differential stress, K_I/K_{IC} and wing length remain at 0 (regime 1). At a given threshold, slightly higher than $Q = 50 \text{ MPa}$, K_I/K_{IC} increases. When $K_I/K_{IC} = 1$, wing cracks start to grow. The crack density increases, which leads to a dilatant component of the volumetric strain. The onset of dilatancy is marked by the stress state C' . At this point elastic compaction and crack propagation inducing dilatancy are taking place simultaneously but compaction is dominant. Dilation becomes dominant at a differential stress of about 150 MPa, marked D' . When cracks start to interact, dilatancy increases faster with the differential stress. At macroscopic failure, K_I and wing crack lengths diverge, as marked by the red arrows. Macroscopic rupture is reached at a differential stress of approximately 205 MPa.

At a confining pressure of 85 MPa (Figure 4.5), inelastic compaction takes place. At low differential stress, elastic deformation is responsible for the overall deformation (Figure 4.5). At higher differential stress values, overall deformation undergoes shear-enhanced compaction (Baud et al., 2000a) due to the onset of plasticity before it becomes dilatant because new cracks nucleate. Let us first examine porosity collapse assuming that no crack nucleation is possible

Figure 2.5 (*following page*) – Influence of the porosity on the ductile behaviour. The model is run for a confining pressure of 85 MPa. The predicted onset on inelastic compaction (C^*) and post-yield onset of dilatancy (C'^*) are shown by arrows. (a) Influence of a 20% variation of the porosity on the inelastic compaction. Pre-existing cracks cannot propagate. No crack nucleation is possible. (b) Influence of a 20% variation of the porosity on the inelastic compaction and nucleation of new cracks. Pre-existing cracks cannot propagate but crack nucleation is possible. (c) Influence of a 20% variation of the porosity on the inelastic compaction. Pre-existing cracks can grow and new cracks can nucleate.

2.4. Results and discussion



Chapter 2. Micromechanical constitutive model for constant strain rate deformation of limestones

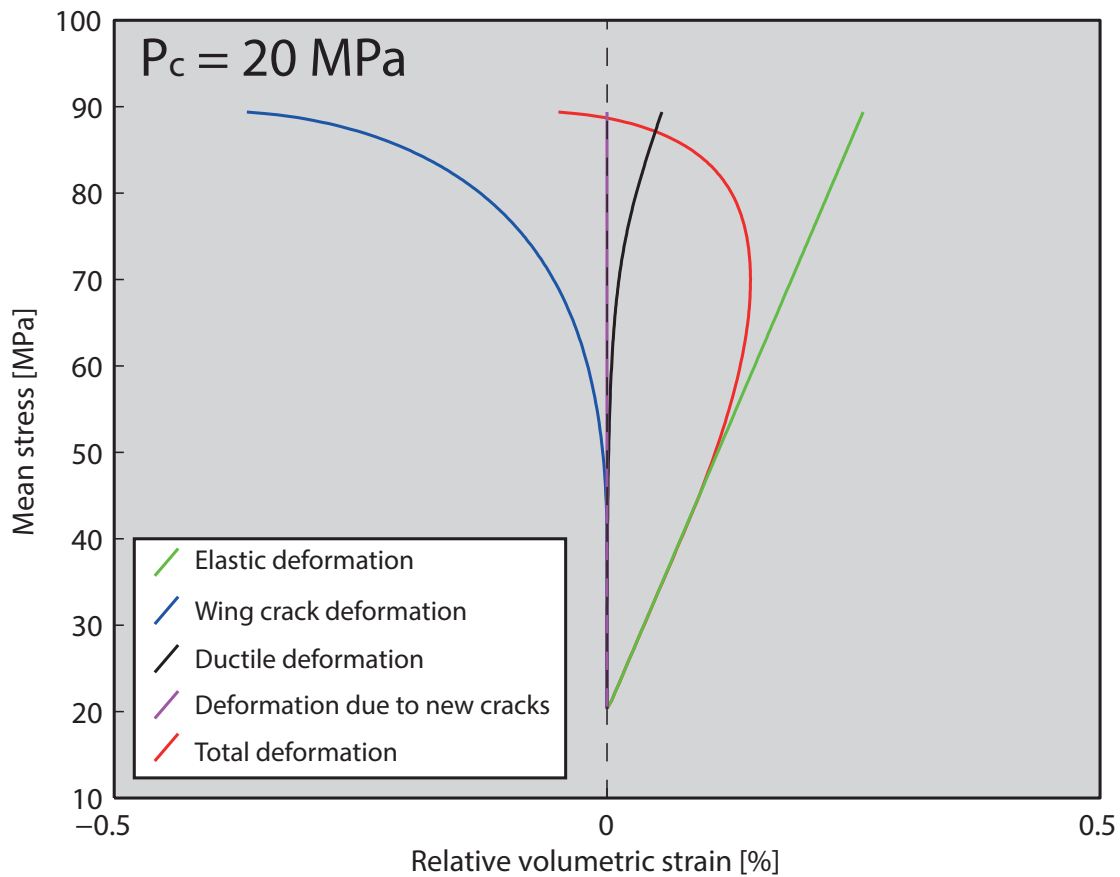


Figure 2.6 – Model predictions for volumetric strain due to all the physical phenomena taken into account for a confining pressure of 20 MPa.

(Figure 2.9). At a given differential stress threshold, ductile strain rates increase sharply. This stress state denotes the onset of inelastic compaction C^* in the macroscopic behaviour. At this point, the normalised dilation rate increases sharply, σ_p/σ_p^i start to increase because hardening is taking place and porosity starts to decrease because of pore collapse. Beyond C^* , axial and volumetric ductile strain rates decrease as σ_p/σ_p^i increases, because of hardening. Porosity decreases as a result of plastic pore collapse.

Let us now assume that new crack nucleation is possible (Figure 2.10). The dislocation density increase accelerates with σ_p/σ_p^i . At low σ_p/σ_p^i values, cracks cannot nucleate because the internal stress is not sufficient. When dislocation pile-ups induce an internal stress high enough, new cracks nucleate, grow and reach a length of over five microns. Induced crack density and volumetric strain increase. At rupture, nucleated dislocation density ρ_{id}^{new} is equal to $\rho_{id}^{new} = 5 \times 10^{12} \text{m}^{-2}$, nucleated crack length is almost 10 μm , crack density is almost 1 and

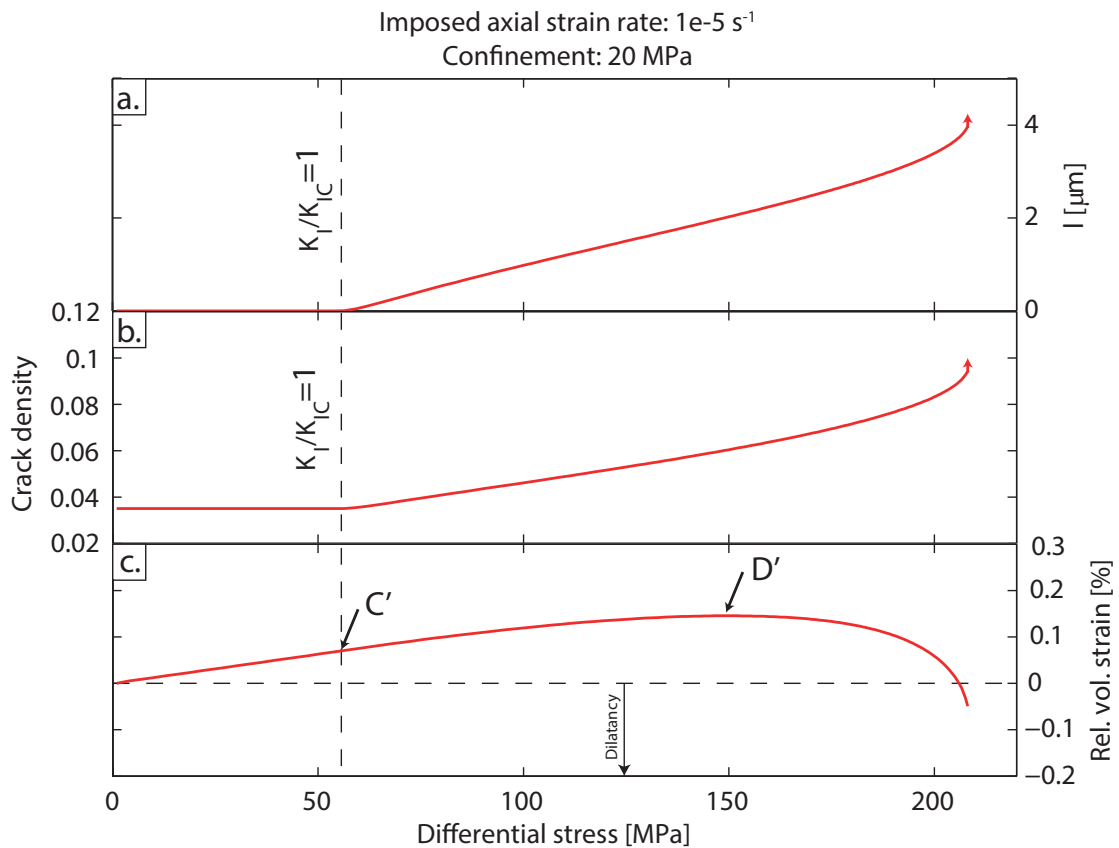


Figure 2.7 – Mechanical parameters evolution during deformation at a confining pressure of 20 MPa. (a) Wing crack length l as a function of Q . The red arrow indicates the divergence of l that happens at failure. (b) Crack density evolution as a function of Q . Initial crack density is 0.035. (c) Relative volumetric strain (i.e. volumetric strain is set to zero before the beginning of differential stress loading) as a function of Q . The onset of dilatancy C' and predominance of dilatancy D' are shown for reference.

dilatancy due to new cracks is almost 1%.

2.4.2 Comparison with available data

Mechanical data

Baud et al. (2000a) performed constant strain rate deformation experiments on Solnhofen limestone. Porosity is composed of microcracks (porosity 0.2%) and equant pores (porosity 2.8%). A detailed curve of the mechanical behaviour of Solnhofen limestone under differential stress is given for a confining pressure of 200 MPa. At this confining pressure, microcracks are closed (Baud et al., 2000a). Microstructural parameters (μ , D_0 among others) are given. In the

Chapter 2. Micromechanical constitutive model for constant strain rate deformation of limestones

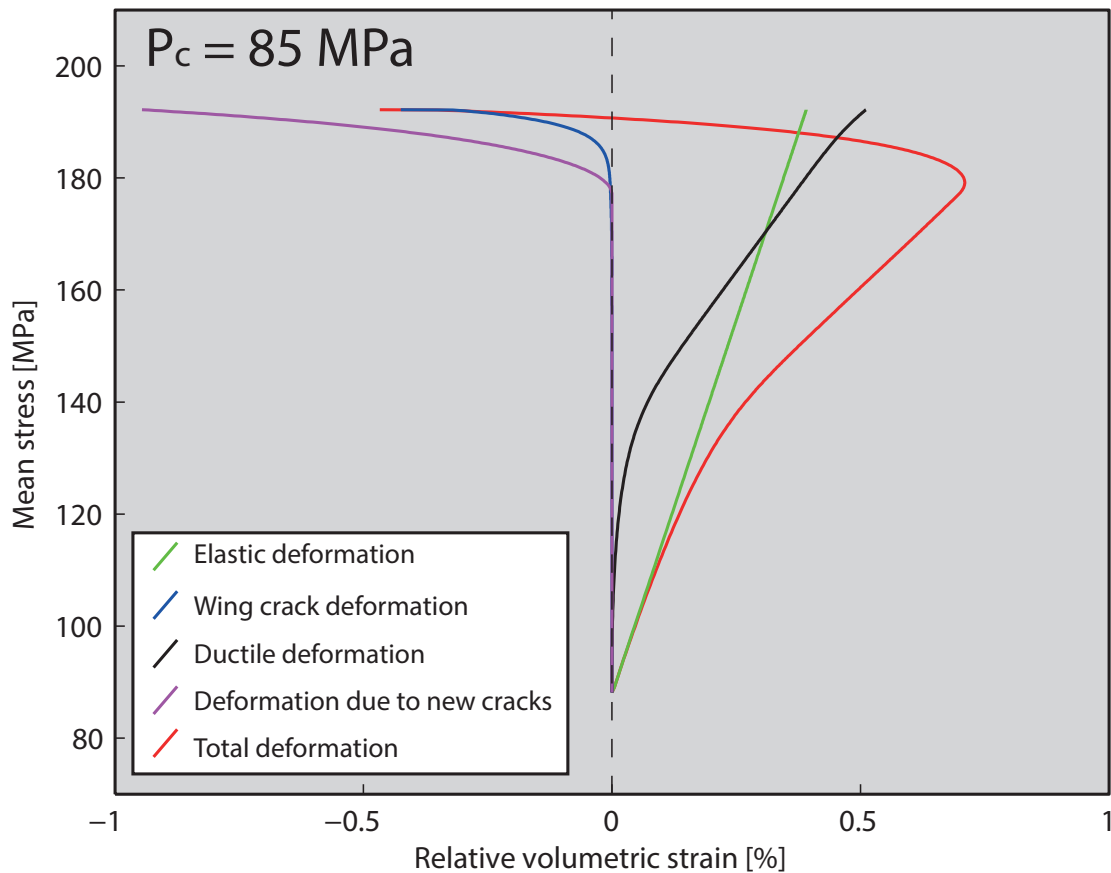


Figure 2.8 – Model predictions for volumetric strain due to all the physical phenomena taken into account for a confining pressure of 85 MPa.

model, initial damage is described by a crack density and a crack initial length. Crack density is fixed at $\rho_c = 0.035$ and initial crack length is $l_c = 1 \mu\text{m}$ (grain size). The model is run with a porosity of 3% made up of equant pores. The reference strain rate $\dot{\epsilon}_0$ and the initial yield stress σ_p^i are fitted to retrieve the macroscopic behaviour measured experimentally. Stress sensitivity n , and strain hardening exponent M are taken equal to 3 and 0.5, respectively. Elastic constants are experimentally measured elastic moduli. All parameters used can be found in Table 4.3.

The model closely reproduces the experimental stress-strain relation (Figure 2.11). Predicted stress states C^* and $C^{*'}$ and corresponding volumetric strains are very close to experimental ones. The onset of dilatancy is controlled by the pile-up density ρ_{pu} . Once fit on an experiment, all the parameters must be kept and model predictions need to be compared to experimental results for other confinements. Note that $\rho_{pu} = 9 \times 10^6 \text{m}^{-2}$ corresponds to about 1 pile-up

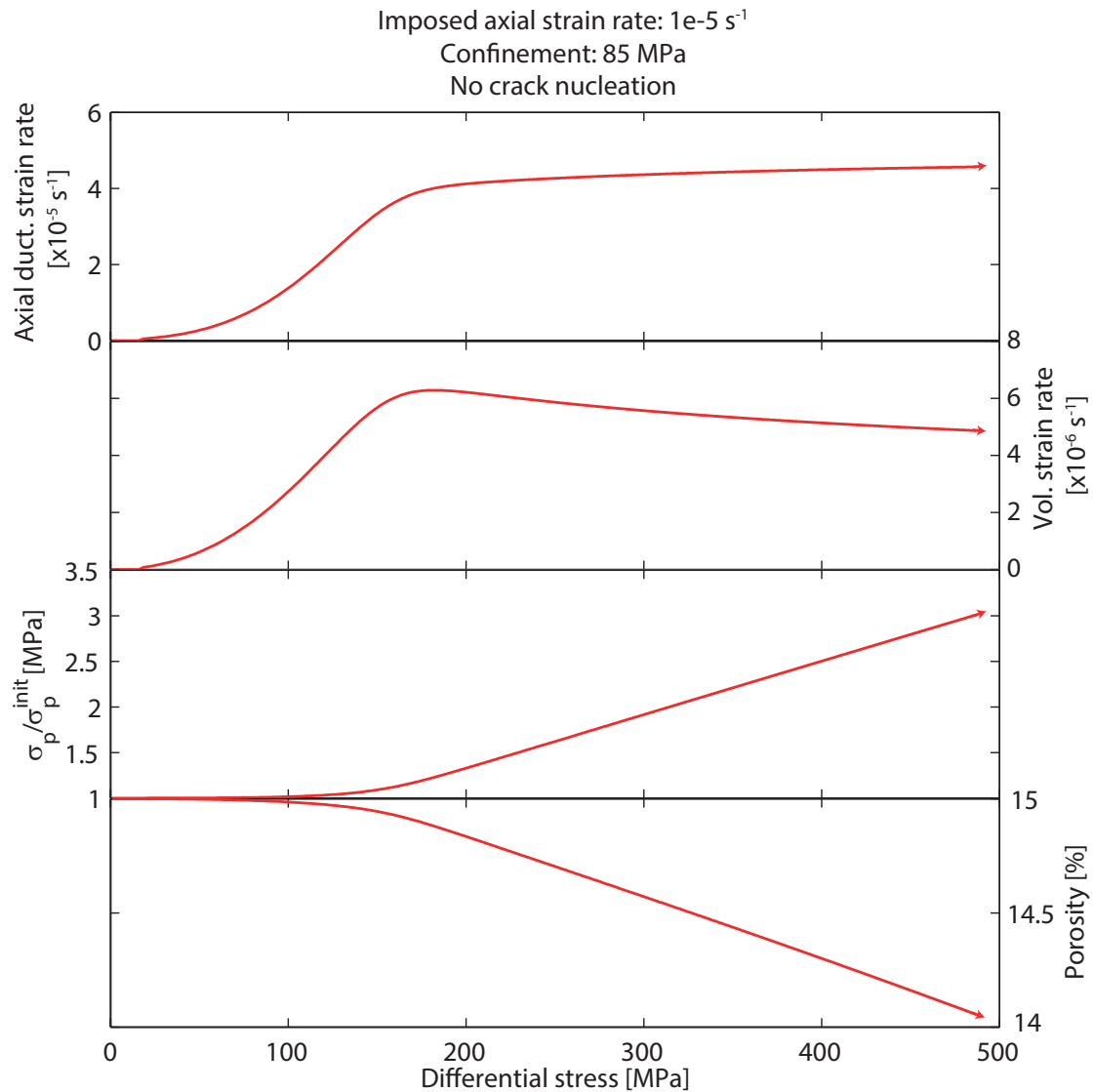


Figure 2.9 – Compilation of mechanical parameters linked to the ductile behaviour. (a) Evolution of the axial ductile strain rate as a function of the differential stress Q . (b) Evolution of the volumetric ductile strain rate as a function of the differential stress Q . (c) Reference stress in the plasticity law normalised by its initial value as a function of Q . (d) Porosity evolution as a function of Q .

over 60 grains of size $1 \mu\text{m}$; which is coherent.

In chapter 1, we showed constant strain rate deformation experiments performed on white Tavel limestone (porosity of 14.7%). At P_c lower than 55 MPa, the mechanical behaviour and failure mode are typical of the brittle faulting regime (Paterson & Wong, 2005). At P_c

Chapter 2. Micromechanical constitutive model for constant strain rate deformation of limestones

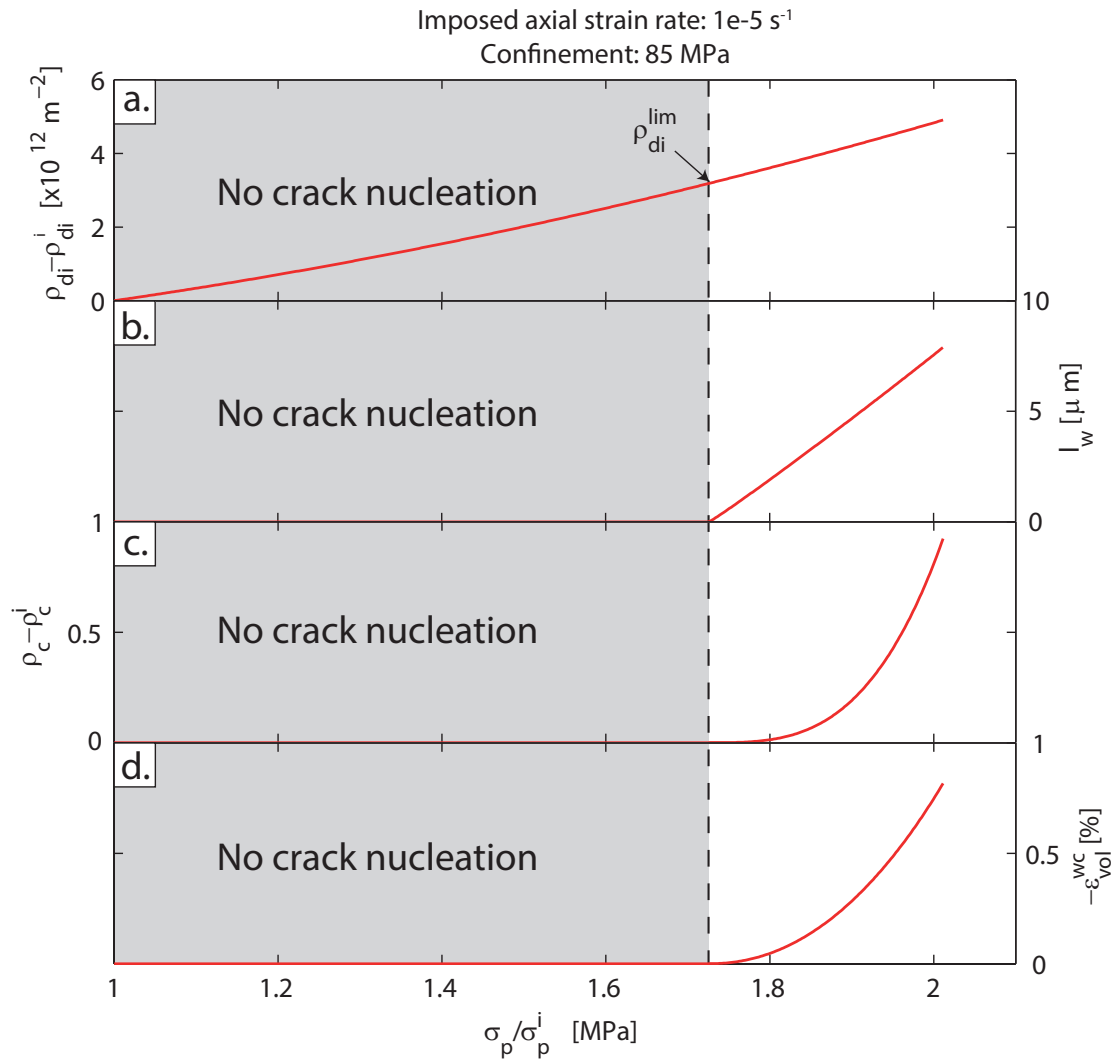


Figure 2.10 – Compilation of mechanical parameters linked to new crack nucleation. (a) Evolution of the strain-induced dislocation density as a function of the reference stress in the plasticity law normalised by its initial value σ_p / σ_p^i . The arrow denotes the onset of new crack nucleation. (b) Evolution of the nucleated crack length as a function of σ_p / σ_p^i . (c) Evolution of the nucleated crack density as a function of σ_p / σ_p^i . (d) Evolution of the volumetric strain due to nucleated cracks as a function of σ_p / σ_p^i .

equal or higher than 55 MPa, the mechanical behaviour is semibrittle and characterized by an elastic compaction beyond which an inelastic compactive regime takes place. At higher strain, dilatancy overcomes compaction. Mean stress versus volumetric strain is shown in Figure 2.12 a for various confining pressures.

Using parameter values reported in Table 4.3, predicted behaviour is reported in Figure 2.12 b. At confining pressures below or equal to 35 MPa, the predicted mechanical behaviour is

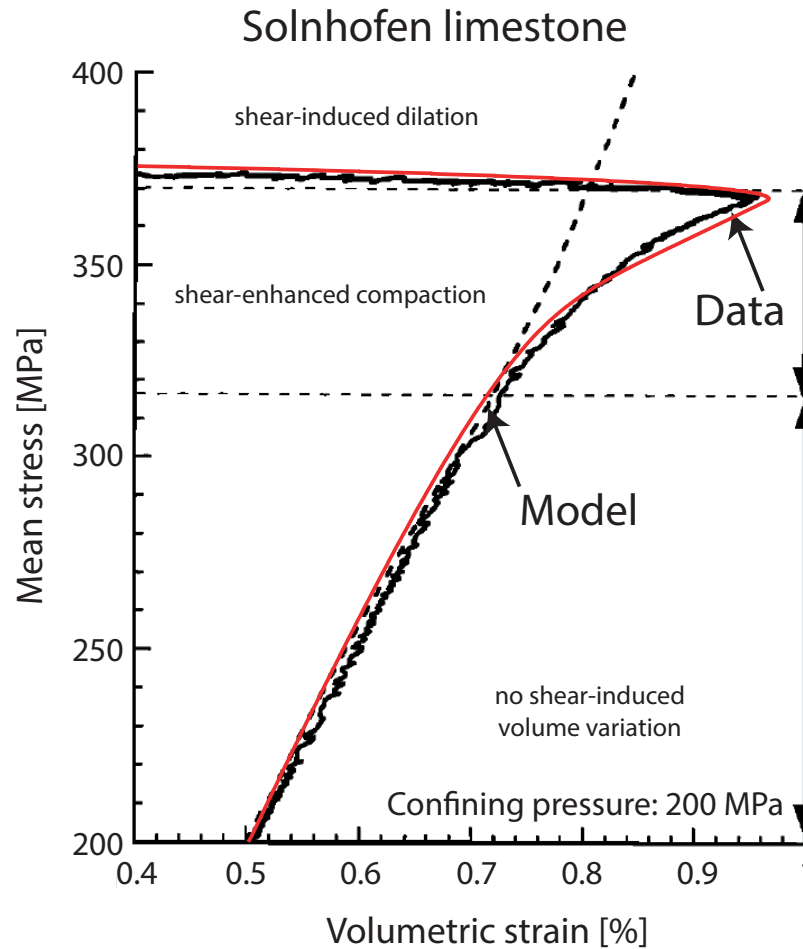


Figure 2.11 – Comparison of the mean stress versus volumetric strain curve predicted by the model developed in this paper with the result of an experiment performed by [Baud et al. \(2000a\)](#) on Solnhofen limestone at a confining pressure of 200 MPa. Parameters used are reported in Table 4.3.

brittle. At confining pressures strictly above 35 MPa, the predicted mechanical behaviour is characterized by elastic compaction, transient inelastic compaction, ultimately leading to dilatancy. The inferred brittle-ductile transition occurs at a confining pressure between 35 MPa and 55 MPa, close to the experimental results value.

Experimental and predicted stress-strain curves are very similar (Figure 2.12). Below the brittle-ductile transition, the model reproduces the general trend of the deformation. Stress states C' and peak stress are generally over estimated, which is probably due to a too small initial crack length. Dilatancy at rupture is overestimated by the model at $P_c = 35$ MPa. However, predicted stress states C^* and C^{*} and related volumetric strains are very close to experimental

Chapter 2. Micromechanical constitutive model for constant strain rate deformation of limestones

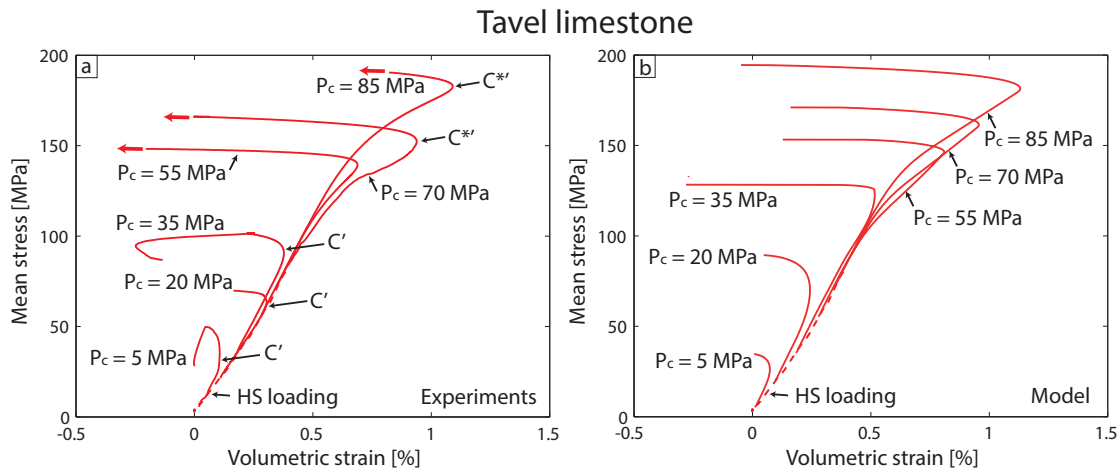


Figure 2.12 – (a) Mean stress as a function of volumetric strain for experiments conducted at confining pressures ranging from 0 to 85 MPa for dry Tavel limestone samples at $T = 70^\circ C$ (chapter 1). The dashed line corresponds to the behaviour under hydrostatic loading and is shown for reference. (b) Corresponding model prediction. The dashed line corresponds to the experimentally obtained behaviour under hydrostatic loading and is shown for reference.

ones. Onset of dilatancy is controlled by the parameter ρ_{pu} , which represents the pile-up density. Note however that the same value of ρ_{pu} is used for all model predictions whatever the confining pressure is. For these predictions, $\rho_{pu} = 1.6 \times 10^8 \text{m}^{-2}$. This corresponds to about 1 pile-up over 15 grains of size $5\mu\text{m}$.

Crack densities

In chapter 1, we inverted elastic wave velocity data to infer axial crack densities (Figure 2.13 a). Experimental results are compared to model predictions (Figure 2.13 b). Initial crack density in the model is 0.035. Experimental and predicted crack density evolution during constant strain rate experiments are reasonably similar (Figure 2.13). Below the brittle-ductile transition, the model reproduces the experimental crack density values during deformation. Model predictions of the volumetric strain at rupture are underestimated. However, predicted crack densities at a given volumetric strain are close to measured ones.

Above the brittle-ductile transition, the model also reproduces well-enough the experimental crack density evolution. Predicted crack densities at a given volumetric strain are very close to measured ones. Both experimental and predicted results show a slight increase between the onset on inelastic compaction (C^*) and the post-yield onset of dilatancy (C^*) and a dramatic

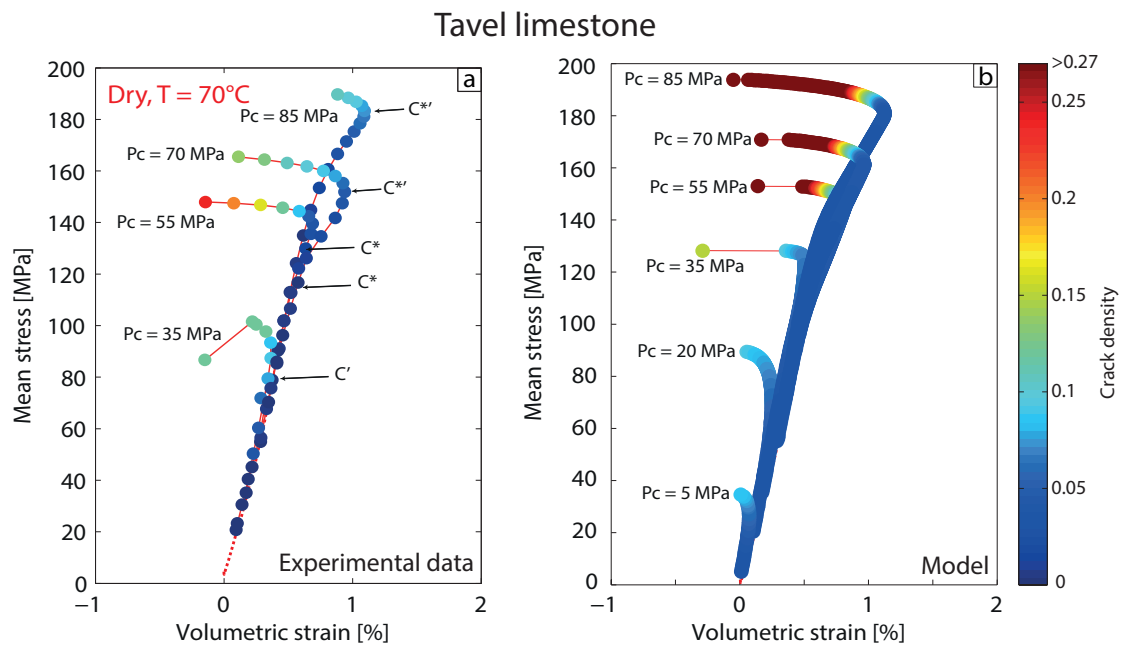


Figure 2.13 – Comparison of the experimental mean stress versus volumetric strain (a) and the model prediction (b) for deformation of Tavel limestone at various confining pressures. The color of the dots represents the vertical crack density. Initial crack density in the model is 0.035.

increase beyond C^{*} .

2.4.3 Limits of the model and possible applications

Initial porosity is a key parameter that controls the deformation and failure modes of limestones (Vajdova et al., 2004). In carbonate rocks, structural heterogeneities can also influence the localisation of damage (Dautriat et al., 2011a), as well as the microporosity distribution (Regnet et al., 2015b). The model takes into account a dilatancy due to crack development at low confining pressure, and a semibrittle behaviour characterized by shear-enhanced compaction due to microplastic flow, switching to dilatancy because local stress concentrations caused by pile-ups. To what extent can the model developed here be applied to various carbonate rocks? Up to what porosities can it be applied?

Baud et al. (2009) investigated systematically the micromechanics of compaction in two high porosity carbonates, Majella grainstone (porosity 30%) and Saint-Maximin limestone (porosity 37%). In Majella grainstone, shear-enhanced compaction is followed by shear failure with the

Chapter 2. Micromechanical constitutive model for constant strain rate deformation of limestones

apparition of a compactive shear band at low confining pressure (5-10 MPa), and homogeneous cataclastic flow at higher confining pressure (> 10 MPa). In both cases, grain crushing is the dominant mechanism of deformation beyond C^* . In Saint-Maximin limestone, [Baud et al. \(2009\)](#) could not unambiguously determine the evolution of the failure mode with increasing pressure but they observed various patterns of strain localization in all their samples. In a third high porosity limestone, Estailades limestone (porosity: 28%), [Dautriat et al. \(2011b\)](#) showed that beyond elastic compaction, cataclastic compaction is coupled with an elastic wave velocity decrease due to grain crushing. It can be concluded that the micromechanisms of deformation in Majella grainstone, Saint-Maximin and Estailades limestones are very different from the micromechanisms taken into account in the model developed in this study. The mechanical behaviour of high porosity limestones cannot be accounted for by the present model.

What is the behaviour for very low porosity limestones? [Baud et al. \(2000a\)](#) interpreted shear-enhanced compaction in Solnhofen limestone (porosity 3%) as resulting from plastic collapse of spherical pores embedded in a solid matrix, as initially modelled by [Curran & Carroll \(1979\)](#). For porosities lower than 15%, deformation beyond C^* in the semibrittle regime and inelastic pore collapse are controlled by plastic micromechanisms (dislocation slip processes, twinning) associated with some microcracking ([Vajdova et al. \(2004\)](#) and chapter 1). Thus, it can be suggested that, as porosity increases, a transitional behaviour is likely to develop and volumetric strain due to shearing and rotation of fragments ([Peng & Johnson, 1972](#), [Vajdova et al., 2012](#)) becomes more important. The transition between shear-enhanced compaction controlled by crystal plasticity and grain crushing is likely to occur for a porosity of approximately 20% ([Vajdova et al., 2004](#)) and the present model probably predicts adequately the stress-strain evolution for carbonates of porosity lower than 20%.

The present model is based on the assumption of homogeneous inelastic compaction. Compaction of porous rocks is known to be localized in many cases, as shown in sandstones by [Mollema & Antonellini \(1996\)](#) and [Fortin et al. \(2005\)](#) among many others. [Baud et al. \(2009\)](#) observed compactive shear bands at low confinement in Majella grainstone and at all confining pressures in Saint-Maximin limestone, suggesting that compaction localization is important in the mechanical compaction of high porosity carbonates. This kind of phenomenon has not been considered in the present model because experimental results do not show localization

for low porosity limestones.

Compaction is sometimes induced by the production of reservoirs (Fredrich et al., 2000). It can cause subsidence (e.g. Morton et al., 2006), which requires to redesign offshore platforms, or induce seismicity (e.g. Segall, 1989b) and well failure (e.g. Bruno et al., 1992), among other problems (Nagel, 2001). As shown by David et al. (1994) among others, compaction can lead to changes of permeability that can impact aquifer and reservoir production. For low porosity (i.e. $\phi < 20\%$) limestones, the present model can provide insights into the macroscopic mechanical behaviour of reservoirs.

2.5 Conclusion

The complex general trends of stress-strain relations of low-porosity limestones is reproduced by a model based on (1) brittle crack propagation, (2) a plasticity law for porous media with hardening and (3) crack nucleation due to dislocation pile-ups. The model is based on (i) three parameters relevant to the brittle behaviour (pre-existing crack length and density, sliding coefficient on these cracks), as previously developed by Ashby & Sammis (1990), (ii) two parameters relevant to the micro-plastic flow in the solid non-porous medium (a reference strain rate and an initial yield stress), and (iii) a parameter characterising the density of large pile-ups. Parameters relevant to the brittle behaviour can be determined from observations of the microstructure. The parameters relevant to the ductile behaviour are fitted to experimental data.

Despite the limited number of parameters, the model adequately predicts a brittle behaviour at low confining pressures, which switches to a semibrittle behaviour characterized by inelastic compaction followed by dilatancy at higher confining pressures. This suggests that the micro-physical phenomena responsible for the deformation are sufficient well captured. Possible applications include reservoir management. More generally, predicting the complex rheology of porous limestones in various conditions is possible through this model.

Supplements

Parameters

$\sigma, \sigma_m, \sigma_e$: remotely applied stress tensor and corresponding mean and von-Mises effective stresses
Q, S	: remotely applied differential and deviatoric stresses
x	: stress triaxiality
ρ_c	: crack density as defined by Budiansky & O'connell (1976)
G_i, G, K_i, K	: initial and current shear moduli, initial and current bulk moduli
ν_i	: initial Poisson's ratio
K_I, K_{IC}	: stress intensity factor, and the critical value of the material
W	: strain energy density
$\epsilon, \dot{\epsilon}$: remote strain and its rate of change
$\dot{\epsilon}_{ax}$: remotely imposed axial strain rate
$\dot{\epsilon}^P$: plastic strain rate
$\dot{\epsilon}^d$: strain rate induced by dislocations
$\epsilon^{md}, \dot{\epsilon}^{md}$: strain induced by mobile dislocation motions and its rate of change
$\dot{\epsilon}_0$: reference strain rate for the non-porous material
ϵ_0	: yield strain for macroscopic plasticity
$\epsilon^e, \epsilon^{cracks}, \epsilon^{mp}$: strain due to elasticity, cracks, and plasticity of the porous material
ρ_d, ρ_{md}	: total and mobile dislocation densities
$\rho_{id}, \rho_{id}^{init}, \rho_{id}^{new}$: immobile dislocation density, decomposed as initial and newly nucleated
b	: Burgers vector
v	: dislocation average slip velocity
V_0	: reference dislocation slip velocity
m, n	: stress sensitivity of the dislocation slip velocity and of the plasticity in the material
M	: strain hardening exponent of the macroscopic plastic law of the non-porous material
σ_0	: reference stress for dislocation slip velocity
σ_p, σ_p^i	: reference stress for plasticity of the non-porous material and its initial value
σ_i	: internal stress
$\sigma_i^i, \epsilon_0^P, \epsilon_0^p$: constants depending on microplastic parameters and relevant to internal stress
L_g	: grain size
τ_d	: characteristic time for dislocation motions
A_p, B_p, C_p, D_p	: constants relevant to microplastic flow
V, \dot{V}	: void volume and its rate of change
x^*, k, f^*	: reference values in the porous medium plasticity law
L	: pile-up length
τ^*, τ_a, τ_f	: dislocation driving shear-stress, resolved shear stress, and lattice friction stress
N_{di}, N_{di}^{pu}	: number of dislocations in a pile-up, and its average value
N_{di}^{crit}	: critical number of dislocations in a pile-up for new crack nucleation
Λ_{pu}	: number of pile-ups intersecting a reference surface
L_{pu}, ρ_{pu}	: average spacing between pile-ups, and pile-up density
θ, γ_w	: angle between wedge crack and pile-up plane, and angle between σ_1 and the pile-up plane
l_w	: wedge crack length
σ_w, τ_w	: normal and shear stresses acting on the wedge crack
γ_s	: surface energy of the material

Table S.2.1 – Summary of all the parameters used for the development of the model.

Derivation of stress intensity factors at tips of cracks forming an array

The stress intensity at the tip of the wings is obtained by considering the sliding wedging force F_w acting at the midpoint of the crack parallel to the X_3 -axis. The wedging force is calculated from the remote load as:

$$F_w = (A_1\sigma_1 - A_3\sigma_3)a^2, \quad (2.41)$$

where A_1 and A_3 are constants that can be found in [Ashby & Sammis \(1990\)](#). These constants were determined for the 2D case, could not be calculated analytically in 3D but were employed successfully in the 3D case ([Ashby & Sammis, 1990](#)).

Beside its contribution on the initial crack, the confining stress σ_3 also tends to close the wing cracks, which adds a contribution ([Tada et al., 2000](#)). Moreover, crack growth leads to their interaction, shown by σ^i in Figure 2.1 (a). Considering an array of N_v cracks per unit volume, all of which have extended to a length $2(l + a \times \cos \psi)$, σ_3^i is responsible for a third component in K_I acting on the wing cracks:

$$\sigma_3^i = \frac{F_w}{S - \pi(l + a \times \cos \psi)^2}, \quad (2.42)$$

where $\pi(l + a \times \cos \psi)^2$ is the total crack area projected normal to the X_3 -axis and S is the area per crack given by $S = \pi^{1/3}(3/4N_v)^{2/3}$. Taking into account all contributions on the initial penny-shaped cracks and its wings, the stress intensity is:

$$K_I = \frac{F_w}{[\pi(l + \beta a)]^{3/2}} - \frac{2}{\pi}(\sigma_3 - \sigma_3^i)\sqrt{\pi l}, \quad (2.43)$$

where the factor β was introduced by [Ashby & Sammis \(1990\)](#) to prevent the stress intensity from becoming infinite when l is vanishingly small. It defines an "effective" crack of length $(l + \beta a)$, with β chosen so that K_I reduces to the solution for an inclined crack in the limit $l = 0$. [Ashby & Sammis \(1990\)](#) found a value of $\beta = 0.27$ for the 2D and 3D cases.

**BRITTLE AND SEMIBRITTLE CREEP IN A
CARBONATE ROCK**

Ce chapitre s'intéresse au comportement mécanique du calcaire de Tavel sous contrainte constante. En se basant sur les micro-mécanismes identifiés lors de la déformation à vitesse contrôlée, les questions qui se posent maintenant sont: *Quels sont les mécanismes de déformation sous contrainte contrôlée? Comment la transition fragile-ductile influence-t-elle ces mécanismes? Quelle est l'influence du fluide de pore?* Nous présenterons donc les résultats mécaniques d'expériences de déformation en conditions de contraintes triaxiales constantes, à différents confinements inclus dans l'intervalle 0-100 MPa, à 20°C en conditions sèches et saturées en eau. Durant ces expériences, l'évolution des vitesses des ondes P et S a été mesurée pour mesurer l'évolution de l'endommagement.

Abstract

Deformation and failure mode of carbonate rocks depend on the confining pressure. In this study, the mechanical behaviour of a limestone with an initial porosity of 14.7% is investigated at constant stress. At low confining pressure, volumetric strain shows dilatancy during constant stress steps, ultimately leading to failure. This is equivalent to the creep mechanisms observed in brittle media such as glass, granite, basalt or sandstones. At higher confining pressures, semibrittle creep is characterized by inelastic compaction and constant elastic wave velocities during the first stress step, due to crystal plasticity. During the following stress steps, dilatancy is occurring due to crack nucleation by local stresses induced by dislocation pile-ups. These micromechanisms are similar to those described for constant strain rate experiments. However, the stress states at which the transitions are undergone are different from those

inferred from constant strain rate experiments. Moreover, creep experiments present higher strains at failure than constant strain rate experiments. This shows that the micromechanisms responsible for deformation, and the localization of damage are strain-rate dependent.

3.1 Introduction

Failure is due to the coalescence of a macroscopic fault caused by the accumulation of damage governed by (1) the increase of applied stress or (2) the progressive time-dependent growth of microcracks, even at constant stress. In the latter case, failure occurs by static fatigue because subcritical crack growth leads to a localization of damage. This was observed in glasses (Orowan, 1944, Charles, 1958, Wiederhorn & Bolz, 1970, Swanson, 1984, Mallet et al., 2014, 2015), sandstones (Heap et al., 2009b), granites (Kranz, 1979, Swanson, 1984, Lockner, 1993), shales (Swanson, 1984), basalts (Swanson, 1984, Heap et al., 2011), or gabbros (Meredith & Atkinson, 1985), among others (Atkinson & Meredith, 1987); and modelled successfully (Amitrano & Helmstetter, 2006).

The mechanical behaviour of limestones depends on the confining pressure. In particular, they undergo a brittle-ductile transition at room temperature (Wong & Baud, 2012). When deformed at confining pressures below the brittle-ductile transition, samples undergo (1) an elastic compaction until a point denoted C' , beyond which (2) some dilatancy takes place, leading to (3) a stress drop denoting macroscopic failure. Brittle micromechanisms of deformation are propagation and coalescence of microcracks, inducing shear localization and a sudden strength loss (Brace, 1978, Baud et al., 2000a, Vajdova et al., 2004, 2010).

When deformed at confining pressures beyond the brittle-ductile transition, samples exhibit (1) elastic compaction and (2) inelastic shear-enhanced compaction beyond a transition denoted C^* (Wong et al., 1997). Micromechanisms of shear-enhanced compaction are microcracking, grain rotation or microscopic plastic flow (crystal plasticity, diffusive mass transfer without volumetric change) (Paterson, 1978, Fredrich et al., 1989, Paterson & Wong, 2005, Dautriat et al., 2011a). Indeed, calcite can deform by processes such as mechanical twinning or r-, f- dislocation glide at room temperature (Turner et al., 1954, Griggs et al., 1960, De Bresser & Spiers, 1997). (3) However, in porous carbonate rocks, inelastic compaction is a transient phenomenon, and as differential stress increases volumetric strain then becomes dilatant

beyond a critical state denoted C^* (Wong et al., 1997), showing that crack nucleation and/or propagation becomes dominant. As showed by previous authors, the brittle-ductile transition depends on several parameters such as grain size and porosity (Fredrich et al., 1990, Vajdova et al., 2004, Wong & Baud, 2012).

The various micromechanisms involved in the deformation of carbonate rocks make it challenging to predict the behaviour of carbonate rocks at constant stress because plastic flows can interact with, annihilate, or enhance crack nucleation and growth (Stroh, 1954, McMeeking, 1977, Kinloch & Williams, 1980, Dresen & Evans, 1993, Faleskog & Shih, 1997). Brantut et al. (2014b) showed that brittle creep was indeed taking place in limestones. Yet, (1) their experiments were performed below the brittle-ductile transition, (2) their samples had significant quartz content, and (3) their experiments were held under water-saturated conditions, enabling mechanisms such as pressure solution. In water-saturated conditions, brittle strength is reduced as a result of adsorption. Water decreases the surface energy, promotes subcritical crack growth and stress corrosion (Clarke et al., 1986, Atkinson & Meredith, 1987, Costin, 1987, Baud et al., 2000b, Røyne et al., 2011, Liteanu et al., 2013). To the authors knowledge the mechanical behavior of limestones at constant stress for confining pressure beyond the brittle-ductile transition has not been investigated in details. As pore fluids vary in natural sites, deformation and failure should be studied in dry and water-saturated conditions.

This study focuses on the mechanical behaviour of white Tavel limestone (initial porosity of 14.7%) at constant stress. We address the following questions: (1) Are the micromechanisms involved in deformation at constant stress (CSE) similar to those observed in Constant Strain Rate Experiments (CSRE)? (2) How does the brittle-ductile transition affect the behaviour at constant stress? (3) What is the influence of water as a pore fluid?

We report results of creep stepping triaxial experiments performed at various effective confining pressures in the range of 20-85 MPa under dry and water-saturated conditions to investigate the influence of confining pressure, differential stress and pore fluid on creep strain rate. In addition, evolution of P- and S- wave velocities were recorded during the experiments to infer the presence of microcracks (e.g. Schubnel et al., 2006b, Benson et al., 2006, Fortin et al., 2007).

3.2 Experimental methods

3.2.1 Rock material and sample preparation

Experiments were performed on white Tavel limestone, a limestone already studied in [Vincké et al. \(1998\)](#), [Vajdova et al. \(2004, 2010\)](#). Scanning Electron Microscope (SEM) investigation indicated a composition of almost 100% calcite, in agreement with [Vajdova et al. \(2004\)](#). This rock is mainly composed of coarse grained micrite particles (mean diameter $\sim 5 \mu\text{m}$) fused from one to another, leading to larger micritic aggregates (Figure 3.1 A and B). In this general micritic layout, some larger micropores (diameter between $2 \mu\text{m}$ and $10 \mu\text{m}$) can be observed in sparitic parts, where cementation or recrystallization of pre-existing bioclasts is incomplete (Figure 3.1 A and C). A more detailed observation on ionic polished thin-sections reveals the presence of a low initial crack porosity, located between micritic aggregates and/or micrite particles (Figure 3.1 D). Average porosity is 14.7%, with maximum porosity variations of about 0.5% around the average value. Porosity values were obtained from two measurements: (1) using the density of dried samples and assuming a 100% calcite matrix composition and (2) using a triple weight procedure.

Cylindrical samples of 40 mm in diameter and 85 mm in length were cored from the same block as the one used in chapter 1. The ends of the cylinders were ground to ensure a good parallelism (Figure 3.1 b). Samples were then dried at $\sim 40^\circ\text{C}$ for several days prior to deformation. Permeability was measured in chapter 1 and is of the order of 10^{-16} m^2 .

3.2.2 Experimental apparatus

Triaxial deformation experiments were performed using the conventional triaxial cell installed in the Laboratoire de Géologie at the École Normale Supérieure in Paris. A precise description of the apparatus can be found in [Ougier-Simonin et al. \(2011\)](#), [Brantut et al. \(2011\)](#). The confining medium is oil and a neoprene tubing is used to separate the sample from oil confining medium. The axial shortening of the samples is measured with three displacement transducers (DCDT) mounted outside the vessel. The mean axial shortening is corrected from the machine stiffness. In addition, axial and radial strain gauges (*Tokyo Sokki TML* type FCB 2-11) are glued directly on the sample. Axial strain gauges are not used because they break

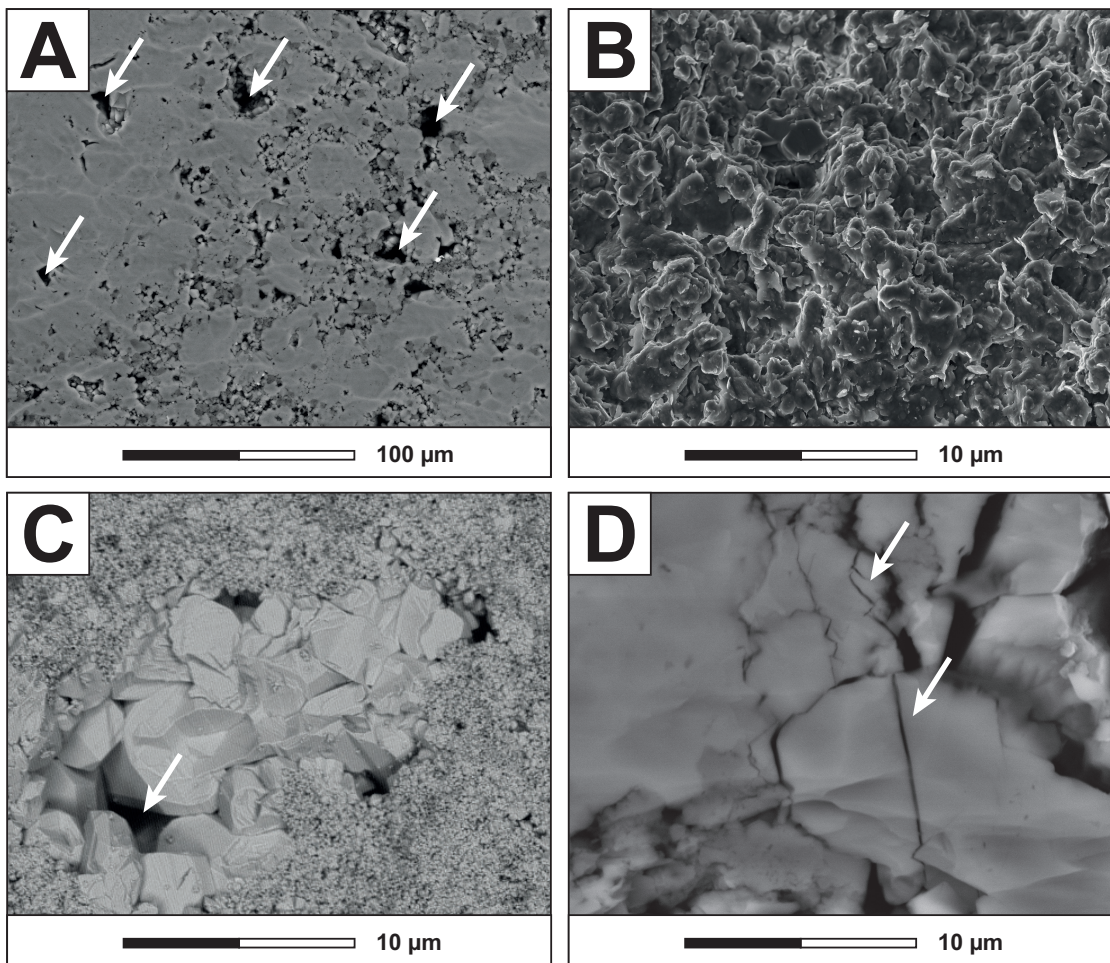


Figure 3.1 – Micrographs of Tavel Limestone in Scanning Electron Microscope taken from chapter 1. A - General observations of the layout. Larger micropores (white arrows) can be observed between or within micritic aggregates. B - Micritic aggregate composed of coarse anedral micrite particles ($\geq 4 \mu\text{m}$) with fused to indistinct contacts. C - Incomplete sparitic cementation in a pre-existing bioclast, at the origin of larger micropores (white arrow). D - Micritic aggregate observed on an ionic polished thin section. Initial crack porosity can be observed (regular or wing cracks, white arrows).

at strains attainable in carbonate rocks ($\epsilon_{ax} \sim 2\%$), whereas DCDTs have no strain limitation. Radial strains are measured with four radial strain gauges. Uncertainty in strain measured with radial gauges are estimated to be 10^{-5} , and DCDT signals have an accuracy of about 10^{-4} . Neglecting second-order contributions of strains to the volume change that may be appreciable at relatively large strains, volumetric strain is calculated as $\epsilon_v = \epsilon_{ax} + 2\epsilon_r$ where ϵ_{ax} and ϵ_r are the axial and radial strains, respectively. For water-saturated experiments, pore pressure is controlled at the top and the bottom of the sample with two micro-volumetric

pumps (Quizix) with an accuracy of about 10^{-2} MPa.

3.2.3 Elastic wave velocities

Sixteen piezoelectric transducers (PZTs) are directly glued onto the sample surface, four being sensitive to S-waves and the others to P-waves. All transducers can be used either as receivers (in passive mode) or as sources (in active mode). No significant acoustic emission activity is recorded so PZTs are used in the active mode to measure the evolution of P- and S-wave velocities during deformation. Depending on the experiment duration, ultrasonic velocity surveys are recorded every 1, 5 or 30 minutes. The arrival time is systematically corrected from the sample deformation. The PZT sensors arrangement (Figure 3.2) gives P-wave velocities along five different angles with respect to the axis of symmetry: 90° (ray perpendicular to the main axis); 70° , 53° , 42° and 34° . In addition, horizontal S_h , and vertical S_v , S-wave velocities are measured at an angle of 90° (radial). Arrival times are known with an accuracy of $0.1 \mu\text{s}$, which leads to a precision of the absolute velocities of the order of 5% and a relative precision of the order of 0.2%.

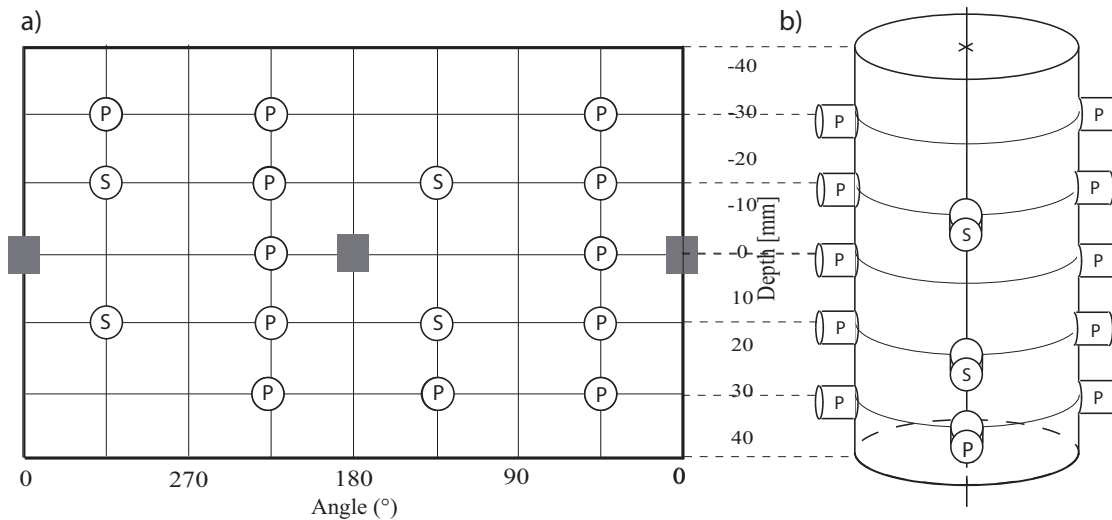


Figure 3.2 – (a) Sensor map used for the experiments. S-wave velocities were measured on directions perpendicular to the sample axis. P-wave velocities were measured on directions forming an angle of 34° , 42° , 53° , 70° and 90° with the sample axis. A schematic view of a prepared sample is given in (b).

3.2.4 Experimental procedure

Samples are deformed using an imposed constant differential stress (creep experiments). For dry experiments, samples are i) first loaded hydrostatically up to the desired confining pressure, ii) then the samples are loaded at an imposed constant axial strain rate ($\sim 10^{-5} \text{ s}^{-1}$) until the target differential stress is reached. This stress-state is then maintained constant over extended periods of time, allowing the samples to deform at constant stress. This procedure is repeated for n steps (Figure 3.3) following a stress-stepping creep procedure (Heap et al., 2009b, 2011, Mallet et al., 2015), until failure of the samples in tertiary creep. For water saturated experiments, dry samples are first loaded hydrostatically up to 20 MPa. Water at equilibrium with calcite is then injected and saturation is controlled with the microvolumetric pumps. The pore pressure is then increased and maintained constant at 5 MPa. At this point, the procedure becomes similar to that for dry samples. Tables 3.1 and 3.2 summarize the experimental conditions for dry and water-saturated experiments, respectively.

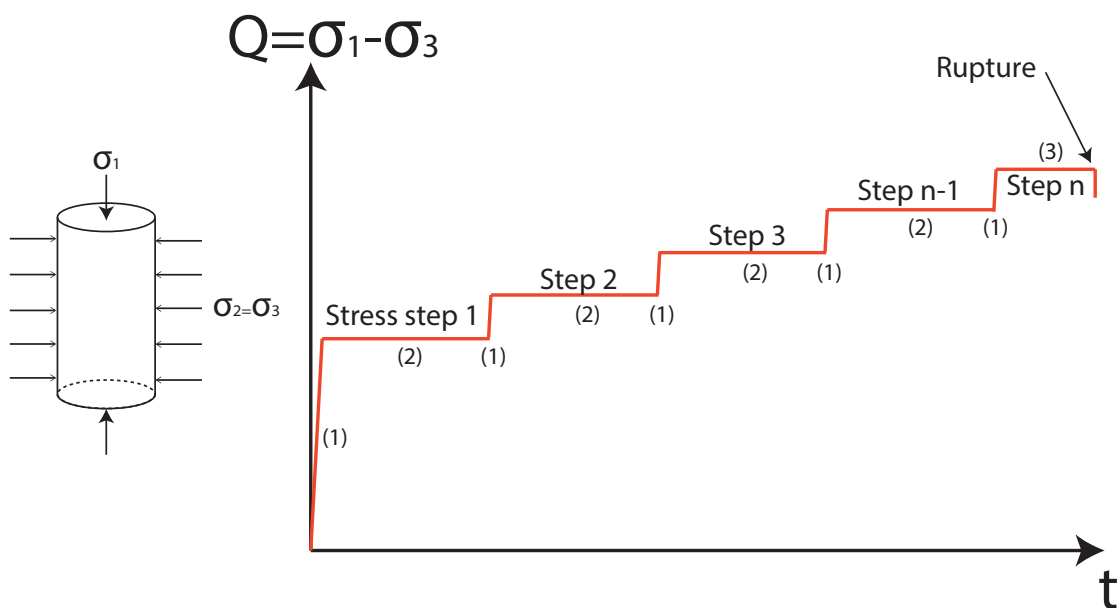


Figure 3.3 – Experimental protocol for stress-stepping creep tests. During phases noted (1), the differential stress is increased with a constant strain rate procedure, during (2), the differential stress is maintained constant for several hours. The phase (3) corresponds to the last step, during which the macroscopic failure occurs in tertiary creep.

Chapter 3. Brittle and semibrittle creep in a carbonate rock

N ^o	P _{eff} (MPa)	Diff. stress (MPa)	min{ $\dot{\epsilon}_{ax}$ } (s ⁻¹)	duration (h)	final strain (%)	notes
1	20	144.4	2.17 10 ⁻⁹	22.1	-0.615	
		146.6	2.56 10 ⁻⁹	19.3	-0.02637	
		149.53	2.66 10 ⁻⁹	22.6	-0.03889	
		152.93	2.21 10 ⁻⁹	33.1	-0.05429	
		155.43	2.67 10 ⁻⁹	16.4	-0.0265	
		161.33	2.14 10 ⁻⁸	4.8	-0.0603	failure
2	35	237.8	4.47 10 ⁻⁷	1.05	-0.02	failure
3	35	195.4	6.11 10 ⁻⁹	42.9	-1.554	
		206.4	2.51 10 ⁻⁷	1.5	-0.2	failure
4	55	9.3	5.19 10 ⁻¹⁰	19.9	-0.02757	
		224.3	2.04 10 ⁻⁹	28.2	-0.5902	
		275	1.04 10 ⁻⁶	1.9	-0.8725	failure
5	55	150	9.11 10 ⁻¹⁰	22.3	-0.5982	
		165	8.06 10 ⁻¹⁰	22.4	-0.07689	
		170	1.48 10 ⁻⁹	25.9	-0.03068	
		175	1.79 10 ⁻⁹	23.1	-0.042	
		181	2.77 10 ⁻⁹	25.8	-0.03854	
		191	2.45 10 ⁻⁹	24.8	-0.085	
		201	4.17 10 ⁻⁹	22.8	-0.1048	
		206	4.17 10 ⁻⁹	22.3	-0.06267	
		211	4.72 10 ⁻⁹	25	-0.06707	
		218.6	7.22 10 ⁻⁹	25.4	-0.1202	
		228.2	8.06 10 ⁻⁹	22.3	-0.2121	
		238.5	6.67 10 ⁻⁹	49.9	-0.485	
		243.7	7.78 10 ⁻⁹	46.2	-0.2168	
279	1.25 10 ⁻⁸	73.2	-0.513	failure		
6	70	210.6	3.06 10 ⁻⁹	20.8	-0.8386	
		260	5.56 10 ⁻⁹	24.7	-0.5762	
		306.2	8.27 10 ⁻⁷	0.4	-2.523	failure
7	70	263.6	1.31 10 ⁻⁸	70.8	-4.56	
		267.3	1.47 10 ⁻⁸	23.9	-0.1681	
		271	1.47 10 ⁻⁸	30.2	-0.2385	
		275	2.08 10 ⁻⁸	23	-0.2272	
		280.6	2.42 10 ⁻⁸	47.4	-1.063	
		288.6	3.74 10 ⁻⁷	0.1	-0.03901	failure
8	85	204.5	4.72 10 ⁻⁹	24.5	-1.118	
		304.6	3.33 10 ⁻⁸	24.3	-5.275	
		354.3	-	24.4	-1.768	EPS
9	85	215.3	8.61 10 ⁻⁹	26.8	-1.586	
		265.3	3.53 10 ⁻⁸	23.4	-2.778	
		290.4	6.22 10 ⁻⁸	20.1	-3.88	
		294	4.81 10 ⁻⁸	27.1	-0.5675	
		300.7	6.39 10 ⁻⁸	21.4	-0.6025	
		322	1.53 10 ⁻⁷	48.3	-0.7793	EPS

Table 3.1 – Summary of the mechanical data for constant stress experiments performed under dry conditions on white Tavel limestone. EPS denotes Ends Piston Stroke.

3.3 Results

In this paper, compressive stresses and compactive strains are counted positive. Principal stresses will be denoted σ_1 and σ_3 , σ_1 being the highest principal stress and σ_3 the confining

N ^o	P _{eff} (MPa)	P _p (MPa)	Diff. stress (MPa)	min{ $\dot{\epsilon}_{ax}$ } (s ⁻¹)	duration (h)	final strain (%)	notes
10	20	5	136.8	4.17 10 ⁻⁹	27.5	-0.5843	
		5	143	4.44 10 ⁻⁹	21.4	-0.06059	
		5	145	3.61 10 ⁻⁹	26.4	-0.04735	
		5	150	4.17 10 ⁻⁹	22.8	-0.04655	
		5	156	3.33 10 ⁻⁹	39.9	-0.1004	
		5	161	5.55 10 ⁻⁹	22.7	-0.07107	
		5	166	1.33 10 ⁻⁸	55.5	-0.249	failure
11	35	5	10.8	~ 0	1.9	~ 0	
		5	236.6	5.63 10 ⁻⁶	2.1	-1.2	failure
12	35	5	186	7.91 10 ⁻⁶	1	-1.1	failure
13	55	5	12.2	4.06 10 ⁻¹⁰	16.7	-0.0361	
		5	220.6	5.83 10 ⁻⁸	23.7	-2.228	
		5	259.4	-	0	-0.1759	failure during loading
14	55	5	150	1.14 10 ⁻⁸	27.5	-0.999	
		5	165	1.39 10 ⁻⁸	26.2	-0.262	
		5	170	1.06 10 ⁻⁸	24.6	-0.144	
		5	175	1.72 10 ⁻⁸	20.4	-0.111	
		5	191	2.72 10 ⁻⁸	25.6	-0.438	
		5	206	1.11 10 ⁻⁷	23	-1.198	
		5	219	7.78 10 ⁻⁷	20.2	-0.210	failure
15	85	5	199.7	4.75 10 ⁻⁸	44.8	-4.313	
		5	293	-	51.1	-1.924	EPS
16	85	5	204.6	8.06 10 ⁻⁹	86.9	-2.013	
		5	309.4	-	47.5	-2.709	EPS
17	85	5	216	2.61 10 ⁻⁸	24.8	-1.941	
		5	264	7.78 10 ⁻⁸	27.6	-2.865	
		5	290	8.06 10 ⁻⁸	38.6	-3.621	
		5	295	2.64 10 ⁻⁸	28.6	-0.9719	
		5	300.6	6.94 10 ⁻⁸	29.8	-0.6773	EPS

Table 3.2 – Summary of the mechanical data for constant stress experiments performed under water-saturated conditions on white Tavel limestone. EPS denotes Ends Piston Stroke.

pressure, P_c . The differential stress $\sigma_1 - \sigma_3$ will be denoted Q and the effective mean stress $(\sigma_1 + 2\sigma_3)/3 - P_p$ will be denoted P , where P_p is the pore pressure.

3.3.1 Mechanical behaviour during constant strain rate deformation

Constant strain rate experiments conducted on Tavel limestone were presented in chapter 1. Here, we give a brief summary of their results that are needed to understand the results from creep experiments. Constant strain rate experiments were conducted at effective confining pressure in the range of 0-85 MPa in dry and water-saturated conditions. Figure 3.4 (a) shows the differential stress as a function of axial strain, and Figure 3.4 (b) shows the effective mean stress versus volumetric strain for experiments performed in dry condition at $P_c = 0, 20, 35,$

55, 70 and 85 MPa.

For $P_c \leq 55$ MPa, the observed features are typical of the brittle regime: i) samples undergo an elastic compaction until a point denoted C' (Wong et al., 1997), beyond which dilatancy takes place (Figure 3.4 b); ii) the differential stress reaches a peak, beyond which strain softening is occurring; iii) Observation of the samples after deformation indicates that the deformation was localized in a shear fault.

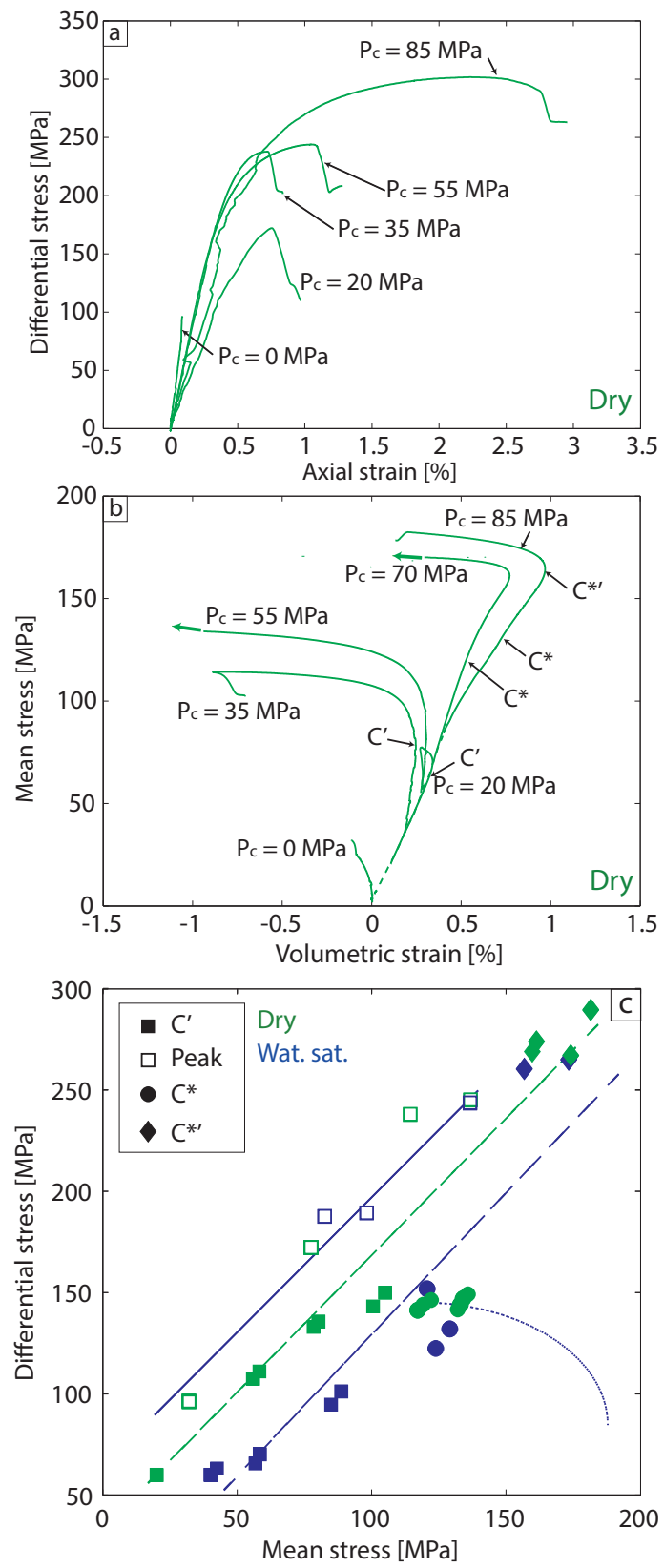
For $P_c \geq 70$ MPa, samples exhibit (1) an elastic compaction and (2) an inelastic shear-enhanced compaction associated with strain hardening beyond a critical stress denoted C^* (Baud et al., 2000a) (Figure 3.4 b). Yet, the inelastic compaction is transient and volumetric strain reverses from inelastic compaction to dilatancy beyond a critical stress denoted $C^{*'} (Wong et al., 1997)$ (Figure 3.4 b). These features (i) involving macroscopically distributed deformation by both crystal plasticity and microcracking; (ii) leading to final axial strains lying in the range 3-5% at failure and (iii) inducing a pressure-dependent strength; are typical of the semibrittle (ductile) regime as defined by Evans et al. (1990).

The critical stresses at (i) the onset of dilatancy C' , (ii) peak stress, (iii) onset of inelastic compaction C^* , and (iv) post-yield dilatancy $C^{*'}$ in dry and water-saturated conditions are shown in the $P - Q$ space in Figure 3.4 (c). In dry and water-saturated conditions, the brittle-ductile transition occurs at $55 \text{ MPa} \leq P_c \leq 70 \text{ MPa}$ in Tavel limestone. In the brittle regime, water decreases the threshold for the onset of dilatancy (C') but has no effect on the peak stress at failure. In the semibrittle regime, water has no clear effect on the threshold for inelastic compaction C^* , nor on the post-yield dilatancy $C^{*'}$ (chapter 1).

3.3.2 Mechanical behaviour during stress-stepping creep experiments

In this study our goal is to investigate the mechanical behaviour of Tavel limestone during brittle and semibrittle creep. Thus, stress-stepping creep experiments are conducted over ef-

Figure 3.4 (*following page*) – Compilation of mechanical data for constant strain rate experiments. (a) Differential stress versus axial strain curves for experiments performed under dry conditions. (b) Mean stress versus volumetric strain curves for experiments performed under dry conditions. (c) Peak stress (empty squares), and thresholds C' (plain squares), C^* (plain dots), and $C^{*'}$ (plain diamonds), shown in the stress space. Green and blue symbols correspond to dry and water-saturated experiments, respectively.



Chapter 3. Brittle and semibrittle creep in a carbonate rock

fective confining pressures ranging across the brittle-ductile transition inferred from constant strain rate experiments, i.e. from 20 to 85 MPa. Figures 3.5 (a) and (b) show the differential stress as a function of axial strain for stress-stepping creep experiments performed in dry and water-saturated conditions, respectively. For these two sets of experiments, volumetric strains are plotted versus mean stress in Figure 3.5 (c) and (d), respectively. All experiments exhibit an elastic behaviour during the first part of loading. Then, the mechanical behaviour depends upon the confining pressure.

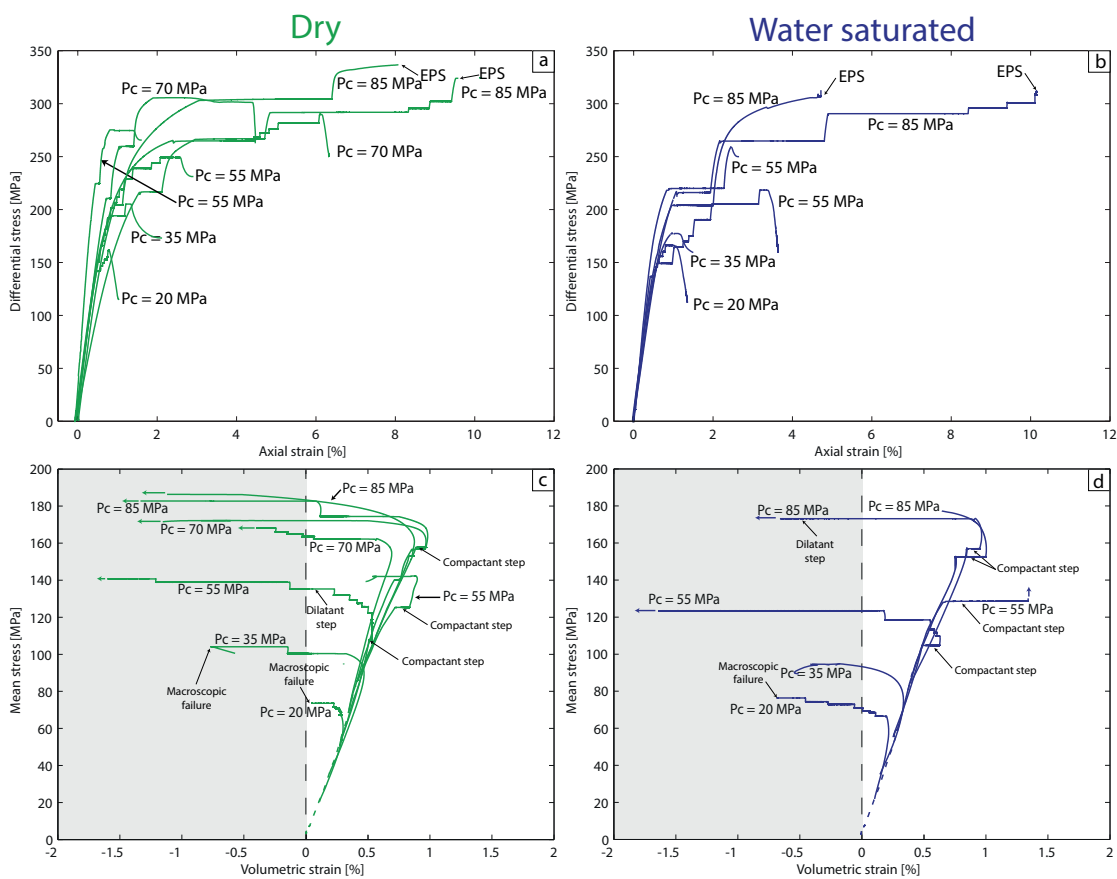


Figure 3.5 – Compilation of mechanical data obtained during stress-stepping creep steps. (a) and (b) are the differential stress versus axial strain for dry experiments and water saturated experiments, respectively. The mean stress versus volumetric strain curves for these two sets of experiments are shown in (c) and (d), respectively. Horizontal arrows mean that radial strain gauges broke, preventing us from recording the volumetric strain any further. EPS means that the moving piston reached its maximum displacement.

Stress-stepping creep experiments in dry conditions

Brittle creep

Here, we focus on experiments conducted at $P_c \leq 35$ MPa, where features observed in conventional triaxial experiments are typical of the brittle regime. A key point before starting stress-stepping creep experiments is to determine the level of differential stress to be applied during the first stress step. Below the onset of dilatancy (C'), the rock is assumed to be poroelastic and should therefore not accumulate damage under constant stress. Figure 3.6 (a) shows

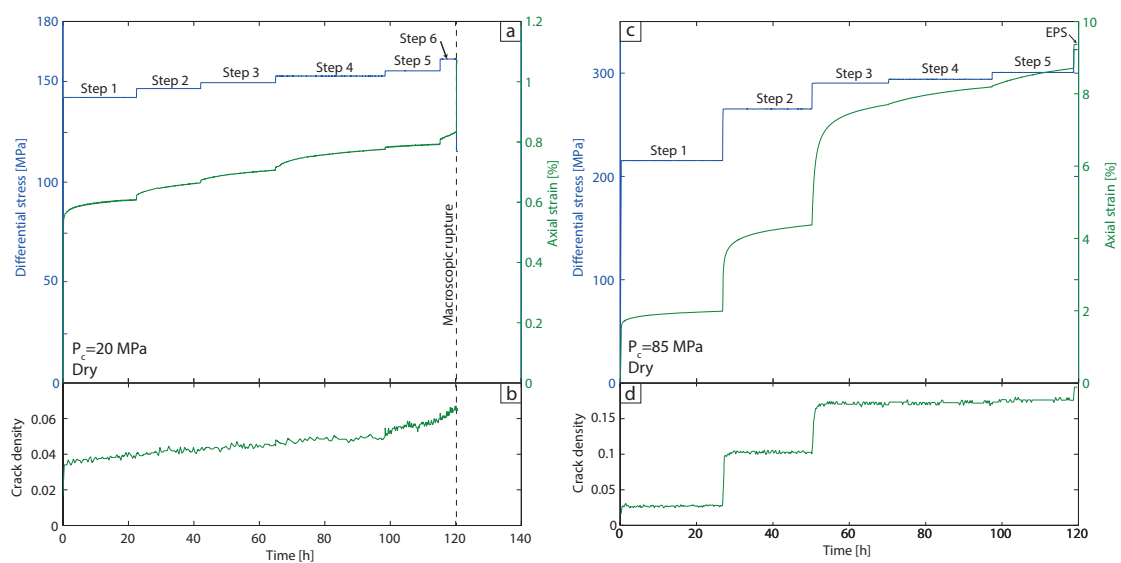


Figure 3.6 – (a) Evolution of the differential stress and axial strain for creep stepping experiment done at $P_c = 20$ MPa under dry conditions. (b) Evolution of crack density during the experiment. (c) Evolution of the differential stress and axial strain for creep stepping experiment done at $P_c = 85$ MPa under dry conditions. (d) Evolution of crack density during the experiment.

the evolution of loading as a function of time for the experiment performed at $P_c = 20$ MPa. In this experiment, the first step was fixed at $Q = 144$ MPa, higher than the critical stress C' ($Q_{C'} = 108$ MPa). During the first step, the sample deformed through primary creep and into secondary creep at constant Q (Figure 3.6 a). After about 24h, the differential stress was stepped up by a small increment (Table 3.1). This cycle was then repeated sequentially until the sample eventually failed (Figure 3.6 a). During this experiment, all steps were associated with dilatancy (Figure 3.5 c). Figure 3.7 focuses on the last step (n^o6) of this experiment. The evolution of the axial and volumetric strains as well as the evolution of P-wave velocities are

plotted as a function of time in Figures 3.7 (e) and (f), respectively. During secondary creep, the axial strain rate for this sixth step was $2.14 \times 10^{-8} \text{s}^{-1}$ (Figure 3.7 e and Table 3.1). The secondary creep is associated with i) dilatancy (decrease of volumetric strain) and ii) a decrease of elastic wave velocities. P-wave velocities decrease at all angles but the higher the angle with respect to σ_1 is, the more important the decrease is. The maximum decrease is observed for the pathway perpendicular to σ_1 (90°), which suggests that the propagating and/or nucleating cracks are mainly axial (Mavko et al., 1995, Ayling et al., 1995, Fortin et al., 2011). Tertiary creep starts 40 minutes before failure, and is associated with accelerations of axial strain rate and P-wave decrease rates for all pathways. At failure, the decreases of P-wave velocities range from -5% at an angle of 90° to -1.7% at an angle of 34° .

Semibrittle creep

Features observed during conventional triaxial experiments conducted at $P_c \geq 70$ MPa are typical of the semibrittle regime as defined by Evans et al. (1990) (see section 3.3.1). Note that constant strain rate experiments conducted at $P_c = 55$ MPa exhibited a brittle behaviour but creep stepping experiments performed at this confining pressure exhibit a semibrittle behaviour. This discrepancy of behaviour is discussed more thoroughly later. In the semibrittle regime, the differential stress to be applied during the first stress step is taken between the threshold for inelastic compaction C^* and the post-yield dilatancy $C^{*'}$, beyond the elastic regime. Figure 3.6 (b) shows the evolution of loading as a function of time for an experiment performed at $P_c = 85$ MPa. The first step of this experiment was fixed at $Q = 215$ MPa, between the critical stresses C^* ($Q_{C^*} = 144$ MPa) and $C^{*'}$ ($Q_{C^{*'}} = 267$ MPa). During the first step, the sample deformed through primary creep and into secondary creep at constant Q (Figure 3.6 b). After about 27h, the stress was stepped up to a differential stress $Q = 265$ MPa (Table 3.1), slightly lower than the post-yield dilatancy ($C^{*'}$) inferred from constant strain rate experiments. This cycle was then repeated sequentially beyond $C^{*'}$ until the piston reached its maximum displacement, which corresponds to a maximum axial strain of 9.5% for this experiment. The first step of this experiment is associated with compaction and the following ones with dilatancy (Figure 3.5 c).

Let us first focus on the compactive first step of this experiment (Figure 3.8). The evolutions of the axial and volumetric strains as well as the evolution of P-wave velocities at different angles

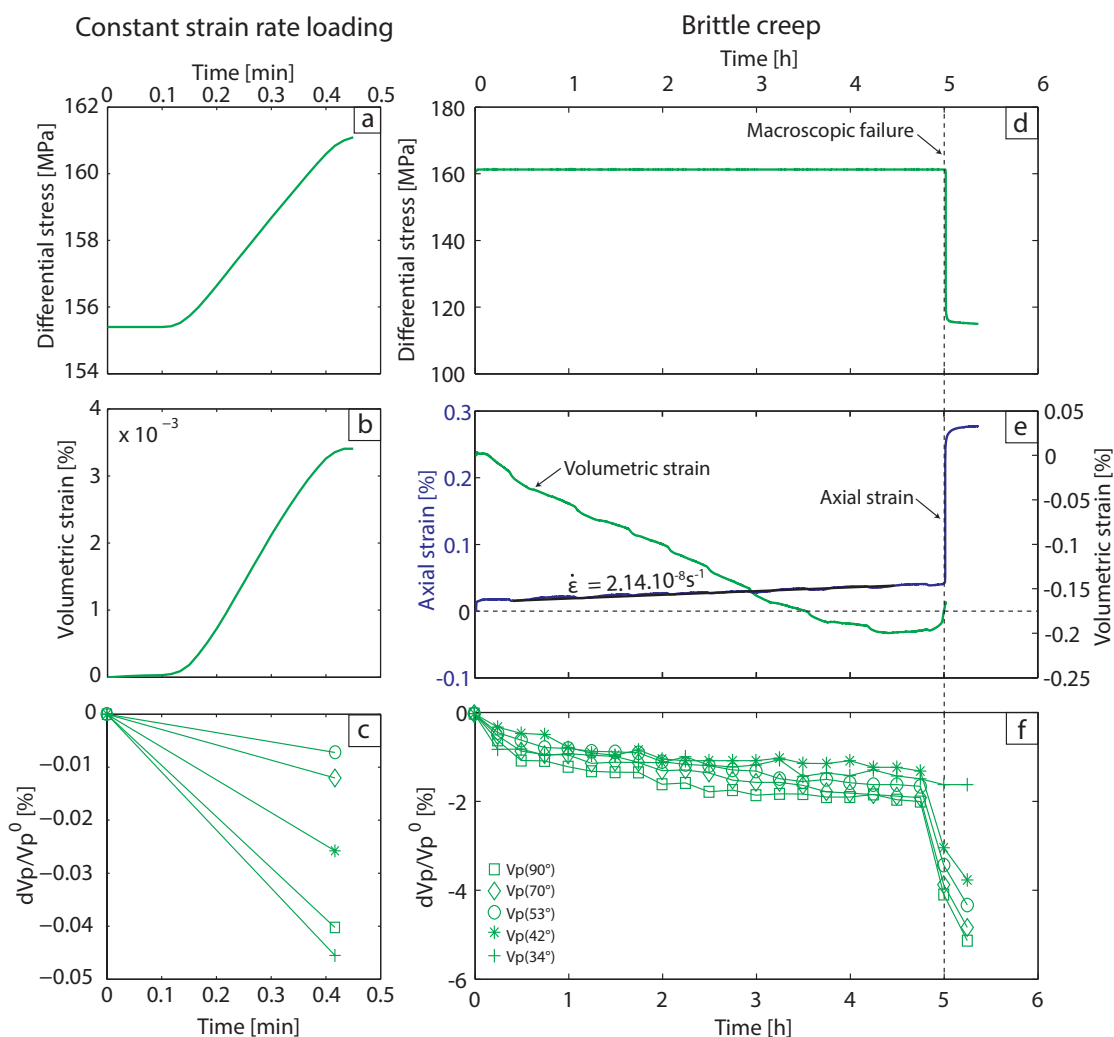


Figure 3.7 – (a) Evolution of the differential stress during loading before the last creep step for the 20 MPa confining pressure dry experiment. (b) Evolution of the axial and volumetric strains during loading. (c) Evolution of $\delta V_p/V_p^0$ (V_p^0 being the P-wave velocity at the end of the preceding constant stress step) at different angles with respect to σ_1 . (d) Evolution of the differential stress during the last creep step of the experiment conducted at a confining pressure of 20 MPa in dry conditions. (e) Evolution of the axial and volumetric strains during this stress step. (f) Evolution of $\delta V_p/V_p^0$ (V_p^0 being the P-wave velocity at the end of the preceding constant strain rate loading) at different angles with respect to σ_1 .

are plotted as a function of time in Figure 3.8 (c) and (d), respectively. During secondary creep, the axial strain rate was $8.6 \times 10^{-9} s^{-1}$ (Figure 3.8 c and Table 3.1). The secondary creep was associated with i) compaction and ii) constant elastic wave velocities at all angles. Compaction reached 0.08% at the end of the stress step.

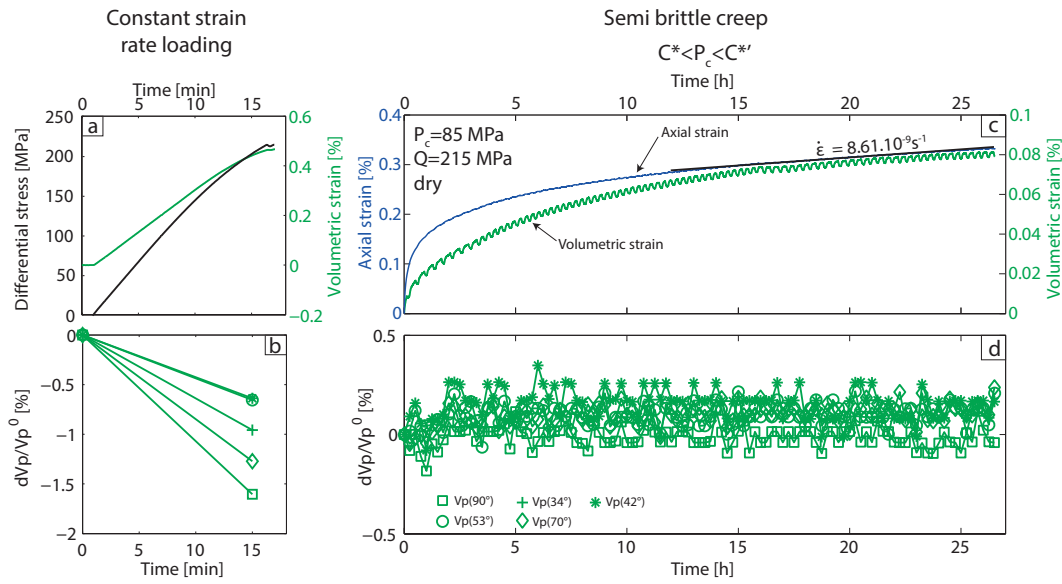


Figure 3.8 – (a) Evolution of differential stress and volumetric strain during loading before the first stress step of the experiment done at $P_c = 85$ MPa under dry conditions. (b) Evolution of the $\delta V_p/V_p^0$ at different angles with respect to σ_1 during loading. (c) Evolution of the axial and volumetric strains during the first creep step. (d) Evolution of the $\delta V_p/V_p^0$ at an angle of 90 degrees with respect to σ_1 during this creep step.

During the second stress step of this experiment (Figure 3.9), elastic wave velocities decreased during primary creep, by 1% to 2.5% depending on the angle with respect to σ_1 . The maximum decrease was observed for the pathway perpendicular to σ_1 (Figure 3.9 d). During secondary creep, the axial strain rate was $3.5 \times 10^{-8} s^{-1}$ (Figure 3.9 c and Table 3.1). For this second step, secondary creep was associated with i) dilatancy and ii) constant elastic wave velocities at all angles. Dilatancy reached a value of -0.6% at the end of this second stress step.

Failure did not occur during this experiment because the piston reached its maximum displacement before. The fifth stress step is the last "full" step of this experiment. During this step, the differential stress Q was fixed at a value of 300 MPa. Figure 3.10 shows the evolutions of (c) the axial strain and (d) P-wave velocities as a function of time during the step. Volumetric strain could not be recorded because radial strain gages had already reached their maximum deformation. During secondary creep, the axial strain rate was $6.4 \times 10^{-8} s^{-1}$ (Figure 3.10 c and Table 3.1). The primary and secondary creeps were associated with a decrease of elastic wave velocities of 1%, independent of the angle of their pathway with respect to σ_1 . Axial strain reached 0.35% at the end of this fifth stress step, a value far below the axial strain reached at

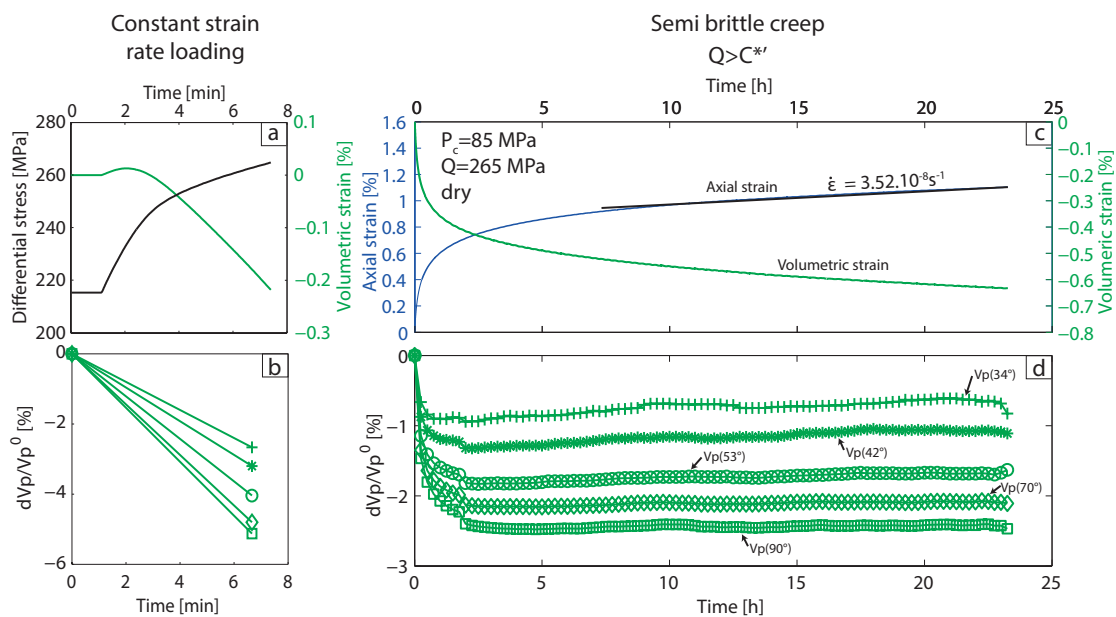


Figure 3.9 – (a) Evolution of the differential stress and volumetric strain during loading between the first and second stress steps for the experiment done at $P_c = 85$ MPa under dry conditions. (b) Evolution of the $\delta V_p/V_p^0$ at different angles with respect to σ_1 during loading. (c) Evolution of the axial and volumetric strains during the second creep step. (d) Evolution of the $\delta V_p/V_p^0$ with respect to σ_1 during this creep step.

the end of the second stress step for e.g. (around 1.2%).

Water-saturated samples

A key point before conducting water-saturated experiments is to check whether we are in drained conditions or not. The maximum strain rate imposed to our samples during loading is $\sim 10^{-5} s^{-1}$, which is sufficiently low to maintain drained conditions in the samples (see chapter 1). During stress steps in the brittle regime, (i) permeability is likely to increase and (ii) strain rates remain lower than the loading strain rate, which ensures drained conditions. During semibrittle stress steps, inelastic compaction may decrease the permeability of the samples. However, our main interest lies in secondary strain rates, which remain much lower than $10^{-5} s^{-1}$ (Table 3.2) thus ensuring that drained conditions are very likely to be maintained. Then, when dilatancy is occurring, permeability is likely to increase, thus implying the same conclusions as for the brittle regime.

Stress-stepping creep experiments performed in water-saturated conditions (Table 3.2) have a

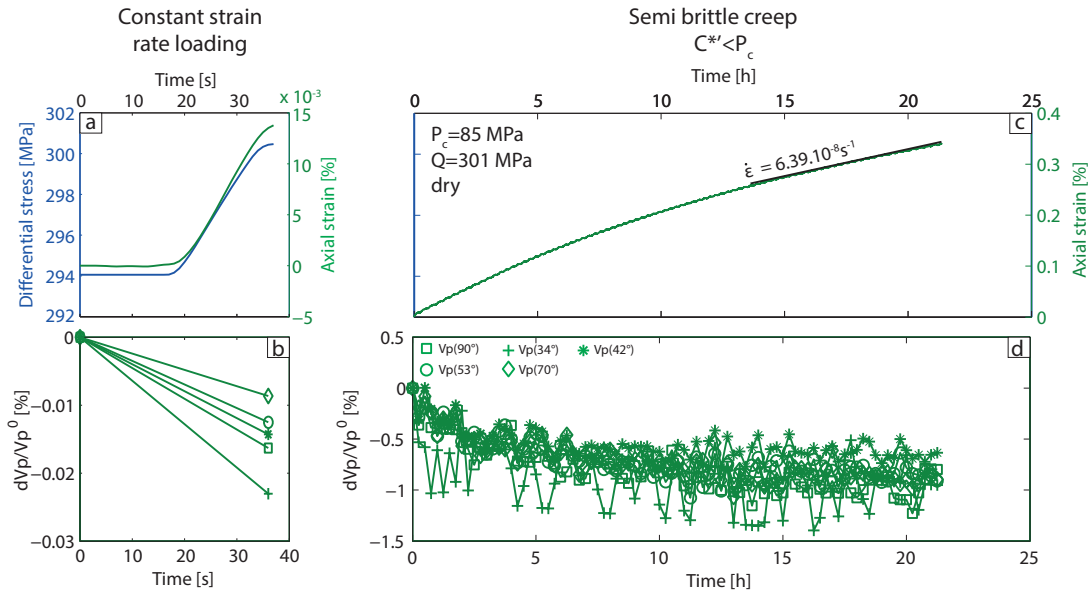


Figure 3.10 – (a) Evolution of axial strain during loading between the fourth and fifth creep steps of the experiment done at $P_c = 85$ MPa under dry conditions. (b) Evolution of the $\delta V_p / V_p^0$ at different angles with respect to σ_1 during loading. (c) Evolution of the axial strain during the fifth creep step. (d) Evolution of the $\delta V_p / V_p^0$ at different angles with respect to σ_1 during this creep step.

qualitatively similar behaviour as those performed in dry conditions. For $P_c^{eff} \leq 35$ MPa, the mechanical response is typical of a brittle behaviour (Figures 3.5 b and d). However, dilatancy observed during constant stress steps is higher in water-saturated conditions than in dry conditions (Figure 3.11), suggesting that water promotes crack growth, as observed in many types of rocks (Rutter, 1974b, Waza et al., 1980, Baud et al., 2000b, Duda & Renner, 2013). For $P_c^{eff} \geq 55$ MPa, no clear difference is observed between experiments conducted in dry and water-saturated conditions.

3.3.3 Crack densities

Under triaxial stresses, our results show that elastic wave velocities depend on the pathway (e.g. Figure 3.7), indicating that cracks are not randomly oriented. The maximum decrease is observed for the pathway perpendicular to σ_1 (90°), which suggests that the propagating and/or nucleating cracks are mainly axial (Mavko et al., 1995, Ayling et al., 1995, Fortin et al., 2011). Thus, we invert elastic wave velocities in terms of axial crack density (Sayers & Kachanov, 1995, Mallet et al., 2013) assuming: (1) a transverse isotropic geometry of axial cracks, reflecting that

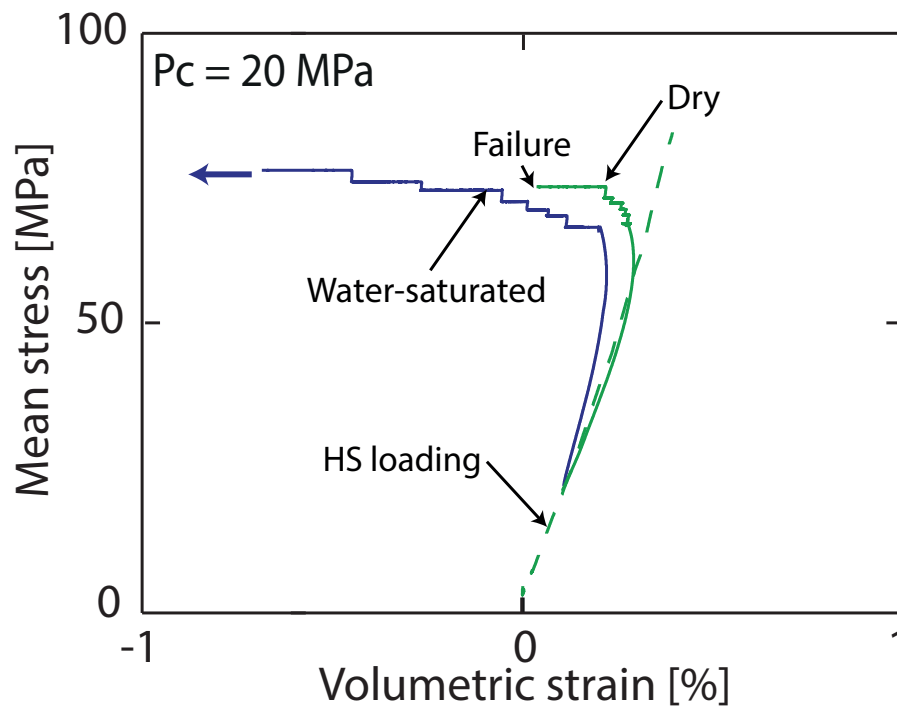


Figure 3.11 – Volumetric strain versus mean stress for creep experiments performed at $P_c = 20$ MPa in dry (green) and water-saturated conditions (blue), respectively.

in our experiments $\sigma_2 = \sigma_3$; (2) an isotropic matrix, in agreement with the isotropic elastic waves velocities measured under hydrostatic conditions; (3) non-interacting cracks, an assumption which is valid for crack densities up to at least 0.15 and probably 0.2-0.25 (Grechka & Kachanov, 2006); (4) a random crack center distribution; and (5) penny-shape cracks of radius c and aperture w . The effective mechanical properties of the calcite aggregate composed of the solid matrix and embedded pores (Young modulus $E_0 = 32.8$ GPa and Poisson's coefficient $\nu_0 = 0.29$) were estimated from velocities measured at $P_c = 85$ MPa, a pressure far above the crack closing pressure (see chapter 1). Details on the procedure are given in appendix 3.5.

In the brittle regime, crack density increased for differential stresses beyond the onset of dilatancy C'). Taking the experiment performed at $P_c = 20$ MPa in dry conditions as an example, crack density increased from 0.02 before triaxial loading to 0.065 at failure by tertiary creep (Figures 3.6 b and 4.9 a). During steps 1 to 5, crack density increased almost linearly with time (Figures 3.6 b). During the last stress step, the rate of crack density increase accelerated. In water-saturated conditions, crack density evolution was similar to that in dry conditions with systematically higher values (Figure 4.9 c), suggesting that water enhances crack propagation.

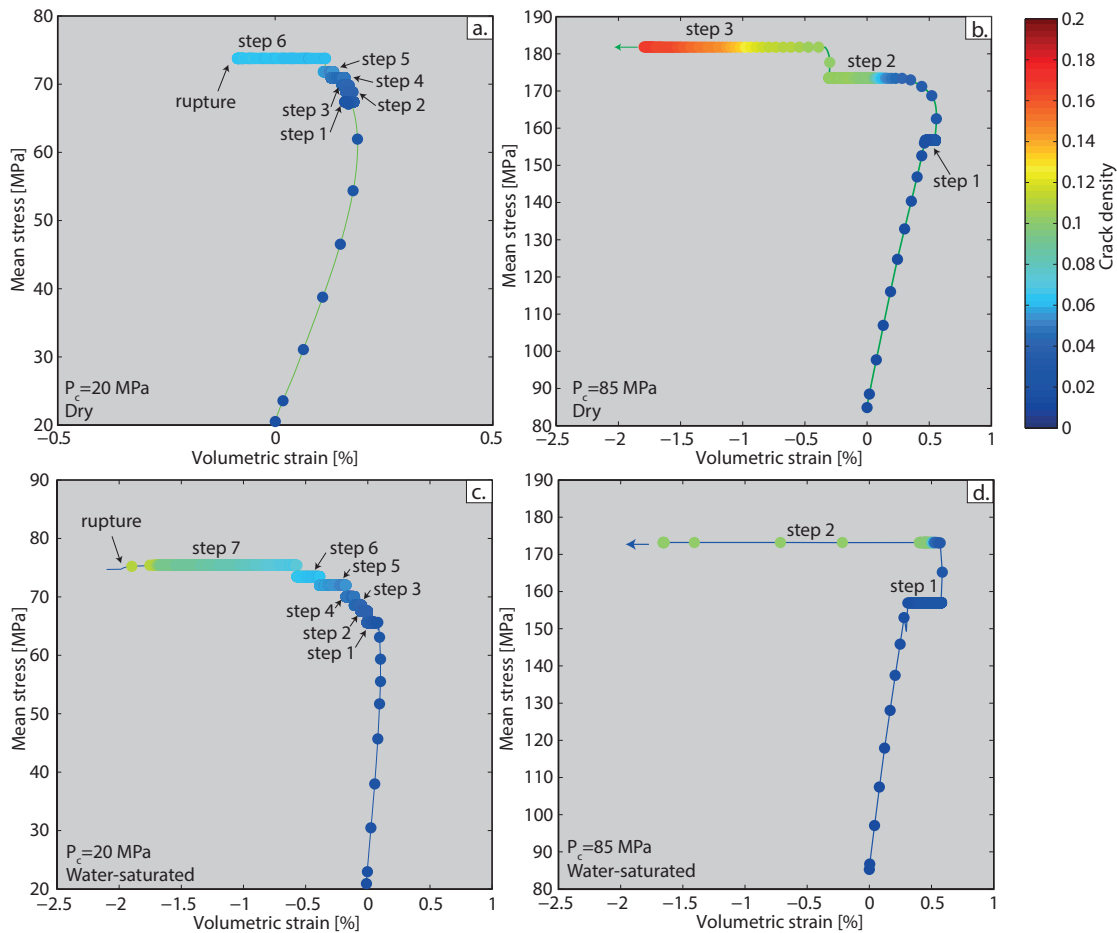


Figure 3.12 – Volumetric strain is plotted as a function of mean stress for experiments performed at $P_c = 20$ MPa in dry conditions (a), $P_c = 85$ MPa in dry conditions (b), at $P_c = 20$ MPa in water-saturated conditions (c), and at $P_c = 85$ MPa in water-saturated conditions (d). Crack density evolution is superimposed for each experiment. The color caption is given on the right.

In the semibrittle regime, the crack density evolution is different from that in the brittle regime. Taking the experiment conducted at $P_c = 85$ MPa in dry conditions as an example, its initial crack density was 0.015 before triaxial loading (Figures 4.9 c and 3.6 d). Crack density increased up to 0.03 at the beginning of the first step and remained constant during this step. A similar behaviour was observed for the next steps: the crack density remained constant at i) 0.1 during the second step; ii) 0.017 during steps 3,4 and 5. It reached 0.19 when the piston reached its maximum displacement during step 6. For $P_c = 85$ MPa, no clear difference of crack density evolutions was observed between experiments performed in dry and water-saturated

conditions (Figure 4.9 b and d).

3.3.4 Strain rates during stress-stepping creep experiments

At constant differential stress, axial strain rate presents (1) a deceleration (primary creep) before (2) an inflexion point (secondary creep) and potentially (3) an acceleration (tertiary creep) leading to the macroscopic failure (e.g. Figure 3.7 and [Scholz \(1968\)](#), [Lockner \(1993\)](#)). The minimum (secondary) strain rate is usually considered to investigate the strain rate sensitivity to stress. Beside applied stress, the strain rate during secondary creep is also sensitive to temperature and pore fluid ([Atkinson, 1984](#), [Meredith & Atkinson, 1985](#), [Heap et al., 2009b, 2011](#), [Mallet et al., 2015](#)). Investigating temperature sensitivity is beyond the scope of this paper and we only consider applied stress sensitivity, in dry and water-saturated conditions.

Let us first focus on experiments conducted in dry conditions. The axial strain rates during secondary creep (from now on referred to as "axial secondary strain rate") of steps that do not lead to failure by tertiary creep are plotted as a function of applied differential stress in Figure 3.13 (a). Secondary strain rates depend on the differential stress as:

$$\dot{\epsilon} \propto \exp(Q/\sigma^*), \quad (3.1)$$

where σ^* is an activation stress found to be $\sigma^* = 38$ MPa (see the dashed black line). However, at $P_c = 20$ MPa, the secondary strain rate presents very little variation with differential stress, which makes it hard to conclude for this confining pressure. Furthermore, only one point is available for $P_c = 35$, thus the trend observed (dashed-black line) is mainly reliable for $P_c \geq 50$ MPa.

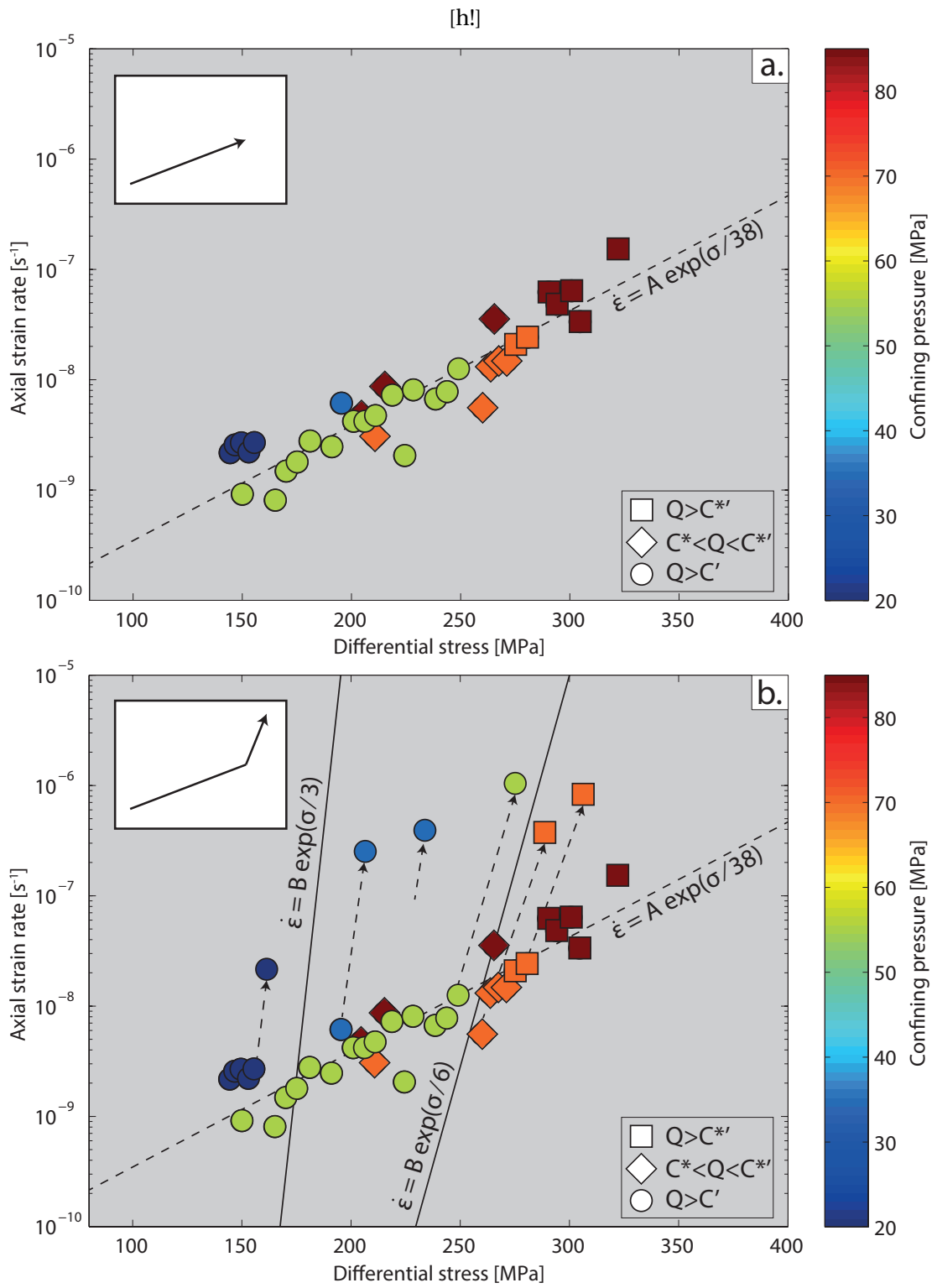
In addition to the data plotted in Figure 3.13 a, it is possible to add the strain rates during secondary obtained during the last step of each experiment. The result is given in Figure 3.13 b. These last data do not follow the previous trend (Figure 3.13 b). Another activation stress is found between the two last stress steps for each experiment (dashed arrows in Figure 3.13 b). For experiments conducted at $P_c \leq 50$ MPa (brittle regime), the second activation stress is found to be $\sigma^* = 3$ MPa. For experiments performed at $P_c \geq 50$ MPa (semibrittle regime), the second activation stress is found to be $\sigma^* = 6$ MPa, higher than that in the brittle regime. The occurrence of different activation stresses probably means different micromechanisms, which

Chapter 3. Brittle and semibrittle creep in a carbonate rock

will be discussed in more details in section 3.4.1.

Secondary strain rates in water-saturated conditions are systematically higher than that in dry conditions (Figure 3.14 b). This is especially true for confining pressures below 85 MPa. Secondary strain rates during steps that do not lead to failure have the same activation stress in water-saturated conditions as in dry conditions but are shifted by a constant value.

Figure 3.13 (*following page*) – (a) Strain rates during secondary creep are plotted versus applied differential stress for stress steps, in dry conditions. In this figure, the secondary strain rate obtained during the last step of each experiment is not plotted. Symbols represent the stress state compared to stress states at the onset of dilatancy C' , onset of inelastic compaction C^* and post-yield dilatancy C^{*} inferred from constant strain rate experiments. Note that constant strain rate experiment done at $P_c = 55$ MPa had a brittle behaviour but as the corresponding constant stress experiments are semibrittle, the symbol were modified to semibrittle ones. The colors represent the confining pressure. The color caption is given on the right. The inset shows the schematic variation of the secondary strain rate variation as a function of the differential stress. (b) Same as (a) for all stress steps, including the secondary creep measured during the last step of each experiment.



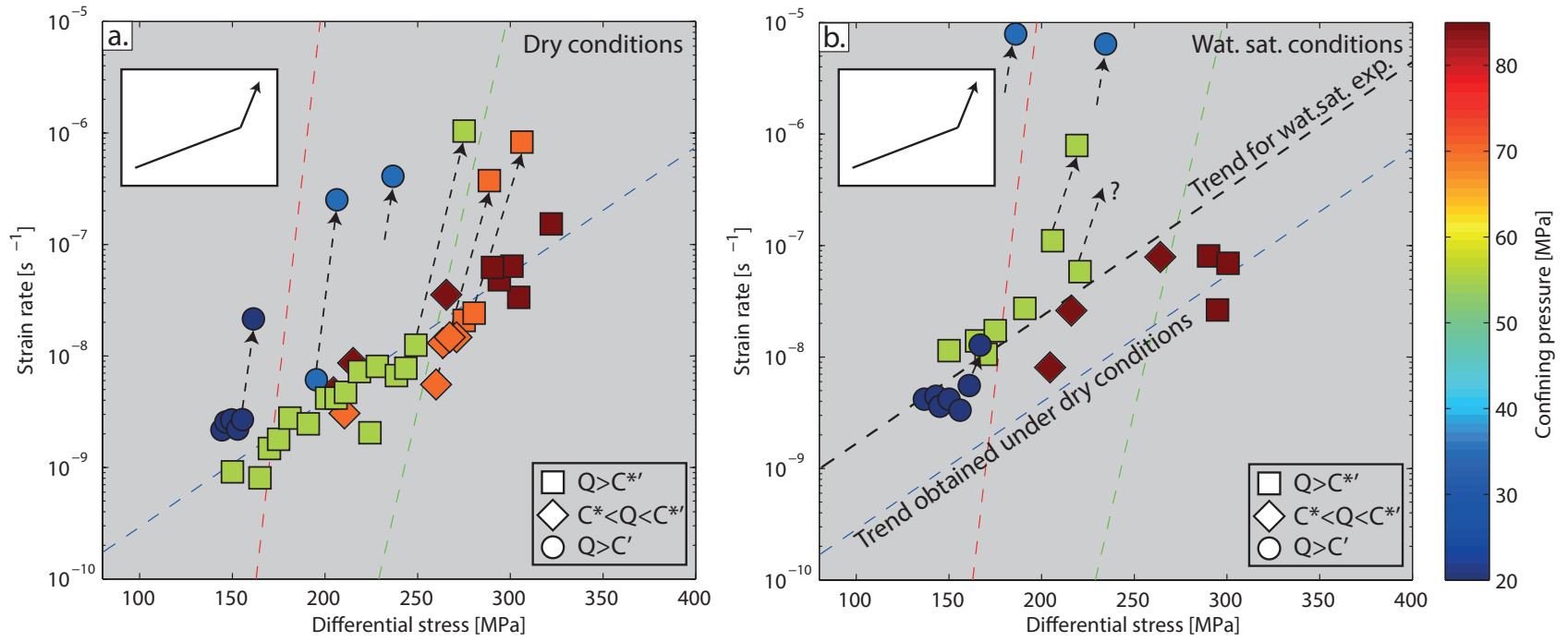


Figure 3.14 – (a) Same as Figure 3.13 b. (b) Strain rate during secondary creep is plotted versus differential stress for creep experiments conducted in water-saturated conditions.

3.4 Discussion

3.4.1 Mechanisms of deformation

The mechanical behaviour of brittle solids at constant stress has been investigated in various materials and under a wide range of P-T conditions (Orowan, 1944, Charles, 1958, Wiederhorn & Bolz, 1970, Atkinson, 1984, Meredith & Atkinson, 1985, Lockner, 1993, Heap et al., 2009b, 2011, Mallet et al., 2015). At low temperature and pressure, brittle materials deform because of subcritical crack growth (Holder et al., 2001). In the brittle regime, Brantut et al. (2014b) showed that creep may occur in a porous water-saturated limestone as consequence of (1) the development of cracks and (2) mechanisms of pressure solution.

At elevated pressure (150-300 MPa) and over a wide range of temperature (20°C-900°C), calcite deformed at constant strain rate accommodates strain by dislocation glide, cross-slip, and climb; mechanical twinning; self-diffusion; and grain boundary sliding (Heard & Raleigh, 1972, Rutter, 1974b, Schmid, 1976). At intermediate confining pressures and room temperature, Fredrich et al. (1989) showed that Carrara marble (deformed at confining pressures in the range 30-300 MPa) exhibits a semibrittle behaviour. This semibrittle deformation involves macroscopically distributed deformation by both crystal plasticity (twinning and dislocation glide) and microcracking (Fredrich et al., 1989, Evans et al., 1990, Dresen & Evans, 1993). In low porosity Carrara marble, the semibrittle regime leads to dilatancy (Fredrich et al., 1989). In more porous limestones, micromechanisms such as plastic pore collapse, grain crushing and dislocation pile-ups induce a transient inelastic compaction ultimately switching to dilatancy (Baud et al., 2000a, Vajdova et al., 2004, Dautriat et al., 2011b). To our knowledge, no previous experimental studies have been conducted on the mechanical behaviour of limestones at constant stress in the semibrittle field. The question raised here is : What are the mechanisms responsible for inelastic strain in Tavel limestone deformed under creep conditions and confining pressures ranging across the brittle-semibrittle (ductile) transition?

Brittle creep

During constant stress steps conducted at $P_c \leq 35$ MPa, the axial deformation is coupled to dilatancy. Meanwhile, elastic wave velocities decrease and crack density increases (Figures

3.6 b, 3.7, 3.11 and 4.9 a). Furthermore, shear bands inclined to the vertical axis are observed in samples post-mortem. The decrease of elastic wave velocity suggests that deformation is due to crack propagation. As in other materials, cracks in calcite can propagate in mode I below the critical stress level corresponding to the critical value of the stress intensity factor K_{IC} (Henry et al., 1977, Dunning et al., 1994, Royne et al., 2008, Rostom et al., 2013), which is typical of brittle creep (Johnson & Paris, 1968, Scholz, 1968, Kranz, 1979, Atkinson, 1984, Heap et al., 2009b, Mallet et al., 2015).

Comparing secondary strain rates obtained during experiments at $P_c \leq 35$ MPa with those obtained on other brittle materials (on Darley Dale, Bentheim and Crab Orchard sandstones by Heap et al. (2009a), on Mount Etna volcano basalt by Heap et al. (2011), and on Purbeck limestone in the brittle regime by Brantut et al. (2014b), all strain rates are highly dependent on the confining pressure and the applied differential stress (Figure 3.15 a). In order to overcome problems of samples variability among others, Brantut et al. (2014b) offset the stress scale by the differential stress reached when deformation becomes dominated by dilatancy, denoted D' and corresponding to the minimum in the porosity change curve. They found that the minimum strain rate could be described by:

$$\min\{\dot{\epsilon}\} \propto \exp((Q - Q_{D'})/\sigma^*), \quad (3.2)$$

where $Q_{D'}$ is the differential stress reached when deformation becomes dominated by dilatancy and σ^* is an activation stress. At a given confining pressure, $Q_{D'}$ is a constant and this expression gives an activation stress equivalent to the one in equation 3.1. Brantut et al. (2014b) found an activation stress of 1.9 MPa for Purbeck limestone deformed in the brittle regime. This activation stress is very close to $\sigma^* = 3$ MPa found for the experiment performed at $P_c = 20$ MPa after the few first stress steps during, which not much deformation is occurring, and for the experiment performed at $P_c = 35$ MPa (blue dots in Figure 3.15).

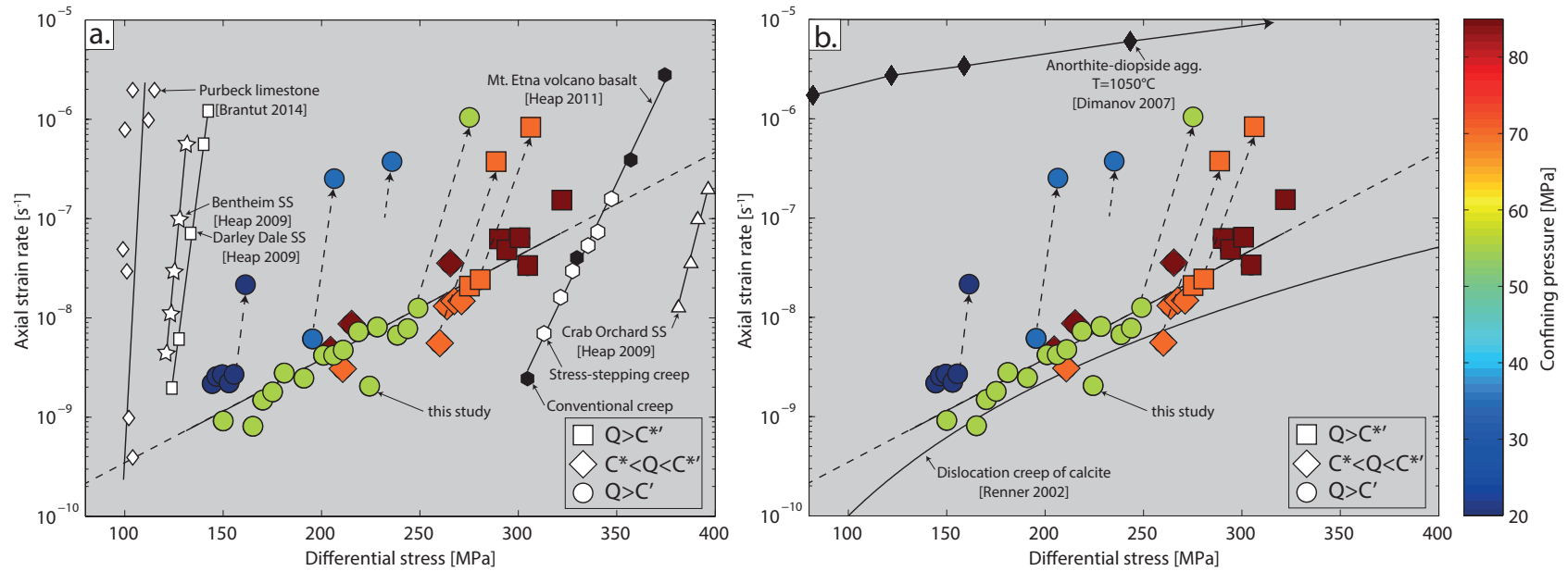


Figure 3.15 – (a) Strain rate during secondary creep versus applied differential stress, for experiments conducted in dry conditions. Symbols and colors have the same meaning as in Figure 3.13. Strain rates during secondary creep obtained by [Heap et al. \(2009a\)](#) on Darley Dale, Bentheim and Crab Orchard sandstones, by [Heap et al. \(2011\)](#) on Mount Etna volcano basalt, and by [Brantut et al. \(2014b\)](#) on Purbeck limestone below the brittle-ductile transition, are also shown for reference.

(b) Same as (a). Strain rates during secondary creep obtained by [Dimanov et al. \(2007\)](#) on anorthite-diopside aggregates at $T = 1050^{\circ}C$ are also shown for reference. Fitting their data on dislocation creep in calcite at temperatures in the range 873-1073 K, [Renner et al. \(2002\)](#) found a stress sensitivity of strain rate $n = 4.5$. This evolution of strain rate during secondary creep for such a stress sensitivity is shown for reference.

As subcritical crack growth is thermally activated, crack length l growth can be described by the law proposed by [Darot & Gueguen \(1986\)](#) and [Mallet et al. \(2015\)](#):

$$\frac{dl}{dt} = \dot{l}_0 e^{\left(\frac{-E_a}{kT}\right)} e^{\left[\frac{s}{kT} \left(\frac{\kappa_T^2}{E_0} - 2\gamma\right)\right]}, \quad (3.3)$$

where \dot{l}_0 is a characteristic crack speed dependant on the interatomic distance and atomic vibration frequency, E_a is an activation energy, s is an elementary surface, k and T have the usual meanings, E_0 is Young's modulus of the crack-free material, and γ is the surface energy. Is this crack growth law in agreement with the secondary strain rate evolution law observed for Tavel limestone? [Mallet et al. \(2015\)](#) showed that brittle creep can be modelled adequately by the propagation of wing cracks. During steps, stresses remain constant and thus, to a first approximation, non-interacting opening mode fractures (which is the case for wing cracks) should keep a constant mean aspect ratio ([Pollard & Segall, 1987](#)), which means that wing opening is proportional to its length. Yet, the opening of the wing is broadly proportional to the sliding on the pre-existing flaw. Thus, from geometrical considerations, the axial strain due to a wing propagation is proportional to the crack length. Finally, the axial strain rate (described by equation 3.1) should be broadly proportional to equation 3.3, which can explain the exponential form of equation 3.1.

Brittle creep observed in our experiment is qualitatively similar in dry and water-saturated conditions, although strains, strain rates and inverted crack densities are higher in water-saturated conditions. These observations suggest that water promotes crack propagation in calcite, as already observed in Solnhofen limestone by [Rutter \(1974b\)](#). Equation 3.3 indicates that crack growth depends on the material surface energy. As surface energy decreases in presence of water ([de Leeuw & Parker, 1997](#), [Røyne et al., 2011, 2015](#)), crack propagation is enhanced in water-saturated conditions ([Rutter, 1972](#), [Røyne et al., 2011, 2015](#)). As suggested by [Brantut et al. \(2014a\)](#), pressure solution may also take place but (i) the water used in this study is at equilibrium with calcite, (ii) the higher crack densities inverted in water-saturated conditions than in dry ones seem to strengthen the idea of enhanced crack propagation with water, and (iii) pressure solution processes are slow at low temperatures and mainly enhanced by high temperatures (e.g. [Rutter & Mainprice, 1978](#)).

Semibrittle creep

During constant stress steps conducted at $P_c \geq 55$ MPa, the axial deformation is coupled either to inelastic compaction (during the first stress step of each experiment) or to dilatancy (during the following ones), which is typical of a semibrittle behaviour (Evans et al., 1990). Yet, the evolution of secondary strain rate as a function of differential stress follow the same trend during compactant and dilatant steps (Figures 3.8, 3.9, 3.10 and 3.13), suggesting a same controlling mechanism during all steps excepted the last step leading to failure in tertiary creep; which is discussed later. Several types of phenomena can account for inelastic compaction and pore collapse: (i) crystal plasticity processes (e.g. Curran & Carroll, 1979, Baud et al., 2000a), (ii) Hertzian fracture processes inducing grain crushing (e.g. Zhang et al., 1990) with eventual localization (e.g. Fortin et al., 2005), (iii) grain rotations and rearrangements (e.g. Tsai et al., 2003, Karner et al., 2003), (iv) chemical reactions (e.g. Niemeijer et al., 2002, Zhang et al., 2010, Croize et al., 2013). All these phenomena can lead to time-dependent deformation under constant stress (e.g. Dusseault & Fordham, 1993, Zhang & Spiers, 2005, Heap et al., 2015).

Let us first focus on stress steps that do not lead to failure in tertiary creep (last step of each experiment). During these steps, the secondary strain rate evolution as a function of stress follows equation 3.1 with an activation stress of 38 MPa, far higher than that observed during brittle creep (Heap et al., 2009a, 2011, Brantut et al., 2014b). Moreover, Heap et al. (2015) recently presented compacting creep experiments during formation of compaction bands on Bleurswiller sandstone, where the main mechanism is grain crushing (Fortin et al., 2005). They found an activation stress $\sigma^* = 4.1$ MPa, far below the measured semibrittle activation stress of 38 MPa. Since the stress sensitivity of subcritical crack growth (or, more precisely, the sensitivity of crack growth rate on the energy release rate at the crack tip) in calcite is close to that of quartz (Røyne et al., 2011, Darot & Gueguen, 1986), this difference implies that grain crushing is likely not to occur during our semibrittle creep steps. Finally, Fortin et al. (2005, 2007) showed that elastic wave velocities decrease during compaction due to grain crushing. As elastic wave velocities remain constant during secondary creep of the first steps of each semibrittle experiment (e.g. Figures 3.8 d and 3.9 d), time-dependent deformation during semibrittle creep steps is not due to Hertzian fracture processes caused by subcritical crack

growth and inducing grain crushing.

Processes such as mechanical twinning and dislocation slips are observed in the semibrittle deformation of carbonate rocks during constant strain rate deformation (Fredrich et al., 1989, Baud et al., 2000a). Baud et al. (2000a) found that their data on the onset of inelastic compaction were in reasonable agreement with Curran & Carroll (1979)'s plastic pore collapse model. Can crystal plasticity explain our semibrittle creep data? To discuss the kinetics of dislocation flow, the most common paradigm is the power law creep equation (Kohlstedt et al., 1995):

$$\dot{\epsilon} = \dot{\epsilon}_0 \sigma^n \exp\left(-\frac{Q}{RT}\right), \quad (3.4)$$

where $\dot{\epsilon}_0$ is a pre-exponential factor, σ is the differential stress, n is an index of the stress sensitivity of strain rate, Q is the activation energy for creep, and RT is the standard Boltzmann term (Kohlstedt et al., 1995). Fitting their data on dislocation creep in calcite at temperatures in the range 873-1073 K, Renner et al. (2002) found a stress sensitivity of strain rate $n = 4.5$. The evolution of strain rate using equation 3.4 for a stress sensitivity of 4.5 is shown in Figure 3.15. The strain rate variation with differential stress is close to what is observed during our semibrittle creep experiments. Furthermore, Dimanov et al. (2007) deformed an anorthite-diopside aggregate at $T = 1050^\circ\text{C}$ at constant stress. They interpreted their deformation as due to dislocations and found a stress sensitivity of strain rate n in the range 0.6-1.2. Part of their data is shown in Figure 3.15. Although (i) temperatures are much higher and (ii) the material used is not calcite, strain rate during their plastic deformation has a dependence to differential stress which is similar to what is observed during our semibrittle creep experiments. These observations suggest that (1) crystal plasticity is occurring during semibrittle creep experiments conducted on Tavel limestone at room temperature on steps that do not lead to failure and (2) it controls the axial strain rate during compactant and dilatant steps. A question remains: During semibrittle creep experiments, inelastic compaction is transient and when differential stress is increased compaction switches to dilatancy, thus if dilatancy is not controlled by subcritical crack growth, what is it due to?

After some inelastic compaction, at the critical stress state C^* , dilatancy due to crack nucleation and/or propagation becomes dominant compared to inelastic compaction. At room temperature, in calcite, dislocation and twin slips are blocked at grain boundaries, which

creates an internal stress sufficient to nucleate new cracks (e.g. [Smith & Barnby, 1967](#), [Evans et al., 1980](#), [Wong, 1990](#)) and leading to dilatancy ([Baud et al., 2000a](#)). In the semibrittle regime, [Stroh's \[1957\]](#) model for microcrack nucleation due to dislocation pileup is commonly used to analyse the transition from shear-enhanced compaction to dilatant cataclastic flow ([Baud et al., 2000a](#)). We suggest that (1) dilatancy during semibrittle steps that do not lead to failure is due to crack nucleation and/or propagation due to pileups, and (2) crack nucleation and/or growth are controlled by pileups and are thus not much sensitive to stress, which explains that secondary strain rates during compacting and dilatant stress step follow the same trend (Figure 3.13). A question remains: Why do elastic wave velocities remain constant -meaning the crack density is constant- during some dilatant secondary creep deformation whereas they decrease during primary creep during the same stress step (e.g. stress step presented in Figure 3.9)?

Assuming a penny shape crack geometry, crack porosity is given by ([Schubnel et al., 2006a](#)):

$$\phi^{crack} = 2\pi\rho_c\xi, \quad (3.5)$$

where ξ is the crack aspect ratio defined as $\xi = w/(2c)$, where w is the crack aperture and c the crack radius. If dilatancy takes place at constant crack density ρ_c , it implies that ξ is increasing. However, equation (3) in [Wong \(1990\)](#) indicates that the aspect ratio of a crack nucleated by a pile-up cannot increase without crack propagation. A possible explanation for these observations is that crack propagation is actually occurring but crack blunting leads to constant inverted crack densities because faces of the cracks remain in contact. Then, if crack propagation is faster than crack blunting characteristic time, it leads to a decrease of elastic wave velocities, as observed during some steps (Figure 3.10 d).

Let us now focus on the last stress step of each experiment, leading to failure in tertiary creep. A break in slop can be observed in the $\sigma-\dot{\epsilon}_{ax}$ plot between the two last stress steps (Figure 3.13 b). Between these two steps, the activation stress is 6 MPa (Figure 3.13 b). This activation stress is much lower than that observed during the previous steps (38 MPa), suggesting that another predominant mechanisms is taking place. This activation stress is slightly higher than that observed in brittle creep. We suggest that crack propagation becomes dominant and is not controlled by pileups any further because interactions become dominant. The difference of activation stress compared to purely brittle experiments could be due to the

several mechanisms occurring simultaneously such as crack propagation and simultaneous crystal plasticity at crack tips. The decrease of elastic wave velocities during the last stress steps at high confining pressure indicates that cracks are nucleating and/or propagating have a lower characteristic time than crack blunting.

Qualitatively similar semibrittle behaviour is observed in dry and water-saturated conditions, excepted that strain rate during secondary creep are slightly higher in water-saturated conditions than in dry ones. The slight enhancement of the strain rates can be explained by the fact that water promotes crack propagation nucleated by pile-ups in calcite.

3.4.2 Comparison with constant strain rate experiments

As discussed in the previous section, similar mechanisms account for deformation in constant stress and constant strain rate experiments. However, the loading path is known to have an influence on failure (Wong et al., 1992). In the brittle regime, dilatancy at a given stress is higher for CSE than for CSRE and strains at failure are greater in CSE than in CSRE in both dry and water-saturated conditions (Figure 3.16 a and b). This enhancement of dilatancy is explained by the subcritical crack propagation, which is likely to induce more diffuse damage (Mallet et al., 2015). The same level of stress does not necessarily correspond to the same stage of damage evolution (Baud & Meredith, 1997).

In the semibrittle regime, in dry and water-saturated conditions, both constant stress and constant strain rate experiments undergo an elastic compaction followed by an inelastic compaction ultimately switching to dilatancy (Figures 3.16 c and d). Let us for example focus on the experiments conducted at $P_c = 85$ MPa. In these experiments, strain gages reach their maximum deformation before failure, excepted for the CSRE done under dry conditions. However, dilatancy when gages break in constant stress experiments are already higher than dilatancy at failure for the CSE (Figure 3.16 c). As observed on brittle experiments, this enhancement of dilatancy is explained by the more diffuse damage in CSE compared to CSRE.

At the beginning of each experiment and between constant stress steps, the samples were loaded at an imposed constant axial strain rate ($\approx 10^{-5}\text{s}^{-1}$) equal to that used in constant strain rate experiments. The mechanical behaviour and elastic wave velocities during loading before each constant stress step presented is given in Figures 3.7 (a), (b) and (c) and in Figures

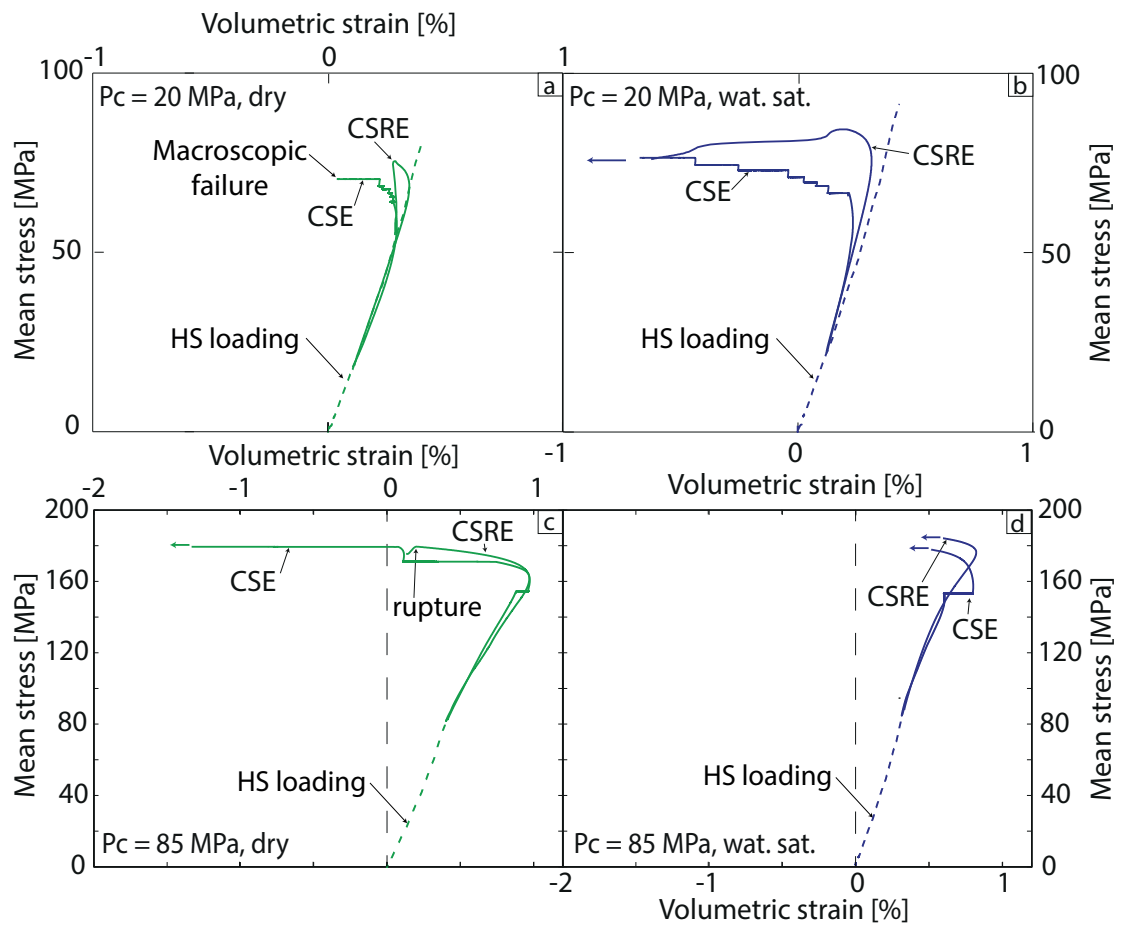


Figure 3.16 – (a) Mean stress is plotted as a function of volumetric strain for a Constant Strain Rate Experiment (CSRE), and a Constant Stress Experiment (CSE) conducted in dry conditions at $P_c = 20$ MPa. The dashed line corresponds to a hydrostatic loading. (b) Same as (a) for water-saturated conditions. (c) Mean stress is plotted versus volumetric strain curves for a CSR and a CS experiment performed at a confining pressure of 85 MPa in dry conditions. (d) Same as (c) for water saturated experiments. Horizontal arrows mean that volumetric strain is not recorded any further because strain gages reached their maximum displacement.

3.8, 3.9, and 3.10 (a) and (b). During loading before brittle constant stress steps (Figure 3.7), the mechanical behaviour are similar to that observed during constant stress steps, and is characterized by dilatancy and a decrease of elastic wave velocities.

During semibrittle experiments, the mechanical behaviour during loadings is not always similar to that during constant stress steps. Let us focus on the experiment conducted at $P_c = 85$ MPa. Before the first compactant stress step, the loading induces an inelastic compaction with a decrease of elastic wave velocities whereas elastic wave velocities remain constant during the stress step. Thus, cracks propagate during loading but not during the stress step. Similar

conclusions can be drawn for the second constant stress step, excepted that elastic wave velocities also decrease during primary creep, which implies that crack blunting kinetic is lower than crack propagation during fast primary creep. These observations are in agreement with [Kranz \(1979\)](#) who suggested that there may be a difference in the mode of crack development between Barre granite deformation at constant stress and deformation at constant strain rate, and that it led to differences in inelastic strain and acoustic emission generated in the two test types.

Finally, observations that (1) failure occurs at a lower dilatancy during CSRE than during CSE, that (2) at $P_c = 55$ MPa CSRE are brittle whereas CSE are semibrittle and that (3) micro-mechanisms are strain-rate dependent suggest that the strain rate has a high influence on the mechanical behaviour of porous limestones and on the strain-damage relation. This is in agreement with the observations by [Sangha et al. \(1974\)](#) that the average crack length in a sandstone at peak stress decreases while the number of cracks slightly increases from the fastest ($2.5 \times 10^{-4} \text{ s}^{-1}$) to the slowest ($2.5 \times 10^{-9} \text{ s}^{-1}$) strain rate.

3.4.3 Maximum inelastic compaction

For constant strain rate and stress-stepping experiments, the maximum compaction at the onset of post-yield dilatancy C^{*} is slightly lower than 1%, far below the initial porosity value of 14.7%. Thus, we conclude that porosity is not the limiting parameter of the compaction process. It is known that in calcite deformed at low temperature, dislocations accumulate at grain joints and defects, which induces stresses sufficient to initiate cracking ([Stroh, 1954](#), [Smith & Barnby, 1967](#), [Wong, 1990](#)). The strain-rate induced by dislocation slip is ([Orowan, 1954](#)):

$$\dot{\epsilon} = d_{dis} b \langle v \rangle, \quad (3.6)$$

where d_{dis} is the dislocation density, b is their Burgers vector and $\langle v \rangle$ is their average slip speed. Integrating equation 5.3 over a characteristic grain size s , one gets: $d_{dis} = \epsilon / bs$. Taking $b = 5 \times 10^{-10}$ m ([De Bresser, 1996](#)), $s \sim 5 \times 10^{-6}$ m, and $\epsilon \sim 1\%$, it gives $d_{dis} = 4 \times 10^{12} \text{ m}^{-2}$. The estimated value of the dislocation density is comparable to observations on significantly deformed materials ([Fredrich et al., 1989](#), [Dimanov et al., 2007](#)). Following this approach, the maximum compaction at a given confining pressure seems to be limited by the grain-size and

dislocation-density rather than controlled by differential stress.

3.4.4 Stabilizing role of inelastic compaction

For experiments conducted in dry conditions, the final strain at failure increases with the confining pressure (Figure 3.17). Below the brittle-ductile transition, final axial strain increases from 0.8 % for $P_c = 20$ MPa to 2.6 % for $P_c = 55$ MPa. Beyond the brittle-ductile transition, final axial strains are much larger and lie between 3.9 % at $P_c = 70$ MPa and 10.2 % at $P_c = 85$ MPa. This discrepancy between samples below and above the brittle-ductile transition suggests that stress-strain curves are significantly affected by the occurrence of volume changes. As suggested by [Edmond & Paterson \(1972\)](#), it can be due to the work done through them by the confining pressure. Macroscopic failure is due to the localization of energy release and the development of a macro-fault. If damage is highly localized, failure will occur at a low final strain whereas the medium will be able to sustain a high damage before macroscopic failure if damage is homogeneously distributed. No significant difference in axial strain at failure is observed under water-saturated conditions, although dilatancy is enhanced in the brittle regime.

3.4.5 From case study to global concepts

Quantitative predictions of the strength of the lithosphere are based on experimentally determined constitutive equations acquired through constant strain rate experiments (e.g. [Brace & Kohlstedt, 1980](#), [Kirby, 1980](#)). In the upper portion of the lithosphere, a relation for frictional sliding is used to describe the deformation on a brittle fault (e.g. [Sibson, 1974](#), [Byerlee, 1978](#), [Chester, 1995](#)). For the deeper part of the lithosphere, power law creep equations are used to estimate the plastic flow strength (e.g. [Weertman et al., 1978](#), [Guéguen & Palciauskas, 1994](#)). Our experiments suggest that (1) mechanisms of deformation depend upon the deformation rate. Monitoring elastic wave velocities evolution can be a way to infer the mechanisms occurring and thus to infer the appropriate model for deformation. Moreover, (2) the amount of deformation that the medium is able to accommodate before failure is highly dependent on the strain rate. The deformation needed to trigger failure increases as the strain rate decreases. Our experiments emphasize the importance of the semibrittle behaviour. In this regime, a

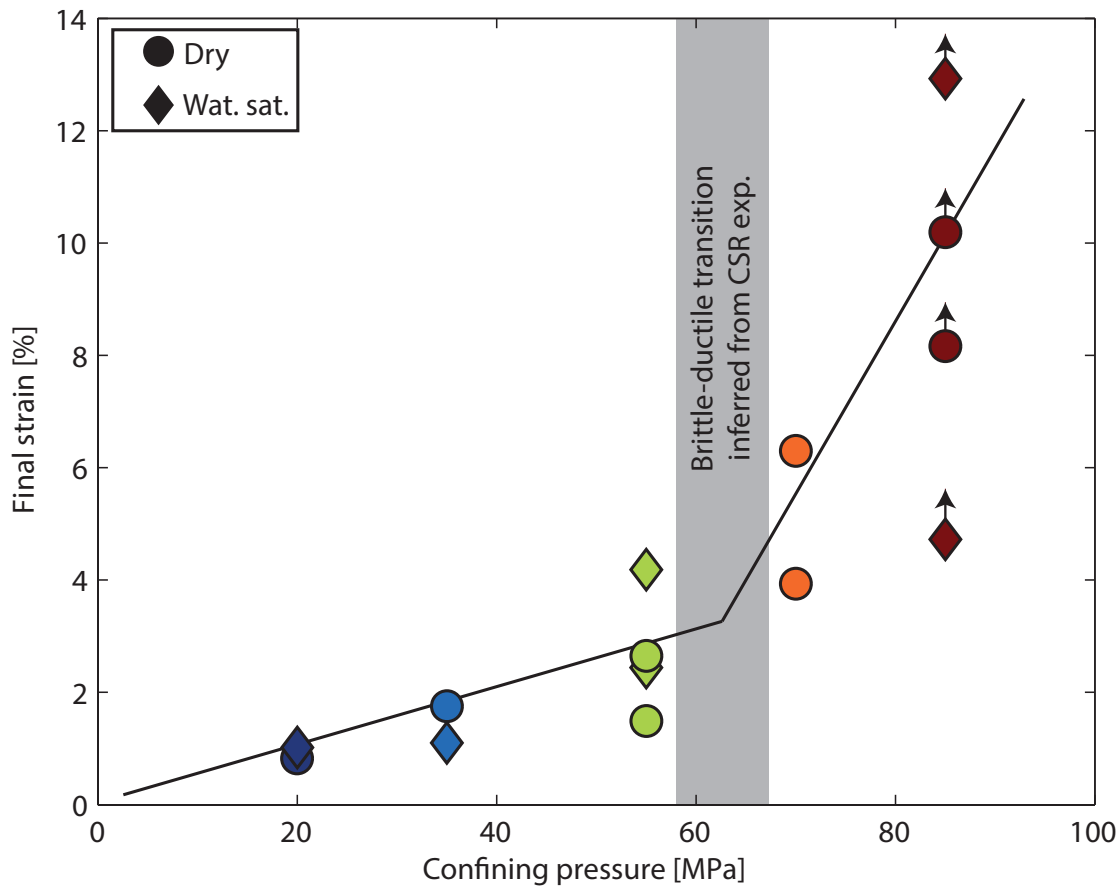


Figure 3.17 – Final strains reached at the macroscopic failure are plotted as a function of the confining pressure. Plain dots correspond to experiments performed in dry conditions and diamonds correspond to water-saturated experiments. Brown arrows mean that the piston reached its maximum displacement before failure and that the sample did not break. The shadowed area corresponds to the brittle-ductile transition inferred from the constant strain rate experiments presented in chapter 1.

mixed behaviour between plastic phenomena and brittle behaviour is observed, which make it difficult to derive a single constitutive equation based on micromechanical observations for deformation behaviour. Based on empirical considerations, Kirby (1980) estimated the pressure at the onset of semibrittle behaviour to be about 0.4 times the frictional strength. Chester (1988) suggested that the strength in the semibrittle regime is a function of the creep and the fracture strengths, which is insufficient for a constitutive equation because temperature is for example known to be an influential parameter on some micromechanisms involved (Ross & Lewis, 1989). However, our experiments suggest that the strain rate also plays a role on the transition from brittle to semibrittle behaviours. Kohlstedt et al. (1995) showed that the

transition from semibrittle deformation to plastic flow can be approximated as the stress at which the pressure exceeds the plastic flow strength. Our results suggest that there is no clear rheology change between semibrittle deformation with dominant compaction and semibrittle deformation with dominant dilatancy. Thus, the transition from a semibrittle to a fully plastic behaviour is likely to be very subtle.

Compaction is sometimes induced by the production of reservoirs (Fredrich et al., 2000). It can cause subsidence (e.g. Morton et al., 2006), which require to redesign offshore platforms, or induce seismicity (e.g. Segall, 1989b) and well failure (e.g. Bruno et al., 1992), among other problems (Nagel, 2001). A recent study by Heap et al. (2015) showed that time-dependent compaction in sandstones can be caused by the development of compaction bands. In this case, it can cause barriers for fluid flows because of the heterogeneous deformation. Our study highlights that time-dependent compaction can be induced by a semibrittle behaviour in carbonate rocks. In this case, the deformation is much more homogeneous than in the case of compaction bands development. However, inelastic compaction due to crystal plasticity can induce a dense micro-cracking and a high damage of the rock, as suggested by the high inverted crack densities. Thus, the semibrittle behaviour of limestone at constant stress should be pursued, especially focusing on the role of temperature in these processes.

3.5 Concluding summary

In this study, the mechanical behaviour at constant stress of a limestone with an initial porosity of 14.7% is investigated. Depending on the confining pressure, brittle or semibrittle creep occurs. Brittle creep leads to dilatancy and the development of a shear fault at low final strains. This is similar to what is commonly observed in brittle media. Semibrittle creep leads to inelastic compaction caused by crystal plasticity and then to dilatancy due to the nucleation of cracks by dislocation pile-ups. Water promotes crack propagation and thus dilatancy.

The strain rate during secondary is very sensitive to the stress in the brittle regime. In the semibrittle regime, two trends can be observed in the σ - $\dot{\epsilon}_{ax}$ plot. When crystal plasticity is dominant, the strain rate during secondary creep is not much stress dependent. This is equivalent to what is observed in fully plastic materials at high temperature (Dimanov et al., 2007). As failure by tertiary creep is approached, the strain rate during secondary creep

Chapter 3. Brittle and semibrittle creep in a carbonate rock

becomes much more stress-dependent.

Micromechanisms of deformation during creep are similar to those described for constant strain rate experiments. However, the stress states at which the transitions are undergone are different from those inferred from constant strain rate experiments, suggesting that the micromechanisms responsible for the deformation and the brittle-ductile transition are strain-rate dependent.

Supplements

Crack density inversion

Axial crack densities were inverted from elastic wave velocity measurements. Here, we recall the inversion process for dry solids but water-saturated solids can be considered in a similar manner (Shafiro & Kachanov, 1997). First, the effective mechanical properties of the calcite aggregate composed of the solid matrix and embedded spherical pores were obtained by inverting the velocity data obtained at $P_c = 85$ MPa hydrostatic stress. The effective Young modulus E_0 and effective Poisson's ratio ν_0 are calculated as:

$$\nu_0 = \left(\frac{1}{2} \left(\frac{V_p}{V_s} \right)^2 - 1 \right) / \left(\left(\frac{V_p}{V_s} \right)^2 - 1 \right), \quad (3.7)$$

$$E_0 = 2\rho(1 + \nu_0)V_s^2, \quad (3.8)$$

where V_p , V_s and ρ are the P-wave velocity, S-wave velocity and the rock density, respectively.

Using $V_p = 4350$ m/s, $V_s = 2350$ m/s and $\rho = 2295$ kg/m³, we get $E_0 = 32.8$ GPa, and $\nu_0 = 0.29$.

For a transverse isotropic symmetry along axis 3, the crack density tensor α is:

$$\alpha = \begin{pmatrix} \alpha_{11} & 0 & 0 \\ 0 & \alpha_{11} & 0 \\ 0 & 0 & \alpha_{33} \end{pmatrix} \quad (3.9)$$

where α_{11} is the axial crack density and α_{33} is the radial crack density. In the case of the non interacting approximation, the relation between the stiffness tensor C and α is given by (Sayers & Kachanov, 1995):

$$\left\{ \begin{array}{l} C_{11} + C_{12} = (1/E_0 + \alpha_{33})/D \\ C_{11} - C_{12} = 1/((1 + \nu_0)/E_0 + \alpha_{11}) \\ C_{33} = ((1 + \nu_0)/E_0 + \alpha_{11})/D \\ C_{44} = 1/(2(1 + \nu_0)/E_0 + \alpha_{11} + \alpha_{33}) \\ C_{13} = (\nu_0/E_0)/D \\ C_{66} = 1/(2(1 + \nu_0)/E_0 + 2\alpha_{11}) \end{array} \right. \quad (3.10)$$

where

$$D = (1/E_0 + \alpha_{33})((1 - \nu_0)/E_0 + \alpha_{11}) - 2(\nu_0/E_0)^2. \quad (3.11)$$

Chapter 3. Brittle and semibrittle creep in a carbonate rock

From the effective stiffness tensor, we calculate the wave phase velocity along the propagation angles ϕ corresponding to our sensors setup (Mavko et al., 1998):

$$V_p(\phi) = \left[(C_{11} \sin^2(\phi) + C_{33} \cos^2(\phi) + C_{44} + \sqrt{M}) / (2\rho) \right]^{1/2}, \quad (3.12)$$

$$V_p(\phi) = \left[(C_{11} \sin^2(\phi) + C_{33} \cos^2(\phi) + C_{44} - \sqrt{M}) / (2\rho) \right]^{1/2}, \quad (3.13)$$

$$V_p(\phi) = \left[(C_{66} \sin^2(\phi) + C_{44} \cos^2(\phi)) / \rho \right]^{1/2}, \quad (3.14)$$

where

$$M = ((C_{11} - C_{44}) \sin^2(\phi) - (C_{33} - C_{44}) \cos^2(\phi))^2 + ((C_{13} + C_{44}) \sin(2\phi))^2. \quad (3.15)$$

We then use a least square procedure to compare predicted synthetic data and measured velocities. The inverted axial crack density corresponds to the value leading to the minimum distance between predicted and measured velocities.

**MICROMECHANICAL CONSTITUTIVE MODEL
FOR DEFORMATION OF LIMESTONES UNDER
CONSTANT STRESS**

Ce chapitre a pour objectif de modéliser le comportement macroscopique sous contraintes constantes, en se basant sur les micro-mécanismes de déformation. Le chapitre précédent a permis de montrer que les micro-mécanismes de déformations sous contraintes constantes et pour une vitesse de déformation constante sont similaires. La différence majeure réside dans la croissance sous-critique des fissures sous contraintes constantes. De ce fait, la modélisation présentée dans le chapitre 2 est adaptée pour les conditions de déformation sous contraintes constantes, en rajoutant une loi de croissance sous-critique pour les fissures. De plus, le chargement de contrainte a une influence sur la déformation lors des paliers, et est pris en compte. Enfin, les prédictions sont finalement comparées aux résultats expérimentaux présentés dans le chapitre précédent.

Abstract

With increasing depth, the mechanical behaviour of rocks changes from a brittle to a ductile regime, which has implications for porosity changes, failure and petrophysical properties. In this study, a constitutive model for the deformation of carbonate rocks under constant stress is derived from the micro-mechanisms identified in previous experimental studies. The micro-mechanical model is based on (1) brittle crack propagation in critical and subcritical conditions, (2) a plasticity law for porous media with hardening and (3) crack nucleation due to dislocation pile-ups. The model predicts the evolution of axial and volumetric strains and crack density as a function of time during deformation at constant stress. The evolution of micro-parameters during loading is taken into account. Model predictions are compared to

Chapter 4. Micromechanical constitutive model for deformation of limestones under constant stress

experimental results from previous studies and are found to be in qualitative agreement with experimental results. However, parameters relative to the plastic behaviour are found to be different during constant strain rate loading and deformation under constant stress. This suggests that micro-physical phenomena responsible for the deformation are likely to have kinetic limits that are important to take into account, depending on the applied conditions.

4.1 Introduction

In the uppermost part of the lithosphere, rocks behave in a brittle manner and accommodate deformation through fracturing and faulting. At greater depth, due to increasing temperature and pressure, plastic deformation becomes predominant. This brittle-ductile transition in the sense of a brittle-plastic transition could be linked to the transition from seismic to aseismic behaviour of the crust (e.g., [Rutter, 1986](#)).

Carbonate rocks are of special interest because they can undergo the brittle-ductile transition at room temperature for confining pressures attainable in the laboratory (e.g., [Robertson, 1955](#), [Paterson, 1958](#)). As a matter of fact, mechanical twinning and r-, f- dislocation glides are accessible at room temperature and relatively low confining pressures in calcite (e.g., [De Bresser & Spiers, 1997](#)). The brittle-ductile transition depends on grain size and porosity (e.g., [Vajdova et al., 2004](#), [Wong & Baud, 2012](#)).

Most experiments on the mechanical behaviour and the brittle-ductile transition in carbonate rocks were based on constant strain rate experiments. However, in the brittle field, rocks can also deform and fail by static fatigue at stresses significantly lower than their short term failure strength (see [Brantut et al. \(2013\)](#) for a review). This subcritical deformation is governed by the progressive time-dependent growth of microcracks, even at constant stress (e.g. [Brantut et al., 2013](#)). In chapter 3, we showed that a semibrittle behaviour can also occur under constant stress. This brittle behaviour at low confining pressure and semibrittle behaviour at higher confining pressure are similar to the behaviours identified in constant strain rate experiments performed on the same rock (chapter 1) and modelled in chapter 2. Thus, based on the micro-mechanical model for constant strain rate deformation of limestones across the brittle-semibrittle transition (chapter 2), this study focuses on the development of a micro-mechanical model for brittle and semibrittle deformation of carbonate rocks under constant

stress, inducing very low strain rates. Model predictions are then compared to experimental results from chapter 3. The question raised is: Can the very low strain rate deformation of carbonate rocks be modelled similarly as the constant high ($\sim 10^{-5} \text{ s}^{-1}$) strain rate deformation experiments?

4.2 From constant strain rate deformation to creep

In this study, the micromechanical constitutive model developed in chapter 2 for constant strain rate deformation is used. Details on the previous derivation of the model are not recalled here. The model is adapted for the purpose of predicting the mechanical behaviour under constant stress. Under constant stress, subcritical crack growth is known to be of major importance (Brantut et al., 2013) and is thus added here. Mechanisms of pressure-solution are not considered in a first approximation; which is discussed further.

We assume that the microstructure is characterized by (1) a matrix composed of pure calcite, (2) porosity made-up of equant pores and (3) cracks. In this paper, compressive stresses and compactive strains are counted positive. The principal stresses of the remotely applied stress σ will be denoted σ_1 and σ_3 , σ_1 being the highest principal stress. The differential stress ($\sigma_1 - \sigma_3$) is denoted Q .

4.2.1 Subcritical crack growth

If the stress intensity factor K_I exceeds the fracture toughness of the solid K_{IC} , cracks propagate until K_I falls to K_{IC} . Under these critical conditions, each increment of crack advance requires an increment of load, until crack interaction becomes predominant. This kind of model alone is not appropriate for low strain rate deformation under constant stress. Cracks can also propagate in mode I below K_{IC} in a subcritical regime (Johnson & Paris, 1968, Lawn, 1993, Røyne et al., 2011). The existence of this subcritical regime makes brittle creep possible. This is why it is important to take it also into account. Empirical power laws are commonly used to describe subcritical crack propagation (Charles, 1958, Wiederhorn & Bolz, 1970, Brantut et al., 2012). A theoretically-derived law can be found in Lawn (1975), Darot & Gueguen (1986), Vanel et al. (2009), Mallet et al. (2015). Crack propagation through an elementary surface s is driven

Chapter 4. Micromechanical constitutive model for deformation of limestones under constant stress

by the energy $s(K_I^2/E_0 - 2\gamma)$, where E_0 and γ are Young's modulus and the thermodynamic surface energy, respectively (Lawn, 1975). The crack propagation rate is (Darot & Gueguen, 1986):

$$\frac{dl}{dt} = \dot{l}_0 e^{-\frac{Ea}{kT}} e^{\left[\frac{s}{kT} \left(\frac{K_I^2}{E_0} - 2\gamma\right)\right]}, \quad (4.1)$$

where T is temperature, \dot{l}_0 is a characteristic crack speed defined as the product of the inter-atomic distance b and the atomic vibration frequency ν . Using $b \simeq 10^{-8}$ m and $\nu \simeq 10^{14}$ s⁻¹ (Lawn, 1975), one gets $\dot{l}_0 \simeq b\nu \simeq 10^6$ ms⁻¹. The values of all the other parameters are discussed in the dedicated section.

4.2.2 Ductile creep law and new crack nucleation

Dislocation glide does not lead to volumetric strain but porosity changes can account for it. The same plasticity law as in chapter 2 is used for the porous medium. The plastic strain rate of the porous medium $\dot{\epsilon}^{mp}$ under the remotely applied stress σ is (chapter 2):

$$\dot{\epsilon}^{mp} = f(\sigma, \dot{\epsilon}_0, \sigma_p^i, n, M), \quad (4.2)$$

where $\dot{\epsilon}_0$ is a reference strain rate of the plasticity law, σ_p^i is the initial yield stress of the plasticity law, n is the stress sensitivity exponent of the plasticity law, and M is the strain hardening exponent. The values of these parameters are discussed further.

New crack nucleation is accounted for in the exact similar way as in chapter 2. New crack nucleation depends on (i) the microplastic strain calculated by integrating equation 4.2 over time and (ii) a pile-up density ρ_{pu} , as defined in chapter 2. The value of the pile-up density is discussed further.

4.2.3 Properties of the material

Properties used for calcite are similar to those used for constant strain rate experiments (chapter 2). Young's modulus $E_0 = 84$ GPa and a Poisson's ratio $\nu_0 = 0.28$ are taken from Homand et al. (2000). Any other set of independent elastic constants of calcite are calculated from these values. Critical stress intensity factor is $K_{IC} = 0.0217$ MPa for dry calcite (Olusunle et al., 2009). The value of the parameters used in the subcritical crack growth law are given

4.2. From constant strain rate deformation to creep

in Table 4.1 and are all based on a previous experimental study focusing on subcritical crack growth in calcite (Røyne et al., 2011).

The properties relevant to voids (porosity, crack density and crack mean size) and the matrix

Parameter	value	unit	reference
s	2.9×10^{-20}	m^2	Røyne et al. (2011)
E_a	7.6×10^{-20}	J	Røyne et al. (2011)
γ	0.32	J.m^{-2}	Røyne et al. (2011)

Table 4.1 – Summary of the value of each parameter used in the subcritical crack growth law.

(grain size) depend on the rock modelled and can be inferred from a combination of elastic wave velocity measurements (e.g. Sayers & Kachanov, 1995, Fortin et al., 2005) and SEM images (e.g. Fredrich et al., 1989, Mallet et al., 2013), as discussed in chapter 2. Burgers vector in calcite was measured at $a_0 = 6.4 \times 10^{-10}$ m (De Bresser, 1996). The reference plastic strain rate $\dot{\epsilon}_0$, the initial yield stress σ_p^i , the stress sensitivity of the plastic law n and the pile-up density ρ_{pu} are fitted to experimental data. This is discussed further. Based on internal stress considerations, the strain hardening exponent M is taken equal to 1/2.

4.2.4 Influence of previous deformation on the initial properties of calcite materials

Deformation of calcite beyond the elastic domain leads to a modification of the microstructure due to crack propagation, dislocation motions, and twinning. This is the reason why calcite can be used as a strain-gauge in field settings (Evans & Groshong, 1994), and why the study of twins can allow to rebuilt paleo stress-strain relations (see Burkhard (1993) for a review).

During laboratory stress-stepping creep experiments, the pre-loading phase and eventual previous creep steps can change the material properties at the beginning of a given creep step. During previous deformation, pre-existing cracks can grow and plasticity can take place, which induce some hardening, changes of porosity and eventually new cracks nucleation. Thus, when model predictions are compared to experimental data, the evolution of the porous medium properties with deformation needs to be taken into account to set the initial properties of the material at a given creep step. To do so, this model is coupled to the previously

Chapter 4. Micromechanical constitutive model for deformation of limestones under constant stress

presented model for constant strain rate deformation (chapter 2). The values of all the microstructural parameters (dislocation density, crack length) at the beginning of the constant stress steps are set to their values at the end of the pre-loading phase. Similarly, the value of these parameters at the beginning of each loading phase (following creep steps) are set to their values at the end of the previous creep step. Loading is accounted for by applying a constant strain rate deformation until the target differential stress is reached.

4.2.5 Sensitivity analysis of the model

The influence of porosity, initial crack length, initial crack density and friction coefficient on the deformation during loading and creep steps is explored hereafter (Figure 4.1). The value of each parameter is varied by 20% around an average value. Average values are taken equal to the set of parameters used in the comparison to white Tavel limestone and are given in Table 4.3. At a confining pressure of 20 MPa, plasticity is set to zero, which is discussed further. The imposed conditions for creep steps modelled for $P_c = 20$ MPa and $P_c = 85$ MPa are given in Tables 4.2 and 4.4, respectively.

Creep step N ^o	Q MPa	duration h
1	144	24
2	146	24
3	149	24
4	153	24
5	155	24
6	158	24

Table 4.2 – Summary of the conditions imposed for the creep steps modelled at a confining pressure of 20 MPa.

Porosity has a small influence on the model prediction (Figure 4.1 a). Volumetric strain at failure increases slightly with the decrease of initial penny-shaped crack radii (Figure 4.1 b). Initial crack density has a strong influence on the strain at a given stress level (Figure 4.1 c). At a given stress (during loading or a creep step), the volumetric strain increases with the crack

4.2. From constant strain rate deformation to creep

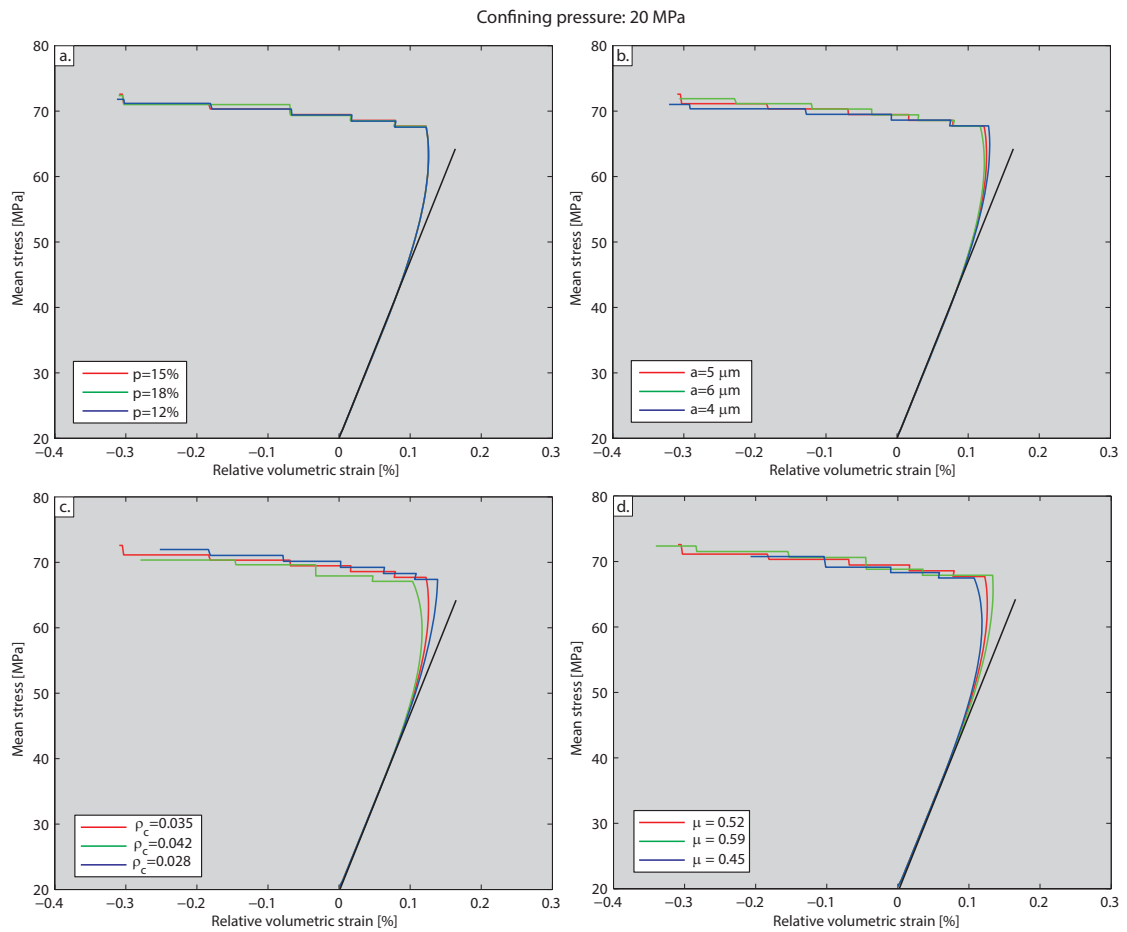


Figure 4.1 – Influence of the input parameters characterizing the brittle behaviour related to critical and subcritical crack growth. The model is run for a confining pressure of 20 MPa. Each parameter is changed by 20% around an average value. (a) Influence of a 20% variation of porosity around the average value. (b) Influence of a 20% variation of initial penny-shaped crack radii around the average value. (c) Influence of a 20% variation of the initial crack density around the average value. (d) Influence of a 20% variation of the friction coefficient on the initial penny-shaped cracks around the average value.

	porosity %	ρ_c	a μm	μ	n	$\dot{\epsilon}_0$ s^{-1}	σ_0^{init} MPa	ρ_{pu}
White Tavel limestone	15	0.035	5	0.6	3	4.5e-9	100	8e6

Table 4.3 – Microstructural parameters used to simulate the macroscopic mechanical behaviour of white Tavel limestone under constant stress.

Chapter 4. Micromechanical constitutive model for deformation of limestones under constant stress

Creep step N ^o	Q MPa	duration h
1	215	24
2	265	24
3	290	24
4	294	24
5	301	24
6	322	24

Table 4.4 – Summary of the conditions imposed for the creep steps modelled at a confining pressure of 85 MPa.

density. Finally, the friction coefficient has the most important influence (Figure 4.1 d). As shown in chapter 2, its variation has an influence on the onset of dilatancy C' during loading. Considering the entire prediction (loadings and creep steps), the volumetric strain at failure decreases with decreasing friction coefficient (Figure 4.1 d).

For the non-porous matrix, the micro-parameters that need to be fixed *a priori* are the reference plastic strain rate of the plasticity law $\dot{\epsilon}_0$, the initial yield stress of the plasticity law σ_p^i , and the stress sensitivity of the plasticity law n . For porous materials, porosity also has to be considered. The sensitivity of the model to each of these parameter is investigated thereafter. The value of each parameter is varied independently. Stress sensitivity n has a strong influence on the mechanical behaviour (Figure 4.2 a). When n is increased, inelastic compaction for a given stress level (during loading and creep steps) is enhanced. The onset of post-yield dilatancy also decreases with increasing stress sensitivity because enhanced plasticity causes the enhancement of pile-up formation and thus new crack nucleation. For constant strain rate deformation of Tavel limestone (chapter 2), we used a constant stress sensitivity $n = 3$, even though creep tests indicate that the stress exponent is actually not constant (Renner et al., 2002). The same value is used in this study. When the reference strain rate $\dot{\epsilon}_0$ is increased by 20%, volumetric strain rate increases (Figure 4.2 b) during all loading phases and creep steps. The dilatancy at failure also increases with $\dot{\epsilon}_0$. The initial yield stress σ_p^i has the exact opposite influence: when it is increased, volumetric strain tends to decrease (Figure 4.2 c). Variation of 20% of M almost has no influence (Figure 4.2 d). Finally, when the porosity is increased by 20%, volumetric strain rate increases (Figure 4.2 e) during all loading phases and creep steps.

The dilatancy at failure also increases with the porosity.

4.3 Results and discussion

4.3.1 Prediction of the strain evolution under constant stress

We investigate the model predictions for deformation under constant stress. The loading strain rate used is $\dot{\epsilon}_{ax} = 10^{-5} \text{ s}^{-1}$. This axial strain rate is the one used in experiments presented in chapter 3. The parameters used are given in Table 4.3. The imposed conditions for creep steps modelled for $P_c = 20 \text{ MPa}$ and $P_c = 85 \text{ MPa}$ are given in Tables 4.2 and 4.4, respectively.

At a confining pressure of 20 MPa, plastic flow is set to zero and thus no crack nucleation takes place (Figure 4.3). The volumetric strain versus mean stress curves first show an elastic compactant behaviour until a critical stress state denoted C' (Wong et al., 1997) beyond which the volumetric strain deviates from elasticity because of the onset of dilatancy (Figure 4.3). Following creep steps are all dilatant, until failure. Elastic and wing crack deformations are responsible for the total deformation during loadings and creep steps.

Details on the behaviour during the fourth creep step (shown by an arrow in Figure 4.4 a) are given in Figures 4.4 b, c and d. During the step, subcritical crack growth takes place and crack propagate even though the differential stress is maintained constant at a value of $Q = 153 \text{ MPa}$ (Figure 4.4 b). The crack density increases (Figure 4.4 c), which leads to a dilatant component of the volumetric strain (Figure 4.4 d). At macroscopic failure, K_I and wing crack lengths diverge. Macroscopic rupture is reached at the beginning of the sixth creep step ($Q = 158 \text{ MPa}$), a differential stress lower than that predicted at failure under constant strain rate deformation (approximately 205 MPa, see chapter 2).

At a confining pressure of 85 MPa, inelastic compaction takes place (Figure 4.5). The first two creep steps are compactant and the following ones are dilatant, until failure (Figure 4.5). During the compactant creep steps, plasticity is responsible for the major part of the total deformation. During the following dilatant creep steps, deformation due to new cracks is responsible for the major part of the total deformation. Deformation due to wing crack propagation from pre-existing flaws increases with Q but remains low compared to the deformation due to new cracks.

Chapter 4. Micromechanical constitutive model for deformation of limestones under constant stress

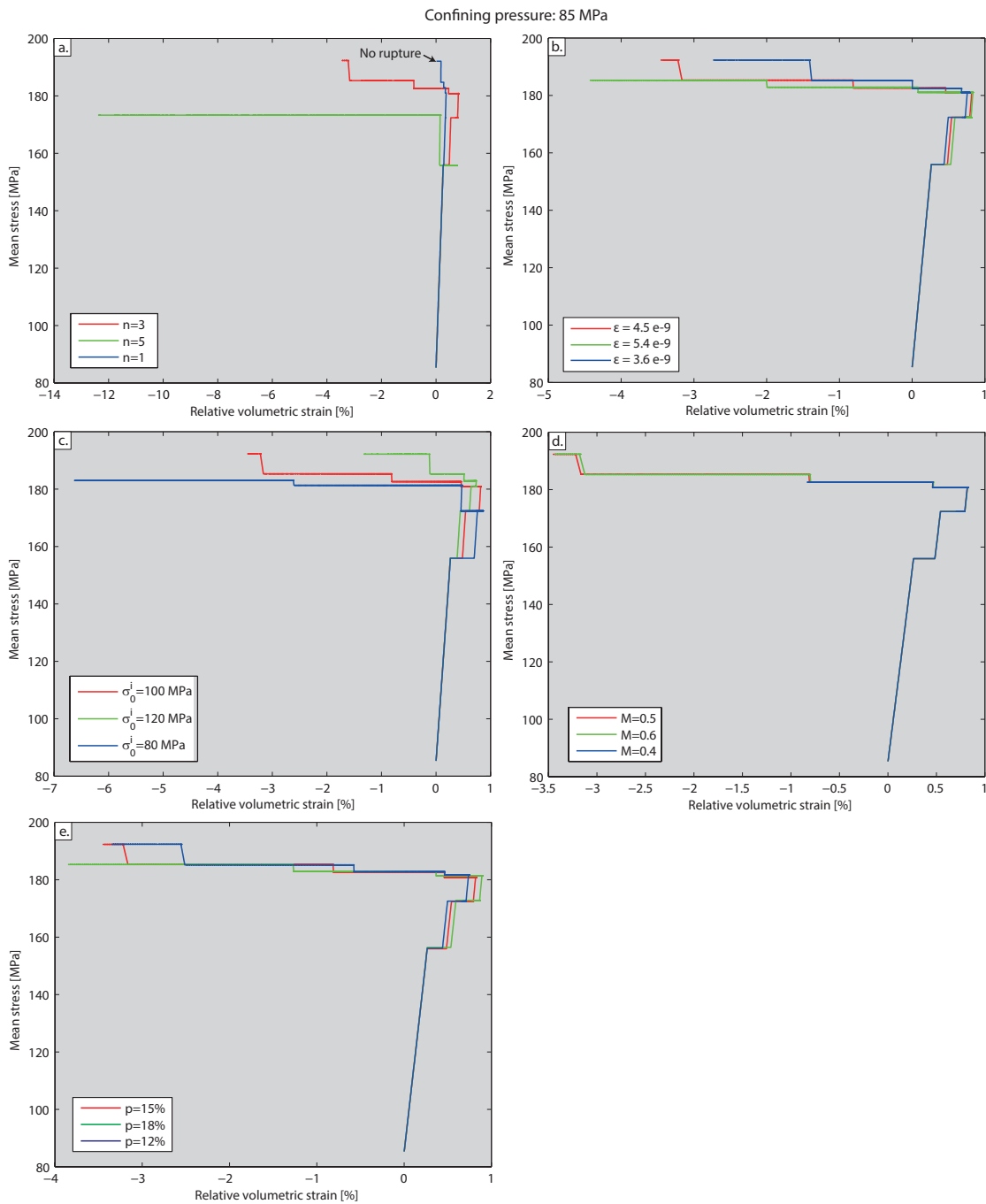


Figure 4.2 – Influence of the input parameters characterizing the ductile behaviour. The model is run for a confining pressure of 85 MPa. (a) Influence of a variation of the stress sensitivity n . (b) Influence of a 20% variation of the reference strain rate around the average value. (c) Influence of a 20% variation of the initial yield stress around the average value. (d) Influence of a 20% variation of the strain hardening exponent around the average value. Arrows represent the onset of shear enhanced compaction C^* . (e) Influence of a 20% variation of the porosity on the inelastic compaction.

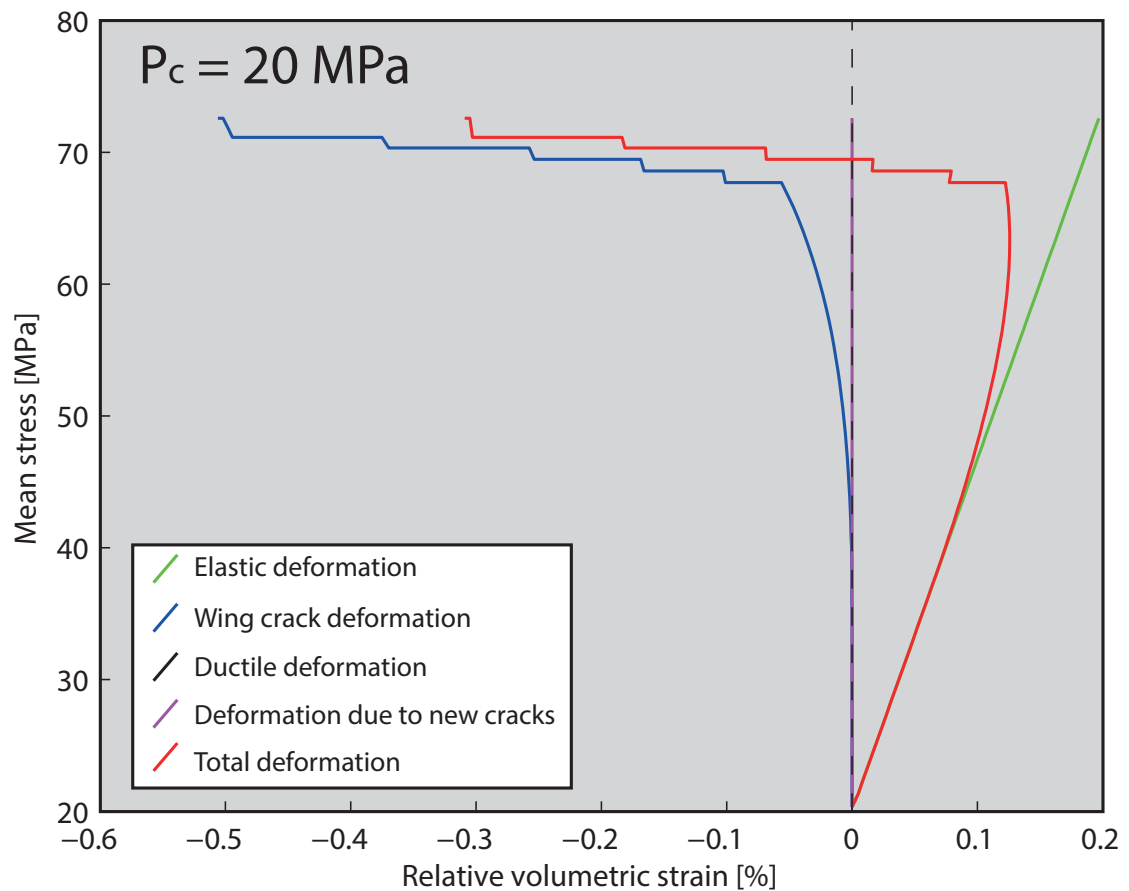


Figure 4.3 – Model predictions for volumetric strain due to all the physical phenomena taken into account for a confining pressure of 20 MPa.

Details on the behaviour during the first compactant creep step (shown by an arrow in Figure 4.6 a) are given in Figures 4.6 b to f. During the step, porosity decreases (Figure 4.6 b), dislocation density increases (Figure 4.6 c) even though the differential stress is maintained constant at a value of $Q = 215$ MPa. No crack nucleation takes place (Figure 4.6 d) but subcritical crack propagation from pre-existing flaws takes place (Figure 4.6 e). The total deformation remains compactant (Figure 4.6 f).

Details on the behaviour during the fifth (dilatant) creep step (shown by an arrow in Figure 4.7 a) are given in Figures 4.7 b to f. During the step, porosity decreases (Figure 4.7 b) and dislocation density increases (Figure 4.7 c) even though the differential stress is maintained constant at a value of $Q = 294$ MPa. Crack nucleation takes place and wedge cracks propagate (Figure 4.7 d). In parallel, subcritical crack propagation from pre-existing flaws takes place (Figure 4.7 e). The total deformation is dilatant (Figure 4.7 f).

Chapter 4. Micromechanical constitutive model for deformation of limestones under constant stress

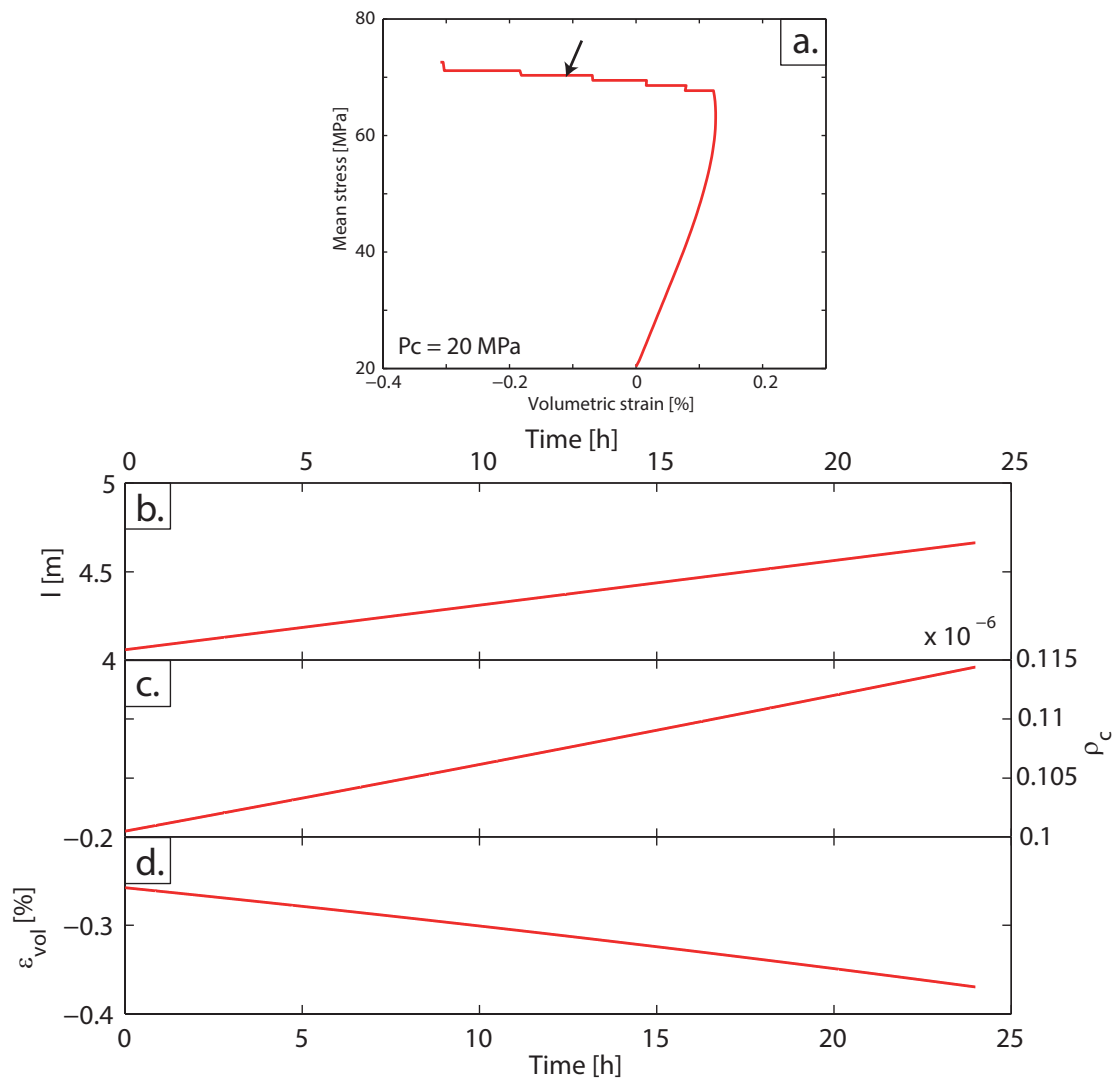


Figure 4.4 – The evolution of mechanical parameters during the fourth creep step of the experiment simulated at $P_c = 20$ MPa is examined. (a) Entire mean stress versus volumetric strain curve. The stress step considered in b, c and d is shown by an arrow. (b) Evolution of the length of wings propagating from pre-existing flaws as a function of time during the fourth stress step. (c) Evolution of the crack density during the same stress step. (d) Evolution of the volumetric strain during the same stress step.

4.3.2 Comparison with available data

Mechanical data

In chapter 3, we presented stress-stepping creep experiments on white Tavel limestone (porosity of 14.7%). At P_c strictly lower than 55 MPa, the mechanical behaviour and failure mode

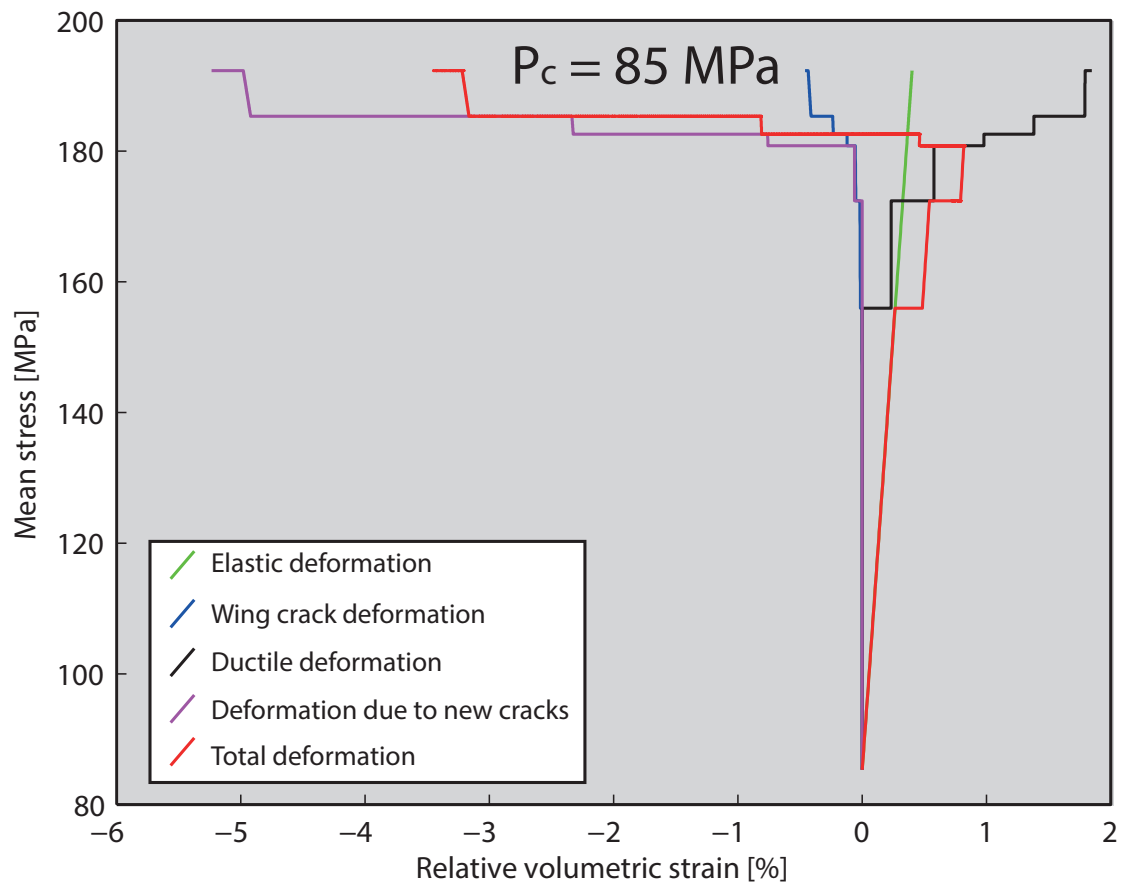


Figure 4.5 – Model predictions for volumetric strain due to all the physical phenomena taken into account for a confining pressure of 85 MPa.

are typical of brittle creep (Brantut et al., 2013). At P_c equal or higher than 55 MPa, creep is semibrittle. When the imposed differential stress is comprised between the onset of inelastic compaction C^* and the post-yield onset of dilatancy $C^{*'} (both inferred from constant strain rate deformation experiments), the volumetric strain during the creep step is compactant. When the imposed differential stress is higher than C^{*}' inferred from constant strain rate deformation experiments, the volumetric strain during the creep step is dilatant (chapter 3). Mean stress versus volumetric strain curves for a dry and a water-saturated stress-stepping creep experiment performed at $P_c = 20$ MPa are shown in Figure 4.8 a. Using parameter values reported in Table 4.3, predicted behaviour is also reported. Differential stresses and durations of the creep steps are given in Table 4.2. The reference strain rate of the plasticity law is set to zero. The predicted mechanical behaviour is brittle. During constant stress steps, dilatancy takes place because of subcritical crack growth. Predicted dilatancy is comprised between$

Chapter 4. Micromechanical constitutive model for deformation of limestones under constant stress

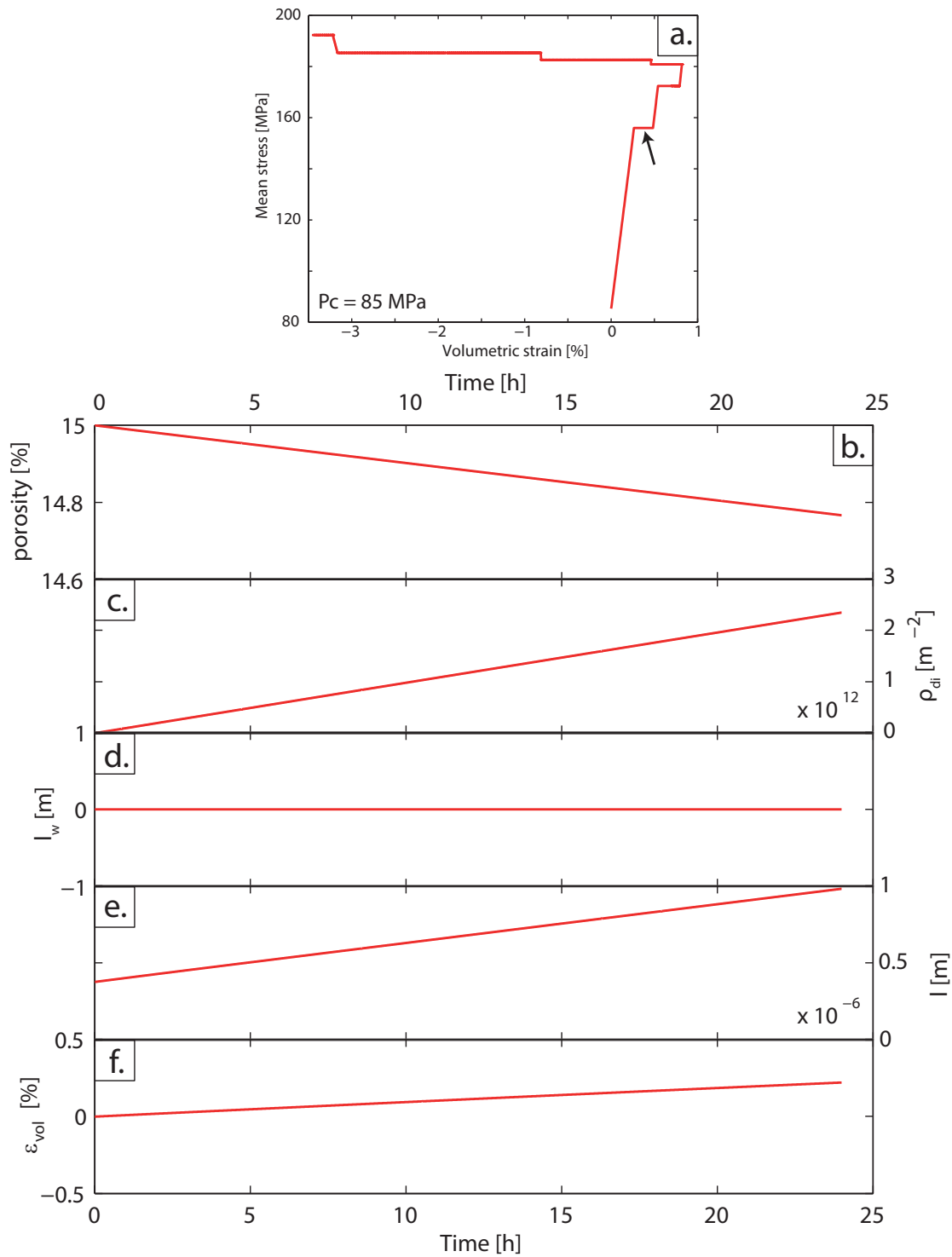


Figure 4.6 – The evolution of mechanical parameters during the first creep step of the experiment simulated at $P_c = 85$ MPa is examined. (a) Entire mean stress versus volumetric strain curve. The stress step considered in b, c, d, e and f is shown by an arrow. (b) Evolution of porosity as a function of time during the first stress step. (c) Evolution of the dislocation density during the same stress step. (d) Evolution of the nucleated wedge crack length during the same stress step. The wedge crack length remain at zero, indicating that no crack is nucleated. (e) Evolution of the length of wings propagating from pre-existing flaws during the same stress step. (f) Evolution of the volumetric strain during the same stress step.

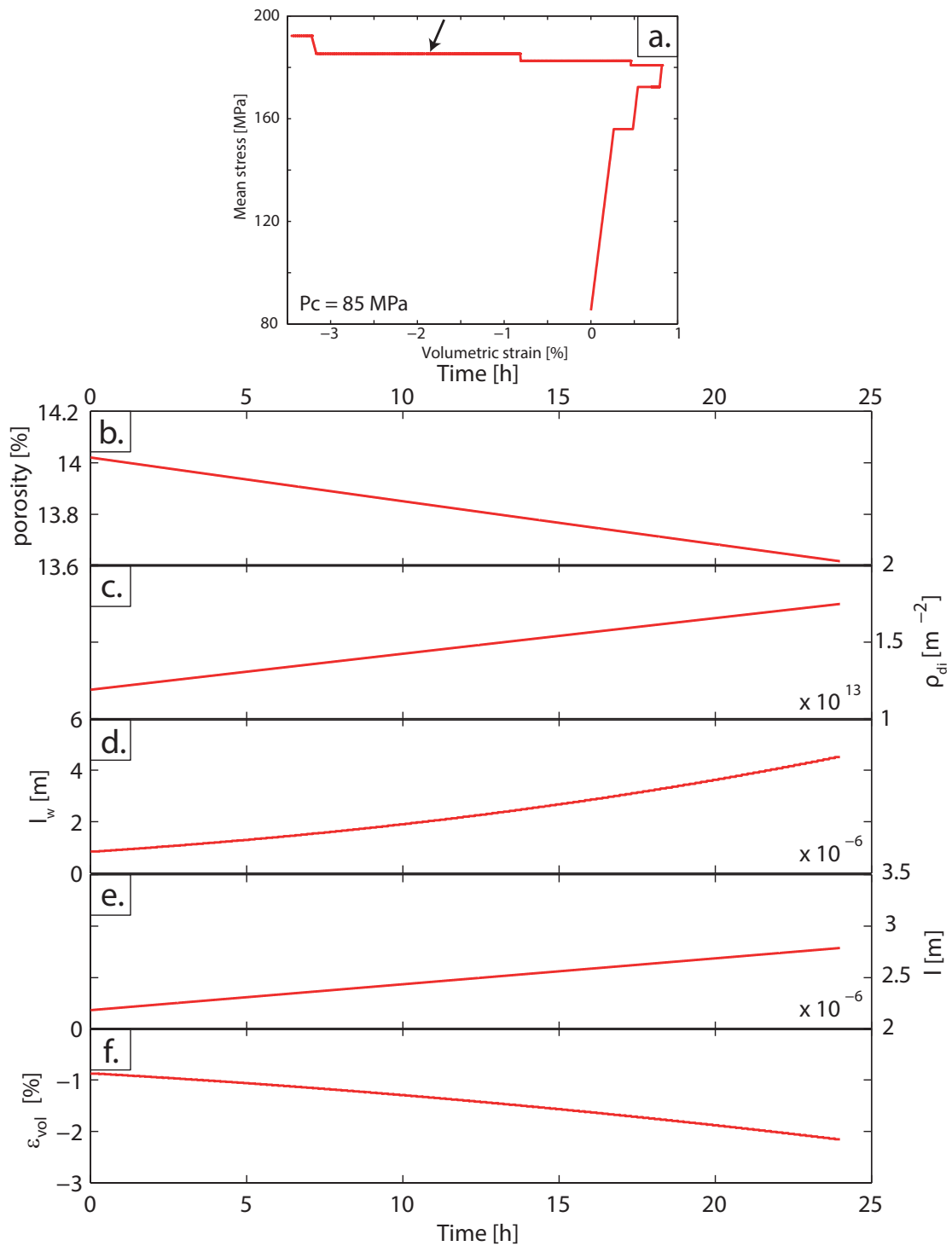


Figure 4.7 – The evolution of mechanical parameters during the fifth creep step of the experiment simulated at $P_c = 85$ MPa is examined. (a) Entire mean stress versus volumetric strain curve. The stress step considered in b, c, d, e and f is shown by an arrow. (b) Evolution of porosity as a function of time during the fifth stress step. (c) Evolution of the dislocation density during the same stress step. (d) Evolution of the nucleated wedge crack length during the same stress step. The wedge crack length increases, indicating that cracks nucleated at pile-ups propagate. (e) Evolution of the length of wings propagating from pre-existing flaws during the same stress step. (f) Evolution of the volumetric strain during the same stress step.

Chapter 4. Micromechanical constitutive model for deformation of limestones under constant stress

experimental values for dry and water-saturated conditions.

Mean stress versus volumetric strain curves for a dry and a water-saturated stress-stepping creep experiment performed at $P_c = 85$ MPa are shown in Figure 4.8 b. Experimental mean stress versus volumetric strain curves for both dry and water-saturated conditions show a first compactant creep step followed by dilatant creep steps. Using parameter values reported in Table 4.3, predicted behaviour is also reported. The predicted mechanical behaviour is semibrittle. Predicted mean stress versus volumetric strain curve is characterized by two compactant creep steps followed by dilatant steps. The general predicted behaviour is qualitatively similar to the experimentally observed behaviour but a quantitative agreement could not be found. This is discussed further.

Crack densities

During the stress-stepping creep experiments (chapter 3), we inverted elastic wave velocity data to infer axial crack densities. Inverted crack densities for experiments performed in dry conditions at confining pressures of 20 MPa and 85 MPa are shown in Figures 4.9 a and c, respectively. These experimental results are compared to model predictions in Figures 4.9 b and d, respectively. Initial crack density in the model is 0.035 (crack density inverted in chapter 1 for $P_c = 0$ MPa). Experimental and predicted crack density evolution during constant stress steps are reasonably similar for $P_c = 20$ MPa (Figures 4.9 a and b). The model reproduces the increase of crack density during the creep steps. However, predicted crack densities are higher than inverted crack densities.

Experimental and predicted crack density evolution during constant stress steps are in reasonable agreement during compactant creep steps for $P_c = 85$ MPa (Figures 4.9 c and d). During dilatant creep steps, predicted crack densities are much higher than inverted crack densities. This can be explained by the fact that crack blunting (Kinloch & Williams, 1980) is very likely to take place (as discussed in chapter 3) and this is not taken into account by the model.

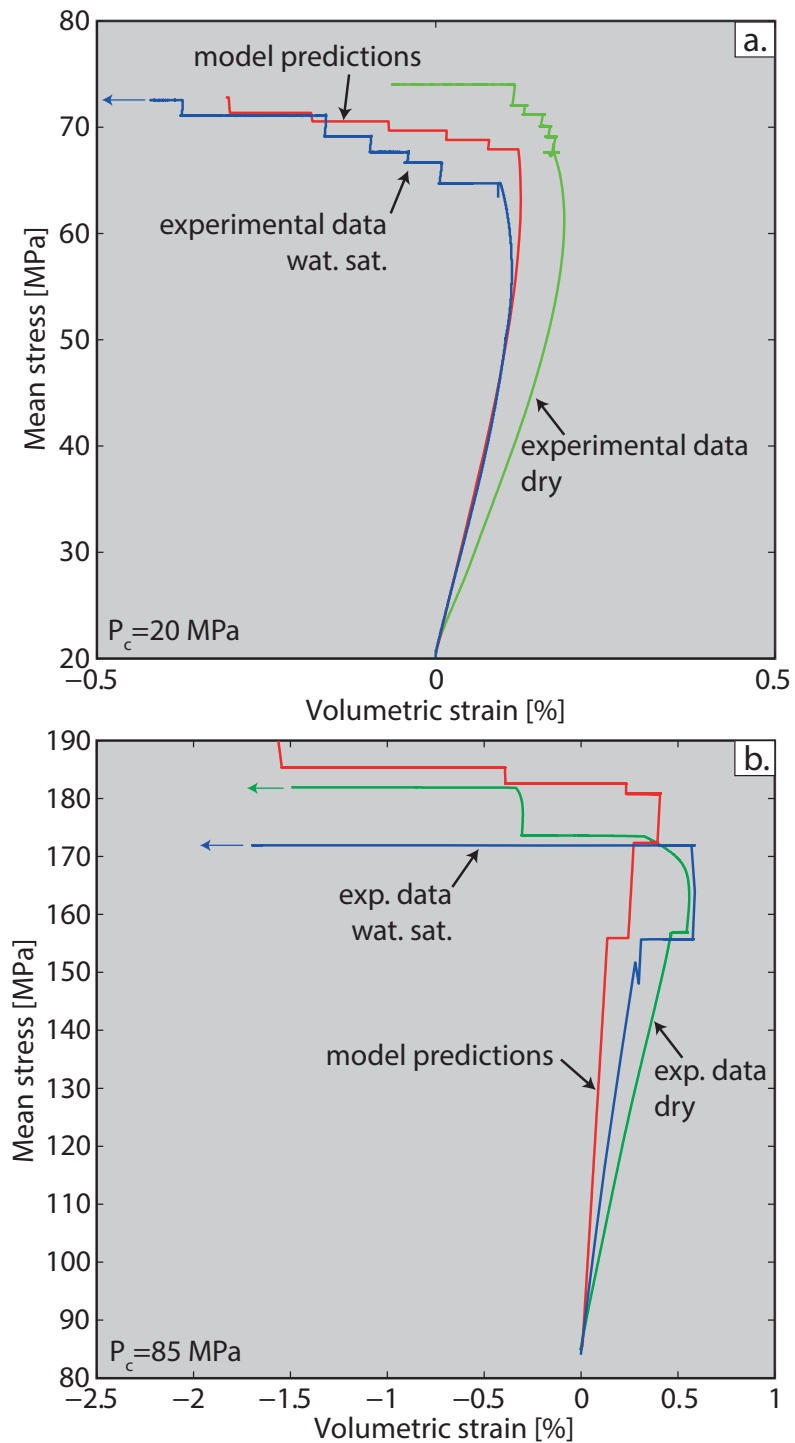


Figure 4.8 – Volumetric strain is plotted as a function of mean stress for experiments performed at $P_c = 20$ MPa in dry and water-saturated conditions and the related model predictions (a), and for experiments performed at $P_c = 85$ MPa in dry and water-saturated conditions and the related model predictions (b).

Chapter 4. Micromechanical constitutive model for deformation of limestones under constant stress

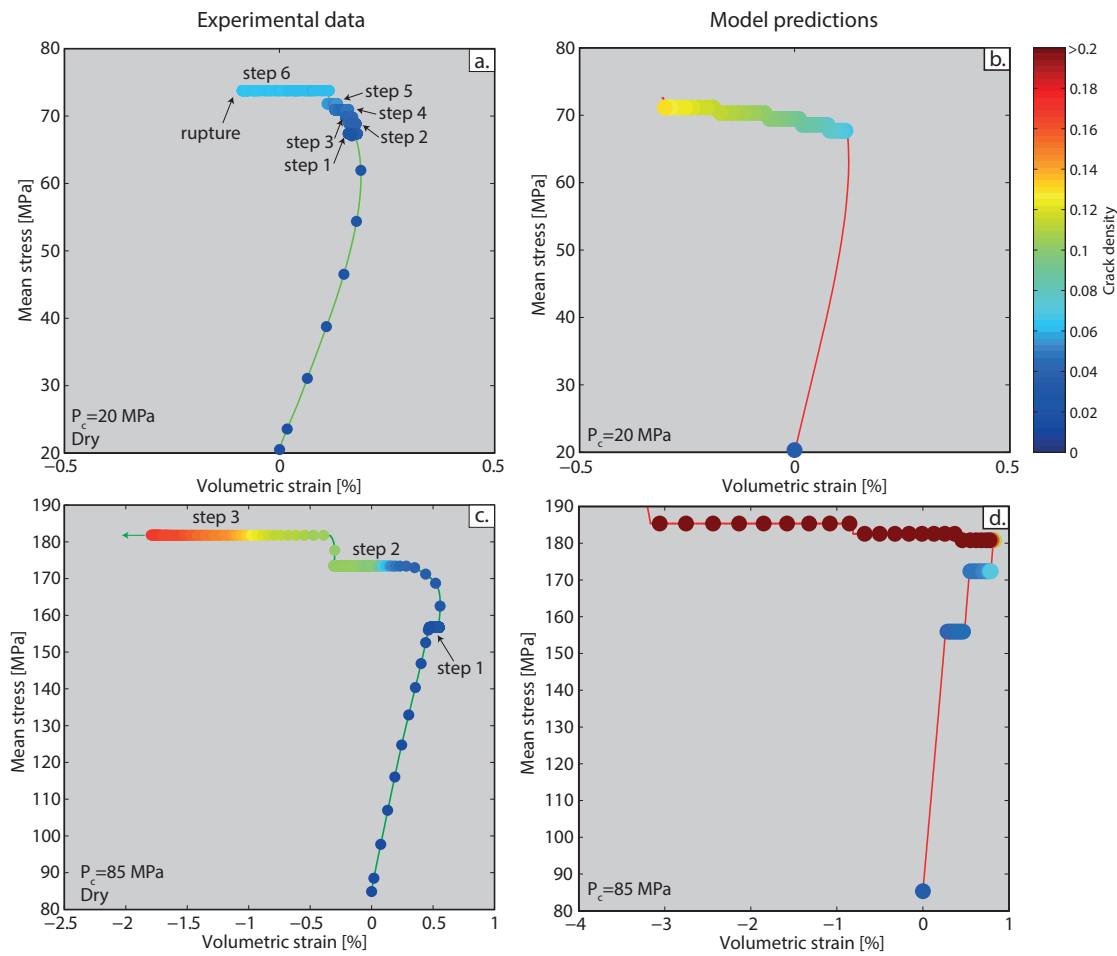


Figure 4.9 – Volumetric strain is plotted as a function of mean stress for experiments performed at $P_c = 20$ MPa in dry conditions (a), model predictions for deformation at $P_c = 20$ MPa in dry conditions (b), for experiments performed at $P_c = 85$ MPa in dry conditions (c), model predictions for deformation at $P_c = 85$ MPa in dry conditions (d). Crack density evolution is superimposed for each experiment. The color caption is given on the right.

4.3.3 Limits of the model and comparison with constant strain rate deformation

Pressure-solution was not considered in this model, which may seem odd for a model focusing on deformation of carbonate rocks under constant stress. However, the differences between dry and water-saturated stress-stepping creep experiments presented in chapter 3 could be explained by surface energy reduction in water-saturated conditions compared to dry conditions (chapter 3). Nevertheless, the water used in these experiments was at equilibrium with calcite. Considering pressure-solution would imply to add parameters to the model, it is not taken into account in this model.

A limit to the model developed in this study is that the plasticity law had to be set to zero for predictions at low confining pressure ($P_c = 20$ MPa). Contrary to the model developed in chapter 2, the parameters of the plasticity law are not constant whatever the confining pressure. Although the general predicted behaviour is qualitatively similar to the experimentally observed behaviour, a quantitative agreement could not be found with a single set of parameter values. This lack of quantitative agreement could probably be resolved with a thorough inversion of the parameters. This will be done in the future.

Physical laws taken into account in this model are the same as those considered in chapter 2 to model constant strain rate deformation of low-porosity limestones, with an additional subcritical crack growth law. Both the constant strain rate deformation and constant stress models are compared to results from experiments performed on the same block of white Tavel limestone. However, the values of the parameters relevant to the plastic law in this study (Table 4.3) are not equal to the values used to model constant strain rate deformation (chapter 2). This probably means that micro-physical phenomena responsible for the deformation are likely to have kinetic limits that are important to take into account, depending on the applied conditions. This subject of concern should be analysed more thoroughly.

4.4 Conclusion

The complex general trends of stress-strain relations of low-porosity limestones deformed in stress-stepping creep is reproduced by a model based on (1) brittle crack propagation in critical and subcritical conditions, (2) a plasticity law for porous media with hardening and (3) crack nucleation due to dislocation pile-ups. The model is based on (i) three parameters relevant to the brittle behaviour (pre-existing crack length and density, sliding coefficient on these cracks), as previously developed by [Ashby & Sammis \(1990\)](#), (ii) two parameters relevant to the micro-plastic flow in the solid non-porous medium (a reference strain rate and an initial yield stress), and (iii) a parameter characterising the density of large pile-ups. Parameters relevant to the brittle behaviour can be determined from observations of the microstructure. The parameters relevant to the ductile behaviour are fitted to experimental data.

Despite the limited number of parameters, model predictions are in qualitative agreement with experimental results presented in chapter 4. The values of the parameters relevant to

Chapter 4. Micromechanical constitutive model for deformation of limestones under constant stress

the plastic law in this study are not equal to those used in chapter 2. An explanation could be that micro-physical phenomena responsible for the deformation are likely to have kinetic limits that depend on the applied conditions. This subject of concern is partially tackled experimentally in the next chapter.

INFLUENCE OF STRAIN RATE ON DEFORMATION AND FAILURE OF A MICRITIC LIMESTONE

Ce chapitre s'intéresse à l'influence de la vitesse de déformation sur le comportement mécanique du calcaire de Tavel. L'idée est que (i) les deux premiers chapitres de ce travail ont permis d'identifier les paramètres extérieurs influençant les mécanismes de déformation dépendant principalement de la contrainte et que (ii) les chapitres 4 et 5 ont permis de discuter l'effet du temps sur ces mécanismes ainsi que d'identifier les mécanismes dépendant du temps, en s'affranchissant des variations de contrainte. En utilisant ces résultats, il devrait en toute logique être possible de prédire l'influence de la vitesse de déformation sur le comportement mécanique lors d'une déformation à vitesse contrôlée.

Dans le régime fragile, le chapitre 4 a montré que les fissures peuvent se propager à contrainte constante. Ainsi, on peut penser que la réduction de la vitesse de déformation permettrait de casser l'échantillon pour des contraintes plus faibles. Dans le régime ductile, le chapitre 4 a montré que la plasticité peut avoir lieu à contrainte constante. La logique voudrait donc que la baisse de la vitesse de déformation renforce la déformation plastique. Ces intuitions sont confrontées aux résultats expérimentaux.

Abstract

Many of the micro-mechanisms responsible for deformation in carbonate rocks (e.g. plasticity, crack growth) are time-dependent. Thus, strain rate is likely to be an influential parameter on the mechanical behaviour. In this study, the role of strain rate on deformation and rupture of a micritic limestone (white Tavel limestone, porosity 14.7%) was investigated under triaxial stresses at room temperature in dry conditions. For each sample, hydrostatic load was applied

up to the desired confining pressure (20 MPa or 85 MPa). At each confinement, three samples were deformed up to failure at strain rate of 10^{-5}s^{-1} , 10^{-6}s^{-1} and 10^{-7}s^{-1} . Our results show that in the brittle regime, the strain rate has (1) no influence on the onset of dilatancy but (2) axial strain and differential stress at rupture increase with decreasing strain rate. In the semibrittle regime, the ductile behaviour increases with decreasing strain rate.

5.1 Introduction

Carbonate rocks are crossed by faults zones and undergo seismic ruptures (e.g. [Mouslopoulou et al., 2014](#)). Yet, even at room temperature, limestones can also deform in a ductile manner, eventually not leading to failure. From laboratory experiments, it is known that deformation can either be coupled with dilatancy, leading to shear localization and therefore brittle failure ([Paterson & Wong, 2005](#)), or result from microscopic plastic flow (mechanical twinning or dislocation glide) at constant solid volume ([Turner et al., 1954](#), [Paterson, 1978](#)). In the case of limestones, dilatancy and plastic flows can combine their effects, leading to transitional behaviour named cataclastic flow, characterized by homogeneously-distributed microcracking, grain rotations and grain plasticity (twinning and dislocations), as discussed by [Fredrich et al. \(1989\)](#). Cataclastic flow can either lead to dilatancy as shown by [Fredrich et al. \(1989\)](#) on a very low porosity Carrara marble or to inelastic compaction as observed by [Baud et al. \(2000a\)](#) on Solnhofen limestone. However, compactive cataclastic flow is commonly observed to be a transient phenomenon, in that the failure mode evolves with increasing axial strain to dilatant cataclastic flow and ultimately localization in a shear band ([Baud et al., 2000a](#)).

Initial porosity, pore fluid and temperature is a key parameter that controls the deformation and failure modes of limestones ([Rutter, 1974a](#), [Vajdova et al., 2004](#)). However, given that cracks in calcite can grow in a subcritical manner ([Røyne et al., 2011](#)) and that the ductile behaviour is time-dependent, the mechanical behaviour of limestones is likely to depend on the deformation strain rate. The question we address is: How does the strain rate influence the deformation mechanisms and failure of limestones in dry conditions? We report preliminary results of conventional triaxial experiments performed at various strain rates and confining pressures of 20 MPa and 85 MPa, at 20°C in dry conditions.

5.2 Experimental material and methods

Cylindrical samples (length=80mm, diameter=40mm) of Tavel limestone, porosity 14.7% (see chapters 1 and 3), were deformed in triaxial cells installed in the Laboratoire de Géologie at the École Normale Supérieure in Paris and at the Chinese University of Hong-Kong (CUHK). Details on sample preparation can be found in chapters 1 and 3. Strains were recorded with electric resistance strain gauges (Tokyo Sokki TML type FCB 2-11, each composed of one axial and one radial gauge) directly glued on the sample. Axial displacement is also measured with one (Hong-Kong) or three (Paris) displacement transducers (DCDT) mounted between the moving piston and a fixed platen and corrected for the stiffness of the cell. DCDT and strain gauge signals have an accuracy of the order of 10^{-4} and 10^{-5} , respectively. Volumetric strain is calculated as $\varepsilon_v = \varepsilon_{ax} + 2\varepsilon_r$ where ε_{ax} and ε_r are the axial and radial strains, respectively. From now on, compressive stresses and compactive strains are counted positive. The principal stresses will be noted σ_1 and σ_3 , σ_1 being the highest principal stress.

Samples were deformed at different strain rates at confining pressures of 20 MPa and 85 MPa, in dry conditions at room temperature. Details are given in Table 5.1. Samples are loaded hydrostatically up to the desired confinement and then triaxially deformed at a fixed strain rate ranging from 10^{-7}s^{-1} to 10^{-5}s^{-1} until a stress drop indicating the macroscopic rupture occurs.

5.3 Mechanical behaviour during deformation and rupture

After a linear elastic trend, axial strain softening occurs until the differential stress reaches a peak, beyond which axial stress cannot be maintained (Figure 5.1 a). The evolution of the volumetric strain versus mean stress shows that samples compact elastically until a critical stress state marking the onset of dilatancy and denoted C' (Wong et al., 1997). Beyond C' , dilatancy increases with the differential stress. At some point denoted D' , dilatancy overcomes elastic compaction. Beyond D' , the overall volumetric remains dilatant until the peak stress is reached and differential stress drops (Figure 5.1 b). The stress state at the onset of dilatancy (C') does not present any significant variation with the strain rate whereas the stress at which dilatancy overcomes compaction D' and the peak stress increase as the strain rate decreases

Chapter 5. Influence of strain rate on deformation and failure of a micritic limestone

$N^{\circ}C$	P_{eff} (MPa)	Strain rate (s^{-1})	C' (MPa)	D' (MPa)	C^* (MPa)	$C^{*'}(MPa)$	Peak stress (MPa)	ϕ ($^{\circ}C$)
1	20	10^{-5}	50 ± 5	70.2 ± 2	-	-	77.4	-
2	20	10^{-6}	56 ± 5	78 ± 2	-	-	81.6	21
3	20	10^{-7}	50 ± 5	86.5 ± 2	-	-	87.5	20
4	85	10^{-5}	-	-	133 ± 7.5	174	184.16	19
5	85	10^{-6}	-	-	110 ± 10	160.9	183.12	25
6	85	5×10^{-7}	-	-	110 ± 20	163.2	185.63	-

Uncertainty is almost zero on these stress states.

ϕ corresponds to the angle between the vertical axis and the macroscopic fault trace in the sample.

Table 5.1 – Summary of the mechanical data obtained on white Tavel limestone. The values given for the onset of dilatancy C' , dilatancy predominance D' , onset of inelastic compaction C^* , post-yield onset of dilatancy $C^{*'}$ and peak stress are effective mean stresses.

(Figures 5.2 a and b). The axial strain at peak stress and the maximum compaction both increase as the strain rate decreases (Figures 5.2 a and b). The time of softening between the peak stress and the stress drop is proportional to the strain rate. It increases from 10 s to 750 s as the axial strain rate decreases from $10^{-5}s^{-1}$ to $10^{-7}s^{-1}$ (Figures 5.1 c and d). The stress drop does not seem to be correlated to the strain rate. The mechanical behaviour and failure are typical of the brittle regime (Paterson & Wong, 2005).

The mechanical behaviour of samples deformed at a confining pressure of 85 MPa is characterised by a compactive elastic behaviour, beyond which a transient inelastic compactive regime occurs, ultimately leading to dilatancy and eventually failure (Figure 5.3). Eventually, a peak stress is reached and a stress drop happens, denoting the localization of strain on a macroscopic fault. This behaviour is referred to as semibrittle (Fredrich et al., 1989, Evans et al., 1990). Inelastic compaction is characterised by a decrease in volume larger than that during elastic compaction; and is interpreted as shear-enhanced compaction (Baud et al., 2000a). The transition between elastic and inelastic compaction is denoted C^* and the transition between inelastic compaction and dilatancy is denoted $C^{*'}$ (Wong et al., 1997). When deformed at a confining pressure of 85 MPa, the lower the strain rate, (1) the higher the axial strain at

5.3. Mechanical behaviour during deformation and rupture

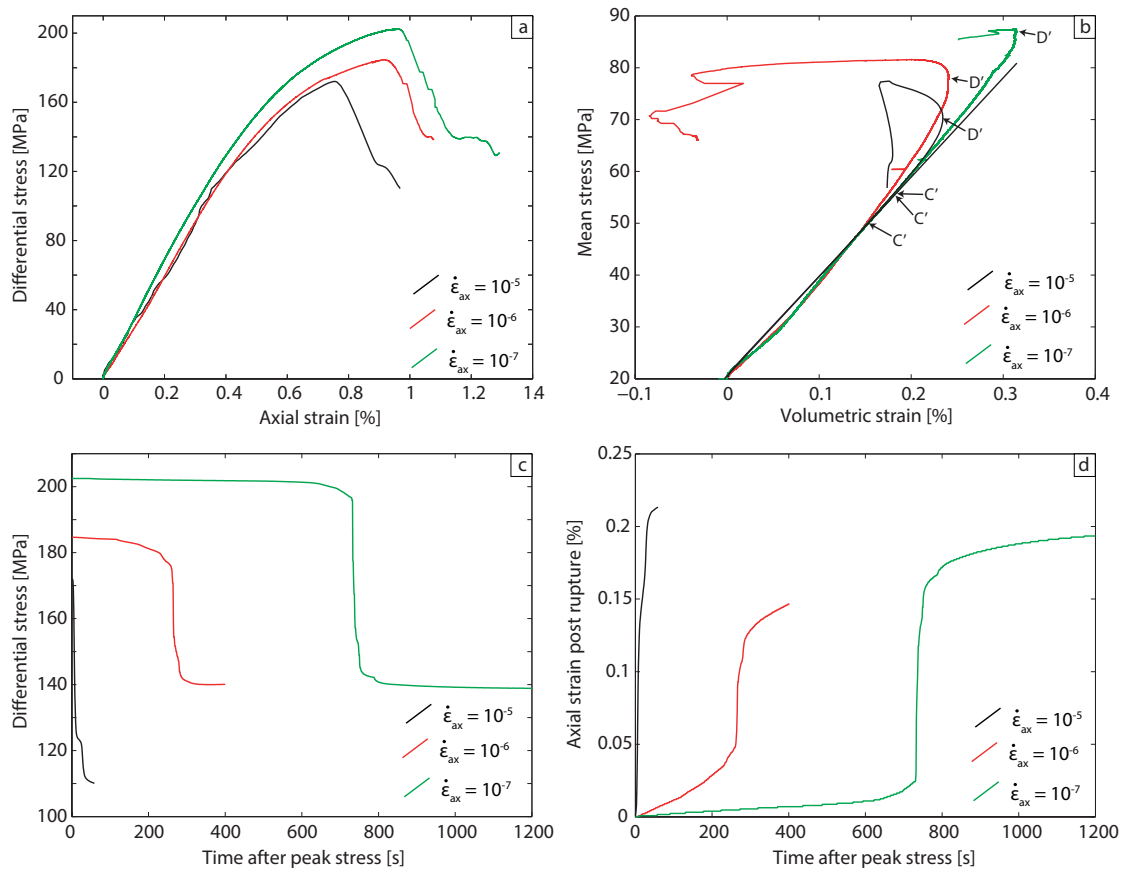


Figure 5.1 – Compilation of all mechanical data for experiments performed at different strain rates at a confining pressure of 20 MPa. (a) The differential stress is plotted as a function of axial strain. The mean stress versus volumetric strain curves for these three experiments are shown in (b). Stress states at the onset of dilatancy (C') and when dilatancy overcomes compaction (D') are given for reference. (c) Evolution of the differential stress after the peak stress is plotted versus time. (d) Evolution of the axial strain after the peak stress is plotted as a function of time.

the stress drop; (2) the smaller the stress drop; and (3) the higher dilatant volumetric strains. These observations suggest that as the strain rate is increased, it enhances the localization of the deformation in the semibrittle regime. As the strain rate decreases, the onset of inelastic compaction (C^*) and the post-yield onset of dilatancy (C^*) decrease (Figure 5.2 c). On the contrary, the peak stress remains constant.

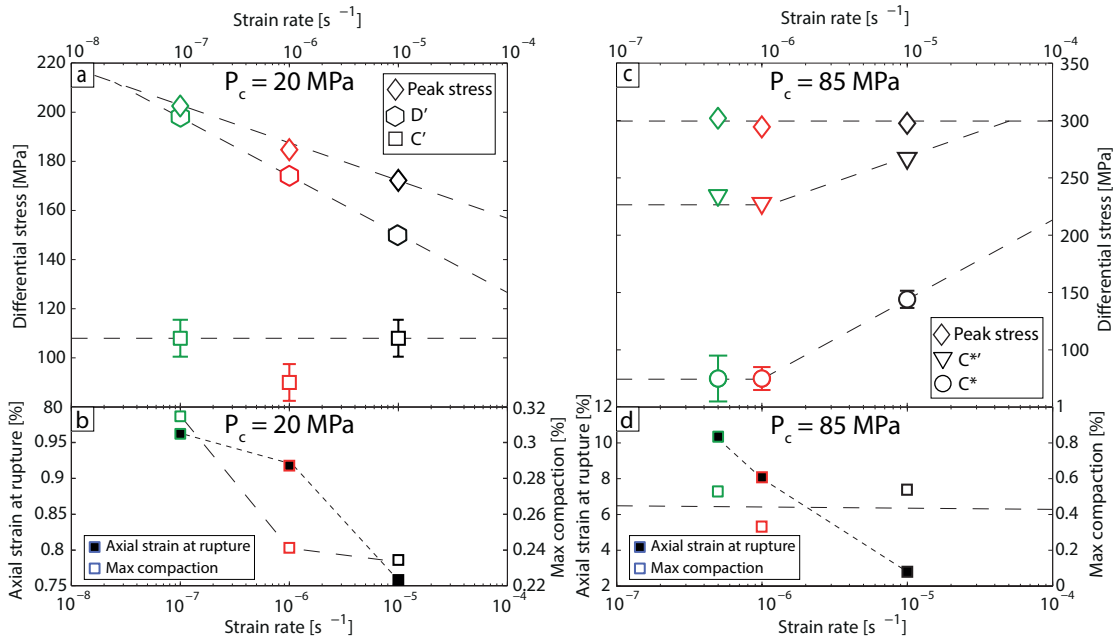


Figure 5.2 – (a) Differential stress at the onset of dilatancy (C') and peak stress are plotted as a function of the strain rate for the experiments performed at a confining pressure of 20 MPa. (b) The maximum volumetric strain and the axial strain at peak stress are plotted as a function of the strain rate for the experiments performed at a confining pressure of 20 MPa. (c) Differential stress at the onset of inelastic compaction (C^*), post-yield onset of dilatancy (C^*), and peak stress are plotted as a function of the strain rate for the experiments performed at a confining pressure of 85 MPa. (d) The maximum volumetric strain and the axial strain at peak stress are plotted as a function of the strain rate for the experiments performed at a confining pressure of 85 MPa.

5.4 Discussion

5.4.1 Effect of strain rate on deformation in the brittle regime

Ashby & Sammis (1990) developed a two-dimensional plane strain model to analyse brittle failure. Brittle faulting can be modelled by a sliding wing crack model. The end of the elastic behaviour is considered as the point of initiation of wing cracks. Assuming randomly oriented initial cracks (isotropic rock), wing cracks should preferentially initiate at an angle of $\varphi = (1/2) \tan^{-1}(1/\mu)$ to σ_1 , where μ is the frictional coefficient. The onset of inelastic strain is expected at an axial stress (e.g. Ashby & Sammis, 1990):

$$\sigma_1 = \frac{\sqrt{1+\mu^2} + \mu}{\sqrt{1+\mu^2} - \mu} \sigma_3 + \left(\frac{\sqrt{3}}{\sqrt{1+\mu^2} - \mu} \right) \frac{K_{IC}}{\sqrt{\pi a}}, \quad (5.1)$$

where a is the radius of initial cracks and K_{IC} is the fracture toughness of the material.

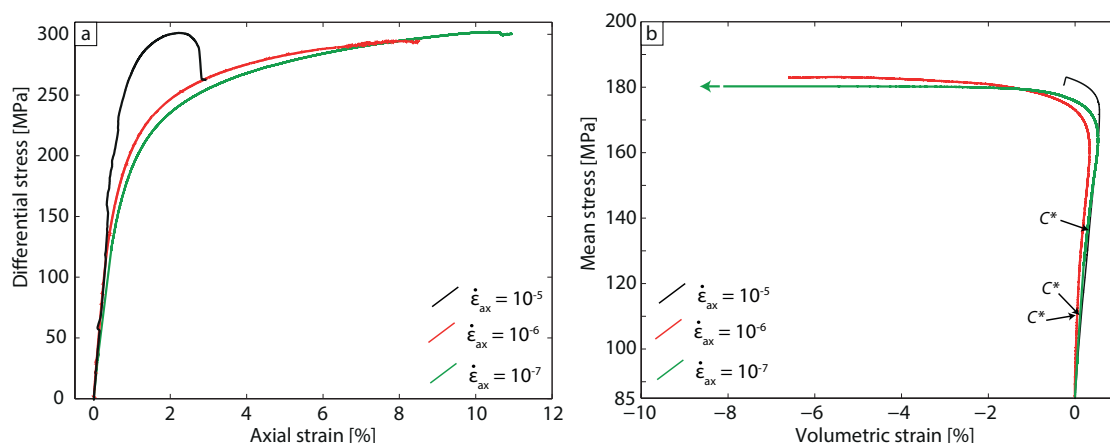


Figure 5.3 – Compilation of all mechanical data for experiments performed at different strain rates at a confining pressure of 85 MPa. (a) The differential stress is plotted versus axial strain. The mean stress versus volumetric strain curves for these three experiments are shown in (b). Note that one curve is incomplete because radial strain gages broke at high strain. Stress states at the onset of inelastic compaction (C^*) and at the post-yield onset of dilatancy (C^*) discussed in the main text are shown by arrows for reference.

According to this model, the onset of dilatancy is only material dependent, in agreement with the experimental results. To a first approximation, failure envelope is described by (Ashby & Sammis, 1990):

$$\sigma_1 = A(\mu, D_0)\sigma_3 + B(\mu, D_0)\frac{K_{IC}}{\sqrt{\pi a}}, \quad (5.2)$$

where A and B depend on μ and $D_0 = \pi(ac\cos\psi)^2 N_A$, where N_A is the number of sliding cracks of uniform orientation ψ per unit area initially present. Thus, according to this model, peak stress is only material dependent and damage due to cracks only depends on the stress state, contrary to what is experimentally observed (Figures 5.1 a,b and 5.2 a,b). As cracks in calcite can grow in a subcritical manner (Røyne et al., 2011), one could expect (1) the peak stress to decrease and (2) the dilatancy to be enhanced with decreasing strain rate. Yet, this is again opposite to experimental results (Figures 5.1 a,b and 5.2 a,b). These observations suggest that a supplementary compactant mechanism of deformation is taking place. We suggest that some plastic phenomena develop meanwhile cracks propagate. For example, it is known that mechanical twinning in calcite initiate at shear stresses as low as 30 MPa.

A question remains: Why is failure occurring at higher differential stress as strain rate is decreased? Several hypothesis can be proposed: (1) plasticity could induce some crack blunting (e.g. Kinloch & Williams, 1980) and/or (2) inelastic compaction due to plasticity could

reduce porosity and increase the contact area between grains, thus strengthening the rock.

5.4.2 Ductile deformation under different strain rates

The strain rate has a major impact on the axial and volumetric strains sustained in the semibrittle regime, but has little effect on the stress states at the onset of inelastic compaction (C^*) and post-yield onset of dilatancy (C^{**}) and no effect on the peak stress (Figures 5.3 and 5.2 c and d). This high strain-rate dependence can be explained by plastic mechanisms (Evans et al., 1990). A commonly accepted way to account for plasticity is to consider dislocation movements. The strain-rate induced by dislocation slip is (Orowan, 1954):

$$\dot{\epsilon} = d_{dis} b \langle v \rangle, \quad (5.3)$$

where d_{dis} is the dislocation density, b is their Burgers vector and $\langle v \rangle$ is their average motion velocity. At low temperature, the mean dislocation velocity is temperature and stress dependent (Meyers et al., 1999).

Why is the onset of inelastic compaction increasing with the strain rate (Figure 5.2 c)? The imposed axial strain can be decomposed as an elastic strain, a strain due to cracks, and a strain due to plastic phenomena. If cracks cannot propagate because σ_1 is lower than the critical value expressed in equation 5.1, then the imposed axial strain rate $\dot{\epsilon}_{ax}$ can be decomposed as:

$$\dot{\epsilon}_{ax} = \frac{1}{E} \dot{\sigma}_1 + \dot{\epsilon}_{pl}, \quad (5.4)$$

where E , $d\dot{\sigma}_1$, and $\dot{\epsilon}_{pl}$ are Young's modulus, the stress rate of σ_1 , and the strain rate due to plastic phenomena, respectively. At high strain rate, the initiation of new dislocations may be simply to low, thus implying that the plastic strain rate cannot account for the total strain rate imposed. It means that the imposed axial strain is at least partially accommodated elastically. From equations 5.3 and 5.4, at high strain rate, elasticity is enhanced whereas plasticity is enhanced at low strain rate. As the onset of inelastic compaction (C^*) is not very well constrained, it leads to an apparent increase of C^* with the strain rate. Beyond the onset of inelastic compaction (C^*), the part of imposed strain rate accommodated by plastic phenomena increases with decreasing strain rate, implying a higher hardening for higher strain rates. Moreover, using equation 5.3, at a given stress, a higher plastic deformation strain rate at constant temperature requires a higher dislocation density, and thus higher

5.5. Conclusions and implications of these preliminary results

hardening (Kassner, 2004). This increase of hardening with increasing strain rate is observed experimentally (Figure 5.3 a).

At room temperature, dislocations cannot be eliminated. They form pile-ups that can lead to stresses that initiate cracking (Wong, 1990). Considering that the post-yield onset of dilatancy (C^*) is mainly due to the propagation of cracks initiated by pile-ups, C^* should be related to a critical dislocation density and thus to a plastic strain. This is in agreement with the experimental observation. Indeed, the maximum compaction in the semibrittle regime (volumetric strain at C^*) is not strain-rate dependent (Figure 5.2 d).

5.5 Conclusions and implications of these preliminary results

Our preliminary experimental results suggest that deformation in dry carbonate rocks is strain-rate dependent. In the brittle regime, the deformation strain rate is observed to have no influence on the onset of dilatancy, which could only be controlled by pre-existing crack length and friction on these cracks. We suggest that even in the macroscopically brittle regime, decreasing strain-rates enhance plasticity thus leading to higher strains and peak stresses at failure. In the semibrittle regime, decreasing strain rates seem to enhance plastic phenomena. This leads to significantly higher axial strains and lower stresses at a given stress. Additional experiments should be performed to confirm or not these preliminary experiments.

CONCLUSIONS & PERSPECTIVES

Conclusions

We investigated the mechanical behaviour of a medium porosity limestone ($\phi = 14.7\%$) deformed at constant strain rate and under constant stress. The influence of water as pore fluid and temperature were examined during constant strain rate deformation (chapter 1); and the influence of water is examined during constant stress steps (chapter 3). Experimental results were then modelled taking into account the micromechanisms experimentally identified (chapters 2 and 4). Finally, the influence of strain rate is investigated in chapter 5.

During constant strain rate deformation experiments (chapter 1), the mechanical behaviour depends on the confining pressure. At low confining pressure, the behaviour is typical of a brittle behaviour characterized by an elastic compactant behaviour until a critical stress state denoted C' (Wong et al., 1997) beyond which the volumetric strain deviates from linear elasticity (onset of dilatancy). Finally, the differential stress reaches a peak, beyond which strain softening is taking place as a consequence of crack propagation and development of a macro-fault. At higher confining pressure, the mechanical behaviour is semibrittle and characterised by an elastic compaction, beyond which an inelastic compactive regime takes place after a transition denoted C^* (Wong et al., 1997). This inelastic compaction is characterised by a decrease in volume larger than the elastic one and is referred to as shear-enhanced compaction (Wong et al., 1997). However, inelastic compaction is a transient phenomenon, in that the volumetric strain evolves with increasing strain to dilatancy beyond a critical state denoted C^{*} (Wong et al., 1997). At C^{*} , dilatancy overcomes compaction. Water has a weakening effect on the onset of dilatancy in the brittle regime but no measurable influence on the peak strength. Temperature decreases the confining pressure at which the brittle-semibrittle transition is observed.

A constitutive model for the deformation of carbonate rocks under constant strain rate is

Conclusions & Perspectives

derived (chapter 2). This micromechanical constitutive model aims at predicting the macroscopic behaviour based on micromechanisms. In this model, the microstructure is assumed to be characterized by (1) a matrix composed of pure calcite, (2) porosity made-up of equant pores and (3) cracks, which is described by (i) a crack density and (ii) a crack mean size. Deformation is calculated taking into account (1) brittle crack propagation modelled by wing crack propagation, (2) a plasticity law for porous media with hardening and (3) crack nucleation due to dislocation pile-ups. The model predicts stress-strain relations and crack density evolution during deformation. Model predictions are compared to experimental results from a previous study and results presented in chapter 1, and are found to be in close agreement with experimental results. This suggests that micro-physical phenomena responsible for the deformation are sufficiently well captured by the model.

The mechanical behaviour under constant stress is then examined experimentally (chapter 3). As observed during constant strain rate experiments, the mechanical behaviour during constant stress steps depends on the confining pressure. At low confining pressure, volumetric strain shows dilatancy, ultimately leading to failure. This is equivalent to the creep mechanisms observed in brittle media such as glass, granite, basalt or sandstones. At higher confining pressures, semi-brittle creep is characterized by inelastic compaction and constant elastic wave velocities during the first stress step, due to crystal plasticity. During the following stress steps, dilatancy is occurring due to crack nucleation induced by local stresses caused by dislocation pile-ups. However, the evolution of secondary strain rate as a function of differential stress are similar during compactant and dilatant stress steps, excepted between the two last stress steps during which we observe an acceleration of the deformation rate. This acceleration is explained by the interaction of newly created cracks. The micromechanisms are similar to those described for constant strain rate experiments. Creep experiments present higher strains at failure than constant strain rate experiments. This shows that the micromechanisms responsible for deformation, and the localization of damage are strain-rate dependent. As the micromechanisms are thought to be identical during constant strain rate and stress-stepping creep experiments (chapter 3), stress-stepping creep experiments are modelled in an almost similar manner as the constant strain rate experiments (chapter 4). However, subcritical crack growth is added in order to account for the evolution of damage during constant stress steps at low confining pressure. Despite the limited number of parameters,

model predictions are in qualitative agreement with experimental results presented in chapter 4. The values of the parameters relevant to the plastic law in this study are not equal to those used in chapter 2. An explanation could be that micro-physical phenomena responsible for the deformation are likely to have kinetic limits that depend on the applied conditions.

As shown in chapters 3 and 4, many of the micro-mechanisms responsible for deformation are time-dependent. Thus, strain rate is likely to be an influential parameter on the mechanical behaviour. Thus, an experimental study is carried out on the role of strain rate on deformation and rupture under triaxial stresses at room temperature in dry conditions. Only two confining pressures were used: one corresponding to a brittle behaviour and one corresponding to a semibrittle one (20 MPa and 85 MPa, respectively). At each confinement, three samples were deformed up to failure at strain rate of 10^{-5}s^{-1} , 10^{-6}s^{-1} and 10^{-7}s^{-1} . In the brittle regime, the strain rate has no influence on the onset of dilatancy but axial strain and differential stress at rupture increase with decreasing strain rate. This is opposite to what we expected if we consider that subcritical crack growth should become more and more important as the deformation strain rate decreases. We explain these results by a slight porosity reduction due to some plasticity processes. In the semibrittle regime, the ductile behaviour increases with decreasing strain rate, leading to much higher axial strain at rupture as the strain rate is decreased. These results were expected as low strain rate favour plastic phenomena.

All these results show that the mechanical behaviour of limestone is complex and highly dependant on the confining pressure. Many parameters such as pore fluid, temperature and strain rate, have a major impact on the micro-mechanisms responsible for deformation and thus on the macroscopic behaviour.

Perspectives

Elastic wave velocities can allow to infer deformation mechanisms (chapter 1), especially to discriminate between plasticity in grains and grain crushing. However, microstructural study should be carried out on the samples deformed under constant stress (chapter 3) and on samples deformed at various constant strain rates (chapter 5). These microstructural studies could confirm that micro-plasticity is involved in deformation processes, and will be carried out.

Conclusions & Perspectives

Concerning experiments focused on the effect of strain rate, a more systematic study should be performed to validate the results, especially owing to the increase of the peak stress with decreasing strain rate in the brittle regime. Moreover, the experimental results should be compared to model predictions from the model developed in chapter 2. Finally, these experiments were conducted on dry samples. Water-saturation can induce an undrained behaviour, which decreases the effective pressure. Constant strain rate deformation experiments performed in water-saturated conditions at different strain rate could thus lead to brittle and semibrittle behaviours, depending on the strain rate.

In this study, the evolution of permeability during deformation was not systematically measured. It is well known that porosity and crack density changes can induce changes of permeability (e.g. [David et al., 1994](#)). For example, inelastic compaction at constant stress could induce a permeability decrease. This would be interesting to verify.

Models developed in this work (chapter 2 and 4) do not account for crack blunting. However, elastic wave velocities recoveries are observed in nature. These recoveries could be due to crack blunting. Models could be modified to take crack blunting into account. Pressure-solution is not considered but could induce significant strain, especially for long-term predictions. It could be added to the models. Taking into account these effects, model predictions could be compared to field measurements.

All results presented in this manuscript were obtained on white Tavel limestone. Yet, the microstructure of limestones has a major influence on the mechanical behaviour ([Regnet et al., 2015b](#)). The effect of microstructure on the mechanical behaviour should be studied systematically in constant strain rate experiments on limestones presenting similar porosities but different microstructures.

The mechanisms of deformation depend on the porosity (see the discussion in chapter 2). To my knowledge, few experiments were carried out on limestones of porosities included between 16% and 25%, where a transitional behaviour is expected. This could be of great interest.

The mechanisms of deformation of very porous ($\phi \geq 25\%$) limestones are mainly grain crushing (see the discussion in chapter 2), which is similar to what is observed in porous sandstones. Thus, very porous limestones deformed under constant stress could have a behaviour similar to that recently presented in ([Heap et al., 2015](#)). This could be verified, and would extend the

results presented in chapter 3.

Finally, this work focuses on centimetric samples carefully chosen; which is far from natural settings often presenting heterogeneities at many scales. The role of heterogeneities should be studied carefully. Heterogeneities include macroscale faulting, and the presence of second-phase particles which may have an influence on the mechanical behaviour ([Dresen & Evans, 1993](#)). A comparison of model predictions with observations from natural settings could also provide a useful basis to validate our predictions.

Une citation de Victor Hugo avait ouvert ce manuscrit. Pour le refermer, je propose un post-scriptum s'y référant:

De toutes époques les hommes ont eu besoin de comprendre leur environnement, d'expliquer les phénomènes naturels pour donner ainsi du sens à leur existence. C'est le triomphe du "savoir" et du "penser". Ainsi, les grands mythes de l'humanité, qui remontent sûrement plus loin que l'antiquité, fournissaient les explications sur les réalités de notre monde. Combien de générations d'hommes pour observer le monde, la nature et construire des explications rassurantes grâce à une pensée collective? Le siècle des lumières européen a accéléré l'utilisation d'une démarche scientifique rationnelle et expérimentale pour les observations. Ainsi, la compréhension de notre monde s'est améliorée de façon prodigieuse. Les progrès scientifiques ont toujours mieux expliqué les "comment" de tous les phénomènes qui régissent l'univers. Ce faisant les "pourquoi" n'ont pas eu de nouvelles explications et ne sont pas considérés dans le champ du domaine scientifique. Cette circonscription du champ scientifique au "comment" laisse la part belle aux rêves, aux poètes et aux croyances. Finalement, avec le rêve, tout est là.

Les progrès scientifiques sont de plus en plus rapides et de plus en plus importants. Nous en savons toujours plus sur notre monde, car les sciences sont cumulatives. Chaque génération approfondit les acquis des précédentes de plus en plus vite. Pourtant, à la veille de l'ouverture de la conférence COP21, il convient d'admettre que malgré les progrès scientifiques, notre planète affiche une dégradation préoccupante et qui n'est plus maîtrisée. De plus, si nous savons explorer l'univers, nous avons de grandes difficultés pour faire vivre les Hommes. Finalement, la nature humaine ne change pas et chaque génération refait la même expérience de sa compréhension intime du "moi", et de son rapport aux générations précédentes. C'est pourquoi le temps n'est pas du même ordre entre les sciences dures et les sciences humaines. C'est aussi pourquoi chaque génération doit (ré)apprendre à maîtriser les techniques et à leur donner un sens au service de l'humanité.

BIBLIOGRAPHY

- Amitrano, D. & Helmstetter, A. (2006). Brittle creep, damage, and time to failure in rocks. *Journal of Geophysical Research: Solid Earth (1978–2012)*, 111(B11).
- Armijo, R., Lyon-Caen, H., & D., P. (1992). East-west extension and holocene normal-fault scarps in the hellenic arc. *Geology*, 20, 491–494.
- Ashby, M. & Hallam, S. (1986). The failure of brittle solids containing small cracks under compressive stress states. *Acta Metallurgica*, 34(3), 497 – 510.
- Ashby, M. & Sammis, C. G. (1990). The damage mechanics of brittle solids in compression. *Pure and Applied Geophysics*, 133, 489–521.
- Atkinson, B. K. (1984). Subcritical crack growth in geological materials. *Journal of Geophysical Research: Solid Earth (1978–2012)*, 89(B6), 4077–4114.
- Atkinson, B. K. & Meredith, P. (1987). *Fracture Mechanics of Rock*, chapter The theory of subcritical crack growth with applications to minerals and rocks, (pp. 111–166). Academic Press, London.
- Ayling, M. R., Meredith, P. G., & Murrell, S. A. (1995). Microcracking during triaxial deformation of porous rocks monitored by changes in rock physical properties, i. elastic-wave propagation measurements on dry rocks. *Tectonophysics*, 245(3), 205–221.
- Baud, P. & Meredith, P. (1997). Damage accumulation during triaxial creep of Darley Dale sandstone from pore volumetry and acoustic emission. *International Journal of Rock Mechanics and Mining Sciences*, 34(3), 24–e1.
- Baud, P., Schubnel, A., & Wong, T.-f. (2000a). Dilatancy, compaction, and failure mode in Solnhofen limestone. *Journal of Geophysical Research: Solid Earth*, 105(B8), 19289–19303.
- Baud, P., Vinciguerra, S., David, C., Cavallo, A., Walker, E., & Reuschlé, T. (2009). Compaction and failure in high porosity carbonates: Mechanical data and microstructural observations. (pp. 869–898).
- Baud, P., Zhu, W., & Wong, T.-f. (2000b). Failure mode and weakening effect of water on sandstone. *Journal of Geophysical Research: Solid Earth*, 105(B7), 16371–16389.

Bibliography

- Bemer, E. & Lombard, J. (2010). From injectivity to integrity studies of CO₂ geological storage chemical alteration effects on carbonates petrophysical and geomechanical properties. *Oil Gas Sci. Technol.-Rev. IFP*, 65, 445–459.
- Benson, P., Schubnel, A., Vinciguerra, S., Trovato, C., Meredith, P., & Young, R. P. (2006). Modeling the permeability evolution of microcracked rocks from elastic wave velocity inversion at elevated isostatic pressure. *Journal of Geophysical Research: Solid Earth*, 111(B4), n/a–n/a.
- Bhat, H., Sammis, C., & Rosakis, A. (2011). The micromechanics of westerley granite at large compressive loads. 168(12), 2181–2198–.
- Bhat, H. S., Rosakis, A. J., & Sammis, C. G. (2012). A micromechanics based constitutive model for brittle failure at high strain rates. *Journal of Applied Mechanics*, 79(3), 031016.
- Boutéca, M., Sarda, J., & Schneider, F. (1996). Subsidence induced by the production of fluids. *Rev. Inst. Fr. Pet.*, 51, 349–379.
- Brace, W. (1978). Volume changes during fracture and frictional sliding: A review. *Pure Appl. Geophys.*, 116, 603–614.
- Brace, W. & Kohlstedt, D. (1980). Limits on lithospheric stress imposed by laboratory experiments. *Journal of Geophysical Research: Solid Earth*, 85(B11), 6248–6252.
- Brandt, H. (1955). A study of the speed of sound in porous granular media. *J. Appl. Mech.*, 22, 479–486.
- Brantut, N., Baud, P., Heap, M., & Meredith, P. (2012). Micromechanics of brittle creep in rocks. *Journal of Geophysical Research: Solid Earth (1978–2012)*, 117(B8).
- Brantut, N., Heap, M., Baud, P., & Meredith, P. (2014a). Rate-and strain-dependent brittle deformation of rocks. *Journal of Geophysical Research: Solid Earth*, 119(3), 1818–1836.
- Brantut, N., Heap, M., Meredith, P., & Baud, P. (2013). Time-dependent cracking and brittle creep in crustal rocks: A review. *Journal of Structural Geology*, 52, 17–43.
- Brantut, N., Heap, M. J., Baud, P., & Meredith, P. G. (2014b). Mechanisms of time-dependent deformation in porous limestone. *Journal of Geophysical Research: Solid Earth*, 119(7), 5444–5463.
- Brantut, N., Schubnel, A., Corvisier, J., & Sarout, J. (2010). Thermochemical pressurization of faults during coseismic slip. *Journal of Geophysical Research: Solid Earth (1978–2012)*, 115(B5).
- Brantut, N., Schubnel, A., & Guéguen, Y. (2011). Damage and rupture dynamics at the brittle-ductile transition: The case of gypsum. *Journal of Geophysical Research: Solid Earth*, 116(B1), n/a–n/a.

- Bristow, J. R. (1960). Microcracks, and the static and dynamic elastic constants of annealed and heavily cold-worked metals. *British Journal of Applied Physics*, 11(2), 81.
- Bruno, M. et al. (1992). Subsidence-induced well failure. *SPE Drilling Engineering*, 7(02), 148–152.
- Budiansky, B., Hutchinson, J., & Slutsky, S. (1982). *Void growth and collapse in viscous solids*. Pergamon Press Oxford.
- Budiansky, B. & O'connell, R. J. (1976). Elastic moduli of a cracked solid. *International Journal of Solids and Structures*, 12(2), 81–97.
- Burkhard, M. (1993). Calcite twins, their geometry, appearance and significance as stress-strain markers and indicators of tectonic regime: a review. *Journal of Structural Geology*, 15(3), 351–368.
- Byerlee, J. (1978). Friction of rocks. *Pure and applied geophysics*, 116(4-5), 615–626.
- Carroll, M. & Holt, A. (1972). Static and dynamic pore-collapse relations for ductile porous materials. *Journal of Applied Physics*, 43(4), 1626–1636.
- Carslaw, H. S. & Jaeger, J. C. (1959). *Conduction of heat in solids*. Oxford: Clarendon Press, 1959, 2nd ed., 1.
- Charles, R. (1958). Static fatigue of glass. i. *Journal of Applied Physics*, 29(11), 1549–1553.
- Chester, F. M. (1988). The brittle-ductile transition in a deformation-mechanism map for halite. *Tectonophysics*, 154(1), 125–136.
- Chester, F. M. (1995). A rheologic model for wet crust applied to strike-slip faults. *Journal of Geophysical Research: Solid Earth (1978–2012)*, 100(B7), 13033–13044.
- Ciccotti, M. & Mulargia, F. (2004). Differences between static and dynamic elastic moduli of a typical seismogenic rock. *Geophysical Journal International*, 157(1), 474–477.
- Clarke, D., Lawn, B., & Roach, D. (1986). *The role of surface forces in fracture*. Springer.
- Costin, L. (1987). *Fracture Mechanics of Rock*, chapter Time-dependent deformation and failure, (pp. 167–216). Academic Press, London.
- Cotterell, B. & Rice, J. R. (1980). Slightly curved or kinked cracks. *International Journal of Fracture*, 16, 155–169.
- Croize, D., Renard, F., & Gratier, J.-P. (2013). Compaction and porosity reduction in carbonates: A review of observations, theory, and experiments. *Advances in Geophysics*, 54, 181–238.

Bibliography

- Curran, J. H. & Carroll, M. M. (1979). Shear stress enhancement of void compaction. *Journal of Geophysical Research: Solid Earth*, 84(B3), 1105–1112.
- Danas, K. & Castaneda, P. P. (2012). Influence of the lode parameter and the stress triaxiality on the failure of elasto-plastic porous materials. *International Journal of Solids and Structures*, 49(11-12), 1325 – 1342.
- Darot, M. & Gueguen, Y. (1986). Slow crack growth in minerals and rocks: Theory and experiments. *Pure and Applied Geophysics*, 124(4-5), 677–692.
- Dautriat, J., Bornert, M., Gland, N., Dimanov, A., & Raphanel, J. (2011a). Localized deformation induced by heterogeneities in porous carbonate analysed by multi-scale digital image correlation. *Tectonophysics*, 503(1), 100–116.
- Dautriat, J., Gland, N., Dimanov, A., & Raphanel, J. (2011b). Hydromechanical behavior of heterogeneous carbonate rock under proportional triaxial loadings. *Journal of Geophysical Research: Solid Earth (1978–2012)*, 116(B1).
- David, C., Wong, T.-F., Zhu, W., & Zhang, J. (1994). Laboratory measurement of compaction-induced permeability change in porous rocks: Implications for the generation and maintenance of pore pressure excess in the crust. *Pure and Applied Geophysics*, 143(1), 425–456.
- De Bresser, J. (1996). Steady state dislocation densities in experimentally deformed calcite materials: single crystals versus polycrystals. *Journal of Geophysical Research: Solid Earth (1978–2012)*, 101(B10), 22189–22201.
- De Bresser, J. & Spiers, C. (1997). Strength characteristics of the r, f, and c slip systems in calcite. *Tectonophysics*, 272(1), 1–23.
- de Leeuw, N. & Parker, S. (1997). Atomistic simulation of the effect of molecular adsorption of water on the surface structure and energies of calcite surfaces. *Journal of the Chemical Society, Faraday Transactions*, 93(3), 467–475.
- Deshpande, V. & Evans, A. G. (2008). Inelastic deformation and energy dissipation in ceramics: A mechanism-based constitutive model. *Journal of the Mechanics and Physics of Solids*, 56, 3077–3100.
- Dimanov, A., Rybacki, E., Wirth, R., & Dresen, G. (2007). Creep and strain-dependent microstructures of synthetic anorthite–diopside aggregates. *Journal of Structural Geology*, 29(6), 1049–1069.
- Dresen, G. & Evans, B. (1993). Brittle and semibrittle deformation of synthetic marbles composed of two phases. *Journal of Geophysical Research: Solid Earth (1978–2012)*, 98(B7), 11921–11933.

- Duda, M. & Renner, J. (2013). The weakening effect of water on the brittle failure strength of sandstone. *Geophysical Journal International*, 192(3), 1091–1108.
- Dunning, J., Douglas, B., Miller, M., & McDonald, S. (1994). The role of the chemical environment in frictional deformation: stress corrosion cracking and comminution. *Pure and Applied Geophysics*, 143(1-3), 151–178.
- Dusseault, M. B. & Fordham, C. J. (1993). Time-dependent behavior of rocks. *Comprehensive Rock Engineering Principles, Practice and Project: Rock Testing and Site Characterization*, 3, 119–149.
- Duva, J. & Hutchinson, J. (1984). Constitutive potentials for dilutely voided nonlinear materials. *Mechanics of materials*, 3(1), 41–54.
- Edmond, J. & Paterson, M. (1972). Volume changes during the deformation of rocks at high pressures. *Int. J. Rock Mech. Min. Sci*, 9(2), 161–182.
- Eissa, E. & Kazi, A. (1988). Relation between static and dynamic young's moduli of rocks. In *International Journal of Rock Mechanics and Mining Sciences & Geomechanics Abstracts*, volume 25 (pp. 479–482).: Elsevier.
- Eshelby, J., Frank, E., & Nabarro, F. (1951). The equilibrium of linear arrays of dislocations. *The London, Edinburgh, and Dublin Philosophical Magazine and Journal of Science*, 42(327), 351–364.
- Evans, A., Meyer, M., Fertig, K., Davis, B., & Baumgartner, H. (1980). Probabilistic models for defect initiated fracture in ceramics. 1(2), 111–122–.
- Evans, B., Fredrich, J. T., & Wong, T.-F. (1990). The brittle-ductile transition in rocks: recent experimental and theoretical progress. *The Brittle-Ductile Transition in Rocks*, (pp. 1–20).
- Evans, M. A. & Groshong, R. H. (1994). A computer program for the calcite strain-gauge technique. *Journal of Structural Geology*, 16(2), 277–281.
- Faleskog, J. & Shih, C. F. (1997). Micromechanics of coalescence—i. synergistic effects of elasticity, plastic yielding and multi-size-scale voids. *Journal of the Mechanics and Physics of Solids*, 45(1), 21–50.
- Fiona, T. & Cook, J. (1995). Effects of stress cycles on static and dynamic young's moduli in castlegate sandstone. (pp. 155).
- Fortin, J., Guéguen, Y., & Schubnel, A. (2007). Effects of pore collapse and grain crushing on ultrasonic velocities and V_p/V_s . *Journal of Geophysical Research: Solid Earth*, 112(B8).

Bibliography

- Fortin, J., Schubnel, A., & Guéguen, Y. (2005). Elastic wave velocities and permeability evolution during compaction of bleurswiller sandstone. *International Journal of Rock Mechanics and Mining Sciences*, 42(7), 873–889.
- Fortin, J., Stanchits, S., Vinciguerra, S., & Guéguen, Y. (2011). Influence of thermal and mechanical cracks on permeability and elastic wave velocities in a basalt from mt. etna volcano subjected to elevated pressure. *Tectonophysics*, 503(1), 60–74.
- Fredrich, J. T., Arguello, J. G., Deitrick, G. L., & de Rouffignac, E. P. (2000). Geomechanical modeling of reservoir compaction, surface subsidence, and casing damage at the Belridge diatomite field. *SPE Reservoir Eval. Eng.*, 3, 348–359.
- Fredrich, J. T., Evans, B., & Wong, T.-F. (1989). Micromechanics of the brittle to plastic transition in Carrara marble. *Journal of Geophysical Research: Solid Earth*, 94(B4), 4129–4145.
- Fredrich, J. T., Evans, B., & Wong, T.-F. (1990). Effect of grain size on brittle and semibrittle strength: Implications for micromechanical modelling of failure in compression. *Journal of Geophysical Research: Solid Earth (1978–2012)*, 95(B7), 10907–10920.
- Ge, S. & Stover, S. C. (2000). Hydrodynamic response to strike-and dip-slip faulting in a half-space. *Journal of Geophysical Research: Solid Earth (1978–2012)*, 105(B11), 25513–25524.
- Ghabezloo, S. (2015). A micromechanical model for the effective compressibility of sandstones. *European Journal of Mechanics-A/Solids*, 51, 140–153.
- Grechka, V. & Kachanov, M. (2006). Effective elasticity of fractured rocks: A snapshot of the work in progress. *Geophysics*, 71, W45–W58.
- Griggs, D. T., Turner, F. J., & Heard, H. C. (1960). Chapter 4: Deformation of rocks at 500° to 800°C. *Geological Society of America Memoirs*, 79, 39–104.
- Guéguen, Y. & Boutéca, M. (1999). Mechanical properties of rocks: pore pressure and scale effects. *Oil & Gas Science and Technology*, 54(6), 703–714.
- Guéguen, Y. & Boutéca, M. (2004). *Mechanics of fluid-saturated rocks*, volume 89. Academic Press.
- Guéguen, Y. & Fortin, J. (2013). Elastic envelopes of porous sandstones. *Geophysical Research Letters*, 40(14), 3550–3555.
- Guéguen, Y. & Kachanov, M. (2011). Effective elastic properties of cracked rocks—an overview. In *Mechanics of Crustal Rocks* (pp. 73–125). Springer.

- Guéguen, Y. & Palciauskas, V. (1994). Introduction to the physics of rocks.
- Gunzburger, Y. (2010). Stress state interpretation in light of pressure-solution creep: Numerical modelling of limestone in the eastern paris basin, france. *Tectonophysics*, 483(3), 377–389.
- Heap, M., Baud, P., & Meredith, P. (2009a). Influence of temperature on brittle creep in sandstones. *Geophysical Research Letters*, 36(19), doi: 10.1029/2009GL039373.
- Heap, M., Baud, P., Meredith, P., Bell, A., & Main, I. (2009b). Time-dependent brittle creep in darley dale sandstone. *Journal of Geophysical Research: Solid Earth (1978–2012)*, 114(B7).
- Heap, M., Baud, P., Meredith, P., Vinciguerra, S., Bell, A., & Main, I. (2011). Brittle creep in basalt and its application to time-dependent volcano deformation. *Earth and Planetary Science Letters*, 307(1), 71–82.
- Heap, M., Mollo, S., Vinciguerra, S., Lavallée, Y., Hess, K.-U., Dingwell, D., Baud, P., & Iezzi, G. (2013). Thermal weakening of the carbonate basement under mt. etna volcano (italy): Implications for volcano instability. *Journal of Volcanology and Geothermal Research*, 250(0), 42 – 60.
- Heap, M. J., Brantut, N., Baud, P., & Meredith, P. G. (2015). Time-dependent compaction band formation in sandstone. *Journal of Geophysical Research: Solid Earth*, (pp. n/a–n/a). 2015JB012022.
- Heard, H. & Raleigh, C. (1972). Steady-state flow in marble at 500 to 800 c. *Geological Society of America Bulletin*, 83(4), 935–956.
- Heard, H. C. (1960). Chapter 7: Transition from brittle fracture to ductile flow in Solenhofen limestone as a function of temperature, confining pressure, and interstitial fluid pressure. *Geological Society of America Memoirs*, 79, 193–226.
- Henry, J. P., Paquet, J., & Tancrez, J. (1977). Experimental study of crack propagation in calcite rocks. *International Journal of Rock Mechanics and Mining Sciences & Geomechanics Abstracts*, 14(2), 85–91.
- Hexsel Grochau, M., Monteiro Benac, P., de Magalhaes Alvim, L., Sansonowski, R. C., da Motta Pires, P. R., & Villaudy, F. (2014). Brazilian carbonate reservoir: A successful seismic time-lapse monitoring study. *The Leading Edge*, 33, no. 2, 164–170.
- Hirth, J. P. & Lothe, J. (1982). Theory of dislocations.
- Holder, J., Olson, J. E., & Philip, Z. (2001). Experimental determination of subcritical crack growth parameters in sedimentary rock. *Geophysical Research Letters*, 28(4), 599–602.

Bibliography

- Homand, F., Duffaut, P., Berest, P., Billiaux, D., Boulon, M., Cornet, F., David, C., Durville, J.-L., Gentier, S., Giraud, A., et al. (2000). Manuel de mécanique des roches (tome 1, fondements).
- Horii, H. & Nemat-Nasser, S. (1986). Brittle failure in compression-splitting, faulting and brittle-ductile transition. *Philosophical Transactions of the Royal Society: A - Mathematical Physical and Engineering Sciences*, 319, 337–374.
- Hugman III, R. & Friedman, M. (1979). Effects of texture and composition on mechanical behavior of experimentally deformed carbonate rocks. *AAPG Bulletin*, 63(9), 1478–1489.
- Ji, Y., Hall, S. A., Baud, P., & Wong, T.-f. (2015). Characterization of pore structure and strain localization in majella limestone by x-ray computed tomography and digital image correlation. *Geophysical Journal International*, 200(2), 701–719.
- Johnson, H. H. & Paris, P. C. (1968). Sub-critical flaw growth. *Engineering Fracture Mechanics*, 1(1), 3–45.
- Kachanov, M. (1993). Elastic solids with many cracks and related problems.
- Karner, S. L., Chester, F. M., Kronenberg, A. K., & Chester, J. S. (2003). Subcritical compaction and yielding of granular quartz sand. *Tectonophysics*, 377(3), 357–381.
- Kassner, M. (2004). Taylor hardening in five-power-law creep of metals and class m alloys. *Acta materialia*, 52(1), 1–9.
- Kemeny, J. M. & Cook, N. G. (1991). Micromechanics of deformation in rocks. *Toughening Mechanisms in Quasi-Brittle Materials, NATO ASI Series*, (pp. 155–188).
- Kinloch, A. & Williams, J. (1980). Crack blunting mechanisms in polymers. *Journal of Materials Science*, 15(4), 987–996.
- Kirby, S. H. (1980). Tectonic stresses in the lithosphere: constraints provided by the experimental deformation of rocks. *Journal of Geophysical Research: Solid Earth (1978–2012)*, 85(B11), 6353–6363.
- Kohlstedt, D., Evans, B., Mackwell, S., et al. (1995). Strength of the lithosphere: constraints imposed by laboratory experiments. *JOURNAL OF GEOPHYSICAL RESEARCH-ALL SERIES-*, 100, 17–587.
- Kranz, R. L. (1979). Crack growth and development during creep of barre granite. 16(1), 23–35.
- Kümpel, H.-J. (1991). Poroelasticity: parameters reviewed. *Geophysical Journal International*, 105(3), 783–799.

- Lavenu, A. P., Lamarche, J., Gallois, A., & Gauthier, B. D. (2013). Tectonic versus diagenetic origin of fractures in a naturally fractured carbonate reservoir analog (nerthe anticline, southeastern france). *AAPG bulletin*, 97(12), 2207–2232.
- Lawn, B. (1975). An atomistic model of kinetic crack growth in brittle solids. *Journal of Materials Science*, 10(3), 469–480.
- Lawn, B. R. (1993). *Fracture of brittle solids*. Cambridge university press.
- Liteanu, E., Spiers, C., & de Bresser, J. (2013). The influence of water and supercritical co₂ on the failure behavior of chalk. *Tectonophysics*, 599, 157–169.
- Lockner, D. (1993). Room temperature creep in saturated granite. *Journal of Geophysical Research: Solid Earth (1978–2012)*, 98(B1), 475–487.
- Lockner, D. & Byerlee, J. (1977). Acoustic emission and creep in rock at high confining pressure and differential stress. *Bulletin of the Seismological Society of America*, 67(2), 247–258.
- Lockner, D., Byerlee, J., Kuksenko, V., Ponomarev, A., & Sidorin, A. (1992). Observations of quasistatic fault growth from acoustic emissions. *International Geophysics*, 51, 3–31.
- Lønøy, A. (2006). Making sense of carbonate pore systems. *AAPG bulletin*, 90(9), 1381–1405.
- Mackenzie, J. K. (1950). The elastic constants of a solid containing spherical holes. *Proceedings of the Physical Society. Section B*, 63(1), 2.
- Mallet, C. (2014). *Etude de la fissuration des verres de stockage, Comportement en condition de stockage géologique*. PhD thesis, Ecole Normale Supérieure.
- Mallet, C., Fortin, J., Guéguen, Y., & Bouyer, F. (2013). Effective elastic properties of cracked solids: an experimental investigation. *International journal of fracture*, 182(2), 275–282.
- Mallet, C., Fortin, J., Guéguen, Y., & Bouyer, F. (2014). Evolution of the crack network in glass samples submitted to brittle creep conditions. *International Journal of Fracture*, 190(1-2), 111–124.
- Mallet, C., Fortin, J., Guéguen, Y., & Bouyer, F. (2015). Brittle creep and subcritical crack propagation in glass submitted to triaxial conditions. *Journal of Geophysical Research: Solid Earth*, 120(2), 879–893.
- Mavko, G., Mukerji, T., & Dvorkin, J. (1998). *The Rock Physics Handbook: Tools for Seismic Analysis in Porous Media*, 329 pp. Cambridge Univ. Press, Cambridge, UK.
- Mavko, G., Mukerji, T., & Godfrey, N. (1995). Predicting stress-induced velocity anisotropy in rocks. *Geophysics*, 60(4), 1081–1087.

Bibliography

- McMeeking, R. M. (1977). Finite deformation analysis of crack-tip opening in elastic-plastic materials and implications for fracture. *Journal of the Mechanics and Physics of Solids*, 25(5), 357–381.
- Meredith, P. & Atkinson, B. (1985). Fracture toughness and subcritical crack growth during high-temperature tensile deformation of westerly granite and black gabbro. *Physics of the earth and planetary interiors*, 39(1), 33–51.
- Meyers, M. A., Armstrong, R. W., & Kirchner, H. O. (1999). *Mechanics and materials: fundamentals and linkages*. Wiley-VCH.
- Miguel, M.-C., Vespignani, A., Zapperi, S., Weiss, J., & Grasso, J.-R. (2001). Intermittent dislocation flow in viscoplastic deformation. *Nature*, 410(6829), 667–671.
- Miller, S. A. (2002). Properties of large ruptures and the dynamical influence of fluids on earthquakes and faulting. *Journal of Geophysical Research: Solid Earth*, 107(B9), ESE 3–1–ESE 3–13.
- Mollema, P. & Antonellini, M. (1996). Compaction bands: a structural analog for anti-mode I cracks in aeolian sandstone. *Tectonophysics*, 267(1), 209–228.
- Morton, R. A., Bernier, J. C., & Barras, J. A. (2006). Evidence of regional subsidence and associated interior wetland loss induced by hydrocarbon production, gulf coast region, usa. *Environmental Geology*, 50(2), 261–274.
- Mouslopoulou, V., Moraetis, D., Benedetti, L., Guillou, V., Bellier, O., & Hristopulos, D. (2014). Normal faulting in the forearc of the hellenic subduction margin: Paleoearthquake history and kinematics of the spili fault, crete, greece. *Journal of Structural Geology*, 66(0), 298 – 308.
- Nagel, N. (2001). Compaction and subsidence issues within the petroleum industry: From Wilmington to Ekofisk and beyond. *Physics and chemistry of the earth. Part A*, 26, 3–14.
- Nasseri, M., Schubnel, A., & Young, R. (2007). Coupled evolutions of fracture toughness and elastic wave velocities at high crack density in thermally treated westerly granite. *International Journal of Rock Mechanics and Mining Sciences*, 44(4), 601–616.
- Nelson, R. (2001). *Geologic analysis of naturally fractured reservoirs*. Gulf Professional Publishing.
- Nemat-Nasser, S. & Horii, H. (1982). Compression-induced nonplanar crack extension with application to splitting, exfoliation, and rockburst. *Journal of Geophysical Research: Solid Earth*, 87(B8), 6805–6821.

- Niemeijer, A., Spiers, C., & Bos, B. (2002). Compaction creep of quartz sand at 400–600 c: Experimental evidence for dissolution-controlled pressure solution. *Earth and Planetary Science Letters*, 195(3), 261–275.
- Olson, J. E. (2003). Sublinear scaling of fracture aperture versus length: an exception or the rule? *Journal of Geophysical Research: Solid Earth (1978–2012)*, 108(B9).
- Olusunle, S., Siyanbola, W., Adetunji, A., & Adewoye, O. (2009). Effect of buffer solutions on the flow and fracture in calcite. *Journal of Minerals and Materials Characterization and Engineering*, 8(03), 189.
- Orowan, E. (1944). The fatigue of glass under stress. *Nature*, 154(3906), 341–343.
- Orowan, E. (1954). Dislocations in metals. *AIME, New York*, 131.
- Ougier-Simonin, A., Fortin, J., Guéguen, Y., Schubnel, A., & Bouyer, F. (2011). Cracks in glass under triaxial conditions. *International Journal of Engineering Science*, 49(1), 105 – 121. Recent Advances in Micromechanics of Materials.
- Paterson, M. (1958). Experimental deformation and faulting in Wombeyan marble. *Geological Society of America Bulletin*, 69(4), 465–476.
- Paterson, M. (1978). *Experimental Rock deformation: the Brittle Field*. Springer-Verlag, New York.
- Paterson, M. S. & Wong, T.-f. (2005). *Experimental Rock Deformation - The Brittle Field*. Springer Verlag.
- Peng, S. & Johnson, A. (1972). Crack growth and faulting in cylindrical specimens of chelmsford granite. *International Journal of Rock Mechanics and Mining Sciences & Geomechanics Abstracts*, 9(1), 37–86.
- Peška, P & Zoback, M. D. (1995). Compressive and tensile failure of inclined well bores and determination of in situ stress and rock strength. *Journal of Geophysical Research: Solid Earth (1978–2012)*, 100(B7), 12791–12811.
- Pimienta, L., Fortin, J., & Guéguen, Y. (2015). Bulk modulus dispersion and attenuation in sandstones. *Geophysics*, 80(2), D111–D127.
- Pollard, D. & Segall, P. (1987). Theoretical displacements and stresses near fractures in rock: with applications to faults, joints, veins, dikes, and solution surfaces. *Fracture mechanics of rock*, 277(349), 277–349.
- Regnet, J., Robion, P., David, C., Fortin, J., Brigaud, B., & Yven, B. (2015a). Acoustic and reservoir properties of microporous carbonate rocks: Implication of micrite particle size and morphology. *Journal of Geophysical Research: Solid Earth*, 120(2), 790–811.

Bibliography

- Regnet, J. B., David, C., Fortin, J., Robion, P., Makhloufi, Y., & Collin, P. (2015b). Influence of microporosity distribution on the mechanical behaviour of oolitic carbonate rocks. *Geomechanics for Energy and the Environment*.
- Renner, J. & Evans, B. (2002). Do calcite rocks obey the power-law creep equation? *Geological Society, London, Special Publications*, 200(1), 293–307.
- Renner, J., Evans, B., & Siddiqi, G. (2002). Dislocation creep of calcite. *Journal of Geophysical Research: Solid Earth*, 107(B12), ECV 6–1–ECV 6–16.
- Renshaw, C. & Park, J. (1997). Effect of mechanical interactions on the scaling of fracture length and aperture. *Nature*.
- Rhett, D. W. & Farrell, H. E. (1991). Effect of reservoir depletion and pore pressure drawdown on in situ stress and deformation in the ekofisk field, north sea. 32, 63.
- Rice, J. & Tracey, D. (1969). On the ductile enlargement of voids in triaxial stress fields. *Journal of the Mechanics and Physics of Solids*, 17(3), 201 – 217.
- Risnes, R., Madland, M., Hole, M., & Kwabiah, N. (2005). Water weakening of chalk: Mechanical effects of water-glycol mixtures. *Journal of Petroleum Science and Engineering*, 48(1), 21–36.
- Robertson, E. C. (1955). Experimental study of the strength of rocks. *Geological Society of America Bulletin*, 66(10), 1275–1314.
- Ross, J. V. & Lewis, P. D. (1989). Brittle-ductile transition: Semi-brittle behavior. *Tectonophysics*, 167(1), 75–79.
- Rostom, F., Røyne, A., Dysthe, D. K., & Renard, F. (2013). Effect of fluid salinity on subcritical crack propagation in calcite. *Tectonophysics*, 583, 68–75.
- Røyne, A., Bisschop, J., & Dysthe, D. K. (2011). Experimental investigation of surface energy and subcritical crack growth in calcite. *Journal of Geophysical Research: Solid Earth (1978–2012)*, 116(B4).
- Røyne, A., Dalby, K. N., & Hassenkam, T. (2015). Repulsive hydration forces between calcite surfaces and their effect on the brittle strength of calcite bearing rocks. *Geophysical Research Letters*.
- Royne, A., Dysthe, D., & Bisschop, J. (2008). Mechanisms of subcritical cracking in calcite. 1, 1857.
- Rutter, E. (1974a). Influence of temperature, strain rate and interstitial water in experimental deformation of calcite rocks. *Tectonophysics*, 22, 311 –334.

- Rutter, E. (1986). On the nomenclature of mode of failure transitions in rocks. *Tectonophysics*, 122(3), 381–387.
- Rutter, E. & Mainprice, D. (1978). The effect of water on stress relaxation of faulted and unfaulted sandstone. *Pure and Applied Geophysics*, 116(4-5), 634–654.
- Rutter, E. H. (1972). The influence of interstitial water on the rheological behaviour of calcite rocks. *Tectonophysics*, 14(1), 13–33.
- Rutter, E. H. (1974b). The influence of temperature, strain rate and interstitial water in the experimental deformation of calcite rocks. *Tectonophysics*, 22(3), 311–334.
- Sammis, C. & Ashby, M. (1986). The failure of brittle porous solids under compressive stress states. *Acta Metallurgica*, 34(3), 511–526.
- Sangha, C., Talbot, C., & Dhir, R. (1974). Microfracturing of a sandstone in uniaxial compression. 11(3), 107–113.
- Sayers, C. M. & Kachanov, M. (1995). Microcrack-induced elastic wave anisotropy of brittle rocks. *Journal of Geophysical Research: Solid Earth*, 100(B3), 4149–4156.
- Schmid, S. (1976). Rheological evidence for changes in the deformation mechanism of solenhofen limestone towards low stresses. *Tectonophysics*, 31(1), T21–T28.
- Scholz, C. (1968). Mechanism of creep in brittle rock. *Journal of Geophysical Research*, 73(10), 3295–3302.
- Schubnel, A., Benson, P. M., Thompson, B. D., Hazzard, J. F., & Young, R. P. (2006a). Quantifying damage, saturation and anisotropy in cracked rocks by inverting elastic wave velocities. (pp. 947–973).
- Schubnel, A., Brunet, F., Hilairet, N., Gasc, J., Wang, Y., & Green, H. W. (2013). Deep-focus earthquake analogs recorded at high pressure and temperature in the laboratory. *Science*, 341(6152), 1377–1380.
- Schubnel, A. & Guéguen, Y. (2003). Dispersion and anisotropy of elastic waves in cracked rocks. *Journal of Geophysical Research: Solid Earth (1978–2012)*, 108(B2).
- Schubnel, A., Walker, E., Thompson, B. D., Fortin, J., Guéguen, Y., & Young, R. P. (2006b). Transient creep, aseismic damage and slow failure in carrara marble deformed across the brittle-ductile transition. *Geophysical Research Letters*, 33(17).
- Segall, P. (1989a). Earthquakes triggered by fluid extraction. *Geology*, 17(10), 942–946.
- Segall, P. (1989b). Earthquakes triggered by fluid extraction. *Geology*, 17(10), 942–946.

Bibliography

- Shafiro, B. & Kachanov, M. (1997). Materials with fluid-filled pores of various shapes: Effective elastic properties and fluid pressure polarization. *International Journal of Solids and Structures*, 34(27), 3517 – 3540.
- Sibson, R. (1982). Fault zone models, heat-flow, and the depth distribution of earthquakes in the continental-crust of the united-states. *Bulletin of the Seismological Society of America*, 72, 151–163.
- Sibson, R. H. (1974). Frictional constraints on thrust, wrench and normal faults.
- Simmons, G. & Wang, H. (1971). *Single Crystal Elastic Constants and Calculated Aggregate Properties*. Mass. Inst. Technol. Press.
- Simpson, D., Leith, W., & Scholz, C. (1988). Two types of reservoir-induced seismicity. *Bulletin of the Seismological Society of America*, 78(6), 2025–2040.
- Smith, E. & Barnby, J. (1967). Crack nucleation in crystalline solids. *Metal Science*, 1(1), 56–64.
- Stroh, A. (1954). The formation of cracks as a result of plastic flow. 223(1154), 404–414.
- Stroh, A. N. (1957). A theory of the fracture of metals. *Advances in Physics*, 6(24), 418–465.
- Swanson, P. L. (1984). Subcritical crack growth and other time- and environment-dependent behavior in crustal rocks. *Journal of Geophysical Research: Solid Earth (1978–2012)*, 89(B6), 4137–4152.
- Tada, H., Paris, P. C., & Irwin, G. R. (2000). *The Stress Analysis of Cracks Handbook*. The American Society of Mechanical Engineers.
- Talwani, P. & Acree, S. (1984). Pore pressure diffusion and the mechanism of reservoir-induced seismicity. *Pure and Applied Geophysics*, 122(6), 947–965.
- Taylor, G. I. (1934). The mechanism of plastic deformation of crystals. part i. theoretical. *Proceedings of the Royal Society of London. Series A, Containing Papers of a Mathematical and Physical Character*, (pp. 362–387).
- Tsai, J.-C., Voth, G. A., & Gollub, J. P. (2003). Internal granular dynamics, shear-induced crystallization, and compaction steps. *Physical review letters*, 91(6), 064301.
- Turner, F. J., Griggs, D. T., & Heard, H. (1954). Experimental deformation of calcite crystals. *Geological Society of America Bulletin*, 65(9), 883–934.
- Vajdova, V., Baud, P., & Wong, T.-F. (2004). Compaction, dilatancy, and failure in porous carbonate rocks. *Journal of Geophysical Research: Solid Earth*, 109(B5).

- Vajdova, V., Baud, P., Wu, L., & fong Wong, T. (2012). Micromechanics of inelastic compaction in two allochemical limestones. *Journal of Structural Geology*, 43(0), 100 – 117.
- Vajdova, V., Zhu, W., Chen, T.-M. N., & Wong, T.-F. (2010). Micromechanics of brittle faulting and cataclastic flow in tavel limestone. *Journal of Structural Geology*, 32(8), 1158 – 1169.
- Vanel, L., Ciliberto, S., Cortet, P.-P., & Santucci, S. (2009). Time-dependent rupture and slow crack growth: Elastic and viscoplastic dynamics. *Journal of Physics D: Applied Physics*, 42(21), 214007.
- Vincké, O., Boutéca, M., & Piau, J. (1998). *Poromechanics, a Tribute to Maurice A. Biot*, chapter Study of the effective stress at failure, (pp. 635–639). A.A. Balkema, Rotterdam.
- Violay, M., Nielsen, S., Spagnuolo, E., Cinti, D., Di Toro, G., & Di Stefano, G. (2013). Pore fluid in experimental calcite-bearing faults: Abrupt weakening and geochemical signature of co-seismic processes. *Earth and planetary science letters*, 361, 74–84.
- Walsh, J. B. (1965a). The effect of cracks on the compressibility of rock. *Journal of Geophysical Research*, 70(2), 381–389.
- Walsh, J. B. (1965b). The effect of cracks on the compressibility of rock. *Journal of Geophysical Research*, 70(2), 381–389.
- Wang, X.-Q., Schubnel, A., Fortin, J., Guéguen, Y., & Ge, H.-K. (2013). Physical properties and brittle strength of thermally cracked granite under confinement. *Journal of Geophysical Research: Solid Earth*, 118(12), 6099–6112.
- Wang, Z.-C., Bai, Q., Dresen, G., Wirth, R., & Evans, B. (1996). High-temperature deformation of calcite single crystals. *Journal of Geophysical Research: Solid Earth*, 101(B9), 20377–20390.
- Waza, T., Kurita, K., & Mizutani, H. (1980). The effect of water on the subcritical crack growth in silicate rocks. *Tectonophysics*, 67(1), 25–34.
- Weertman, J., White, S., & Cook, A. H. (1978). Creep laws for the mantle of the earth [and discussion]. *Philosophical Transactions of the Royal Society of London A: Mathematical, Physical and Engineering Sciences*, 288(1350), 9–26.
- Wiederhorn, S. & Bolz, L. (1970). Stress corrosion and static fatigue of glass. *STRESS*, 3(4), 5.
- Willemse, E. J., Peacock, D. C., & Aydin, A. (1997). Nucleation and growth of strike-slip faults in limestones from Somerset, UK. *Journal of Structural Geology*, 19(12), 1461–1477.

Bibliography

- Wong, T.-F. (1990). A note on the propagation behavior of a crack nucleated by a dislocation pileup. *Journal of Geophysical Research: Solid Earth*, 95(B6), 8639–8646.
- Wong, T.-F. & Baud, P. (2012). The brittle-ductile transition in porous rock: A review. *Journal of Structural Geology*, 44(0), 25 – 53.
- Wong, T.-f., David, C., & Zhu, W. (1997). The transition from brittle faulting to cataclastic flow in porous sandstones: Mechanical deformation. *Journal of Geophysical Research: Solid Earth*, 102(B2), 3009–3025.
- Wong, T.-F., Szeto, H., & Zhang, J. (1992). Effect of loading path and porosity on the failure mode of porous rocks. *Appl. Mech. Rev.*, 45, 281–293.
- Xiao, X. & Evans, B. (2003). Shear-enhanced compaction during non-linear viscous creep of porous calcite–quartz aggregates. *Earth and Planetary Science Letters*, 216(4), 725–740.
- Zhang, J., Wong, T.-F., & Davis, D. M. (1990). Micromechanics of pressure-induced grain crushing in porous rocks. *Journal of Geophysical Research: Solid Earth (1978–2012)*, 95(B1), 341–352.
- Zhang, X. & Spiers, C. (2005). Compaction of granular calcite by pressure solution at room temperature and effects of pore fluid chemistry. *International Journal of Rock Mechanics and Mining Sciences*, 42(7), 950–960.
- Zhang, X., Spiers, C. J., & Peach, C. J. (2010). Compaction creep of wet granular calcite by pressure solution at 28°C to 150°C. *Journal of Geophysical Research: Solid Earth (1978–2012)*, 115(B9).
- Zhu, W., Baud, P., & Wong, T.-f. (2010). Micromechanics of cataclastic pore collapse in limestone. *Journal of Geophysical Research: Solid Earth (1978–2012)*, 115(B4).
- Zimmerman, R. W. (1990). *Compressibility of sandstones*. Elsevier.